Università degli studi di Napoli Federico II
Dipartimento di Ingegneria Industriale

Dottorato di Ricerca in Ingegneria Aerospaziale, Navale e della Qualità - XXVII ciclo

PhD Thesis

Volume A

On the characterization of a synthetic jet actuator driven by a piezoelectric disk

MICHELE GIRFOGLIO

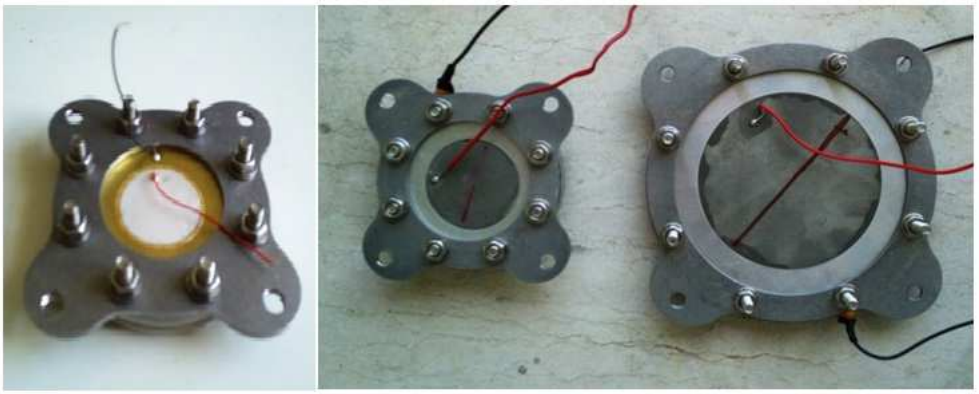

Supervisor:
Luigi de Luca

Coordinator:
Luigi de Luca

March 2015

Preface

My research activity has been focused on two topics very different from each other. For this reason, the present PhD thesis consists of two volumes:

- The volume A deals with the modeling and the experimental validation of the frequency response and the energy conversion efficiency of a synthetic jet actuator driven by a thin piezoelectric disk.
- The volume B deals with the global dynamics of gravitational liquid sheet flows subjected to surface tension.

Results showed in this volume have been published in the following journal/conference papers:

1. M. Girfoglio, C. Salvatore Greco, L. de Luca, "Modelling of the efficiency of synthetic jet actuators", 21 pp., Sensors and Actuators A: Physical, in press, 2015.
2. L. de Luca, M. Girfoglio, G. Coppola, "Modeling and Experimental Validation of the Frequency Response of Synthetic Jets Actuators", AIAA Journal, vol. 52, pp. 1733-1748, 2014. ISSN: 0001-1452, doi: 10.2514/1.J052674
3. M. Girfoglio, M. Chiatto, L. de Luca, "Fluid-structure coupling effects in synthetic jet devices", Aerotecnica Missili e Spazio, vol. 92; pp. 110-122, 2013, ISSN: 0365-7442
4. L. de Luca, M. Girfoglio, M. Chiatto, G. Coppola, "Characterization of synthetic jet resonant cavities", FLINOVIA – Flow induced noise and vibration issues and aspects, pp. 101-118, Springer International Publishing, Berlin, 2014. ISBN: 9783319097121, doi: 10.1007/978-3-319-09713-8_6
5. M. Girfoglio, M. Chiatto, L. de Luca, "Fluid-structure coupling effects in synthetic jet devices", In: AIDAA Napoli XXII, pp. 1-10. Napoli, 9-12 september 2013. Italian Association of Aeronautics and Astronautics. ISBN: 9788890648427

6. M. Girfoglio, L. de Luca, “Acoustic-structural coupling in the frequency response of synthetic jet devices”, In: Atti del XXI Congresso Associazione Italiana di Meccanica Teorica e Applicata, pp. 1-10. Torino, 17-20 september 2013. ISBN: 9788882391836

Abstract

The literature about synthetic jet actuators includes a very wide field of technological applications. They can be basically used to control surface flows due to their capability of delaying laminar and/or turbulent separation. Synthetic jet devices can be also employed in heat transfer problems as well as to enhance mixing between fluid currents.

The overall design of the actuators needs practical modeling tools. The present work is aimed at characterizing the frequency response of a synthetic jet actuator driven by a thin piezoelectric disk. Previous contributions of literature are due to Gallas et al. [1], Sharma [2], Persoons [3]. The present one is particularly inspired by the Sharma's model [2], directly based on fluid dynamics equations.

A lumped element mathematical model ([4],[5], [6], [7]) of the operation of a synthetic jet actuator is both analytically and numerically investigated in order to obtain information about the frequency response of the device. The model considers the three basic elements of the actuator: the oscillating membrane, the cavity, the orifice. The dynamics of the diaphragm is described through the motion equation of a one-degree of freedom forced-damped spring-mass system, while the resonant cavity and orifice components are described by means of proper forms of the continuity and Bernoulli's unsteady equations. Direct numerical simulation of the non-linear governing equations system has been carried out by a home-made code written in MATLAB environment.

From the analytical viewpoint, it is found that the device behaves as a two-coupled oscillators system; by neglecting the non-linear damping term of the acoustic oscillator and by solving numerically the relevant eigenvalues problem, it is possible to obtain an accurate estimate of the two resonant modes of the system; moreover, by making the further assumption of complete absence of damping effects, simple closed-form analytical formulas are given in order to predict the two modified peak frequencies, as functions of the uncoupled first-mode structural and Helmholtz resonance frequencies. These predictions are well confirmed by numerical simulations of the fully non-linear equations.

Furthermore, a dimensionless form of the governing equations system, based on a particular choice of the reference variables, is obtained in order to achieve further insights on the coupling degree of the two oscillators for the different flow regimes characterized by the operating Strouhal number [8].

The model is also validated through systematic experimental tests carried out on three devices, one with the membrane in brass and two in aluminum, having different mechanical and geometrical characteristics leading to an increasing coupling factor; it is found a very strict agreement between exit flow velocity measurements and analogous numerical data for any tested device, for different supply voltages.

Finally, a comprehensive and detailed modelling to evaluate the efficiency of energy conversion of the device is developed. The contribution is original because the analysis is based on the energy equations of the two coupled oscillators, the membrane and the acoustic one, which are directly derived from the corresponding motion equations. The modelling is validated against numerical as well as experimental investigations carried out on the device exhibiting the strongest coupling effect. A major result is that for the actuator under investigation the global efficiency (representing the conversion of input Joule power to kinetic power) decreases with increasing the applied voltage. Considerations are reported to relate the theoretical orifice efficiency to the practical jet efficiency issuing in the external field.

Acknowledgements

First and foremost, I would like to thank my mother and my father (God bless you!) for their constant and unconditional affection.

I would like to thank my friends, in particular Mario and Ivan, and my colleagues, Fortunato, Matteo, Annagrazia and Armandojanni, for their emotional support.

A special acknowledgment goes to Prof. Gennaro Cardone, who gave me the possibility to became a PhD student.

The support and the guidance of my project advisor, Prof. Luigi de Luca, has been crucial for the most critical aspects of my research activity.

Finally, I would like to acknowledge my girlfriend, Giusy: thanks for being what you are, for all that you mean to me, I don't know how I could have lived if you had never existed or if we had never met.

Contents

List of Figures

List of Tables

Chapter 1

Introduction

1.1 Synthetic jets overview

Thanks to advances in smart materials such as piezoceramics it is now possible to develop a much more efficient method of adding energy to a flow. Synthetic jet actuators are compact fluidic devices consisting of an oscillating surface embedded in a cavity which can transfer linear momentum to the flow system without net mass injection. They provide a system of periodic addition of energy to the flow. It has been demonstrated that periodic addition of energy allows to obtain the same control efficiency as is achieved by steady energy input, with an important improvement: the cost of unsteady methods is less than that of steady methods. In some instances this difference reaches an order of magnitude, as showed by Wygnaski et al. [10].

The concept of synthetic jet dates back to as early as 1950. At that time, however, this idea was exclusively used to provide insights on the circulation effects and the impedance of orifices (Ingrad and Labate [11]). Later on, Lebedeva et al. [12] created a round synthetic jet with velocities of up to 10 m/s, by transmitting high amplitude sound waves through an orifice placed at the end of a tube. In a related investigation, Mednikov and Novitskii [13] reported the formation of a zero net mass flux jet and average streaming velocities of up to 17 m/s by inducing a low frequency oscillatory velocity field with a mechanical piston. Early relevant investigations on synthetic jets as flow manipulation devices have been carried out by Smith and Glezer [14] and Smith and Glezer [15] that investigated the interaction of synthetic jets with an external flow near the flow boundary. They concluded that this interaction can lead to the formation of closed recirculation flow regions and consequently to an apparent modification of the flow boundary. On the other hand, Ziada [16] used synthetic jets to suppress the oscillations of jet-edge and jet-slot oscillators. Over the years, synthetic jets have gained

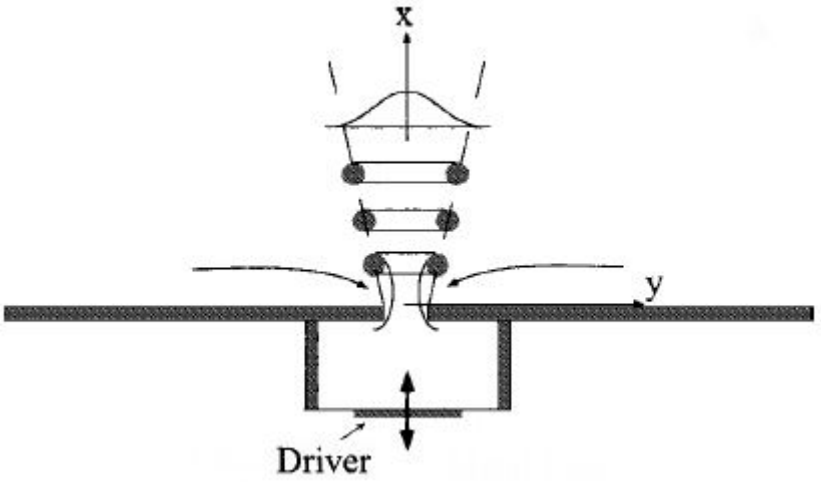

FIGURE 1.1: Schematic of a synthetic jet actuator (Smith and Glezer [9])

an increased amount of attention by researchers and, recently, they have emerged as a versatile actuation technology tool for a broad range of applications such as flow control, heat transfer from small-size surfaces, overall enhancement of mixing between fluid currents, generation of microthrust for propulsion or attitude control of a micro aerial vehicle (MAV).

1.2 Formation of a synthetic jet

A synthetic jet is generated by a membrane oscillation in a relatively small cavity (Fig. 1.1), which produces a periodic cavity volume change and thus pressure variation. As the membrane oscillates, fluid is periodically entrained into and expelled out from an orifice connecting the cavity with the external ambient (to be controlled). During the expulsion phase of the cycle, due to the flow separation, a vortex ring forms near the orifice exit section which, under favorable operating conditions (Holman et al. [17]), convects away towards the far field and breaks up due to the viscous dissipation eventually "synthesizing" a turbulent jet always directed downstream (Smith and Glezer [9]).

Since the jet formation depends on the ability of the vortex ring to escape to the subsequent ingestion phase, following Smith and Glezer [9], a basic parameter characterizing the jet strength is the so called stroke length $\overline{L}$, namely the integral of the (spatially averaged) velocity at the orifice exit over the ejection phase only of the cycle:

$$\overline{L} = \int_0^{\tau/2} U(t)dt \tag{1.1}$$

where τ is the actuation period and $U(t)$ is the fluid velocity at the exit section. The stroke length can also be expressed conveniently as the product $\overline{L} = \overline{U}\tau$, where $\overline{U}$ is a proper reference velocity defined as:

$$\overline{U} = \frac{1}{\tau}\int_0^{\tau/2} U(t)dt \tag{1.2}$$

Therefore, it is natural to expect that the jet is formed or not according to whether the parameter $\overline{L}/d_o$ is greater or less than 0.16π, with d_o being the orifice diameter. In the literature the parameter $\overline{L}/d_o$ is generally referred to as the reciprocal of the Strouhal number (Cater and Soria [18]).

The importance of the stroke length, or of the average velocity $\overline{U}$, lies in the fact that to compare the performance of a synthetic jet with that of a continuous jet, it is usual to refer to a Reynolds number based on the velocity $\overline{U}$, i.e.:

$$Re = \frac{\rho\overline{U}d_o}{\mu} \tag{1.3}$$

where ρ and μ are respectively the air density and the air dynamic viscosity.

The formation and evolution of synthetic jets have been the subject of a number of experimental and numerical investigations of plane and round jets with emphasis on near field formation, evolution and advection of the jet vortices and on scaling of the time-averaged flow (examples of experimental investigations: plane jets (Smith and Glezer [9], Yao et al. [19]), round jets (Cater and Soria [18], Shuster and Smith [20]); and of numerical investigations: plane jets (Rizzetta et al. [21], Lee and Goldstein [22], Kotapati et al. [23]).

1.3 Motivation and objectives

Although understanding of the evolution and characteristics of synthetic jets is important in the development of its applications, the design and optimization of actuators are equally as important. Many authors focused their attention on the development of practical modeling tools in order to design devices able to yield suitable operating characteristics (see Section 2.2)

It is worth noting that, although synthetic jets have been widely explored, only few studies on the efficiency of energy conversion of synthetic jet actuators have been carried out (see Chapter 4).

By considering the observations above, the main objective of this thesis is to develop a lumped-element mathematical model in order to characterize the operation of a synthetic jet actuator driven by a thin piezoelectric disk. Furthermore, an energy balance equation derived directly from the equations governing the dynamics of the actuator is used to give some insights on the efficiency of energy conversion of the device so to fill this lack of information. The analytical and numerical investigation is corroborated by a parallel campaign of experimental tests.

1.4 Thesis layout

This thesis is presented in four chapters followed by a conclusion and an appendix. In Chapter 1 a synthetic jets overview is given, together with the motivation and the objectives of the research. Chapter 2 provides a survey of the most representative literature related to the synthetic jets by differentiating the articles between applicative papers and design papers. Chapter 3 describes the lumped-element modeling, together with the comparisons of experimental, numerical, and analytical findings. In Chapter 4 the analysis of the efficiency of energy conversion of the device is reported. The appendix collects the most relevant conference/journal papers published during the research activity.

Chapter 2

Literature review

The scientific and technical literature quotes documents dealing with synthetic jets since no more than two decades. Nevertheless, the bulk of such a literature is remarkably thick and includes a very wide field of applications such as flow control, heat transfer from small-size surfaces, overall enhancement of mixing between fluid currents, generation of microthrust for propulsion or attitude control of a micro aerial vehicle (MAV).

This chapter provides a survey of the most representative literature related to the synthetic jets by differentiating the articles between applicative papers (i.e., papers devoted to the development and description of a particular application) and design papers (i.e., papers oriented toward the description of the device design able to yield suitable operating characteristics).

Further details on the works published until 2011 can be found in Glezer and Amitay [24], Zhang et al. [25], Cattafesta and Sheplak [26] and Glezer [27].

2.1 Synthetic jets: applicative papers

2.1.1 Flow control

Modern synthetic jet actuators are compact devices (Bottomley and Packwood [28]; Bhatt et al. [29]; Jabbal et al. [30]) that weigh less than more complex steady flow control systems having similar performance characteristics. This is mainly due to the fact that they do not require plumbing and a separate source to create the flow. This major advantage makes synthetic jet actuators attractive fluidic devices for a broad range of flow control applications.

Synthetic jets were widely used in control of flow around a circular cylinder for the separation delay or drag reduction. Early investigations belonging to this application field have been published by Amitay et al. [31] and Amitay et al. [32]. Synthetic jets were issuing from two parallel slots with the jet exit angle varied from 0° to 180°. By using the smoke visualization and surface pressure measurement in a wind tunnel, they found that when the synthetic jets were positioned at the front stagnation point, the interaction between the synthetic jets and the on-coming flow led to the formation of a closed recirculation region, resulting in a further upstream motion of the front stagnation point and in an apparent modification of the flow boundary layer on scales that are one to two orders of magnitude larger than the characteristic length scale of the jets themselves (the so called virtual aeroshaping effect), so the pressure distributions around the circular cylinder has been dramatically changed. On the other hand, when the synthetic jets were placed at the rear stagnation point with a sufficiently high exit velocity, the recirculation region behind the circular cylinder became smaller significantly and the separation point was delayed to near the rear stagnation point, meaning that the flow was almost reattached. Crook et al. [33] placed the synthetic jet just upstream of the separation point with two trip wires attached at ±40° from the front stagnation point to force boundary layer transition. Surface flow visualization demonstrated that the synthetic jet created strong entrainment surrounding the cylinder flow boundary layer, which offered an explanation for the large vortical structures downstream of the orifice. Bera et al. [34] and Tensi et al. [35] investigated the action of synthetic jets implemented on a circular cylinder by using wall pressure and velocity field measurements. They found that the synthetic jets could efficaciously delay flow separation and enable the separation region to become much smaller and even completely disappearing, which led to a reduction in drag. Fujisawa et al. [36] analyzed the phase-averaged characteristics of the flow around a circular cylinder under acoustic excitation control by carrying out particle image velocimetry (PIV) measurements. Their results indicated that a series of discrete vortices were generated over the circular cylinder surface interacting with the wall boundary layers, which led to the modification of the surface pressure distribution and the delay of the separation point. More recently, Feng and Wang [37] used a synthetic jet generated by a non-sinusoidal waveform positioned at the rear stagnation point. The flow around the circular cylinder was measured by PIV technique and the authors showed that increasing the ratio of the time duration of the suction cycle to the blowing cycle, the exit velocity and entrainment effect of the synthetic jet were enhanced, flow separation was delayed and drag reduction by up to 29% was achieved. Feng and Wang [38], Feng et al. [39] and Feng et al. [40] indicated that the control of a synthetic jet positioned at the rear stagnation point could also change the wake vortex shedding mode and demonstrated that such control strategy could lead to a drag reduction. On the other hand, when the synthetic jet ejected toward upstream from the front stagnation

point of the cylinder, by using hydrogen bubble flow visualization technique, Wang et al. [41] found that the flow separation could also be efficiently delayed, whilst the vortex shedding pattern changed as well. Ma and Feng [42] positioned synthetic jets at both the front and rear stagnation points and carried out experimental tests in order to study and to control the vortical structures around the circular cylinder. The flow field was measured by using PIV technique and the proper othogonal decomposition (POD) was used to analyze the vortex dynamics. The synthetic jet was positioned at the front stagnation point of the circular cylinder in the study of Feng and Wang [43]. On the base of the qualitative results provided by Wang et al. [41], by using PIV and POD techniques, they carried out quantitative measurement of the vortex dynamics to further reveal the modification of the near wake and the mechanism underlying with synthetic jet control.

The investigation of the interaction between a synthetic jet (or jet arrays) with a cross-flowing boundary layer (both laminar and turbulent) has been of significant interest in light of the applications to flow control. Mittal and Rampunggoon [44] used an incompressible Navier-Stokes solver to carry out a systematic parametric study of the interaction of a synthetic jet with a flat plate boundary layer for various diaphragm amplitude, Reynolds numbers and orifice dimensions. They found that large mean recirculation bubbles were formed in the external boundary layer only if the jet velocity was significantly higher than the cross flow velocity. Zhong et al. [45] used flow visualization to investigate the interaction of a round synthetic jet with a flat plate laminar boundary layer, and the evolution of the jet vortices for various Reynolds numbers, velocity ratios and actuation frequencies. They concluded that the highly stretched hairpin vortices attached to the wall produced at low Reynolds numbers and velocity ratios are likely to be the desirable structures for effective flow separation control. In a related investigation, by using oil flow visualization and hot wire anemometry techniques, Liddle and Wood [46] considered streamwise symmetric and asymmetric interactions of clusters of round synthetic jets with the boundary layer. Jabbal and Zhong [47] carried out PIV measurements and concluded that trains of stretched vortex rings would be most effective for separation control based on changes in wall shear stress within a laminar boundary layer. Zhou and Zhong [48] carried out numerical simulation in FLUENT of circular synthetic jets issued into a laminar boundary layer developing over a flat plane and observed two types of vortical structures, depending on the injection conditions: hairpin structures, at relatively low frequency, and tilted vortex rings at higher frequency. A variety of induced vortices were identified and these were shown to depend on the injection frequency. Smith [49] carried out an experimental investigation of the interaction between an array of rectangular synthetic jets and a turbulent boundary layer by using hot wire anemometry. They concluded that when the orifice was normal to the mean

flow direction, the boundary layer was characterized by a wake-like region, while when the orifice was aligned with the mean flow direction, the flow structure was consistent with the longitudinal, counter-rotating vortex pairs. Rathnasingham and Breuer [50] used a spanwise array of synthetic jet actuators for active control of the near wall region of a turbulent boundary layer and developed transfer functions to predict downstream characteristics of the streamwise velocity fluctuations. Dandois and Garnier [51] used large eddy simulation (LES) and unsteady Reynolds-averaged Navier Stokes equations (URANS) for studying the interaction of a synthetic jet with a turbulent boundary layer using the geometry adopted by Rumsey et al. [52]. Even though the primary objective was to compare numerical simulations with experimental data, the authors provided detailed informations about the alteration of the velocity field within the boundary layer and the structure of the jet in the vicinity of the orifice. Lardeau and Leschziner [53] carried out LES of the interaction between a turbulent boundary layer separating from a rounded ramp in a duct and a pair of round synthetic jets, actuated upstream of the nominal separation line. The global effect of the actuation is a reduction of 10–20% in the length of the separated region and 20–40% in the thickness of the reverse-flow layer. This reduction is mainly associated with a delay in separation.

The separation delay is vital near stall conditions where aerodynamic performance deteriorate rapidly. Higher lift and increased stall incidence, possibly associated to low drag, are required to have an efficient flow control technique. Seifert et al. [54] demonstrated that much less power is required to produce equivalent increases in the lift coefficient for oscillatory control rather than for steady blowing techniques. Early relevant studies related to such a topic have been proposed by Smith, [55], Amitay et al. [56] and Amitay and Glezer [57] which used synthetic jet actuators for the control of separation over an unconventional airfoil based on an uniformly stretched NACA 0015 airfoil. They showed that when the actuators were typically operated at dimensionless frequencies f^* of one order of magnitude higher than the shedding frequency of the airfoil ($f^* = \mathcal{O}(10)$, based on the airfoil chord length and the incoming flow velocity), the boundary layer separation point on the suction side of the airfoil can be delayed by obtaining an improvement of the airfoil aerodynamic characteristics. Smith [55] found that the stall attack angle of the airfoil could be delayed from 5° to 18°, and the lift to drag ratio also could be increased. Amitay et al. [56] and Amitay and Glezer [57] studied the effect of f^* on the flow separation control around the airfoil. They showed that for $f^* < 4$, the lift to pressure drag ratio decreases with the increase of the exciting frequency while for $f^* > 10$, the lift to pressure drag ratio increases by 27% compared with that of the unforced case and has little difference with the exciting frequency variation. When the attack angle of the airfoil is 20°, the angle between the centerline of the jet and the free stream is 45°, the momentum coefficient is 4.5×10^{-3} and $f^* = \mathcal{O}(1)$, a series of small

vortices are produced and the large separation region diminishes. With the increase of the actuator frequency, the scale of the vortices decreases. When $f^* = \mathcal{O}(10)$, the small scale vortices around the actuator orifice disappears and the separated shear layer fully attaches to the airfoil. Donovan et al. [58] used the Reynolds-averaged Navier-Stokes equations (RANS) for studying the effect of actuation on a NACA0012 airfoil at a chord Reynolds number of 8.5×10^6. They obtained a significant increase in lift (29%) by using the synthetic jet actuator in the post-stall regime. Duvigneau and Visonneau [59] solved unsteady Reynolds-averaged Navier-Stokes (URANS) equations in order to characterize the flow around the NACA 0015 airfoil, including a synthetic jet located at 12% of the chord, for incidences between 12 to 24° and a Reynolds number of 8.95×10^5. An increase of 52% of the maximum lift coefficient with respect to the baseline airfoil was achieved in the attack angle range of 16° - 22°. Therefore, the drag of the airfoil decreased a lot after stall angle, so the lift to drag ratio could be greatly enhanced. Holman et al. [60] experimentally studied the interaction of adjacent synthetic jets with the cross flow developing on a NACA 0025 airfoil at an angle of attack of 12° and a Reynolds number equal to 105. The authors used piezoelectric actuators varying the relative phasing and the oscillation frequency and amplitude to control the flow separation. The authors observed that the jet formation was not a necessary condition to achieve an effective control. Moreover, also the relative phasing of the jets did not appear to play a significant role in the separation delay. Wilson et al. [61] experimentally investigated the effects of a 2D synthetic jet positioned at 30% and 65% of the chord on a NACA 0036 airfoil at a Reynolds number equal to 106. Forcing frequencies up to 120Hz were tested, giving a maximum momentum coefficient equal to 0.0086. Hot wire measurements in the wake of the airfoil showed a reduced portion of separated flow in the controlled conditions and brought the high Reynolds shear stress layer closer the airfoil surface. Zhang and Wang [62] studied the aerodynamic characteristics of a NACA 0015 airfoil forced by an actuator located at 13% chord length of the airfoil, and indicated that the lift of the airfoil increases monotonously with the momentum coefficient. Tuck and Soria [63] controlled the flow around a NACA 0015 airfoil with the actuator located at the front stagnation point of the airfoil, and the jet was opposite to the incoming flow. When f^* was 1.3, the lift coefficient of the airfoil increased monotonously with the momentum coefficient. The numerical simulations of Raju et al. [64] considered separation control of a stalled NACA 4418 aerofoil. The simulations suggested that actuation at frequencies that are close to the separation bubble frequency are most effective in diminishing separation, while actuation at frequencies that are commensurate with the separating shear layer tend to enhance separation. You et al. [65] used large-eddy simulation (LES) to investigate turbulent separation over a NACA 0015 aerofoil at a Reynolds number equal to 8.96×10^5 and showed that when the flow separates around a midchord, the LES agrees well with the measurements of Gilarranz et al. [66], who obtained separation

delay and a significant increase in the lift by synthetic jet actuation. High momentum 2D synthetic jet actuators have been tested experimentally focusing the investigation on the separation delay over the airfoil NACA 0024 at high angles of attack by Lasagna et al. [67]. At the maximum frequency (68.3 Hz) the maximum lift coefficient raised by 20% while the stall incidence increased from 16° to 22°. When the attack angle of the airfoil is 20° the amount of drag reduction at the maximum frequency was of the order of 70%. However, when the flow separates near the leading edge, the same actuation is only marginally effective. Bottomley and Packwood [28] used an array of circular synthetic jets to control the flow around a NACA 0015 wing at a Reynolds number equal to 8.9×10^5 and an incidence of 14°. The onset of flow separation was delayed, and both the lift and drag characteristics of the wing were improved. Rathay et al. [68] used a synthetic jets array operated at high frequency on a scaled model of a tail rudder. They observed that by situating the array of actuators at a specific location they could improve the side force on the model by up to 18%. They concluded that actuators located at mid-span provide the greatest contribution at moderate rudder deflections, and actuators located at the root provide the greatest contribution at high rudder deflections. Jabbal et al. [30] used an inclined configuration actuator array on an aircraft wing to improve lift production. By experimentally studying the parameter space associated with an array of 30 actuators they determined an optimum arrangement for installation of the actuators to achieve a specified lift configuration.

2.1.2 Heat transfer applications

Gutmark et al. [69] published the first relevant literature work on synthetic jets used as cooling devices. They employed synthetic jets to enhance both natural and forced convection and concluded that the acoustically excited airflow allows to obtain an overall heat transfer coefficient of four times larger. Mahalingam and Glezer [70] characterized from the thermal and the design point of views a heat sink for high power dissipation in electronics enhanced with synthetic jet impingement. The results revealed a case temperature decrease from 71.5 to 36°C with synthetic jets operation; furthermore, it has been obtained a power dissipation of 20–40% higher with respect to the same heat sink with a fan in the flow rate range of 3–5 cubic feet per minute. The experimental investigation carried out by Chaudhari et al. [71] on the cooling of a flat plate by using a synthetic jet generated through a circular orifice showed that the Nusselt number is comparable with that of continuous axisymmetric jets at low Reynolds number (up to 4000), expecting it to be higher at greater values of Reynolds number. Valiorgue et al. [72] identified two different flow regimes through defining a dimensionless critical stroke length equal to 2.5. They found that the heat transfer rate is linearly proportional

with the dimensionless critical stroke length up to 2.5; for higher values, it results to be constant. Arik and Icoz [73] provided a closed form empirical correlation which allows to predict the heat transfer coefficient as a function of Reynolds number (less than 2900), dimensionless nozzle to plate distance (less than 20) and jet driving frequency (between 0.16 times the resonance frequency and the resonance frequency). They observed that the heat transfer coefficient on a vertical surface increases with the driving voltage; it has a peak at the resonance frequency and the effect of the axial distance on the heat transfer becomes stronger as the jet driving frequency increases. Persoons et al. [74] found, for an axisymmetric synthetic jet, a general correlation for the stagnation point Nusselt number including the effect of all appropriate scaling parameters: Reynolds number (ranging between 500 and 1500), jet to surface spacing (ranging between 2 and 16) and dimensionless stroke length (ranging between 2 and 40). Based on such correlation, Persoons et al. [74] defined four heat transfer regimes, in function of the values assumed by the stroke length to nozzle to plate ratio. The fourth regime, related to a value greater than 2.5, shows an asymptotical behavior achieving the highest stagnation Nusselt number values with respect to the other regimes. The flow field features of such four heat transfer regimes were reported by McGuinn et al. [75] that carried out high speed Particle Image Velocimetry (PIV) and single point hot wire anemometry experiments in order to highlight the dependence of the impinging synthetic jet flow field (and of the corresponding surface heat transfer distribution) on the dimensionless stroke length for a wide range of nozzle-to-surface spacing (2-16) and a single Reynolds number (1500). Some recent studies have been focused on the design of special configurations in order to improve synthetic jet heat transfer performances in practical applications. Rylatt and O'Donovan [76] showed that, by confining the impinging synthetic air jet, it is possibile achieve a heat transfer enhancement of up to 36% in the stagnation region. Chaudhari et al. [77] experimentally investigated, varying both the Reynolds number (1000-2600) and the normalized axial distance (1-30), a particular synthetic jet device by means of a center orifice encircled by multiple satellite orifices. Thanks to this innovative configuration, authors obtained a maximum heat transfer coefficient which is approximately 30% more than the one of the conventional single orifice jet. Luo et al. [78] numerically investigated a new generation of synthetic jet actuators consisting in two cavities sharing the same wall equipped with a single piezoelectric diaphragm and a slide block separating the two exit slots at an appropriate distance. They demonstrated that the device not only doubles the function of the existing synthetic jet with a single diaphragm but also resolves the problems of pressure loading and energy inefficiency of the existing synthetic jet. Luo et al. [79] carried out PIV measurements of such a dual synthetic jets actuator, at Reynolds number and Strouhal number equal respectively to 2500 and 0.17, by showing that in the near field a more complex flow field characterized by a "self-support" phenomenon between the two synthetic jets is present, while in the

far field the two jets merge a single and more stable synthetic jet. Persoons et al. [80] experimentally investigated a configuration constituted of two adjacent synthetic jets, with slot orifice, which allows to direct the flow by changing the phase between the jets. They carried out both PIV and IR thermography heat transfer measurements, at a fixed Reynolds number (600), and dimensionless stroke length equal to 29, for different values of phase and jet-to-surface spacing (6, 12 and 24), by obtaining a 90% enhancement of the maximum and overall cooling rate, compared to a single jet, for a phase equal to 120° and a jet-to-surface spacing equal to 12. Lasance et al. [81] showed that a double circular configuration allows to reduce the noise (Russell et al. [82]) and to improve the heat transfer performances (Lasance et al. [83]). Greco et al. [84] experimentally investigated the impingement heat transfer in single circular synthetic jets and twin circular synthetic jets in phase opposition. All experiments have been performed at Reynolds number equal to 5100 and Strouhal number equal to 0.024 varying the jet axes distance and nozzle to plate distance. An IR camera is used as temperature transducer for both time average and phase average heat transfer measurements. While obviously the twin configurations produce an heat transfer enhancement due to the fact that two jets instead of one are impinging, the interaction is found in general to have a beneficial effect.

2.1.3 Other applications

Synthetic jets have been used for a variety of applications that ranges from mixing enhancement to acoustic noise reduction. Smith and Glezer [15] used synthetic jets to effect thrust vectoring and manipulate small-scale motions in conventional air jets. Smith and Glezer [85] and Luo et al. [86] investigated the interaction between a primary air jet and a co-flowing synthetic jet (jet vectoring), the former experimentally, the latter numerically. Thomas [87] demonstrated that synthetic jet thrusters are a viable propulsion method for small underwater vehicles. More recently, Zelenyak et al. [88] suppressed noise produced by turbulent steady jet by positioning 8 synthetic jet actuators in correspondence of the periphery of the exit orifice and carrying out actuation at specific frequencies. Xia and Zhong [89] showed that synthetic jets can be used to enhance mixing of two laminar, parallel streams of water. Mahalingam et al. [90] demonstrated that synthetic jets can be used to replace conventional cooling components with moving parts such as fans. Montoya et al. [91] demonstrated the capability of synthetic jets to control particle dispersion in a closed camber and to improve indoor air quality while minimizing the energy burden on heating, ventilating, and air conditioning systems. Bhatt et al. [29] used synthetic jets for MAV flight control.

2.2 Synthetic jets: design papers

The overall design of synthetic jet actuators needs practical modeling tools. The first significant lumped-element model of a piezoelectric-driven synthetic jet device is described by Prasad [92] and Prasad et al. [93]. By resorting to the approach based on the equivalent electric circuit, these authors developed a modeling of the electromechanical behavior of the piezoceramic composite membrane and gave detailed relationships for the transverse deflection of the inner and outer membrane regions in the simultaneous presence of applied voltage and pressure load. They were able to evaluate both the short-circuit compliance and the effective acoustic piezoelectric coefficient. Gallas et al. [1] modeled the individual components of the actuator as elements of an equivalent electric circuit by using conjugate power variables. On the basis of practical considerations made on the relationships found by Prasad [92], they noted that, in a lumped model, one may use the acoustic compliance of the shim only reduced by a proper factor depending on the ratio of the radius, thickness, and Young's modulus of the piezoceramic and shim materials. They showed a very good agreement between the predicted and measured frequency response functions. Later on, Sharma [2] proposed a different model directly based on the basic equations of fluid dynamics, where the oscillating membrane is considered as a single degree- of-freedom mechanical system, while the cavity-orifice component is described by means of proper forms of the continuity and Bernoulli's unsteady equations. Sharma [2] validated his model on the very same experimental data of Gallas et al. [1]. One of the most significant experimental investigations on the frequency response of a synthetic jet cavity is due to Chaudhari et al. [94], who carried out systematic measurements about the effects of the excitation frequency on the ejection and suction velocities, by varying the geometrical parameters of the cavity. The paper of Krishnan and Mohseni [95] was oriented essentially to the study of the characteristics of the flow field produced by a round synthetic jet by using detailed numerical simulations of the turbulent Navier- Stokes equations. To validate their numerical results, they carried out also interesting experimental measurements of the centerline deflection of the membrane by evidencing its nonlinear dependence on the excitation frequency and driving voltage. Seeley et al. [96] described a simplified fluid–structure interaction model based on the implementation of commercial Finite Element codes and proved its validity at relatively low frequency, namely well below the Helmholtz frequency. Persoons [3] proposed a low-order model of prediction of the frequency response of synthetic jet actuators driven by electromagnetic or piezoelectric supply. Based on the equivalent circuit approach, the model yields analytical expressions for the two resonance frequencies, as a function of the structural and Helmholtz resonance frequencies. The investigation of Persoons [3] is corroborated by a parallel campaign of experimental tests. Regarding the present author, de Luca et al. [4], de Luca et al. [8], Girfoglio and de Luca [5], Girfoglio

et al. [6] and Girfoglio et al. [7] presented a fluidic type lumped element modeling, that has been inspired by the Sharma's work [2], yielding the frequency response of the resonant cavity in terms of pressure disturbances, membrane displacement and external jet velocity. The model, validated against systematic experimental measurements, gave also simple but accurate analytical relationships for the two resonance frequencies characterizing the overall system response.

Chapter 3

Frequency response of piezoelectrically driven synthetic jet actuators

In this chapter, a lumped element mathematical model of the operation of a synthetic jet actuator driven by a thin piezoelectric disk is both analytically and numerically investigated in order to obtain information about the frequency response of the device. The model is validated through systematic experimental tests carried out on three devices having different mechanical and geometrical characteristics.

It should be noted that just some results are showed; an accurate description of all findings obtained can be found in [4], [5], [6], [7], [8] from which the treatment described hereafter has been arisen (the references [4] and [8] are reported in Appendix).

3.1 Model formulation

The model refers to the three basic elements of the actuator: the oscillating membrane (diaphragm or wall, constituted by a thin round metal shim on which a smaller diameter piezo-ceramic disk is bonded), the cavity, the orifice.

The dynamics of the diaphragm is described through the motion equation of a one-degree of freedom forced-damped spring-mass system:

$$m_{wt}\ddot{x}_w + c_{wt}\dot{x}_w + k_w x_w = F - p_i A_w \tag{3.1}$$

where $m_{wt} = m_w + m_a$ is the total mass (m_w being the oscillating diaphragm mass, including both the shim and the piezo element, and m_a the added mass term); $x_w(t)$ is the diaphragm position at a generic time instant t, and superscript dot stands for time derivative; $c_{wt} = c_w + c_a$ is the total damping coefficient (c_w being the structural damping coefficient and c_a is a further damping coefficient due to the interaction with the external air); k_w is the equivalent spring stiffness; $F = F_o \sin \omega t$ is the electrodynamic force (communicated to the membrane by the piezo-electrical element), F_o being the force magnitude and ω the circular frequency of the applied voltage (often the natural or cyclic frequency $f = \omega/2\pi$ will be used hereafter); p_i is the differential (relative to the unperturbed external atmosphere) pressure within the cavity (internal pressure); A_w is membrane wall area. The added mass terms are evaluated by means of the procedure of Kinsler et al. [97], as reported by Sharma [2]. Following Sharma [2] the "pure" mechanical damping ratio is assumed equal to 0.03.

The equivalent spring stiffness of the diaphragm can be obtained as

$$k_w = m_w (2\pi \tilde{f}_w)^2 \tag{3.2}$$

where $\tilde{f}_w$ is the frequency of the principal mode of vibration of the rigidly clamped composite disk. Although the presence of the piezoceramic element bonded to the metal shim enhances the flexural rigidity of the membrane (and in principle the very thin layer of glue should be taken into account as well), for standard operating conditions $\tilde{f}_w$ can be referred to the first fundamental mode of the shim only (that is the membrane structural element actually clamped) and calculated by using the standard formula reported in many textbooks (among others, Kinsler et al. [97]), and used by other authors (e.g. by Rathnasingham and Breuer [98]):

$$\tilde{f}_w = \frac{10.2}{\pi\sqrt{3}} \frac{th_w}{d_w^2} \sqrt{\frac{E_w}{\rho_w (1 - \nu_w^2)}} \tag{3.3}$$

in which th_w, d_w, E_w, ρ_w and ν_w are, respectively, the thickness, the diameter, the Young's modulus, the density and the Poisson's ratio of the shim. Note that the operation at frequencies higher than the fundamental one is not convenient because the membrane produces little net displacement of the surrounding air.

The amplitude of the forcing F_o is obtained conveniently as

$$F_o = \frac{k_w d_A V_a}{A_w} = k_w \Delta x_w \tag{3.4}$$

where d_A is the effective acoustic piezoelectric coefficient that represents the ratio between the cavity volume variation ΔV and the applied voltage V_a, when the driving

differential pressure p is equal to zero [93]:

$$d_A = \left.\frac{\Delta V}{V_a}\right|_{p=0} \tag{3.5}$$

Note that in the previous equation (3.4) the cavity volume variation $\Delta V = d_A V_a$ is divided by the membrane area A_w in order to obtain the average linear membrane displacement Δx_w (to be multiplied by k_w in order to obtain F_o).

The coefficient d_A could be evaluated analytically by means the distribution of the transverse displacement of the composite diaphragm ([92], [93]). This procedure is not practical due to the difficulty of determining the required coefficients. An alternative way consists in determining the acoustic compliance of the membrane C_{ac} which, through a dual definition of d_A, is given by the ratio of the volume variation ΔV to a uniformly distributed pressure load p, in condition of electrical short-circuit [93]:

$$C_{ac} = \left.\frac{\Delta V}{p}\right|_{V_a=0} \tag{3.6}$$

Of course the evaluation of C_{ac} would require the same difficulties. However, one can refer to the acoustic compliance of a homogeneous circular plate (namely, having the properties of the metal shim or those of the piezoceramic) that yields insight into the scaling behavior of the diaphragm [1], and ultimately obtain d_A by means of the relationship

$$d_A = C_{ac}\phi_a \tag{3.7}$$

in which ϕ_a is the electroacoustic transduction coefficient [93].

In the present work it will be made reference to the piezoceramic properties, thus

$$C_{ac} = \left.\frac{\Delta V}{p}\right|_{V_a=0} = \frac{\pi d_{pc}^2(1-\nu_{pc}^2)}{1024 E_{pc} th_{pc}^3} \tag{3.8}$$

th_{pc}, d_{pc}, E_{pc}, and ν_{pc} being, respectively, the thickness, the diameter, the Young's modulus and the Poisson ratio of the piezoceramic.

The electroacoustic transduction coefficient ϕ_a has been considered here as a fitting parameter of the present model (the only one) to be determined by optimizing the agreement between numerical and experimental data. Numerical values of ϕ_a will be reported hereafter, while showing the comparison of computer simulation and experimental results.

For future purpose it is convenient to divide Eq. (3.1) by m_{wt} , thus obtaining

$$\ddot{x}_w + 2\zeta_w \omega_w \dot{x}_w + \omega_w^2 x_w = \omega_w^2 \Delta x_w \sin \omega t - \frac{p_i A_w}{m_{wt}} \tag{3.9}$$

where ζ_w and ω_w are respectively given by:

$$\zeta_w = \frac{c_{wt}}{2\sqrt{m_{wt} k_w}} \tag{3.10}$$

$$\omega_w = \sqrt{\frac{k_w}{m_{wt}}} \tag{3.11}$$

ζ_w is the actual damping ratio in which both c_{wt} and m_{wt} take into account the motion of the surrounding air. $\omega_w = 2\pi f_w$ represents the (first mode) structural circular frequency of the diaphragm.

The second equation of the model is essentially the conservation of mass in the cavity under the assumption of zero-dimensional (lumped) system. By relating the density and pressure variations by means of an isentropic compression/expansion transformation, the continuity equation can be formulated as

$$\frac{V_c}{\gamma p_o} \frac{dp_i}{dt} - A_w \dot{x}_w = -A_o U \tag{3.12}$$

where $V_c = A_w H$ is the cavity volume (H being the cavity height), A_o is the orifice area, γ is the specific heat ratio of air, p_o is the external ambient pressure and U is the instantaneous flow velocity through the orifice.

The application of the unsteady Bernoulli's equation between a point inside the cavity where the flow velocity is practically null and a point, just outside the cavity, representing the location where the pressure matches the unperturbed external ambient value, yields the third equation of the model:

$$\dot{U} + \frac{K}{l_e} |U| \dot{U} + \omega_h^2 U = \frac{A_w}{A_o} \omega_h^2 \dot{x}_w \tag{3.13}$$

in which K is the head loss coefficient, including the inviscid contribution (equal to unity) due to the kinetic energy recovery at ambient pressure, minor (entrance/exit) losses, as well as distributed losses due to friction inside the orifice duct. The distance between the two points of application of the Bernoulli's equation, i.e. the modified (effective) length of the orifice l_e, is basically evaluated according to the description of Sharma [2], namely

$$l_e/d_0 = l_0/d_0 + \Delta l_e \tag{3.14}$$

The choice of the values to be attributed to the head loss coefficient and to the effective length of the orifice constitutes a key point of the model, and is very critical because it needs detailed information about the complex unsteady flow field inside the reduced size cavity and orifice [4]. It has been performed the numerical simulations with the basic values of $K = 1.14$ and $\Delta l_e = 0.62$ with the aim of optimizing the prediction capability of the numerical code in terms of jet-flow velocity.

The so called Helmholtz frequency ω_h is usually recognized to be:

$$\omega_h = \sqrt{\frac{\gamma A_o^2 p_o / V_c}{\rho_a l_e A_o}} = \sqrt{\frac{k_a}{M_a}} \tag{3.15}$$

where k_a and M_a are, respectively, the equivalent stiffness of the air inside the cavity, $k_a = \gamma A_o^2 p_o / V_c$, and the effective mass of the air at the orifice, $M_a = \rho_a l_e A_o$.

For the sake of convenience, the three differential equations which describe the dynamics of the actuator are summarized below

$$\ddot{x}_w + 2\zeta_w \omega_w \dot{x}_w + \omega_w^2 x_w = \omega_w^2 \Delta x_w \sin \omega t - \frac{p_i A_w}{m_{wt}} \tag{3.16}$$

$$\frac{V_c}{\gamma p_o} \frac{dp_i}{dt} - A_w \dot{x}_w = -A_o U \tag{3.17}$$

$$\ddot{U} + \frac{K}{l_e} |U| \dot{U} + \omega_h^2 U = \frac{A_w}{A_o} \omega_h^2 \dot{x}_w \tag{3.18}$$

3.2 Evaluation of the coupled natural frequencies

The behavior of the synthetic jet actuator can be described by the dynamics of two mutually coupled oscillators: the first one, describing the membrane displacement x_w, is characterized by its uncoupled natural frequency ω_w, while the second one, the acoustic oscillator, describing the dynamics of the mass of air at the orifice, M_a, through its velocity U, is characterized by the its natural frequency ω_h. The system of equations (3.16)-(3.18) shows that both the dynamics of the membrane and of the orifice air mass are forced by the cavity pressure which couples them by means of the continuity equation (3.17). An external forcing due to the supply power also acts on the membrane dynamics. In order to investigate in more detail the coupling of the two oscillators, it is convenient to reformulate the equations.

By taking the time derivative of Eq. (3.16), in which both the added mass and the additional damping coefficient are independent of the time, and by eliminating the pressure derivative by means of Eq. (3.17), one obtains:

$$\ddot{V}_w + 2\zeta_w\omega_w\dot{V}_w + \left(\omega_w^2 + \omega_{wp}^2\right)V_w - \frac{A_o}{A_w}\omega_{wp}^2 U = (\omega\Delta x_w)\omega_w^2 cos\omega t \tag{3.19}$$

which is coupled with the Eq. (3.18). Note that another characteristic frequency ω_{wp} is introduced in Eq. (3.19), defined as

$$\omega_{wp} = \sqrt{\frac{\gamma A_w^2 p_o/V_c}{m_w}} = \sqrt{\frac{\gamma A_w p_o}{m_w H}} \tag{3.20}$$

which, according to Sharma [2], may be interpreted as the natural frequency of the pneumatic spring made of the air enclosed within the cavity of volume V_c and of the diaphragm mass m_w. Note that the height of the cavity, H, is explicitly introduced and V_w denotes the membrane velocity.

After introducing the positions: $x_1 = V_w$, $x_2 = U$, $b_1 = 2\zeta_w\omega_w$, $b_2 = K/l_e$, $k_{11} = \omega_w^2 + \omega_{wp}^2$, $k_{12} = -A_o\omega_{wp}^2/A_w$, $k_{21} = -A_w\omega_h^2/A_o$, $k_{22} = \omega_h^2$, the following governing system is finally written:

$$\ddot{x}_1 + b_1\dot{x}_1 + k_{11}x_1 + k_{12}x_2 = (\omega\Delta x_w)\omega_w^2 cos\omega t \tag{3.21}$$

$$\ddot{x}_2 + b_2|x_2|\dot{x}_2 + k_{21}x_1 + k_{22}x_2 = 0 \tag{3.22}$$

As shown by Eqs. (3.21)-(3.22), the coupling of the two oscillators is of elastic type. Furthermore, a linear damping term appears in the first equation and a non-linear damping term in the second one. Apart from the mutual influence of the two oscillators represented by the off-diagonal terms (that scale with $(d_w/d_o)^2$), one may note that the diagonal stiffness element k_{11} results to be modified compared with the uncoupled case by a factor $1 + CF$, where CF is the coupling ratio defined as

$$CF = \left(\frac{\omega_{wp}}{\omega_w}\right)^2 \tag{3.23}$$

CF represents the ratio of the air stiffness to the membrane stiffness; on the other hand, by inspecting Eq. (3.19) it is evident that if $CF \ll 1$ the membrane dynamics is de-coupled from the acoustic oscillator, with the variation of cavity pressure vanishing.

In order to evaluate the coupled natural frequencies, a study of free vibrations of the system will be hereafter carried out; initially the non-linear damping term of the second oscillator will be neglected and the relevant analytical treatment will be developed. However, despite this simplification, it will be showed hereafter that the analytical predictions of the resonance frequencies, even though not corrected rigorously, are in several

circumstances in very good agreement with data obtained by experimental measurements. Of course direct numerical solutions will be also performed, by integrating the fully non-linear governing system (3.16)-(3.18), that will show the crucial role played by the non-linear flow damping on the amplitude of the oscillations, as is well recognized in the literature, e.g. by Gallas et al. [1] (who attributed to it the absence of the first resonance peak for their device of case 2), Persoons [3], Kooijman and Ouweltjes [99].

Thus, neglected the non-linear damping, by introducing the following state vector

$$q = \{x_1 \quad x_2 \quad \dot{x}_1 \quad \dot{x}_2\}^T \tag{3.24}$$

and by reformulating the system (3.21)-(3.22) in matrix form, in the absence of forcing (i.e. null voltage) one obtains:

$$\{\dot{q}\} = [A]\,\{q\} \tag{3.25}$$

where

$$[A] = \begin{bmatrix} 1 & 0 & 0 & 0 \\ 0 & 1 & 0 & 0 \\ -b_1 & 0 & -k_{11} & -k_{12} \\ 0 & 0 & -k_{21} & -k_{22} \end{bmatrix} \tag{3.26}$$

and the natural frequencies of the mechanical system are related to the eigenvalues of the matrix $[A]$. It should be noted that $[A]$ is a 4×4 matrix and thus has four eigenvalues; with reference to Eq. (3.21), since the devices analyzed in the present work (that will be described later on) satisfy the condition $\zeta_w < 1$ (remember that the pure mechanical damping ratio has been assumed equal to 0.03, and it has been noted that this value is not substantially modified by interactions with the ambient air), the eigenvalues are two pairs of complex conjugate quantities; the natural frequencies, f_{1d} and f_{2d}, are of course given by the imaginary coefficients. For the actuators under analysis such eigenvalues are computed numerically and will be shown in the following Table 3.1.

Moreover, to the aim of obtaining convenient closed-form analytical evaluations of the natural frequencies, it is convenient to make the further assumption of absence of damping effects (the practical validity of such an assumption will be considered later, when discussing the results) so as to obtain the following relationship (normalized respect to ω_w^2)

$$\frac{\omega_{1,2}^2}{\omega_w^2} = \frac{-(1 + \frac{\omega_{wp}^2}{\omega_w^2} + \frac{\omega_h^2}{\omega_w^2}) \pm \sqrt{(1 + \frac{\omega_{wp}^2}{\omega_w^2} + \frac{\omega_h^2}{\omega_w^2})^2 - 4\frac{\omega_h^2}{\omega_w^2}}}{2} \tag{3.27}$$

In conclusion, the natural coupled frequencies in the totally undamped case are given by

$$f_{1,2} = \frac{\omega_{i1,2}}{2\pi} \tag{3.28}$$

that yields the relationships of such frequencies as a function of the first mode structural and Helmholtz frequencies. It is confirmed that if $CF \ll 1$ the two resonance frequencies tend to those of the uncoupled oscillators.

In some applications a desirable operating condition is represented by a relatively high plateau of fluid ejection velocity over a rather wide range of frequencies. This condition can be attained by designing the devices so as to have the two frequencies ω_1 and ω_2 close to each other. By inspecting the relationship (3.27) it can be verified that if $\omega_w \ll \omega_h$ then the distance between the two eigenvalues $|\omega_1^2 - \omega_2^2|/\omega_h^2$ does not depends on the cavity height H and therefore

$$|\omega_1^2 - \omega_2^2| \simeq \frac{1}{H/d_o} \tag{3.29}$$

On the contrary, if $\omega_w \gg \omega_h$, then $|\omega_1^2 - \omega_2^2|/\omega_h^2$ scales with H/d_o, hence

$$|\omega_1^2 - \omega_2^2| \simeq const \tag{3.30}$$

The numerical results presented will confirm these predictions and will show that for a strongly coupled actuator with $\omega_h > \omega_w$, the jet-flow velocity is maximized for relatively large cavity height.

In the next sections, it will be showed that the values estimated by means of the present relationships are in good agreement with those measured experimentally as well as calculated by computer direct simulations

3.3 Dimensionless form of the equations

In order to give more insight to the problem physics, it is worth recasting the governing equations into a convenient dimensionless form. As far as the acoustic oscillator is concerned, proper choices of the reference quantities for time, length and velocity are the reciprocal of the operating frequency $1/\omega$, the cavity height H and the speed of sound of air c, respectively. The dimensionless form of the dynamics of the acoustic oscillator accordingly is:

$$St^2 \frac{d^2U^*}{dt^{*2}} + St\left[K\sqrt{\frac{H}{l_e}}|U^*|\right]\frac{dU^*}{dt^*} = V_w^* - \frac{A_o}{A_w}U^* \tag{3.31}$$

where the Strouhal number is defined as

$$St = \frac{\omega H}{c}\sqrt{\frac{l_e}{H}} \tag{3.32}$$

It is easy to verify that the relationship holds

$$St = \frac{\omega}{\omega_h}\frac{d_o}{d_w} \tag{3.33}$$

The condition corresponding to $St \ll 1$ is physically relevant. Apart from the scaling quantity represented by the factor $\sqrt{l_e/H}$, this situation represents the case of acoustically thin cavity, with the traveling time of a small pressure disturbance over the distance H being much smaller than the reference time $1/\omega$; in other terms, the air inside the cavity behaves as an incompressible medium (i.e., the air stiffness is infinite). By inspecting Eq. (3.31), it is evident that this equation reduces to the dimensional relationship:

$$A_w V_w = A_o U \tag{3.34}$$

namely, the volume rate entering the cavity as a consequence of the membrane displacement equals the volume rate of air expelled through the orifice. On the other hand, Eq. (3.16) shows that the membrane dynamics is decoupled from that of the acoustic oscillator, with the membrane being driven by the piezo-electric forcing only. When $St \ll 1$, once the air velocity at the orifice has been obtained from Eq. (3.34), the cavity pressure may be evaluated by using the unsteady form of the Bernoulli's equation.

The physical situation of $St \gg 1$ also corresponds to decoupled membrane dynamics. In this case, however, the air stiffness is vanishing (the pressure field inside the cavity is practically unperturbed), so that the air jet velocity U is vanishing too.

In general, the coupling effects represented by the CF parameter refer to a certain device and may be neglected on the basis of design characteristics of the actuator, whatever is the operating condition. On the contrary, the conditions of decoupling occurring for $St \ll 1$ and $St \gg 1$ depend basically on the operating condition and they may occur for any device.

The dimensionless form of the acoustic oscillator can be used also to obtain useful information about the formation strength of the jet at the Helmholtz frequency. It should be remembered preliminarily that, within the framework of the classic linear theory of damped-driven harmonic oscillators, the acoustic oscillator can be defined underdamped or overdamped according as the acoustics damping coefficient, $\left(\frac{1}{2}K\sqrt{\frac{H}{l_e}}|U^*|\right)$, is less

than or greater than unity. The underdamped case corresponds to the occurrence of the resonance amplifications and therefore, if one extends such implications to the actual non-linear case, the jet should form sharply when driven at Helmholtz frequency. The difficulty here is that the damping coefficient is not a constant. It is straightforward to observe that such a formation criterion can be also expressed as

$$\frac{K}{2}\frac{|U_{med}|/l_e}{\omega_h} < 1 \tag{3.35}$$

where of course the jet velocity should refer to a proper scaling value, namely to the average value, U_{med}, yielding the equivalent amount of energy dissipated in a quarter of period by the variable damping coefficient. It is easy to verify that $U_{med} = U_{max}/2$, with U_{max} denoting the maximum value reached in the cycle. As will be shown in the section 3.7, the numerical simulations and the analytical evaluations of the operation of the devices under analysis show that the formation condition of Eq. (3.35) is usually fulfilled (with $K = 1.14$) and therefore the jet does form at Helmholtz frequency. Of course, since the acoustic damping coefficient depends on the jet flow velocity, the fulfillment of the formation criterion can be verified ex-post, namely as a result of the simulation.

In the case where the jet issues from a relatively long duct, distributed major head losses prevail on minor entrance losses. In this case the acoustic damping coefficient (i.e., the term in square brackets of Eq. (3.31)) results to be classically $32\nu/(d_o^2\omega_h)$, i.e. independent of the flow velocity, where ν is the kinematic viscosity of air, and the condition that guarantees underdamped oscillations writes:

$$\frac{|U_{med}|}{d_o\omega_h} < \frac{Re}{16} \tag{3.36}$$

where Re is defined by Eq. (1.1). Note explicitly that in the case of distributed head losses the acoustic damping effect is a standard linear term. By combining the above criterion with the celebrated formation criterion of Holman et al. [17], that refers to the generation and subsequent escape of the external vortex ring, one obtains:

$$0.16 < \frac{|U_{med}|}{d_o\omega_h} < \frac{Re}{16} \tag{3.37}$$

Note that Holman et al. [17] employ the average jet velocity during the expulsion stroke defined by Eq. (1.2), thus here $U_{med} = \overline{U} = (2/\pi)U_{max}$.

The equation of motion of the membrane is made dimensionless with the aid of different time and velocity scales, a convenient choice being $1/\omega_w$ and $\omega \Delta x_w$, respectively. The non-dimensional form of such an equation is

$$\ddot{V}_w^* + 2\zeta_w \dot{V}_w^* + V_w^* + CF\left(V_w^* - \frac{A_o}{A_w} U_w^*\right) = cos\omega t \tag{3.38}$$

The equation (3.38) further confirms that under the condition for which $CF \ll 1$ the membrane dynamics is decoupled from the acoustic oscillator one.

3.4 Numerical investigation

A numerical code has been written in which the governing equations system (3.16)-(3.18) has been numerically integrated by means of a standard 4th order Runge-Kutta method in MATLAB environment with *ode45* routine. Initial conditions of $x_w = 0$, $\dot{x}_w = 0$, $p_i = 0$, and $U = 0$ have been assumed for all the computations. By using a time step of the order of $1/(200f)$, it has been observed that the quasi-steady oscillatory solution is generally reached in about 20-30 cycles.

The uncertainty errors of the numerical data have been evaluated especially with respect to variations of the values of the head loss coefficient as well as of the effective orifice length [4].

3.5 Experimental investigation

In order to verify the analytical developments reported before, as well as to validate the numerical code, systematic experimental tests have been carried out on three different synthetic jet actuators designed to the purpose. The basic characteristics of such actuators are summarized in Table 3.1. The actuator with the membrane in brass and the two in aluminum are reported in Fig. 3.1, the brass one on the left, the aluminum ones on the right. They have been designed essentially in order to obtain different values of the coupling ratio, ranging from about zero to 1.88. The schematic of the devices is shown in Fig. 3.2 highlighting their modular structure, which permits independent variations of cavity diameter and height, orifice diameter, and piezoelectric diaphragm.

The brass actuator is a commercially available piezoelectric ceramic disk bonded to a thin brass metal plate fabricated by Murata Manufactoring Co. On the contrary, the

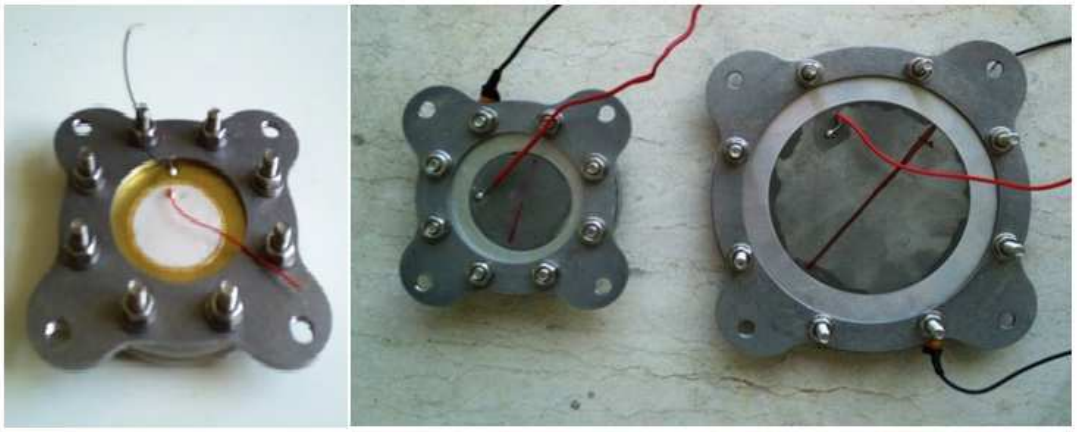

FIGURE 3.1: Pictures of the tested actuators. The brass shim is on the left, the aluminum shims on the right.

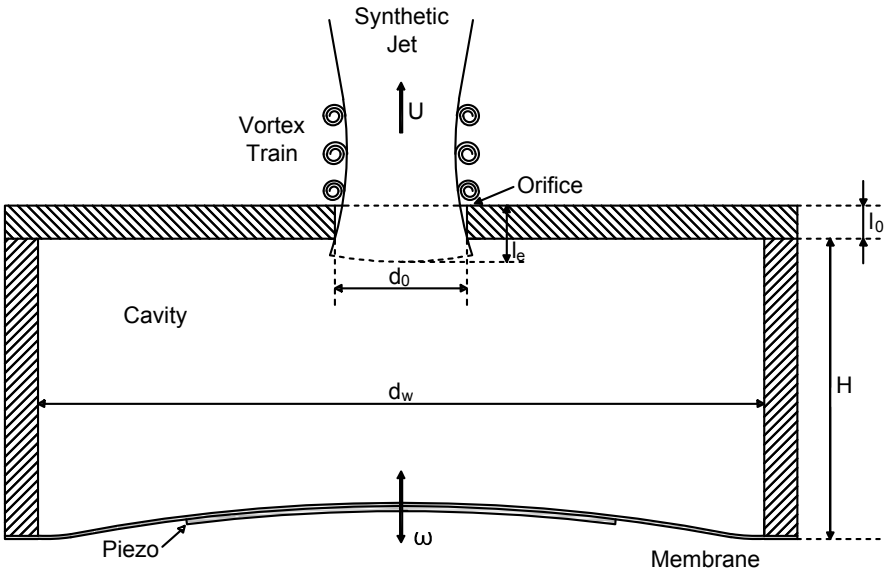

FIGURE 3.2: Modular structure of a typical device.

aluminum membranes were built in-house by gluing a LZT piezoceramic disk (manufactured by PIEZO Inc.) on a thin aluminum foil.

In Table 3.1 geometrical and mechanical properties, as well as nominal characteristic frequencies of the tested devices, listed on the basis of the shim material, are summarized. The frequencies reported in Table 3.1 have been calculated by means of the analytical model illustrated before. It should be remembered that f_w and f_h denote the (uncoupled) first-mode structural and Helmholtz natural frequencies, respectively, defined through Eqs. (3.11) and (3.15), respectively; f_1 and f_2 are the frequencies of the two coupled oscillators, i.e. the modified first-mode structural and Helmholtz resonance frequencies, defined by Eq. (3.28); f_{1d} and f_{2d} take into account linear damping effects and arise from the eigenvalues problem of Eqs. (3.24), (3.25) and (3.26). The coupling ratio CF introduced by Eq. (3.23) is reported in the last line.

TABLE 3.1: Features of the tested devices predicted analytically

	Property	Brass	Aluminum 1	Aluminum 2
Geometry	Shim diameter (mm)	35	42	80
	Shim thickness (mm)	0.4	0.24	0.25
	Piezoelectric diameter (mm)	23	31.8	63.5
	Piezoelectric thickness (mm)	0.23	0.191	0.191
	Cavity diameter (mm)	35	42	80
	Cavity height (mm)	$3-5$	$3-8$	$4-7-11$
	Orifice diameter (mm)	2	2	5
	Orifice length (mm)	2	2	2
	H/d_o	$1.5-2.5$	$1.5-4$	$0.8-1.4-2.2$
	l_e/d_o	1	1	0.4
Shim	Young's Module (Pa)	$9.7\text{x}10^{10}$	$7.31\text{x}10^{10}$	$7.31\text{x}10^{10}$
	Poisson's Module	0.36	0.31	0.31
	Density (Kg/m^3)	8490	2780	2780
Piezoelectric	Young's Module (Pa)	$6.7\text{x}10^{10}$	$6.6\text{x}10^{10}$	$6.6\text{x}10^{10}$
	Poisson's Module	0.31	0.31	0.31
	Density (Kg/m^3)	8000	7800	7800
Frequency response	f_w (Hz)	2176	1376	401
	f_1 (Hz)	$2256-2221$	$1632-1462$	$307-297-283$
	f_{1d} (Hz)	$2255-2220$	$1632-1461$	$307-297-283$
	f_h (Hz)	$1000-775$	$833-510$	$723-547-436$
	f_2 (Hz)	$964-759$	$702-480$	$944-737-617$
	f_{2d} (Hz)	$964-759$	$702-480$	$944-737-616$
	CF	$0.06-0.04$	$0.30-0.11$	$1.88-1.08-0.68$

As shown in Table 3.1, the nominal structural frequency of the brass devices is very close to the value predicted by the model of the coupled oscillators, evaluated both including damping effects (on the first oscillator) and neglecting them; in fact, it results also $f_1 \cong f_{1d}$. As a general trend, on the grounds of Eq. (3.27) the coupling effect increases the structural resonance frequency and lowers the Helmholtz resonance frequency. Furthermore, the coupling ratio CF is higher as the cavity height decreases. However, since for the aluminum 2 device the nominal structural frequency is less than the Helmholtz one, the situation is reversed in the sense that the coupling of the oscillators lowers f_1 and f_{1d} and raises f_2 and f_{2d}.

For the brass device it results that also the Helmholtz frequency (i.e., the natural frequency of the acoustic oscillator) is almost coincident with the value predicted by means of the coupling model; furthermore, it results $f_2 = f_{2d}$. The quasi-coincidence between the uncoupled natural structural and Helmholtz frequencies and the corresponding values of $\omega_{1,2}$, observed for the brass actuator, is much more weak for the aluminum 1 and totally disappears for the aluminum 2 actuator which exhibits the strongest coupling effect.

A brief description of the experimental set-up (depicted in Fig. 3.3) is reported in the following. The devices have been electrically excited with a sine signal generated in MATLAB environment through the routine *chirp* and then transmitted via a USB Instruments DS1M12 "Stingray" data acquisition system to a linear gain amplifier (typical gain factor is 5); an oscilloscope has been also employed to set the voltage amplitude V_a with a higher accuracy. The frequency of the signal has been varied typically over the range from 0 to 3000 Hz.

To the aim of detecting the frequency response of the actuators, measurements of pressure disturbances produced by the motion of the membrane into the external ambient and deflection of the (composite) membrane by means of a laser scanning vibrometer have been made. These experimental tests are described in detail in [4].

The experimental study of the frequency response of the three devices has been completed through a further testing session where the flow exit velocity has been measured in the external ambient at a station located on the jet axis approximately 1 orifice diameter downstream of the exit section. For these measurements a standard Kanomax Mini Pitot tube, 1/8" in diameter and 6" in length, has been employed in connection with a Mouser/All Sensor pressure transducer, whose output signal is acquired by means of the same DAQ unit and phase locked to the actuator excitation signal. The output signals are phase-averaged over typically 10 periods in order to obtain an uncertainty estimate of the jet velocity of 5%, calculated with the standard procedures of literature.

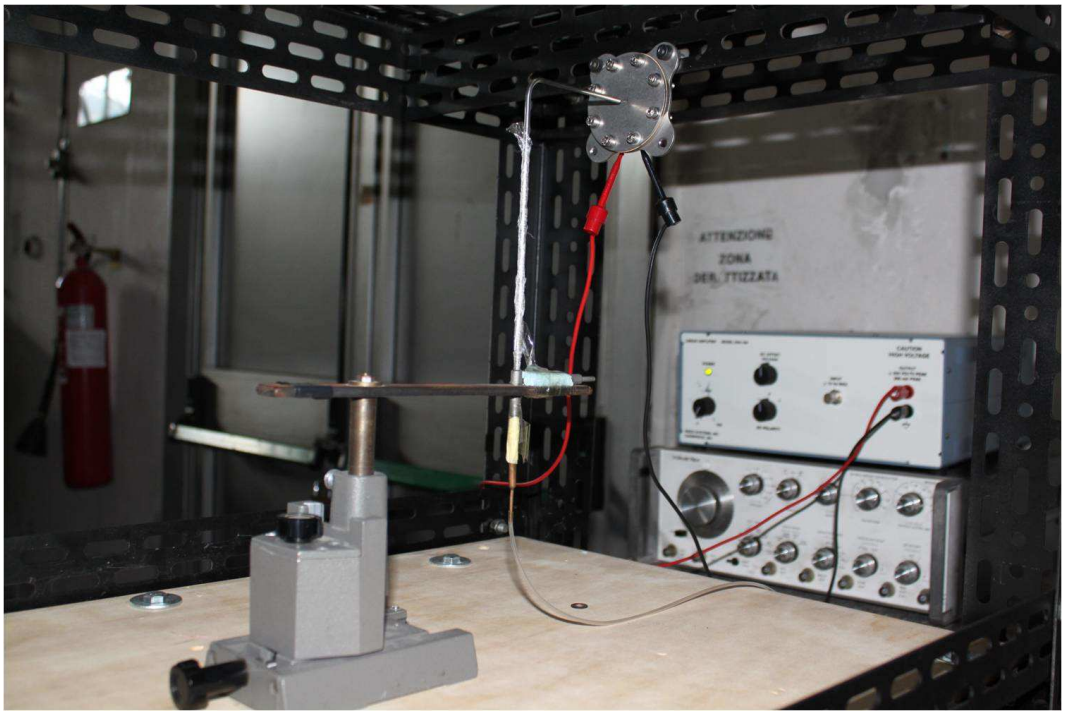

FIGURE 3.3: Sketch of the experimental setup.

Plots showing the frequency response of the actuators in terms of the downstream-directed velocity U_e measured by means of the Pitot tube, at a point one orifice diameter downstream of the orifice exit, and therefore approximately corresponding to the saddle point, are reported in Figs. 3.4, 3.5, 3.6. Following the basic definitions and findings of literature (e.g., Smith and Glezer [9], Smith and Swift [100]), the saddle point velocity is roughly 1.1 times the stroke length velocity (Eq. (1.2)). Thus, in order to compare experimental measurements of U_e to numerical computations of the peak value U_{max} of the exit velocity U, the following relationship is used: $U_e \cong (1.1/\pi)U_{max}{=}U_{max}/2.85$.

Data points of Figs. 3.4, 3.5, 3.6 are compared to the corresponding numerical values obtained by integrating numerically the complete governing equations. Typical values of the electroacoustic transduction coefficient ϕ_a that best fit the continuous numerical curves to the velocity measurements are 105, 133, 47.7 for brass, aluminum 1, aluminum 2 actuators, respectively. As reported previously, the numerical simulations have been performed with the basic values of $K = 1.14$ and $\Delta l_e = 0.62$ with the aim of optimizing the prediction capability of the numerical code in terms of jet-flow velocity.

Table 3.2 reports the resonance frequencies calculated numerically for each device at $V_a = 35$ V. This table should be compared to Table 3.3 showing analogous experimental findings in order to appreciate the data agreement. For the sake of convenience, data to be compared are reported in bold type in both tables. Data spread is generally less than 4% except for the value of the modified structural frequency of aluminum 2 actuator,

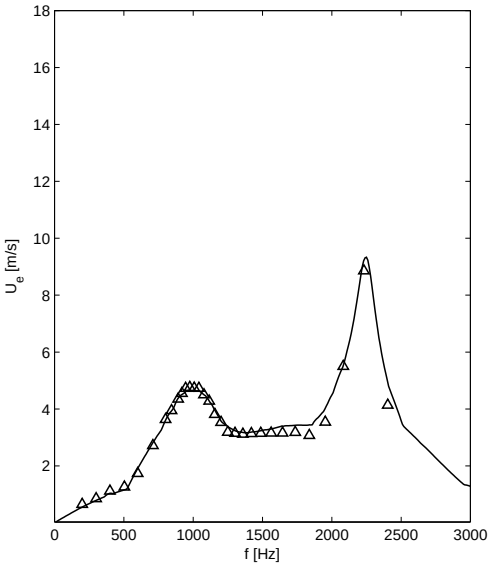

a)

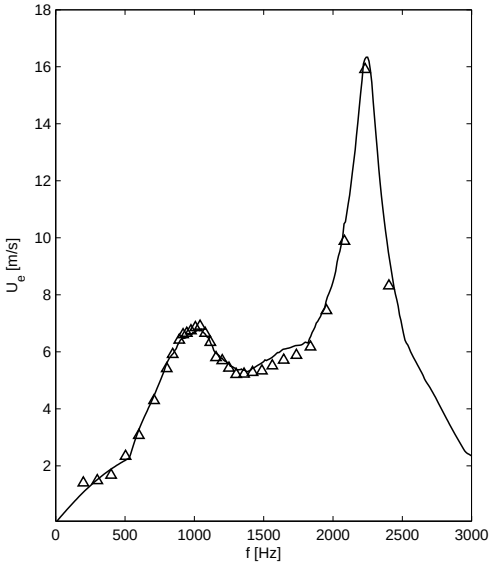

b)

FIGURE 3.4: Numerical-experimental comparison of average exit flow velocity frequency response for the brass actuator ($H = 3$ mm); triangles represent the experimental measurements, black curves represent the numerical solution; a) $V_a = 35$ V, b) $V_a = 70$ V.

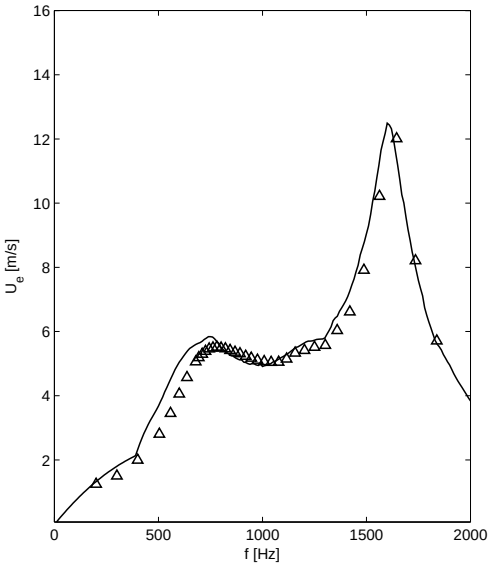

a)

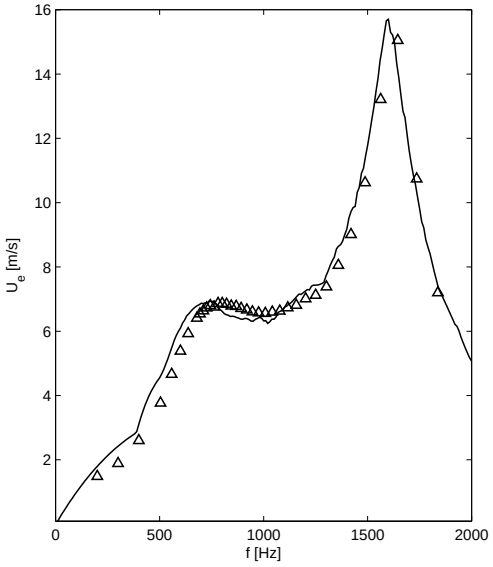

b)

FIGURE 3.5: Numerical-experimental comparison of average exit flow velocity frequency response for the aluminum 1 actuator ($H = 3$ mm); black curves represent the numerical solution, triangles represent the experimental measures; a) $V_a = 25$ V, b) $V_a = 35$ V.

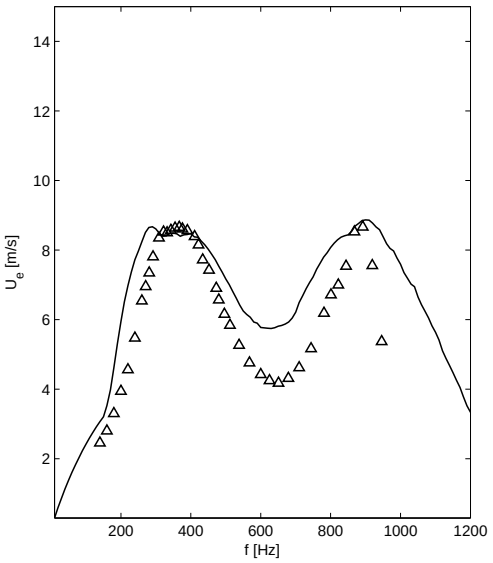

a)

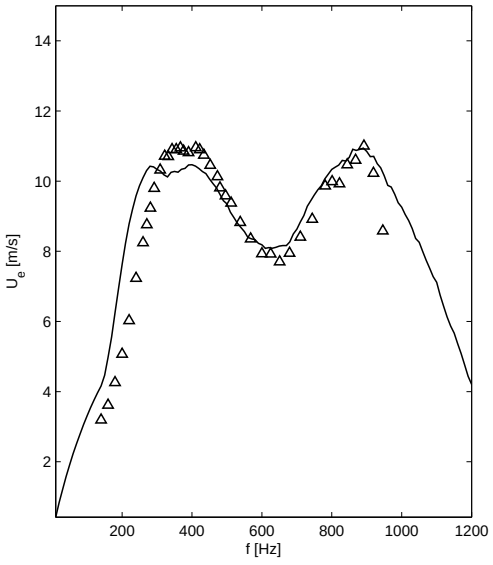

b)

FIGURE 3.6: Numerical-experimental comparison of average exit flow velocity frequency response for the aluminum 2 actuator ($H = 4$ mm); triangles represent the experimental measures; black curves represent the numerical solution; a) $V_a = 35$ V, b) $V_a = 50$ V.

for which it appears to be about 26%. However, it should be noted that computer simulations of Fig. 3.6 show a rather wide plateau around this peak frequency, whereas the data spread of 26% refers exactly to the peak value.

3.6 Further numerical insights

The results illustrated in the previous section exhibit a quite satisfactory agreement between the (fully nonlinear) numerical simulations of the frequency response of the resonant actuators considered in this work and the experimental and analytical findings. Thus, once the prediction capability of the numerical code has been established, it has been used to determine many other features of frequency response, very useful for design purposes. The maximum jet-flow exit velocity trends as functions of the operation frequency are depicted in Figs 3.7, 3.8, 3.9 for the three tested devices and for various dimensionless cavity heights H/d_o. The supply voltage V_a is equal to 35V in all these simulations.

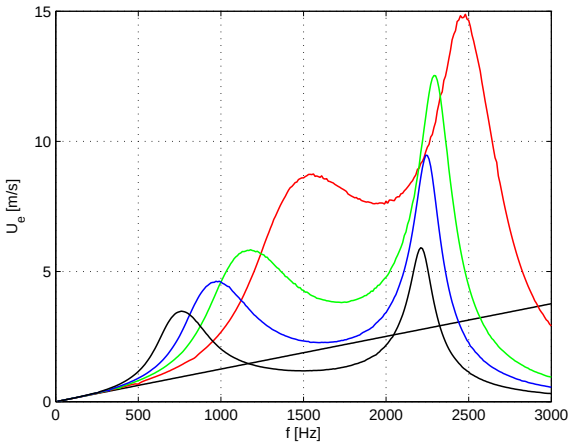

FIGURE 3.7: Frequency response of average exit flow velocity for the brass actuator at $V_a = 35$V; red line is for $H/d_o = 0.5$, green $H/d_o = 1$, blue $H/d_o = 1.5$, black $H/d_o = 2.5$. The straight line refers to Eq. (3.34).

For all the devices two velocity peaks corresponding to the two resonance frequencies are clearly evident. For the brass device both the velocity peaks increase with decreasing the cavity height, whilst for the aluminum 1 one the trend is that the velocity peak of the structural resonance reaches a plateau for intermediate values of H/d_o and then it decreases at the largest height. For the brass actuator the distance between the two resonance frequencies slightly increases with increasing H/d_0, in agreement with experimental results of Gomes et al. [101] obtained for $l_o/d_o > 1$, while for the aluminum 1 such a distance slightly decreases. Note that the experimental findings of Gomes et al. [101] show also that the resonance frequencies distance becomes practically constant as

TABLE 3.2: Numerical resonance frequencies at $\boldsymbol{V_a = 35}$V

	H (mm)	Modified Helmholtz frequency (Hz)	Modified structural frequency (Hz)
Brass	3	**960**	**2260**
	5	760	2210
Aluminum 1	3	**770**	**1630**
	8	490	1480
Aluminum 2	4	**900**	**290**
	7	690	320
	11	570	330

TABLE 3.3: Experimental resonance frequencies from Pitot tube

	V_a (V)	Modified Helmholtz frequency (Hz)	Modified structural frequency (Hz)
Brass ($H = 3$ mm)	35	**976**	**2232**
	70	1042	2232
Aluminum 1 ($H = 3$ mm)	25	781	1645
	35	**801**	**1645**
Aluminum 2 ($H = 4$ mm)	35	**892**	**367**
	50	892	367

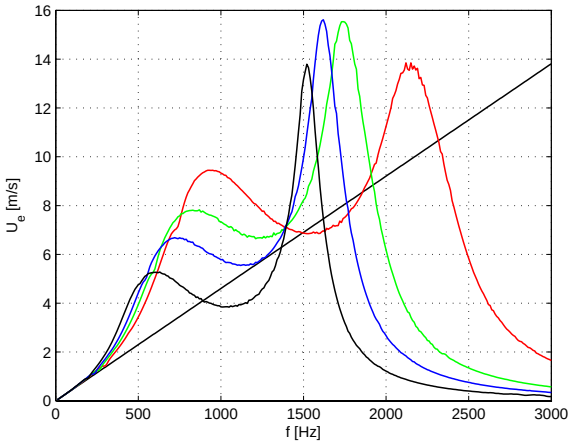

FIGURE 3.8: Frequency response of average exit flow velocity for the aluminum 1 actuator at $V_a = 35$V; red line is for $H/d_o = 0.5$, green $H/d_o = 1$, blue $H/d_o = 1.5$, black $H/d_o = 2.5$. The straight line refers to Eq. (3.34).

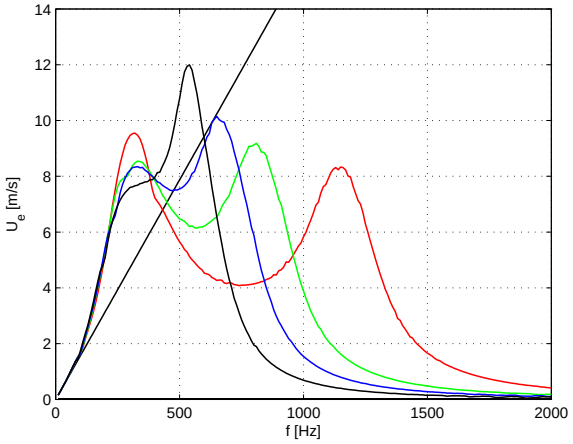

FIGURE 3.9: Frequency response of average exit flow velocity for the aluminum 2 actuator at $V_a = 35$V; red line is for $H/d_o = 0.5$, green $H/d_o = 1$, blue $H/d_o = 1.5$, black $H/d_o = 2.5$. The straight line refers to Eq. (3.34).

H/d_0 further increases, in agreement with the analytical prediction (3.30) valid in the case of $\omega_w \gg \omega_h$.

The straight lines present in the plots of Figs 3.7, 3.8, 3.9 refer to the linear dependance of the jet velocity upon the operating frequency given by the incompressible model described by the Eq. (3.34). For the brass and the aluminum 1 and 2 actuators it is clearly evident that such a simplified model closely agrees with the simulations of the complete model at low frequencies, the frequencies range of such an agreement widening for the smaller cavity heights, as predicted by the theory for $St \ll 1$. Note also that for this range of frequencies the response in terms of jet velocity is the same whatever is the cavity height, thus confirming that the membrane dynamics is decoupled from the acoustic oscillator one. These figures show that the uncoupled behavior is recovered also

for relatively high frequencies, i.e. $St \gg 1$, where the expected response is of vanishing U_e, anticipated at lower frequencies for the highest cavity heights.

In order to complete the discussion about the behavior of the aluminum 2 device, note that the two nominal Helmholtz and structural frequencies, which for this actuator are reversed, are remarkably modified by the high coupling ratio. The jet velocity decreases with increasing the cavity height at the structural resonance frequency, whereas it increases with increasing H/d_o at the Helmholtz resonance frequency, with the result that the maximum peak is reached at the Helmholtz frequency for the highest simulated cavity height. This particular finding agrees with the theoretical prediction (3.29). The quasi-coincidence of the two resonance frequencies justifies that the maximum peak is reached for the highest cavity height.

3.7 Formation strength of the jet at Helmholtz frequency

In the sect. 3.3 the role played by the non-linear damping term on the formation strength of the jet has been stressed theoretically. By resorting to the classic linear theory of damped driven harmonic oscillators, the acoustic oscillator has been defined underdamped or overdamped according as the acoustics damping coefficient, $\frac{K}{2}\frac{|U_{med}|/l_e}{\omega_h}$, with $U_{med} = U_{max}/2$, is less than or greater than unity, respectively. The underdamped case corresponds to the occurrence of the resonance amplifications and therefore, if one extends such implications to the present non-linear case, the jet should form sharply when driven at Helmholtz frequency. These predictions are confirmed by numerical simulations reported in Figs. 3.10 and 3.11, referring to the brass and the aluminum 2 actuators, respectively. For each device the membrane peak velocity, frame a), the average jet velocity, frame b), and the acoustic damping coefficient, frame c), are reported as functions of the operating frequency, for values of the head loss coefficient (mostly unphysical) of 0.14 (black line), 1.14 (red line), 3.14 (blue line), 5.14 (green line). Membrane velocity and jet velocity are also evaluated by means of the incompressible model of Eq. (3.34), whose behavior is reported with straight lines. Within this context the incompressible model represents also the static (namely for vanishing operation frequency) reference value to be used to evaluate the amplifications of the oscillations amplitude due to the resonance.

As far as the brass device is concerned, Fig. 3.10 a) confirms that, due to the vanishing coupling factor, the membrane dynamics is decoupled from the acoustic oscillator. In fact, the trends of the membrane velocity are practically independent of the head loss coefficient, there is no resonance at the Helmholtz frequency (about 1000Hz) and the incompressible model applies well up to frequencies not too greater than the Helmholtz

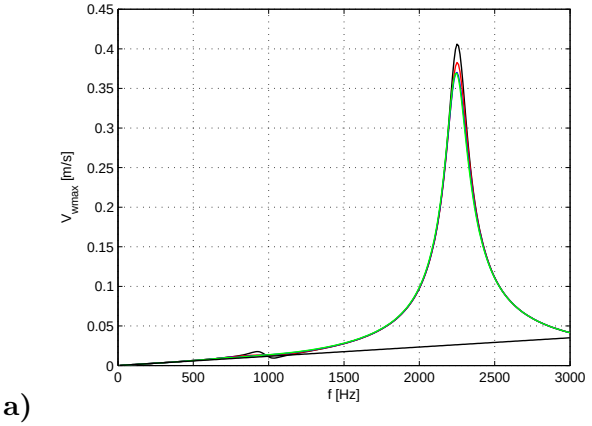

a)

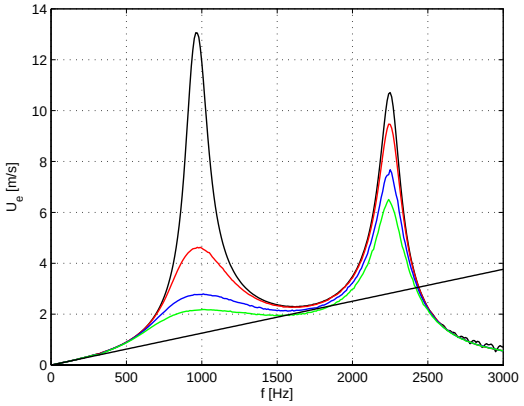

b)

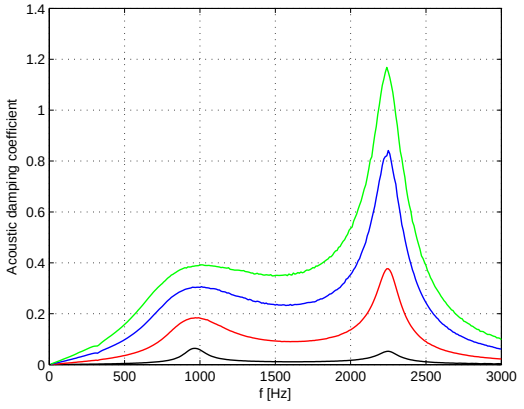

c)

FIGURE 3.10: Frequency response of the membrane peak velocity a), the average jet velocity b), and the acoustic damping coefficient c), for the brass actuator; black line is for $K = 0.14$, red $K = 1.14$, blue $K = 3.14$, green $K = 5.14$. The straight line refers to Eq. (3.34).

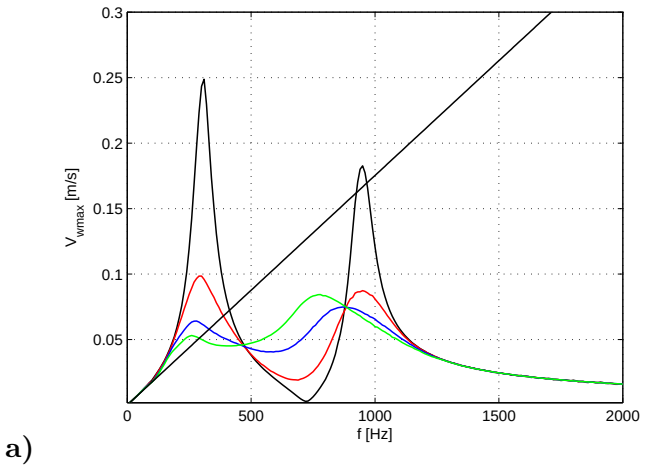

a)

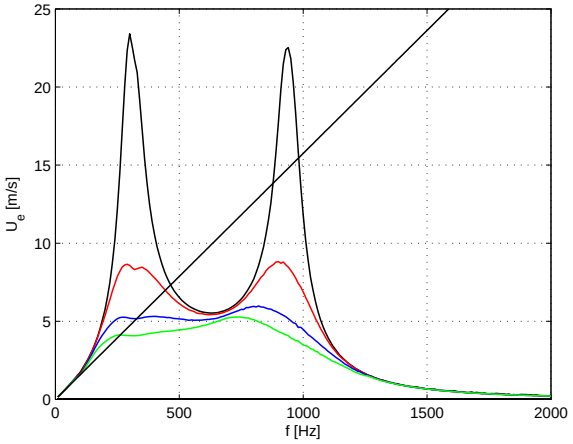

b)

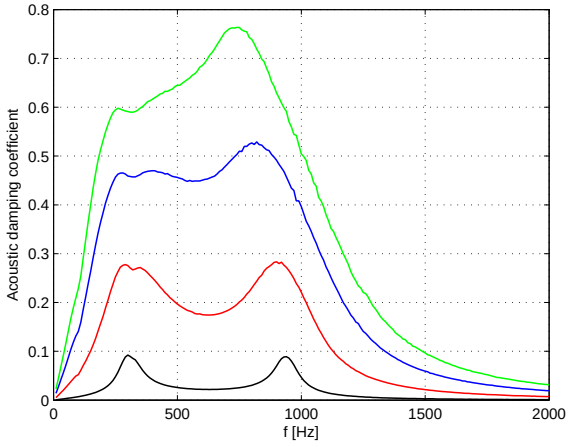

c)

FIGURE 3.11: Frequency response of the membrane peak velocity a), the average jet velocity b), and the acoustic damping coefficient c), for the aluminum 2 actuator; black line is for $K = 0.14$, red $K = 1.14$, blue $K = 3.14$, green $K = 5.14$. The straight line refers to Eq. (3.34).

frequency. Fig. 3.10 b) shows that the acoustic oscillator is always forced by the membrane one, and exhibits two resonance peaks, at Helmholtz and structural frequencies. However, the amplification factor of the oscillations, evaluated with reference to the static solution of Eq. (3.34), is remarkably grater than unity only for head loss coefficients equal to 1.14 and 0.14, which yield acoustic damping ratios well below 0.5 at the Helmholtz frequency.

Fig. 3.11 shows that for the aluminum 2 device the oscillators are fully coupled, as one expects from the relatively high coupling factor $CF = 1.88$. In fact, the membrane velocity, frame a), exhibits two resonance peaks (remember that for this device the structural resonance frequency is less than the Helmholtz one). Both velocity resonance peaks are influenced by the non-linear damping coefficient and for values of $K = 3.14$ and $K = 5.14$ (with the corresponding values of the damping coefficient being equal to about 0.5 and greater than 0.5, respectively) the jet velocity does not present resonance peaks. Moreover, note that for $K = 3.14$ and $K = 5.14$ the Helmholtz resonance frequency moves remarkably towards lower values compared with the value of the almost undamped situation ($K = 0.14$).

3.8 Fully non-linear analytical solution

By introducing the following positions:

$$\widetilde{V}_w = V_{wmax} e^{j(\omega t + \phi_{V_w})} \tag{3.39}$$

$$\widetilde{U} = U_{max} e^{j(\omega t + \phi_U)} \tag{3.40}$$

where $\widetilde{V}_w$ and $\widetilde{U}$ denote the complex membrane velocity and jet velocity, respectively, and ϕ_{V_w} and ϕ_U are the phase angles of the corresponding quantities, and by substituting them into Eqs. (3.21)-(3.22), it is possible to obtain the following "modal" solutions:

$$j\omega b_2 |\overline{U}| U_{max} + \left(-\omega^2 + k_{22} - \frac{k_{12} k_{21}}{-\omega^2 + j\omega b_1 + k_{11}} \right) U_{max} + \frac{j\omega k_{21} \Delta x_w \omega_w^2}{-\omega^2 + j\omega b_1 + k_{11}} = 0 \tag{3.41}$$

$$\Delta\phi_{U-V_w} = \phi_U - \phi_{V_w} = arctan\left(\frac{BC - AD}{AC + BD} \right) - arctan\left(\frac{C}{D} \right) \tag{3.42}$$

where

$$A = -b_2 \Delta x_w \omega^2 \omega_w^2 |U_{med}| \tag{3.43}$$

$$B = -\Delta x_w \omega^3 \omega_w^2 + k_{22} \Delta x_w \omega \omega_w^2 \tag{3.44}$$

$$C = \omega^4 - k_{22}\omega^2 - b_1 b_2 |U_{med}| \omega^2 - k_{11}\omega^2 + k_{11}k_{22} - k_{12}k_{21} \tag{3.45}$$

$$D = b_2 |U_{med}| (-\omega^3 + k_{11}\omega) - b_1 \omega^3 + b_1 k_{22} \omega \tag{3.46}$$

On the basis of the discussion made in the sect. 3.3, it has been assumed $U_{med} = U_{max}/2$. The "modal" solution for the aluminum 2 device is reported in Fig. 3.12 , in blue line and is compared to the corresponding numerical trend, in black line.

As can be seen, the numerical-analytical comparison is quite satisfactory.

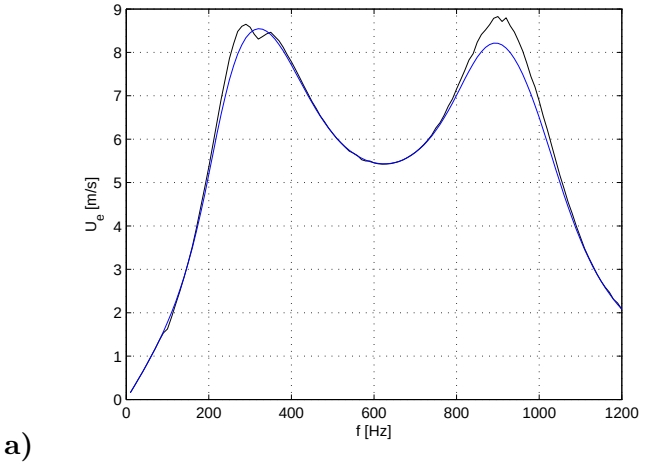

a)

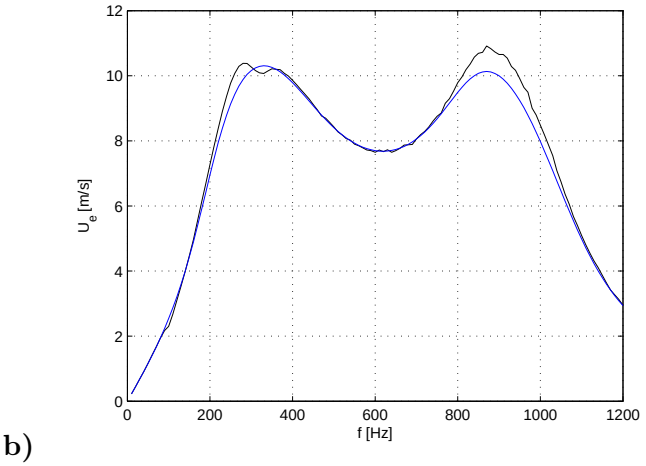

b)

FIGURE 3.12: Numerical-analytical comparison of average exit flow velocity for the aluminum 2 actuator ($H = 4$ mm); blue curves are analytical, black curves numerical; a) $V_a = 35$ V, b) $V_a = 50$ V.

Chapter 4

Efficiency of synthetic jet actuators

Although synthetic jets have been been so widely explored only few studies on the synthetic jet efficiency have been carried out. One of the first works on the efficiency of synthetic jet was undertaken by Tesar and Zhong [102] who based their definition of efficiency on the capability of jet generation rather than on energy conversion considerations. They found experimentally a constant efficiency value equal to 7.2% for several values of Reynolds number (ranging from 4000 to 8000) and for two values of dimensionless stroke length $\overline{L}/d_o$ (equal to 223.9 and 527.8). They also compared their experimental evaluation with a numerical prediction made by using the commercial code FLUENT, and found that this last is twice the experimental one. Subsequently Crowther and Gomes [103] studied the system costs associated with the application of flow control system to civil transport aircraft based on the use of electrically powered synthetic jet actuators. They defined the efficiency of the actuator as fluid power (scaling with the cube of the exit velocity) divided by absorbed electrical power, and analyzed it as a function of the operating conditions and actuator geometry, which were chosen reasonably close to those expected for industrial applications. For this reason the experiments were carried out basically with a chamber depth to orifice diameter ratio equal to 0.56 and an orifice depth to diameter ratio equal to 2.1. By resorting to the energy balance principle, Crowther and Gomes [103] considered that the difference between the supplied electrical power and the gained fluid power was lost because of electrical impedance (ascribed to the piezo-electric actuator), mechanical impedance (related to the diaphragm dynamics) and acoustic impedance (due to the fluid-acoustic coupling of the flow within the cavity and though the orifice), however without accurately quantifying each term of the balance. They showed their experimental findings in terms of a map of the electric-fluidic conversion efficiency, where such an efficiency was reported

as a function of excitation voltage amplitude (for peak-to-peak excitation voltage up to 250V) and actuation frequency (up to 4000Hz). They found that the efficiency attains a maximum equal to about 14% and noted that it did not correspond to the condition of maximum exit velocity because of the dielectric saturation effect affecting the commercial piezo-electric patch (i.e., the piezo-element bonded to the brass shim). A more recent work, focusing specifically on the energy conversion efficiency of synthetic jets devices, was presented by Li et al. [104] who tried to express on an analytical basis every term contributing to the energy rate balance. They argued that once the synthetic jet has received electric energy input, due to the capacitance of the piezo-electric actuator, a part of the energy is stored as electric potential energy while the rest of the energy is converted to mechanical energy accompanied by energy dissipation. The mechanical energy includes vibration of piezo-electric actuators and kinetic energy of air flow. For piezo-electric actuators two forms of energy, i.e. strain energy and kinetic energy, are temporarily stored by the vibrating structure. Energy dissipation (namely energy loss) occurs in piezo-electric actuators due to the deflection dynamics, as well as in the air flow motion (i.e., the head losses) when traversing the jet orifice. The synthetic jet device efficiency is defined as the ratio of the kinetic power of the air flow to the input electric energy. The authors carried out experiments on two slot synthetic jets having orifice length of 4mm and 15mm, for two values of voltage amplitude (80V and 100V) and actuation frequency ranging from 200Hz to 1100Hz. Li et al. [104] found that the efficiency of energy conversion is dependent on the orifice size and on the operating conditions (namely, voltage and frequency) showing a peak (of about 40% for the 15mm orifice) close to the mechanical resonance frequency of the actuator. They claim that the uncertainty of their experimental evaluation was of about 34%.

The aim of the present chapter is to assess a rigorous and comprehensive physical approach to the evaluation of the efficiency of piezo-electrically driven synthetic jet actuators, based on the rather detailed modelling of the actuator dynamics, described in the previous chapter. The peculiarity of the present approach is that the energy balance equation, properly averaged over the actuation period, is derived directly from the equations governing the dynamics of the actuator. The advantage is that the presence of each term of the resulting energy balance draws its justification from the corresponding dynamics term and, in principle, there is no need to perform experimental measurements to evaluate the actuator efficiency at the orifice exit section. Since the physical model described in the previous chapter has been tested and calibrated against a systematic experimental campaign, the uncertainty of the efficiency estimation should be reduced. The modelling is validated against numerical as well as experimental investigations carried out on the aluminum 2 device.

The treatment described hereafter has been arisen by [105] (see Appendix)

4.1 Derivation of the energy balance equation and definition of efficiency

Multiplying the equation (3.1) by the membrane velocity $\dot{x}_w$, yields:

$$\frac{dE_w}{dt} = F\dot{x}_w - p_i A_w \dot{x}_w - c_w \dot{x}_w^2 \tag{4.1}$$

where E_w is the diaphragm energy defined as

$$E_w = \frac{1}{2} m_w \dot{x}_w^2 + \frac{1}{2} k_w {x_w}^2 \tag{4.2}$$

that takes into account both kinetic and elastic strain contributions.

The unsteady Bernoulli's equation (3.13) can be expressed in the following way

$$M_a \frac{dU}{dt} = p_i A_o - \frac{1}{2} K \rho_a A_o U|U| \tag{4.3}$$

Similarly, the product between the equation (4.3) and the jet exit velocity U yields

$$\frac{dE_o}{dt} = p_i A_o U - \frac{1}{2} K \rho_a A_o |U|^3 \tag{4.4}$$

where E_o is given by

$$E_o = \frac{1}{2} M_a U^2 \tag{4.5}$$

and represents the kinetic energy flow rate of the air mass through the orifice.

The (instantaneous) energy balance equation of the actuator system can be obtained by summing the equations (4.1) and (4.4). Moreover, since we are interested in characterizing the actuator behavior over an operating cycle, it is convenient to apply the time average operator on the resulting equation, defined as

$$\bar{\varphi} = \frac{1}{\tau} \int_0^\tau \varphi dt \tag{4.6}$$

where φ is the generic time-dependent variable.

The energy balance equation averaged over an actuation cycle (i.e., over a time equal to the period τ) is given by

$$\underbrace{\frac{1}{\tau}\int_0^\tau d(E_w+E_o)}_{\overline{\Delta E}} = \underbrace{\frac{1}{\tau}\int_0^\tau F\dot{x}_w dt}_{\bar{P}_e} + \underbrace{\frac{1}{\tau}\int_0^\tau p_i(A_o U - A_w\dot{x}_w)dt}_{\bar{P}_m} - \underbrace{\frac{1}{\tau}\int_0^\tau c_{wt}\dot{x}_w^2 dt}_{\bar{D}_s} - \underbrace{\frac{1}{\tau}\int_0^\tau \frac{1}{2}(K-1)\rho_a A_o|U|^3 dt}_{\bar{D}_f} - \underbrace{\frac{1}{\tau}\int_0^\tau \frac{1}{2}\rho_a A_0|U|^3 dt}_{\bar{P}_k} \quad (4.7)$$

An accurate description of the various contributions of equation (4.7) is reported hereafter:

- $\overline{\Delta E}$ is the total energy variation. Note that this term is null because, for each cycle, there is no change for E_w and E_o.
- $\bar{P}_e$ is the electrodynamic power provided to the membrane by the applied voltage.
- $\bar{P}_m$ is the mechanical power due to the work done by the differential pressure p_i which acts on the wall surface A_w and on the orifice surface A_o. By using the equation (3.17), it can be shown that this term is proportional to $\frac{1}{2}({p_i}^2(\tau)-{p_i}^2(0))$ and, therefore, it does not give any contribution because p_i assumes the same value at the beginning and end of each cycle. One can reach the same result by observing that the pressure work is conservative by definition.
- $\bar{D}_s$ is the power dissipation due to the structural damping effects of the membrane.
- $\bar{D}_f$ is the power dissipation due to the head loss of fluid dynamics type at the orifice.
- $\bar{P}_k$ is the kinetic power of air flow at the orifice. Note explicitly that the kinetic power here refers by definition to the entire cycle, i.e. the suction phase included.

Then, by deleting $\overline{\Delta E}$ and $\bar{P}_m$ terms, the equation (4.7) becomes

$$\bar{P}_e - \bar{D}_s - \bar{D}_f - \bar{P}_k = 0 \quad (4.8)$$

and, once defined the kinetic efficiency η_c as the ratio of the kinetic power of the exit flow $\bar{P}_k$ to the electrodynamic power $\bar{P}_e$, one obtains

$$\eta_k = \frac{\bar{P}_k}{\bar{P}_e} = 1 - \frac{\bar{D}_s + \bar{D}_f}{\bar{P}_e} \quad (4.9)$$

It is worthwhile to stress that in practice the global efficiency of an actuator has to quantify the amount of Joule power provided to the system $\bar{P}_j$ that is actually converted in $\bar{P}_e$. This can be done by introducing the electrodynamic transduction efficiency η_e

$$\eta_e = \frac{\bar{P}_e}{\bar{P}_j} \tag{4.10}$$

Hence, finally, one can define the (global) efficiency of the actuator η as the product of η_k by η_e

$$\eta = \eta_k \eta_e = \frac{\bar{P}_k}{\bar{P}_j} \tag{4.11}$$

where the external Joule power supply $\bar{P}_j$ provided to the actuator is calculated as

$$\bar{P}_j = \frac{1}{\tau} \int_0^\tau VI dt \tag{4.12}$$

with $V = V_a \sin \omega t$ being the applied voltage and I the electric current flowing through the piezo-electric element.

The rate of $\bar{P}_j$ not turned into $\bar{P}_e$ is converted into a variation of internal energy $\dot{Q}$ of the air inside the cavity (heat generation per unit time), which is transferred in part to the external ambient through a natural convection mechanism, and, in part, into enthalpy flow rate of the air leaving the orifice

$$\bar{P}_j - \bar{P}_e = \dot{Q} \equiv h A_e \Delta T + \dot{m} c_p \Delta T \tag{4.13}$$

where h is the convective heat transfer coefficient by natural convection, A_e is the exchange surface (which depends on the relevant geometry of actuator), ΔT is the average-per-cycle temperature difference between the system and the colder surrounding external air, $\dot{m} = \rho_a \bar{U} A_o$ where $\bar{U}$ is the average velocity associated to the stroke length (eq. 1.2), and c_p is the specific heat coefficient at constant pressure. For the sake of simplicity it has been assumed that the air inside the cavity is isothermal with the device case.

From equation (4.13) one obtains also

$$\eta_e = 1 - \frac{\dot{Q}}{\bar{P}_j} \tag{4.14}$$

4.2 Validation of the model and results

For the aluminum 2 device, the modeling developed before has been employed to estimate the various contributions of the energy budget equations (4.7, 4.8) by carrying

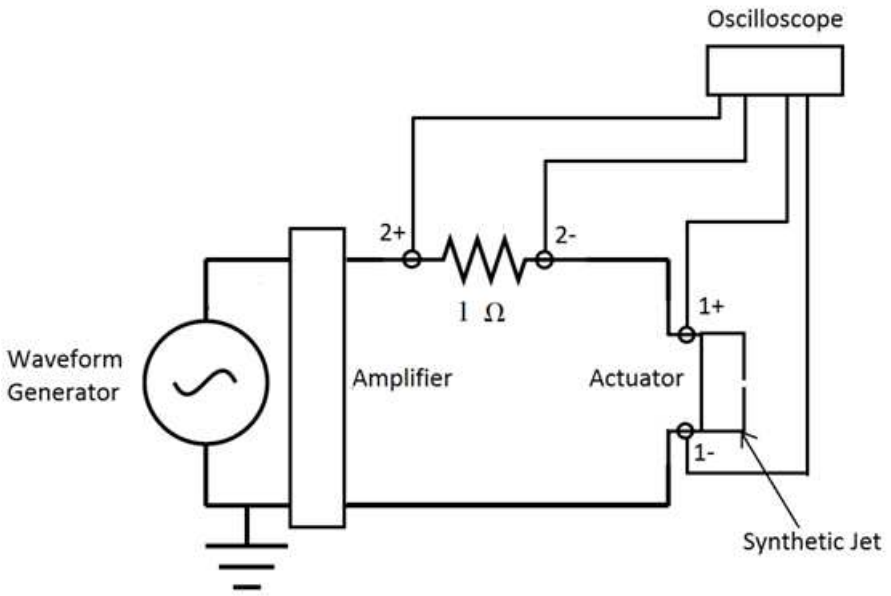

FIGURE 4.1: Sketch of the experimental setup.

out direct numerical simulations of the governing equations (3.16, 3.17, 3.18). For a proper operating frequency f, the time trends of the relevant quantities, in practice the membrane velocity and the air velocity at the orifice exit, have been used to evaluate, ultimately, the energy conversion efficiencies (4.9, 4.10, 4.11). The time averages here performed refer typically to the 23^{th} cycle.

For a given operating voltage, the evaluation of the Joule power supply (equation (4.13)) needs the knowledge of the current intensity. This has been done by means of the theoretical relationship

$$I_t = 2\pi f C V_a \tag{4.15}$$

where I_t denotes the theoretical current intensity peak, and C is the electric capacitance of the piezo-ceramic disk (furnished by the manufacturer). To verify this estimation, the current intensity peak has been also measured directly by means of the experimental apparatus sketched in Fig. 4.1. A waveform generator (Wavetek model 164) creates an electrical sinusoidal signal which is amplified (by EPA 104 PIEZO System inc. unit) and sent to the synthetic jet device. Voltage and current are acquired by a two channels oscilloscope (Tektronix tds 2024).

In Table 4.1, experimental measurements of the electric current peak I_e are compared to the corresponding theoretical values I_t. The data spread is generally less than 9% except for $V_a = 50V$, for which it appears to be about 13%.

TABLE 4.1: Comparison of theoretical current peak with measured data (Ampere)

$V_a(V)$	$I_t(A)$	$I_e(A)$
25	0.038	0.036
30	0.045	0.044
35	0.052	0.054
40	0.059	0.056
45	0.066	0.060
50	0.073	0.064
55	0.079	0.074
60	0.085	0.080
65	0.093	0.086
70	0.099	0.094
75	0.106	0.104

TABLE 4.2: Efficiencies and dissipation terms at modified Helmholtz frequency

$V_a(V)$	$\eta_k(\%)$	$\eta_e(\%)$	$\eta(\%)$	$\bar{D}_f/\bar{P}_e(\%)$	$\bar{D}_s/\bar{P}_e(\%)$
25	79.6	90.7	72.2	11.1	9.3
30	79.8	85.4	68.1	11.2	8.7
35	79.5	79.6	63.3	11.1	8.7
40	79.3	74.8	59.3	11.1	8.8
45	80.2	69.6	55.8	11.2	7.9
50	79.6	66.8	53.2	11.1	8.1
55	81.3	64.2	52.2	11.4	7.8
60	81.7	59.1	48.3	11.4	7.2
65	80.8	58.8	47.5	11.3	7.8
70	79.7	54.6	43.5	11.2	7.7
75	80.8	51.5	44	11.3	7.8

The efficiency values computed for the tested device at the modified Helmholtz resonance frequency (which is of 900Hz, as reported in the previous chapter) are listed in Table 4.2, together with the two power dissipation terms.

As one can observe (Table 4.2), the influence of the driving voltage is rather weak for η_k, $\bar{D}_f/\bar{P}_e$ and $\bar{D}_s/\bar{P}_e$; conversely, η_e decreases with increasing V_a, thus determining the same trend for the global efficiency η. For the sake of completeness, to give the reader the possibility to check the calculations, the following additional parameters have been considered, according to the complete description of the actuator under examination made in the previous chapter: $\rho_a = 1.205\ Kg/m^3$; $k_w = 9.48 \cdot 10^4\ N/m$; $d_A = 4.01 \cdot 10^{-9}\ m^3/V$; $c_{wt} = 2.75\ Ns/m$, evaluated at the frequency of 900Hz.

Hereafter it will show that the trends against voltage of the quantities shown in Table 4.2 are well fitted by simple power laws which, in turn, can be justified on the basis of scaling theoretical considerations.

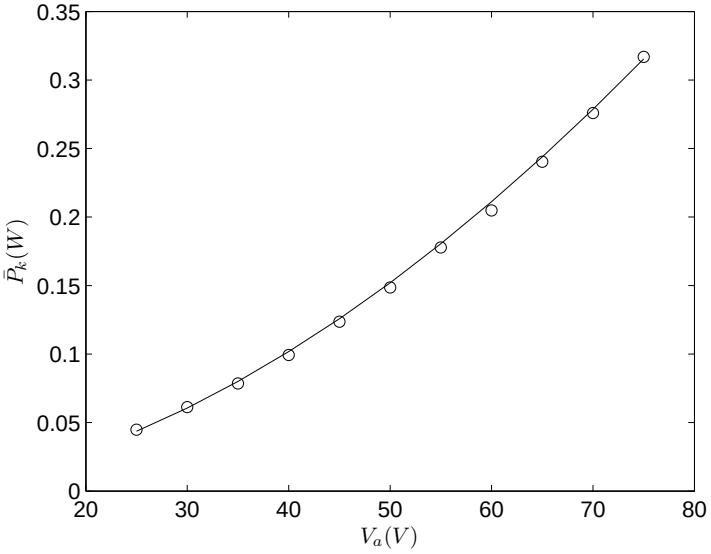

FIGURE 4.2: Kinetic power at orifice exit versus voltage. Circle symbols are computed data, continuous line represents eq. (4.16)

From the numerical integration of the governing equations it has been found that the variations of exit kinetic power and electrodynamic power follow the following trends

$$\bar{P}_k \approx {V_a}^{1.8} \tag{4.16}$$

$$\bar{P}_e \approx {V_a}^{1.8} \tag{4.17}$$

as is depicted in Figs. 4.2 and 4.3, respectively, where circle symbols refer to computed data e continuous lines refer to the analytical relationships. Therefore, being η_k given by the ratio between two quantities both proportional to ${V_a}^{1.8}$, it does not depend on V_a. Since one expects that $\bar{D}_f$ has the same scaling law as $\bar{P}_k$, the fluid dynamic dissipation rate $\bar{D}_f/\bar{P}_e$ is constant too. Indeed, according to their definitions in equation (4.7), $\bar{P}_k$ and $\bar{D}_f$ vary as U_0^3 and $\bar{P}_e$ as $F_0\dot{x}_{w0}$ (with U_0 and $\dot{x}_{w0}$ being the fluid and membrane peak velocities, respectively), and therefore one could expect that they scale as V_a^3 and V_a^2, respectively. However, due to the complex coupling between the two oscillators, the membrane and the acoustic one, in the presence of significant non linear damping acting on the acoustic one, such theoretical laws are remarkably modified. Here it has been that $U_0 \approx {V_a}^{0.6}$ and $\dot{x}_{w0} \approx {V_a}^{0.8}$. Since F_0 scales with V_a, the scaling relationships of equations (4.16) and (4.17) are justified.

Fig. 4.4 shows that the Joule power, evaluated experimentally, increases with increasing the voltage amplitude following a power law of the kind

$$\bar{P}_j \approx {V_a}^{2.3} \tag{4.18}$$

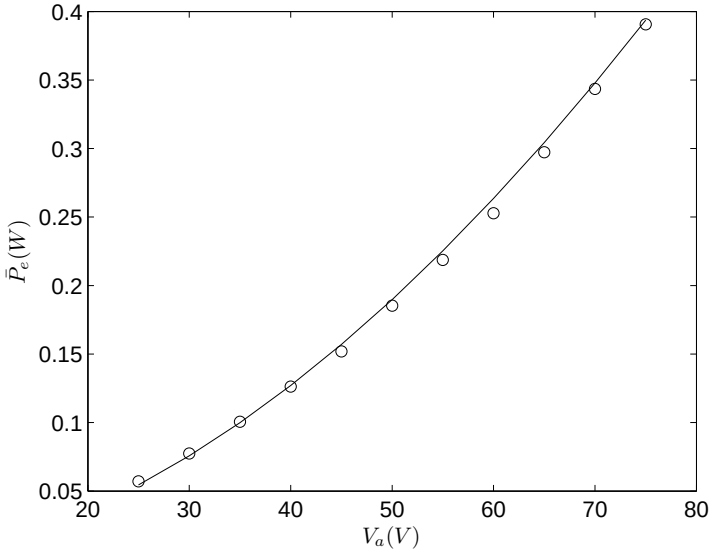

FIGURE 4.3: Electrodynamic power versus voltage. Circle symbols are computed data, continuous line represents eq. (4.17)

Note that if the behavior of the piezo-ceramic element was governed perfectly by the Ohm's law, i.e. if the capacitance was constant, $\bar{P}_j$ would be directly proportional to ${V_a}^2$. In effect, the relationship (4.18) tells us that the piezo-element capacitance varies as a function of the voltage and, furthermore, that the output instantaneous current is a distorted sine wave.

Finally, as depicted in Fig. 4.5, the behavior of the transduction coefficient η_e defined by equation (4.10) and relating the Joule power to the electrodynamic one, taking into account also the relationship (4.17), is well fitted by a power law of the following type

$$\eta_e \approx {V_a}^{-0.5} \tag{4.19}$$

A similar trend holds for the global efficiency η (equation (4.11)).

Hereafter this section will end with some practical remarks. Remember that the kinetic power defined by equation (4.7), and the related kinetic efficiency of equation (4.9), refer by definition to the entire cycle, i.e. the suction phase included. In effect, in some specific applications where, for instance, the final goal is to obtain a proper trust linked to the downstream momentum flux, or in heat transfer situations where the goal is to achieve a proper jet Reynolds number based on the stroke length velocity of equation (1.2), the kinetic power should be referred to the ejection phase only and evaluated just downstream of the so called saddle point, namely the stagnation point along the jet axis separating, during the suction phase, the ingestion near field and the ejection far field. Of course, an accurate evaluation of the time variation of the jet velocity at the saddle

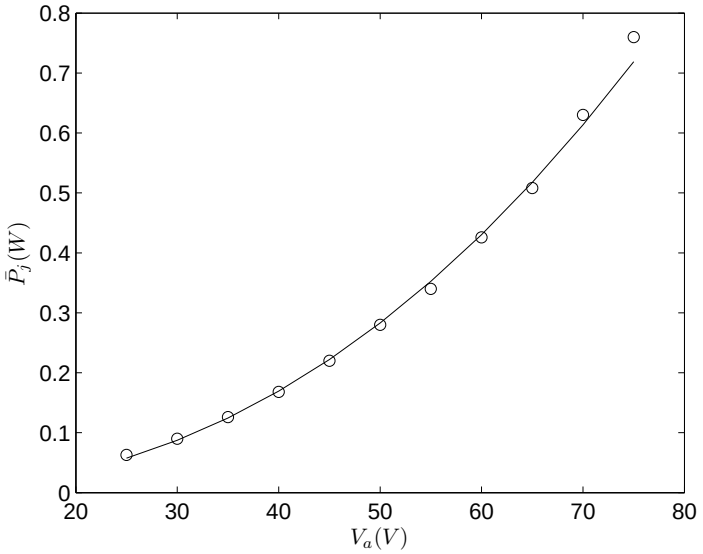

FIGURE 4.4: Measured Joule power versus voltage. Circle symbols are experimental data, continuous line represents eq. (4.18)

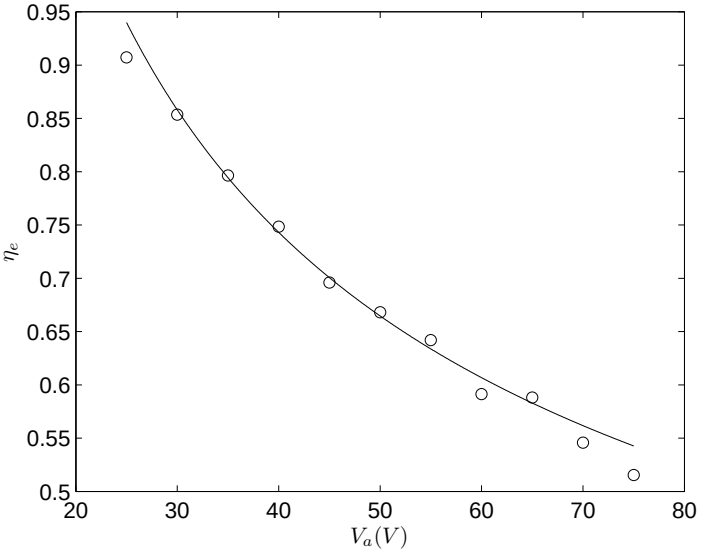

FIGURE 4.5: Electrodynamic efficiency versus voltage. Circle symbols are measured data, continuous line represents eq. (4.19)

point could be made by proper measurements (e.g., by means of PIV techniques) or by detailed CFD computations. However, according to the experimental findings of Smith and Glezer [9], one can admit that the jet velocity peak is about the same as the air velocity peak at the orifice; thus, under the assumption of sine temporal variation of the jet velocity just downstream of the saddle point during the ejection phase, one could conclude that the kinetic power is roughly speaking the half of the quantity estimated by equation (4.7). In practice, due both to a temporal distortion of the velocity signal from the sine trend, and to addition fluid dynamic dissipations in the external air field, the kinetic power can lower down to about 1/3 of the quantity defined in equation (4.7). Thus, the values of efficiency reported in Table 4.2 should be reduced by a factor ranging from 1/2 to 1/3 accordingly. For instance, the global efficiency of 44% corresponding to the voltage of $V_a = 75V$ would be reduced down to about 15%.

Moreover, when a numerical modelling is not available to estimate the electrodynamic power, the electric efficiency can be evaluated through the equivalent relationship (4.14), which requires essentially the measurement of the mass flow rate of air at the orifice, the Joule power and the average-per-cycle temperature difference between the system and the colder surrounding external air ΔT introduced in equation (4.13). Here equation (4.13) has been employed within a reverse procedure to estimate ΔT. If we assume $h = 10W/m^2$, which is a typical value in natural convection, for the standard value of the specific heat coefficient at constant pressure at ambient temperature, ΔT ranges from $0.02°C$ (corresponding to the lower voltage) to $0.78°C$.

Conclusions

This thesis has been aimed to yield insights on the frequency response of synthetic jet actuators driven by piezoelectric thin elements by using a lumped-element mathematical model. The model is fluid-dynamics based, and although its genesis is inspired by an analogous model of previous literature, it is innovative because it needs in input just electromechanical properties easily available from the commercial data sheet of the materials. For a certain class of devices, a numerical fitting parameter only is required, namely the electroacoustic transduction coefficient ϕ_a, which is the ratio of the effective acoustic piezoelectric coefficient to the acoustic compliance. From this viewpoint, the proposed model represents a practical tool for the overall design of the actuator. Among other quantities, the model can yield the frequency response characteristics of synthetic jet devices in terms of membrane displacement, pressure cavity, and exit jet-flow velocity. The computer code has been validated via comparisons with both analytical and experimental parallel investigations.

In the analytical study, the actuator has been idealized as an acoustic-mechanical system of two-coupled oscillators, and simple but rather accurate relationships have been given to predict the two peak frequencies, corresponding to the modified Helmholtz and first-mode structural resonance frequencies. Scaling laws of the distance between the two resonance frequencies as a function of the nondimensional cavity height H/d_o have been yielded. It is found that the role of the coupling effects is twofold; on one hand, they modify the nominal Helmholtz and structural resonance frequencies, and on the other hand, they introduce crossed linear reaction terms driving mutually the oscillators. The system suffers a nonlinear damping due to entrance head losses, which are proportional to the head loss coefficient and inversely proportional to the effective orifice length. The analytical investigation has been completed by inspecting the dimensionless form of the governing equations, which introduce two characteristic parameters: the frequencies coupling factor and the Strouhal number. The study showed that the acoustic oscillator is always driven by the membrane dynamics, while there exist conditions under which the membrane behavior is decoupled from the Helmholtz oscillator. The case of $St \ll 1$ is very interesting too. It physically corresponds to acoustically thin cavity and, for a

given device, occurs at relatively low operation frequencies. In this decoupled regime it has also been found that the behavior of the actuator is well described by the so called incompressible model, where the air volume rate entering the cavity as a consequence of the membrane displacement equals the air volume rate leaving the cavity through the orifice.

To perform comparisons with numerical data, various measurement campaigns have been carried out on three different actuators especially designed and manufactured to the purpose. The devices make use of brass or aluminum shims and standard piezoelectric disks driven by a sine input voltage. They have been designed essentially to achieve an increasing coupling ratio. A digitized pitot probe has been also used to measure the jet velocity in the external field at a location approximately coincident with the saddle-point (i.e., about one orifice diameter downstream of the exit section).

The overall comparison among numerical and analytical as well as experimental findings is quite satisfactory. In particular, the predictions of the peak frequencies made by using the simple analytical relationships are confirmed by both the numerical computations and the various measurements. For the device exhibiting the strongest coupling, a perhaps not expected result is that the jet velocity peak occurs for the highest cavity height. The present study has confirmed the crucial role played by the nonlinear damping term on the acoustic (Helmholtz) oscillator of the model in reducing or suppressing the corresponding resonance peak. The numerical code has been, in general, calibrated on jet velocity data by using $K = 1.14$ and $\Delta l_e = 0.62$.

A comprehensive and detailed physical modelling to evaluate the efficiency of synthetic jet actuators, driven by piezoelectric effect. This approach is original because is based on relevant energy equations written for both the membrane and acoustic oscillators, which are derived from the corresponding motion equations.

It has been shown that the global efficiency, which is defined as the ratio of the useful kinetic power to the input Joule power, can be expressed as the product of the electrodynamic efficiency (defining the conversion of Joule power to electrodynamic power) and the kinetic efficiency (defining the conversion of electrodynamic power to kinetic energy). Both the efficiency can be also estimated in terms of the relevant dissipation terms. In particular, the electrodynamic efficiency is related to the variation of internal energy of air inside the cavity, or heat generation, which is dissipated towards the external ambient both by natural convection on the walls of the actuator case, and through the enthalpy flow rate traversing the orifice. On the contrary, the kinetic efficiency is produced by fluid dynamics and structural dissipations.

The physical model has been validated against experimental measurements carried out on a built-in-house device having the piezo-ceramic disk glued on an aluminum shim. Combined numerical and experimental investigations allowed us to find that, for the particular actuator under examination, analyzed at modified Helmholtz frequency, the kinetic efficiency does not vary with applied voltage, whereas the electrodynamic efficiency scales with the reciprocal of the voltage square root. These trends have been also justified according to theoretical scaling laws discussed for each relevant power term.

A discussion has been made on the connection between the energy conversion efficiency at orifice (which is the base subject of the present paper) and the corresponding efficiency in the external jet field, estimated approximately at the stagnation point (or saddle point) separating, during the suction phase, the ingestion near field from the ejection far field. It has been argued that the saddle point efficiency is lower than the orifice efficiency by a factor that can range from 1/2 to 1/3.

Finally, it has been shown that the electrodynamic efficiency can be conveniently evaluated by measuring, among other standard quantities, the average-per-cycle temperature difference between the air inside the cavity and the external ambient. In the present application a reverse procedure allowed us to evaluate such a temperature difference, which is limited to a maximum of almost one degree centigrade.

Bibliography

[1] Q. Gallas, R. Holman, T. Nishida, B. Carroll, M. Sheplak, and L. Cattafesta. Lumped element modeling of piezoelectric-driven synthetic jet actuators. *AIAA Journal*, 41(2):240–247, 2003.

[2] R.N. Sharma. Fluid dynamics based analytical model for synthetic jet actuation. *AIAA Journal*, 45(8):1841–1847, 2007.

[3] T. Persoons. General reduced-order model to design and operate synthetic jet actuators. *AIAA Journal*, 50(4):916–927, 2012.

[4] L. de Luca, M. Girfoglio, and G. Coppola. Modeling and experimental validation of the frequency response of synthetic jet actuators. *AIAA Journal*, 52(8):1733–1748, 2014.

[5] M. Girfoglio and L. de Luca. Acoustic-structural coupling in the frequency response of synthetic jet devices. In *Proceedings of XXI Congresso Associazione Italiana di Meccanica Teorica e Applicata (AIMETA)*, pages 1–10, 2013.

[6] M. Girfoglio, M. Chiatto, and L. de Luca. Fluid-structure coupling effects in synthetic jet devices. In *Proceedings of Italian Association of Aeronautics and Astronautics (AIDAA) XXII Conference*, pages 1–10, 2013.

[7] M. Girfoglio, M. Chiatto, and L. de Luca. Fluid-structure coupling effects in synthetic jet devices. *Aerotecnica Missili & Spazio*, 92(3/4):1733–1748, 2013.

[8] L. de Luca, M. Girfoglio, M. Chiatto, and G. Coppola. *Characterization of synthetic jet resonant cavities*. Flinovia - Flow Induced Noise and Vibration Issues and Aspects. Springer International Publishing, Berlin, 2014. Book ISBN: 978-3-319-09712-1, 2014.

[9] B.L. Smith and A. Glezer. The formation end evolution of synthetic jets. *Physics of Fluids*, 10(9):2281–2297, 1998.

[10] I. J. Wygnanski. Boundary layer and flow control by periodic addition of momentum. In *4th Shear Flow Control Conference*. AIAA Paper 97-2117, 1997.

[11] U. Ingrad and S. Labate. Acoustic circulation effects and the nonlinear impedance of orifices. *Journal of the Acoustic Society of America*, 22(2):211–218, 1950.

[12] I. V. Lebedeva. Experimental study of acoustic streaming in the vicinity of orifices. *Soviet Physics Acoustics*, 26:331–333, 1980.

[13] E. P. Mednikov and B. G. Novitskii. Experimental study of intense acoustic streaming. *Soviet Physics Acoustics*, 21(2):152–154, 1975.

[14] B.L. Smith and A. Glezer. Vectoring a high aspect ratio rectangular air jet using a zero-net-mass-flux control jet. *Bulletin of the American Physical Society*, 39, 1994.

[15] B.L. Smith and A. Glezer. Vectoring and small-scale motions effected in free shear flows using synthetic jet actuators. In *35th Aerospace Scienze meeting*. AIAA Paper 97–0213, 1997.

[16] S. Ziada. Feedback control of globally unstable flows: Impinging shear flows. *Journal of Fluids and Structures*, 9:907–923, 1995.

[17] R. Holman, Y. Utturkar, R. Mittal, B.L. Smith, and L. Cattafesta. Formation criterion for synthetic jets. *AIAA Journal*, 43(10):2110–2116, 2005.

[18] J.E. Cater and J. Soria. The evolution of round zero-net-mass-flux jets. *Journal of Fluid Mechanics*, 472:167–200, 2002.

[19] C.S. Yao, F.J. Chen, and D. Neuhart. Synthetic jet flowfield database for computational fluid dynamics validation. *AIAA Journal*, 44:3153–3157, 2006.

[20] J.M. Shuster and D.R. Smith. Experimental study of the formation and scaling of a round synthetic jet. *Physics of Fluids*, 19:045109, 2007.

[21] D.P. Rizzetta, M.R. Visbal, and N.J. Stanek. Numerical investigation of synthetic-jet flow fields. *AIAA Journal*, 37:919–927, 1999.

[22] C.Y. Lee and D.B. Goldstein. Two-dimensional synthetic jet simulation. *AIAA Journal*, 40:510–516, 2002.

[23] R. Kotapati, R. Mittal, and L. Cattafesta. Numerical simulation of a transitional synthetic jet in quiescent external flow. *Journal of Fluid Mechanics*, 581:287–321, 2007.

[24] A. Glezer and M. Amitay. Synthetic jets. *Annual Review of Fluid Mechanics*, 34: 503–529, 2002.

[25] P. Zhang and J. Wang and. L. Feng. Review of zero-net-mass-flux jet and its application in separation flow control. *Science in China Series E: Technological Sciences*, 51(9):1315–1344, 2008.

[26] L.N. III Cattafesta and M. Sheplak. Actuators for active flow control. *Annual Review of Fluid Mechanics*, 43:247–272, 2011.

[27] A. Glezer. Some aspects of aerodynamic flow control using synthetic-jet actuation. *Philosophical Transactions of the Royal Society A*, 369:1476–1494, 2011.

[28] M. Bottomley and A. Packwood. Experimental investigation of high-frequency-actuation synthetic jet flow control. In *52nd Aerospace Sciences Meeting AIAA Sci-Tech.*, 2014.

[29] S. Bhatt, R. Gondaliya, V.V. Golubev, X. Wang, and Y. Tang. Design, modeling and testing of synthetic jet actuators for mav flight control. In *52nd Aerospace Sciences Meeting AIAA Sci-Tech.*, 2014.

[30] M. Jabbal, S. Liddle, J. Potts, and W. Crowther. Development of design methodology for a synthetic jet actuator array for flow separation control applications. *Journal of Aerospace Engineering*, 227(1):110–124, 2013.

[31] M. Amitay, A. Honohan, M. Trautman, and A. Glezer. Modification of the aerodynamic characteristics of bluff bodies using fluidic actuators. In *28th AIAA Fluid Dynamics Conference*. AIAA Paper 97-2004, 1997.

[32] M. Amitay, B.L. Smith, and A. Glezer. Aerodynamic flow control using synthetic jet technology. In *36th Aerospace Sciences Meeting and Exhibit*. AIAA Paper 98-0208, 1998.

[33] A. Crook, A.M. Sadri, and N.J. Wood. The development and implementation of synthetic jets for the control of separated flow. In *17th Applied Aerodynamics Conference*. AIAA Paper 99-3176, 1999.

[34] J.C. Béra, M. Michard, M. Sunyach, and G. Comte-Bellot. Changing lift and drag by jet oscillation: experiments on a circular cylinder with turbulent separation. *European Journal of Mechanics - B/Fluids*, 19(5):575–595, 2000.

[35] J. Tensi, I. Boué, F. Paillé, and G. Dury. Modification of the wake behind a circular cylinder by using synthetic jets. *Journal of Visualization*, 5(1):37–44, 2002.

[36] N. Fujisawa, G. Takeda, and N. Ike. Phase-averaged characteristics of flow around a circular cylinder under acoustic excitation control. *Journal of Visualization*, 19 (2):159–170, 2004.

[37] L.H. Feng and J.J. Wang. Synthetic jet control of separation in the flow over a circular cylinder. *Experiments in Fluids*, 53(2):467–480, 2012.

[38] L.H. Feng and J.J. Wang. Circular cylinder vortex-synchronization control with a synthetic jet positioned at the rear stagnation point. *Journal of Fluid Mechanics*, 662:232–259, 2010.

[39] L.H. Feng, J.J. Wang, and C. Pan. Proper orthogonal decomposition analysis of vortex dynamics of a circular cylinder under synthetic jet control. *Physics of Fluids*, 23(1):014106, 2011.

[40] L.H. Feng, J.J. Wang, and C. Pan. Effect of novel synthetic jet on wake vortex shedding modes of a circular cylinder. *Journal of Fluids and Structures*, 26(6): 900–917, 2010.

[41] J.J. Wang, L.H. Feng, and C.J. Xu. Experimental investigations on separation control and flow structure around a circular cylinder with synthetic jet. *Science in China Series E*, 50(5):550–559, 2007.

[42] L.Q. Ma and L.H. Feng. Experimental investigation on control of vortex shedding mode of a circular cylinder using synthetic jets placed at stagnation points. *Science China Technological Sciences*, 56(1):158–170, 2013.

[43] L.H. Feng and J.J. Wang. Modification of a circular cylinder wake with synthetic jet: Vortex shedding modes and mechanism. *European Journal of Mechanics - B/Fluids*, 43:14–32, 2014.

[44] R. Mittal, P. Rampunggoon, and H. S. Udaykumar. Interaction of a synthetic jet with a flat plate boundary layer. AIAA Paper 2001-2773, 2001.

[45] S. Zhong, F. Millet, and N.J. Wood. The behaviour of circular synthetic jets in a laminar boundary layer. *Aeronautical Journal*, 109:461–470, 2005.

[46] S.C. Liddle and N.J. Wood. Investigation into clustering of synthetic jet actuators for flow separation control applications. *Aeronautical Journal*, 109:35–44, 2005.

[47] M. Jabbal and S. Zhong. Particle image velocimetry measurements of the interaction of synthetic jets with a zero-pressure gradient laminar boundary layer. *Physics of Fluids*, 22:063603, 2010.

[48] J. Zhou and S. Zhong. Numerical simulation of the interaction of a circular synthetic jet with a boundary layer. *Computers & Fluids*, 38(2):393–405, 2009.

[49] D.R. Smith. Interaction of a synthetic jet with a cross flow boundary layer. *AIAA Journal*, 40:2277–2288, 2002.

[50] R. Rathnasingham and K.S. Breuer. Active control of turbulent boundary layers. *Journal of Fluid Mechanics*, 495:209–233, 2003.

[51] J. Dandois and E. Garnier. Unsteady simulation of a synthetic jet in a crossflow. *AIAA Journal*, 44:225–238, 2006.

[52] C.L. Rumsey, T.B. Gatski, W.L. Sellers III, V.N. Vatsa, and S.A. Viken. Summary of the 2004 computational fluid dynamics validation workshop on synthetic jets. *AIAA Journal*, 44:194–207, 2006.

[53] S. Lardeau and M.A. Leschziner. The interaction of round synthetic jets with a turbulent boundary layer separating from a rounded ramp. *Journal of Fluid Mechanics*, 683:172–211, 2011.

[54] A. Seifert, A. Darabi, and I. Wygnanski. Delay of airfoil stall by periodic excitation. *Journal of Aircraft*, 33(4):691–698, 1996.

[55] D.R. Smith, M. Amitay, V. Kibens, D. Parekh, and A. Glezer. Modification of lifting body aerodynamics using synthetic jet actuators. In *36th AIAA Aerospace Sciences Meeting and Exhibit*. AIAA Paper 98-0209, 1998.

[56] M. Amitay, D.R. Smith, V. Kibens, D. Parekh, and A. Glezer. Aerodynamic flow control over an unconventional airfoil using synthetic jet actuators. *AIAA Journal*, 39(3):361–370, 2001.

[57] M. Amitay and A. Glezer. Role of actuation frequency in controlled flow reattachment over a stalled airfoil. *AIAA Journal*, 40(2):209–216, 2002.

[58] J.F. Donovan, L.D. Kral, and A.W. Cary. Active flow control applied to an airfoil. In *36th AIAA Aerospace Sciences Meeting and Exhibit*. AIAA Paper 98-0210, 1998.

[59] R. Duvigneau and M. Visonneau. Simulation and optimization of stall control using a synthetic jet. In *2nd AIAA Flow Control Conference*. AIAA Paper 2004-2315, 2004.

[60] R. Holman, Q. Gallas, B. Carroll, and L. Cattafesta. Interaction of adjacent synthetic jets in an airfoil separation control application. In *33rd AIAA Fluid Dynamics Conference and Exhibit*. AIAA Paper 2003-3709, 2003.

[61] J.S. Wilson, B.M. Preston, C. Tung, and J. Tso. Turbulence measurements of a two-dimensional NACA 0036 airfoil with synthetic jet flow control. In *24th AIAA Applied Aerodynamics Conference*. AIAA Paper 2006-3157, 2006.

[62] P.F. Zhang and J.J. Wang. Numerical simulation on flow control of stalled NACA0015 airfoil with synthetic jet actuator in recirculation region. *Journal of Beihang University (*IN CHINESE*)*, 34(4):443–446, 2008.

[63] A. Tuck and J. Soria. Separation control on a NACA 0015 airfoil using a 2D micro ZNMF. *Aircraft Engineering and Aerospace Technology*, 28(2):175–180, 2008.

[64] R. Raju, R. Mittal, and L. Cattafesta. Dynamics of airfoil separation control using zero-net mass-flux forcing. *AIAA Journal*, 46:3103–3115, 2008.

[65] D. You, F. Ham, and P. Moin. Discrete conservation principles in large-eddy simulation with application to separation control over an airfoil. *Physics of Fluids*, 20:101515, 2008.

[66] J.L. Gilarranz, L.W. Traub, and O.K. Rediniotis. A new class of synthetic jet actuators: application to flow separation control. *Journal of Fluids Engineering*, 127:377–387, 2005.

[67] D. Lasagna, S. Donello, F. De Gregorio, M. Orazi, and G. Iuso. Separation delay on thick airfoil using multiple synthetic jets. In *Proceedings of XXI Congresso Associazione Italiana di Meccanica Teorica e Applicata (AIMETA)*, 2013.

[68] N.W. Rathay, M.J. Boucher, and M. Amitay. Performance enhancement of a vertical tail using synthetic jet actuators. *AIAA Journal*, 52(4):810–820, 2014.

[69] E. Gutmark, Y. Yassour, and M. Wolfshtein. Acoustic enhancement of heat transfer in plane channels. In *Proceedings of Seventh International Heat Transfer Conference*, pages 441–445, 1982.

[70] R. Mahalingam and A. Glezer. Design and thermal characteristic of a synthetic jet ejector heat sink. *Journal of Electronic Packaging*, 127:172–177, 2005.

[71] M. Chaudari, B. Puranik, and A. Agrawal. Heat transfer characteristics of synthetic jet impingement iooling. *International Journal of Heat and Mass Transfer*, 53:1057–1069, 2010.

[72] P. Valiorgue, T. Persoons, A. McGuinn, and D.B. Murray. Heat transfer mechanisms in an impinging synthetic jet for small jet-to-surface spacing. *Experimental Thermal and Fluid Science*, 33:597–603, 2009.

[73] M. Arik and T. Icoz. Predicting heat trasnfer from unsteady synthetic jets. *Journal of Heat Transfer*, 134:1–8, 2012.

[74] T. Persoons, A. McGuinn, and D.B. Murray. A general correlation for the stagnation point nusselt number of an axisymmetric impinging synthetic jet. *International Journal of Heat and Mass Transfer*, 54:3900–3908, 2011.

[75] A. McGuinn, R. Farrelly, T. Persoons, and D.B. Murray. Flow regime characterisation of an impinging axisymmetric synthetic jet. *Experimental Thermal and Fluid Science*, 47:241–251, 2013.

[76] D.I. Rylatt and T.S. O'Donovan. Heat transfer enhancement to a confined impinging synthetic air jet. *Applied Thermal Engineering*, 51:468–475, 2013.

[77] M. Chaudhari, B. Puranik, and A. Agrawal. Multiple orifice synthetic jet for improvememnt in impingement heat transfer. *International Journal of Heat and Mass Transfer*, 54:2056–2065, 2011.

[78] Z.B. Luo, Z.X. Xia, and L. Bing. New generation of synthetic jet actuators. *AIAA Journal*, 44(10):2418–2419, 2006.

[79] Z.B. Luo, X. Deng, L. Wang, and Z.X. Xia. Experimental technique based on delay phase angle and PIV measurements of a dual synthetic jets actuator. In *Proceedings of the 2011 Symposium on Piezoelectricity, Acoustic Waves and Device Applications*, pages 1–5, 2011.

[80] T. Persoons, T.S. O'Donovan, and D.B. Murray. Heat transfer in adjacent interacting impinging synthetic jets. In *Proceedings of 2009 ASME Summer Heat Transfer Conference*, pages 1–8, 2009.

[81] C.J.M. Lasance and R.M. Aarts. Synthetic jet cooling part i: overview of heat transfer and acoustic. In *24th Annual IEEE Semiconductor Thermal Measurement and Management Symposium*, pages 20–35, 2008.

[82] D.A. Russell, J.P. Titlow, and Y.-J. Bemmen. Acoustic monopoles, dipoles, and quadrupoles: an experiment revisited. *American Journal of Physics*, 67:660–664, 1999.

[83] C.J.M. Lasance, R.M. Aarts, and O. Ouweltjes. Synthetic jet cooling part ii: experimental results of an acoustic dipole cooler. In *24th Annual IEEE Semiconductor Thermal Measurement and Management Symposium*, pages 26–31, 2008.

[84] C.S. Greco, A. Ianiro, T. Astarita, and G. Cardone. On the near field of single and twin circular synthetic air jets. *International Journal of Heat and Fluid Flow*, 44:41–52, 2013.

[85] B.L. Smith and A. Glezer. Jet vectoring using synthetic jets. *Journal of Fluid Mechanics*, 458:1–34, 2002.

[86] Z. Luo, Z. Xia, and Y. Xie. Jet vectoring control using a novel synthetic jet actuator. *Chinese Journal of Aeronautics*, 20(3):193–201, 2007.

[87] A.P. Thomas, M.G. G'Sell, and K. Fischer. Synthetic jet propulsion for small underwater vehicles. In *2005 IEEE International Conference on Robotics and Automation (ICRA)*, pages 181–187, 2005.

[88] A. Zelenyak, Z. Berger, M. Berry, P. Shea, and M. Glauser. Characterization of synthetic jet actuators used for jet noise reduction by flow control. In *66th Annual Meeting of the APS Division of Fluid Dynamics*, volume 58, 2013.

[89] Q. Xia and S. Zhong. Enhancement of laminar flow mixing using a pair of staggered lateral synthetic jets. *Sensors and Actuators A: Physical*, 207(18):75–83, 2014.

[90] R. Mahalingam, A. Glezer, S.N. Heffington, and R. Lutz. Synthetic jet ejector for the thermal management of PCI cards. *Sensors and Actuators A: Physical*, 2013.

[91] L.D. Montoya, J.L. Jackson, and M. Amitay. Control of aerosol dispersion and removal in a room using synthetic jet actuators. *Building and Environment*, 45 (1):165–175, 2010.

[92] S.A.N. Prasad. *Two-Port Electroacoustic Model of Piezoelectric Composite Circular Plate*. PhD thesis, Dept. of Aerospace Engineering, Mechanics, and Engineering Sciences, Univ. of Florida, Gainesville, FL, 2002.

[93] S.A.N. Prasad, Q. Gallas, S. Horowitz, B. Homeijer, B.V. Sankar, L.N. Cattafesta, and M. Sheplak. Analytical electroacoustic model of a piezoelectric composite circular plate. *AIAA Journal*, 44(10):2311–2318, 2006.

[94] M. Chaudhari, G. Verma, B. Puranik, and A. Agrawal. Frequency response of a synthetic jet cavity. *Experimental Thermal and Fluid Science*, 33(3):439–448, 2009.

[95] G. Krishnan and K. Mohseni. Axisymmetric synthetic jets: An experimental and theoretical examination. *AIAA Journal*, 47(10):2273–2283, 2009.

[96] C. Seeley, Y. Utturkar, M. Arik, and T. Icoz. Fluid–structure interaction model for low-frequency synthetic jets. *AIAA Journal*, 49(2):316–323, 2011.

[97] L.E. Kinsler, A.R. Frey, A.B. Coppens, and J.V. Sanders. *Fundamentals of acoustics*. 4th ed., Wiley, New York, 2000.

[98] R. Rathnasingham and K.S. Breuer. Coupled fluidstructural characteristics of actuators for flow control. *AIAA Journal*, 35(5):832–837, 1997.

[99] G. Kooijman and O. Ouweltjes. Finite difference time domain electroacoustic model for synthetic jet actuators including nonlinear flow resistance. *Journal of the Acoustical Society of America*, 125(4):1911–1918, 2009.

[100] B.L. Smith and G.W. Swift. A comparison between synthetic jets and continuous jets. *Experiments in Fluids*, 34(4):467–472, 2003.

[101] L.D. Gomes, W.J. Crowther, and N.J. Wood. Towards a practical piezoceramic diaphragm based synthetic jet actuator for high subsonic applications - effect of chamber and orifice depth on actuator peak velocity. In *3rd AIAA Flow Control Conference*. AIAA Paper 2006-2859, 2006.

[102] V. Tesar and S. Zhong. Efficiency of generating the synthetic jets. *Transactions of Aeronautical and Astronautical Society of the Republic of China*, 35(1):45–53, 2003.

[103] W.J. Crowther and L.T. Gomes. An evaluation of the mass and power scaling of synthetic jet actuator flow control technology for civil transport aircraft applications. In *Proceedings of the Institution of Me- chanical Engineers, Part I: Journal of Systems and Control Engineering*, pages 357–372, 2008.

[104] R. Li, R. Sharma, and M. Arik. Energy conversion efficiency of synthetic jets. In *ASME 2011 Pacific Rim Technical Conference and Exhibition on Packaging and Integration of Electronic and Photonic Systems.* American Society of Mechanical Engineers, 2011.

[105] M. Girfoglio, C.S. Greco, and L. de Luca. Modelling of the efficiency of synthetic jet actuators. *Sensors and Actuators A: Physical (in press)*, 2015.

Appendix

The most relevant conference/journal papers published during the research activity are hereafter collected.

AIAA JOURNAL
Vol. 52, No. 8, August 2014

Modeling and Experimental Validation of the Frequency Response of Synthetic Jet Actuators

Luigi de Luca,* Michele Girfoglio,† and Gennaro Coppola‡
University of Naples Federico II, Naples 80125, Italy

DOI: 10.2514/1.J052674

A lumped-element mathematical model of the operation of a synthetic jet actuator driven by a thin piezoelectric disk is both analytically and numerically investigated to obtain information about the frequency response of the device. It is shown that the actuator behaves as a two-coupled oscillator system, and simple relationships are given to predict the two peak frequencies, corresponding to the modified Helmholtz and first-mode structural resonance frequencies. The model is validated through experimental tests carried out on three devices having different mechanical and geometrical characteristics, designed primarily to achieve an increasing coupling strength. A strict agreement between overall theoretical scaling laws and numerical computations is also found.

Nomenclature

A_o	=	orifice area
A_w	=	diaphragm/membrane wall area
C_{ac}	=	acoustic compliance of the diaphragm
c_a	=	added diaphragm damping coefficient
c_w	=	diaphragm damping coefficient
c_{wt}	=	total diaphragm damping coefficient
d_A	=	effective acoustic piezoceramic coefficient
d_o	=	orifice diameter
d_{pc}	=	piezoceramic diameter
d_w	=	diaphragm diameter
E_{pc}	=	Young's modulus of the piezoceramic
E_w	=	Young's modulus of the diaphragm shim
F	=	force
F_o	=	force amplitude
f	=	frequency
f_h	=	Helmholtz resonance frequency
f_w	=	diaphragm (structural) resonance frequency
f_w	=	frequency of the principal mode of vibration of a rigidly clamped disk
f_1	=	modified structural resonance frequency without damping
f_{1d}	=	modified structural resonance frequency with damping
f_{1P}	=	modified structural resonance frequency by Persoons
f_2	=	modified Helmholtz resonance frequency without damping
f_{2d}	=	modified Helmholtz resonance frequency with damping
f_{2P}	=	modified Helmholtz resonance frequency by Persoons
H	=	cavity height
K	=	head loss coefficient
k_a	=	air equivalent stiffness
k_w	=	diaphragm equivalent stiffness
l_e	=	effective length of the orifice
l_o	=	orifice length
M_a	=	mass of the air at the orifice
m_a	=	added mass
m_w	=	diaphragm mass
m_{wt}	=	diaphragm total mass
p	=	differential pressure
p_i	=	cavity (internal) differential pressure
p_o	=	ambient pressure
th_{pc}	=	piezoceramic thickness
th_w	=	diaphragm thickness
U	=	instantaneous orifice jet-flow velocity
U_e	=	cycle-averaged jet-flow velocity at saddle point
$U_{\max}$	=	jet-flow velocity peak at orifice
V_a	=	voltage amplitude
V_c	=	cavity volume
γ	=	specific heat ratio
Δl_e	=	additive constant of the effective orifice length
Δx_w	=	average linear membrane displacement
ΔV	=	cavity volume variation
ζ_w	=	diaphragm damping ratio
ν_w	=	Poisson's modulus of the diaphragm
ν_{pc}	=	Poisson's modulus of the piezoceramic
ρ_a	=	air density
ρ_w	=	diaphragm density
ϕ_a	=	electroacoustic transduction coefficient
ω	=	$2\pi f$, circular frequency
ω_h	=	$2\pi f_h$
ω_w	=	$2\pi f_w$
ω_{wp}	=	frequency of the pneumatic spring
$\omega_{1,2}$	=	$2\pi f_{1,2}$

Received 20 March 2013; revision received 16 December 2013; accepted for publication 28 December 2013; published online 22 April 2014.

*Professor, Department of Industrial Engineering, Aerospace Sector, Piazzale Tecchio 80; deluca@unina.it. Senior Member AIAA.

†Ph.D. Student, Department of Industrial Engineering, Aerospace Sector, Piazzale Tecchio 80.

‡Assistant Professor, Department of Industrial Engineering, Aerospace Sector, Piazzale Tecchio 80.

I. Introduction

THE scientific and technical literature quotes documents about the so-called synthetic jets (whose physical principles appear nowadays well established and will not be recalled hereafter) since no more than two decades. Nevertheless, the bulk of such a literature is remarkably thick and includes a very wide field of applications such as flow control (perhaps the early one), heat transfer from small-size surfaces, overall enhancement of mixing between fluid currents, generation of microthrust for propulsion or attitude control of a micro aerial vehicle. We limit to cite here the review papers of Glezer and Amitay [1] and Cattafesta and Sheplak [2]. The interested reader can of course refer to the related literature. Regarding present authors, previous contributions dealt with the direct numerical simulation of jet vectoring, as described by Mongibello et al. [3], and a design procedure of synthetic jet actuator to be employed as heat transfer device, as reported by Monaco et al. [4].

Besides classifying the articles dealing with synthetic jets on the basis of their application field, it is also helpful to differentiate them between applicative papers (i.e., papers devoted to the development and description of a particular application) and design papers (i.e., papers oriented toward the description of the device design able to yield suitable operating characteristics). The present paper belongs to

the second category and is aimed, in particular, at characterizing the frequency response of a synthetic jet actuator driven by a thin lead zirconate titanate (LZT) piezoelectric disk.

The overall design of the actuator needs practical modeling tools. The first significant lumped-element model of a piezoelectric-driven synthetic jet device is described by Prasad [5] and Prasad et al. [6]. By resorting to the approach based on the equivalent electric circuit, these authors developed a modeling of the electromechanical behavior of the piezoceramic composite membrane and gave detailed relationships for the transverse deflection of the inner and outer membrane regions in the simultaneous presence of applied voltage and pressure load. They were able to evaluate both the short-circuit compliance and the effective acoustic piezoelectric coefficient. Gallas et al. [7] modeled the individual components of the actuator as elements of an equivalent electric circuit by using conjugate power variables. On the basis of practical considerations made on the relationships found by Prasad [5], they noted that, in a lumped model, one may use the acoustic compliance of the shim only reduced by a proper factor depending on the ratio of the radius, thickness, and Young's modulus of the piezoceramic and shim materials. They showed a very good agreement between the predicted and measured frequency response functions. Later on, Sharma [8] proposed a different model directly based on the basic equations of fluid dynamics, where the oscillating membrane is considered as a single-degree-of-freedom mechanical system, while the cavity-orifice component is described by means of proper forms of the continuity and Bernoulli's unsteady equations. Sharma [8] validated his model on the very same experimental data of Gallas et al. [7]. One of the most significant experimental investigations on the frequency response of a synthetic jet cavity is due to Chaudhari et al. [9], who carried out systematic measurements about the effects of the excitation frequency on the ejection and suction velocities, by varying the geometrical parameters of the cavity. The paper of Krishnan and Mohseni [10] was oriented essentially to the study of the characteristics of the flowfield produced by a round synthetic jet by using detailed numerical simulations of the turbulent Navier–Stokes equations. To validate their numerical results, they carried out also interesting experimental measurements of the centerline deflection of the membrane by evidencing its nonlinear dependence on the excitation frequency and driving voltage. Seeley et al. [11] described a simplified fluid–structure interaction model based on the implementation of commercial finite-element codes and proved its validity at relatively low frequency, namely well below the Helmholtz frequency. To our knowledge, the last very significant contribution is the recent paper of Persoons [12], who proposed a low-order model of prediction of the frequency response of synthetic jet actuators driven by electromagnetic or piezoelectric supply. Based on the equivalent circuit approach, the model yields analytical expressions for the two resonance frequencies, as a function of the structural and Helmholtz resonance frequencies. The investigation of Persoons [12] is corroborated by a parallel campaign of experimental tests.

At the time, when the present authors were preparing their manuscript, they were not aware of Persoons's paper [12], which undoubtedly shows very strong analogies with the aims of the present one. However, one has to consider that the lumped-element modeling hereafter presented is of fluidic type, that is to say it is directly based on the fluid-dynamics equations. Thus, one can say that the present (in principle alternative) contribution approaches the frequency response analysis from the same perspective as Sharma's work [8], whereas Persoons's contribution [12] follows more directly the Gallas et al. [7] perspective. As a matter of fact, the analytical relationships for the two resonance frequencies characterizing the overall system response (as a function of the structural and Helmholtz resonance frequencies) presented in the present work are different from those of Persoons [12], although both approaches yield predictions generally in close agreement with numerical and experimental findings.

This paper is outlined as follows. Section II describes the lumped-element modeling, giving the equations for the oscillating membrane (which is considered as a single-degree-of-freedom mechanical system) and the cavity-orifice component (which is described by means of proper forms of the continuity and Bernoulli's unsteady equations). The analytical relationships for the coupled resonance frequencies are obtained in Sec. III. The numerical approach is summarized in Sec. IV, while the experimental one is presented in Sec. V, together with the description of the tested actuators. Section VI overall reports the comparisons of experimental, numerical, and analytical findings, and finally Sec. VII yields further numerical insights mainly devoted to investigating the influence of the cavity height. The conclusions are summarized in Sec. VIII.

II. Description of the Model

The model described hereafter is essentially derived from the original paper of Sharma [8], who models the three basic elements of the actuator: the oscillating membrane (diaphragm or wall, constituted by a thin round metal shim on which a smaller diameter piezoceramic disk is bonded), the cavity, and the orifice. The peculiar contributions of the present paper will be evidenced only, with the description of the modeling details being left to Sharma's [8] paper.

The dynamics of the diaphragm is described through the motion equation of a one-degree-of-freedom forced-damped spring–mass system [8]:

$$m_{wt}\ddot{x}_w + c_{wt}\dot{x}_w + k_w x_w = F - p_i A_w \tag{1}$$

where $m_{wt} = m_w + m_a$ is the total mass (with m_w being the oscillating diaphragm mass, including both the shim and the piezo element, and m_a the added mass term); $x_w(t)$ is the diaphragm position at a generic time instant t, and superscript dot stands for time derivative; $c_{wt} = c_w + c_a$ is the total damping coefficient (with c_w being the structural damping coefficient, and c_a is a further damping coefficient due to the interaction with the external air); k_w is the equivalent spring stiffness; $F = F_o \sin \omega t$ is the electrodynamic force (communicated to the membrane by the piezoelectrical element), with F_o being the force magnitude and ω the circular frequency of the applied voltage (often the natural or cyclic frequency $f = \omega/2\pi$ will be used hereafter); p_i is the differential (relative to the unperturbed external atmosphere) pressure within the cavity (internal pressure); and A_w is membrane wall area. The added mass terms are evaluated by means of the procedure of Kinsler et al. [13], as reported by Sharma [8]. Following Sharma, the "pure" mechanical damping ratio is assumed equal to 0.03.

The equivalent spring stiffness of the diaphragm can be obtained as

$$k_w = m_w(2\pi\tilde{f}_w)^2 \tag{2}$$

where $\tilde{f}_w$ is the frequency of the principal mode of vibration of a rigidly clamped disk. Although the presence of the piezoceramic element bonded to the metal shim enhances the flexural rigidity of the membrane (and, in principle, the very thin layer of glue should be taken into account as well), for standard operating conditions, $\tilde{f}_w$ can be referred to the first fundamental mode of the shim only (that is, the membrane structural element actually clamped) and calculated by using the standard formula reported in many textbooks (among others, Kinsler et al. [13]), and used by other authors (e.g., by Rathnasingham and Breuer [14]):

$$\tilde{f}_w = \frac{10.2}{\pi\sqrt{3}} \frac{th_w}{d_w^2} \sqrt{\frac{E_w}{\rho_w(1-\nu_w^2)}} \tag{3}$$

in which th_w, d_w, E_w, ρ_w, and ν_w are, respectively, the thickness, the diameter, Young's modulus, the density, and Poisson's ratio of the shim. Note that the operation at frequencies higher than the fundamental one is not convenient because the membrane produces little net displacement of the surrounding air.

The amplitude of the forcing F_o is obtained conveniently as

$$F_o = \frac{k_w d_A V_a}{A_w} = k_w \Delta x_w \tag{4}$$

where d_A is the effective acoustic piezoelectric coefficient that represents the ratio between the cavity volume variation ΔV and the applied voltage V_a, when the driving differential pressure p is equal to zero [6]:

$$d_A = \left.\frac{\Delta V}{V_a}\right|_{p=0} \tag{5}$$

Note that, in the previous equation [Eq. (4)], the cavity volume variation $\Delta V = d_A V_a$ is divided by the membrane area A_w to obtain the average linear membrane displacement Δx_w (to be multiplied by k_w to obtain F_o).

The coefficient d_A could be evaluated analytically by means of the distribution of the transverse displacement of the composite diaphragm [5,6]. This procedure is not practical due to the difficulty of determining the required coefficients. An alternative way consists in determining the acoustic compliance of the membrane C_{ac}, which, through a dual definition of d_A, is given by the ratio of the volume variation ΔV to a uniformly distributed pressure load p, in the condition of an electrical short circuit [6]:

$$C_{\text{ac}} = \left.\frac{\Delta V}{p}\right|_{V_a=0} \tag{6}$$

Of course, the evaluation of C_{ac} would require the same difficulties. However, one can refer to the acoustic compliance of a homogeneous circular plate (namely, having the properties of the metal shim or those of the piezoceramic) that yields insight into the scaling behavior of the diaphragm [7] and ultimately obtain d_A by means of the relationship

$$d_A = C_{\text{ac}}\phi_a \tag{7}$$

in which ϕ_a is the electroacoustic transduction coefficient [6].

In the present work, we made reference to the piezoceramic properties, thus

$$C_{\text{ac}} = \left.\frac{\Delta V}{p}\right|_{V_a=0} = \frac{\pi d_{\text{pc}}^2(1-\nu_{\text{pc}}^2)}{1024 E_{\text{pc}} th_{\text{pc}}^3} \tag{8}$$

with th_{pc}, d_{pc}, E_{pc}, and ν_{pc} being, respectively, the thickness, the diameter, Young's modulus, and Poisson's ratio of the piezoceramic.

The electroacoustic transduction coefficient ϕ_a has been considered here as a fitting parameter of the present model (the only one) to be determined by optimizing the agreement between numerical and experimental data. Numerical values of ϕ_a will be reported hereafter, while showing the comparison of computer simulation and experimental results.

For future purpose, it is convenient to divide Eq. (1) by m_{wt}, thus obtaining

$$\ddot{x}_w + 2\zeta_w\omega_w\dot{x}_w + \omega_w^2 x_w = \omega_w^2\Delta x_w \sin\omega t - \frac{p_i A_w}{m_{wt}} \tag{9}$$

where ζ_w and ω_w are respectively given by

$$\zeta_w = \frac{c_{wt}}{2\sqrt{m_{wt}k_w}} \tag{10}$$

$$\omega_w = \sqrt{\frac{k_w}{m_{wt}}} \tag{11}$$

ζ_w is the actual damping ratio, in which both c_{wt} and m_{wt} take into account the motion of the surrounding air. $\omega_w = 2\pi f_w$ represents the (first mode) structural circular frequency of the composite diaphragm.

The second equation of the model is essentially the conservation of mass in the cavity under the assumption of zero-dimensional (lumped) system. By relating the density and pressure variations by means of an isentropic compression/expansion transformation, the continuity equation can be formulated as [8]

$$\frac{V_c}{\gamma p_o}\frac{\mathrm{d}p_i}{\mathrm{d}t} - A_w\dot{x}_w = -A_o U \tag{12}$$

where $V_c = A_w H$ is the cavity volume (H being the cavity height), A_o is the orifice area, γ is the specific heat ratio of air, p_o is the external ambient pressure, and U is the instantaneous flow velocity through the orifice.

The application of the unsteady Bernoulli's equation, between a point inside the cavity where the flow velocity is practically null and a point just outside the cavity representing the location where the pressure matches the unperturbed external ambient value, yields the third equation of the model [8]:

$$\dot{U} + \frac{K}{l_e}|U|\dot{U} + \omega_h^2 U = \frac{A_w}{A_o}\omega_h^2\dot{x}_w \tag{13}$$

in which K is the head loss coefficient, including the inviscid contribution (equal to unity) due to the kinetic energy recovery at ambient pressure, minor (entrance/exit) losses, and distributed losses due to friction inside the orifice duct. The distance between the two points of application of the Bernoulli's equation, i.e., the modified (effective) length of the orifice l_e, is basically evaluated according to the description of Sharma [8], namely

$$l_e/d_0 = l_0/d_0 + \Delta l_e \tag{14}$$

Typically, we adopted $\Delta l_e = 0.62$. Values of the additive constant greater than 0.62 have been also used in some computations. Further considerations will be made when carrying out the comparison between experimental and numerical data.

The choice of the values to be attributed to the head loss coefficient and to the effective length of the orifice constitutes a key point of the model, and it is very critical because it needs detailed information about the complex unsteady flowfield inside the reduced size cavity and orifice. Because of the very short length of the orifice the frictional distributed losses are definitely negligible. The sharp-edged geometry of both internal and external orifice sections would suggest the standard value of 0.5 for the entrance loss coefficient during both the ejection and suction phases. By following the same reasoning the exit loss contribution should be equal to about unity. However, the presence of the saddle point outside the cavity, located about one diameter away from the orifice exit, and the very short cavity height H adopted in the prototype devices realized to validate experimentally the present model, allows us to argue that there is practically no dissipation at the orifice exit section; hence, the minor exit losses will be neglected. As far as the evaluation of the contribution of the minor entrance losses is concerned, first one should consider that Raju et al. [15] developed a reduced-order model to evaluate the orifice pressure drop in the oscillatory flow of a synthetic jet actuator, as a function of the Stokes number (representing the importance of unsteady versus viscous effects). They found that, beyond a certain critical threshold of Stokes number, the pressure loss coefficient drops by a factor of about 3. Unfortunately, their finding cannot be applied here on a quantitative basis because the model of Raju et al. [15] refers to a two-dimensional slot. Another very valuable contribution of literature is given by Persoons [12], who furnished for both circular and slot orifices values from direct experimental measurements and values obtained from a best-fitting procedure to match computed and measured coefficients. For circular geometry in the former case, he found $K = 1.14$, and in the latter one, $K = 1.25$. We decided to adopt the value $K = 1.14$ for all the computations hereafter presented. Note further that Rathnasingham and Breuer [14] assumed $K = 1$, while Sharma [8] used $K = 0.78$.

The so-called Helmholtz frequency ω_h is usually recognized to be

$$\omega_h = \sqrt{\frac{\gamma A_o^2 p_o / V_c}{\rho_a l_e A_o}} = \sqrt{\frac{k_a}{M_a}} \tag{15}$$

where k_a and M_a are, respectively, the equivalent stiffness of the air inside the cavity, $k_a = \gamma A_o^2 p_o / V_c$, and the effective mass of the air at the orifice, $M_a = \rho_a l_e A_o$.

For the sake of convenience, the three differential equations that describe the dynamics of the actuator are summarized next:

$$\ddot{x}_w + 2\zeta_w \omega_w \dot{x}_w + \omega_w^2 x_w = \omega_w^2 \Delta x_w \sin \omega t - \frac{p_i A_w}{m_{wt}} \tag{16}$$

$$\frac{V_c}{\gamma p_o}\frac{\mathrm{d}p_i}{\mathrm{d}t} - A_w \dot{x}_w = -A_o U \tag{17}$$

$$\ddot{U} + \frac{K}{l_e}|U|\dot{U} + \omega_h^2 U = \frac{A_w}{A_o}\omega_h^2 \dot{x}_w \tag{18}$$

III. Evaluation of the Coupled Natural Frequencies (Analytical Approach)

The behavior of the synthetic jet actuator can be described by the dynamics of two mutually coupled oscillators; the first one, describing the membrane displacement x_w, is characterized by its uncoupled natural frequency ω_w, while the second one, the acoustic oscillator, describing the dynamics of the mass of air at the orifice, M_a, through its velocity U, is characterized by the its natural frequency ω_h. The system of Eqs. (16–18) shows that both the dynamics of the membrane and of the orifice air mass are forced by the cavity pressure, which couples them by means of the continuity equation [Eq. (17)]. An external forcing due to the supply power also acts on the membrane dynamics. To investigate in more detail the coupling of the two oscillators, it is convenient to reformulate the equations.

By taking the time derivative of Eq. (16), in which both the added mass and the additional damping coefficient are independent of the time, and by eliminating the pressure derivative by means of Eq. (17), one obtains

$$\dddot{x} + 2\zeta_w \omega_w \ddot{x} + (\omega_w^2 + \omega_{wp}^2)\dot{x} - \frac{A_o}{A_w}\omega_{wp}^2 U = \omega_w^2 \Delta x_w \omega \cos \omega t \tag{19}$$

which is coupled with the Eq. (18). Note that another characteristic frequency ω_{wp} is introduced in Eq. (19), defined as

$$\omega_{wp} = \sqrt{\frac{\gamma A_w^2 p_o / V_c}{m_{wt}}} = \sqrt{\frac{\gamma A_w p_o}{m_{wt} H}} \tag{20}$$

which, according to Sharma [8], may be interpreted as the natural frequency of the pneumatic spring made of the air enclosed within the cavity of volume V_c and of the diaphragm mass m_{wt}. Note that the height of the cavity, H, is explicitly introduced.

After introducing the positions $x_1 = \dot{x}_w$, $x_2 = U$, $b_1 = 2\zeta_w \omega_w$, $b_2 = K/l_e$, $k_{11} = \omega_w^2 + \omega_{wp}^2$, $k_{12} = -A_o \omega_{wp}^2 / A_w$, $k_{21} = -A_w \omega_h^2 / A_o$, $k_{22} = \omega_h^2$, the following governing system is finally written:

$$\ddot{x}_1 + b_1 \dot{x}_1 + k_{11} x_1 + k_{12} x_2 = \omega_w^2 \Delta x_w \omega \cos \omega t \tag{21}$$

$$\ddot{x}_2 + b_2 |x_2| \dot{x}_2 + k_{21} x_1 + k_{22} x_2 = 0 \tag{22}$$

As shown by Eqs. (21) and (22), the coupling of the two oscillators is of the elastic type; apart from the mutual influence of the two oscillators represented by the off-diagonal terms (that scale with $(d_w/d_o)^2$), one may note that the diagonal stiffness element k_{11} results to be modified compared with the uncoupled case by a factor $1 + \mathrm{CR}$, where CR is the coupling ratio, defined as

Table 1 Features of the tested devices predicted analytically

Property	Brass	Aluminum 1	Aluminum 2
	Geometry		
Shim diameter, mm	35	42	80
Shim thickness, mm	0.4	0.24	0.25
Piezoelectric diameter, mm	23	31.8	63.5
Piezoelectric thickness, mm	0.23	0.191	0.191
Cavity diameter, mm	35	42	80
Cavity height, mm	3–5	3–8	4–7–11
Orifice diameter, mm	2	2	5
Orifice length, mm	2	2	2
H/d_o	1.5–2.5	1.5–4	0.8–1.4–2.2
l_e/d_o	1	1	0.4
	Shim		
Young's modulus, Pa	9.7×10^{10}	7.31×10^{10}	7.31×10^{10}
Poisson's modulus	0.36	0.31	0.31
Density, kg/m^3	8490	2780	2780
	Piezoelectric		
Young's modulus, Pa	6.7×10^{10}	6.6×10^{10}	6.6×10^{10}
Poisson's modulus	0.31	0.31	0.31
Density, kg/m^3	8000	7800	7800
	Frequency response		
f_w, Hz	2176	1376	401
f_1, Hz	2256 – 2221	1632 – 1462	307 – 297 – 283
f_{1P}, Hz	2241 – 2215	1569 – 1451	426 – 380 – 336
f_{1d}, Hz	2255 – 2220	1632 – 1461	307 – 297 – 283
f_h, Hz	1000 – 775	833 – 510	723 – 547 – 436
f_2, Hz	964 – 759	702 – 480	944 – 737 – 617
f_{2P}, Hz	971 – 760	730 – 483	680 – 577 – 520
f_{2d}, Hz	964 – 759	702 – 480	944 – 737 – 616
CR	0.06 – 0.04	0.30 – 0.11	1.88 – 1.08 – 0.68

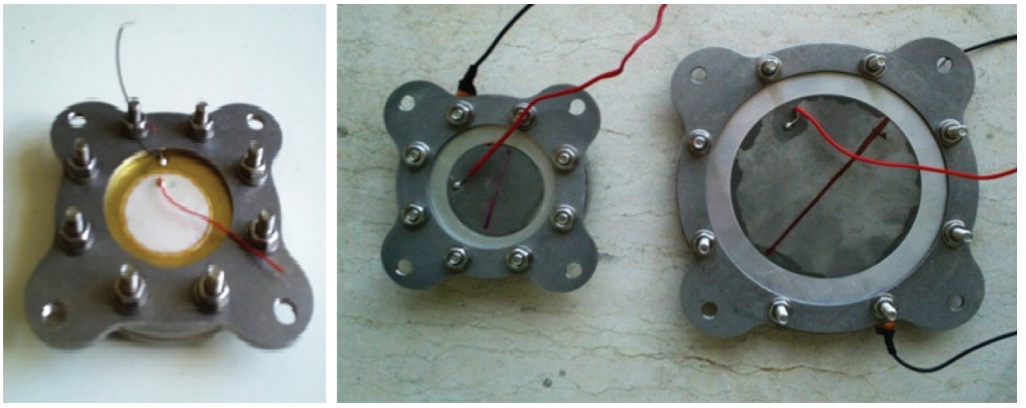

Fig. 1 Pictures of the tested actuators. The brass shim is on the left, and the aluminum shims are on the right.

$$\mathrm{CR} = \left(\frac{\omega_{wp}}{\omega_w}\right)^2 \tag{23}$$

CR represents the ratio of the air stiffness to the membrane stiffness; on the other hand, by inspecting Eq. (19), it is evident that, if CR $\ll 1$, the membrane dynamics is decoupled from the acoustic oscillator, with the variation of cavity pressure vanishing. Furthermore, a linear damping term appears in the first equation and a nonlinear damping term in the second one.

To evaluate the coupled natural frequencies, a study of free vibrations of the system will be hereafter carried out; initially, we will neglect the nonlinear damping term of the second oscillator, and we will develop the relevant analytical treatment. However, despite this simplification, we will show hereafter that the analytical predictions of the resonance frequencies, even though not corrected rigorously, are in several circumstances in very good agreement with data obtained by experimental measurements. Of course, direct numerical solutions will be also performed, by integrating the fully nonlinear governing system [Eqs. (16–18)], which will show the crucial role played by the nonlinear flow damping on the amplitude of the oscillations, as is well recognized in the literature, e.g., by Gallas et al. [7] (who attributed to it the absence of the first resonance peak for their device of case 2), Persoons [12], Kooijman, and Ouweltjes [16].

Thus, after neglecting the nonlinear damping, by introducing the following state vector

$$q = \{x_1 \quad x_2 \quad \dot{x}_1 \quad \dot{x}_2\}^T \tag{24}$$

and by reformulating the system of Eqs. (21) and (22) in matrix form, in the absence of forcing (i.e., null voltage), we obtain

$$\{\dot{q}\} = [A]\{q\} \tag{25}$$

where

$$[A] = \begin{bmatrix} 1 & 0 & 0 & 0 \\ 0 & 1 & 0 & 0 \\ -b_1 & 0 & -k_{11} & -k_{12} \\ 0 & 0 & -k_{21} & -k_{22} \end{bmatrix} \tag{26}$$

and the natural frequencies of the mechanical system are related to the eigenvalues of the matrix $[A]$. It should be noted that $[A]$ is a 4×4 matrix, and thus we expect to obtain four eigenvalues; with reference to Eq. (21), because the devices analyzed in the present work satisfy the condition $\zeta_w < 1$ (remember that the pure mechanical damping ratio has been assumed equal to 0.03, and we noted that this value is not substantially modified by interactions with the ambient air), the eigenvalues are two pairs of complex conjugate quantities and the natural frequencies f_{1d} and f_{2d} are of course given by the imaginary coefficients. For the actuators under analysis, such eigenvalues are computed numerically and will be shown in the following Table 1.

Moreover, to the aim of obtaining convenient closed-form analytical evaluations of the natural frequencies, we can make the further assumption of absence of damping effects (the practical validity of such an assumption will be considered later, when discussing the results) so as to obtain the following relationship:

$$\omega_{1,2}^2 = \frac{-(\omega_w^2 + \omega_{wp}^2 + \omega_h^2) \pm \sqrt{(\omega_w^2 + \omega_{wp}^2 + \omega_h^2)^2 - 4\omega_h^2\omega_w^2}}{2} \tag{27}$$

In conclusion, the natural coupled frequencies in the totally undamped case are given by

$$f_{1,2} = \frac{\omega_{i1,2}}{2\pi} \tag{28}$$

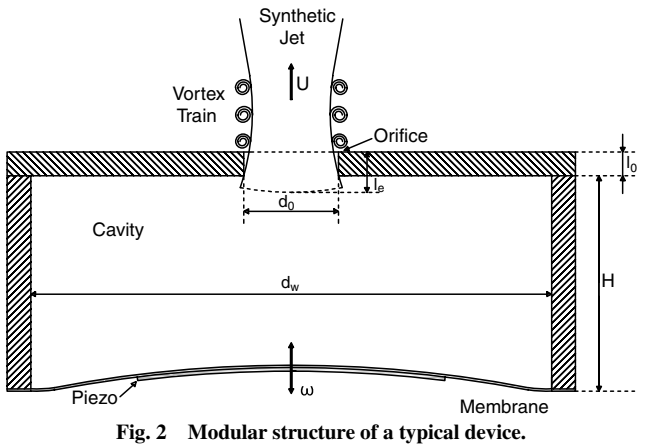

Fig. 2 Modular structure of a typical device.

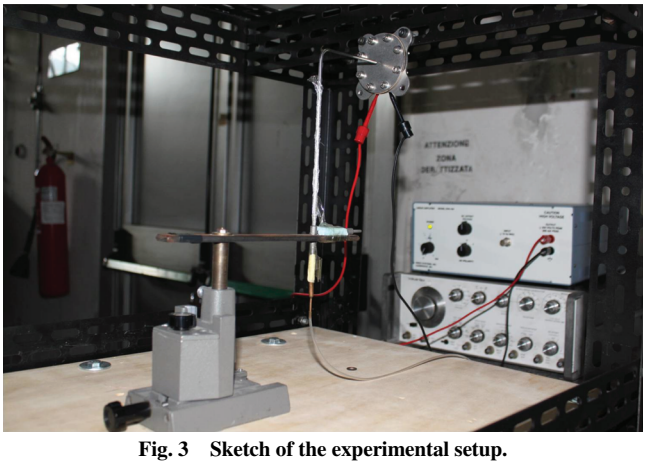

Fig. 3 Sketch of the experimental setup.

Table 2 Experimental resonance frequencies

Voltage amplitude V_a, V	From microphone, Hz	From vibrometer, Hz
	Brass ($H = 3$ mm)	
0.8	2255	2194
1.4	2230	2186
3	— —	2194
9	2230	— —
	Brass ($H = 5$ mm)	
0.8	2379	— —
1.4	2392	— —
9	2357	— —
	Aluminum 1 ($H = 3$ mm)	
0.8	1510	1653
1.4	1500	1647
3	— —	1641
9	1489	— —
	Aluminum 1 ($H = 8$ mm)	
0.8	1443	— —
1.4	1439	— —
9	1385	— —
	Aluminum 2 ($H = 4$ mm)	
0.8	310–885	338–891
1.4	310–885	338–894
3	— —	344–891
9	332–903	— —
	Aluminum 2 ($H = 7$ mm)	
0.8	320–719	— —
1.4	325–719	— —
9	353–735	— —
	Aluminum 2 ($H = 11$ mm)	
0.8	300–601	— —
1.4	302–601	— —
9	335–620	— —

that yields the relationships of such frequencies as a function of the first mode structural and Helmholtz frequencies. It is confirmed that, if $CR \ll 1$, the two resonance frequencies tend to those of the uncoupled oscillators.

In some applications, a desirable operating condition is represented by a relatively high plateau of fluid ejection velocity over a rather wide range of frequencies. This condition can be attained by designing the devices so as to have the two frequencies ω_1 and ω_2 close to each other. By inspecting the relationship of Eq. (27), it can be verified that, if $\omega_w \ll \omega_h$, then the distance between the two eigenvalues $|\omega_1^2 - \omega_2^2|/\omega_h^2$ does not depend on the cavity height H, and therefore

$$|\omega_1^2 - \omega_2^2| \simeq \frac{1}{H/d_o} \tag{29}$$

On the contrary, if $\omega_w \gg \omega_h$, then $|\omega_1^2 - \omega_2^2|/\omega_h^2$ scales with H/d_o; hence

$$|\omega_1^2 - \omega_2^2| \simeq \text{const} \tag{30}$$

The numerical results presented in Sec. VII will confirm these predictions and will show that, for a strongly coupled actuator with $\omega_h > \omega_w$, the jet-flow velocity is maximized for relatively large cavity height.

The relationships of Eqs. (27) and (28) are to be compared to the analogous formulas of Persoons [12] that, indeed, seem to be derived on heuristic basis. In the next sections, it will be showed that the values estimated by means of the present relationships are in good agreement with those measured experimentally as well as calculated by computer direct simulations.

IV. Numerical Approach

A numerical code has been written in which the governing equations system [Eqs. (16–18)] has been numerically integrated by means of a standard fourth-order Runge–Kutta method in the MATLAB environment with the *ode45* routine. Initial conditions of $x_w = 0$, $\dot{x}_w = 0$, $p_i = 0$, and $U = 0$ have been assumed for all the computations, and it has been observed that the quasi-steady oscillatory solution is generally reached in about 20–30 cycles.

The uncertainty errors of the numerical data have been evaluated especially with respect to variations of the values of the head loss coefficient as well as of the effective orifice length. For K varying in the range $1 < K < 1.46$, the variations of the resonance frequencies are restricted within a maximum of 2%, while the corresponding variations of the velocity peaks are generally of the order of 10%. In this last case, the exit velocity can be recalibrated by means of comparisons with experimental data (when available) by adjusting the fitting parameter ϕ_a. Note that Persoons [12] assumed the coefficient K as a fitting parameter and found deviations of 13%.

For values of the additive constant of l_e [Eq. (14)] ranging from 0.62 to 1.6, the peak frequencies vary within an uncertainty band of 5%, which may grow up to a maximum of 10% for relatively low

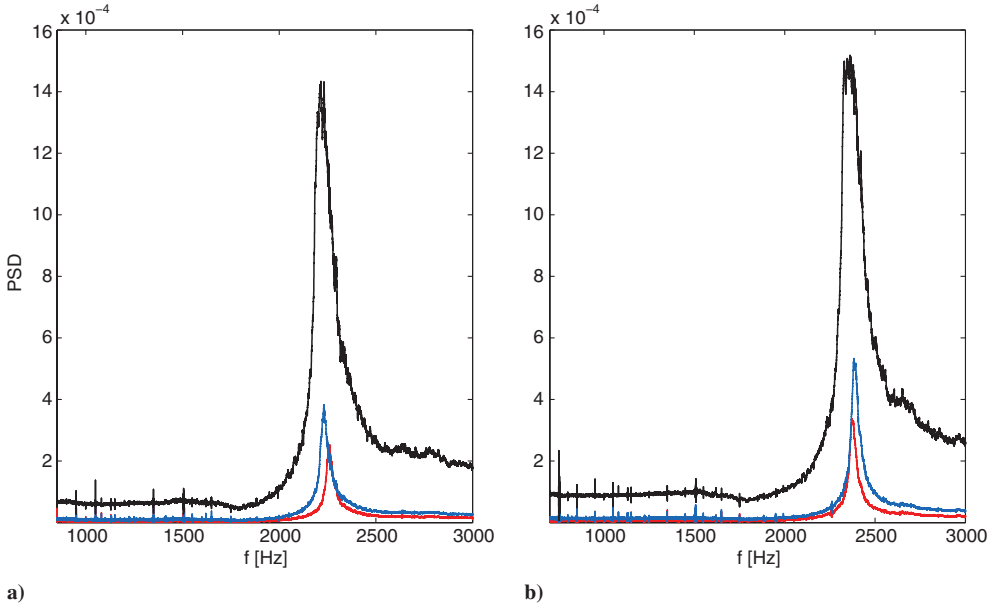

Fig. 4 Experimental PSD monitoring of the brass actuator; $V_a = 0.8$ V (red curve), $V_a = 1.4$ V (blue curve), $V_a = 9$ V (black curve): a) $H = 3$ mm, and b) $H = 5$ mm.

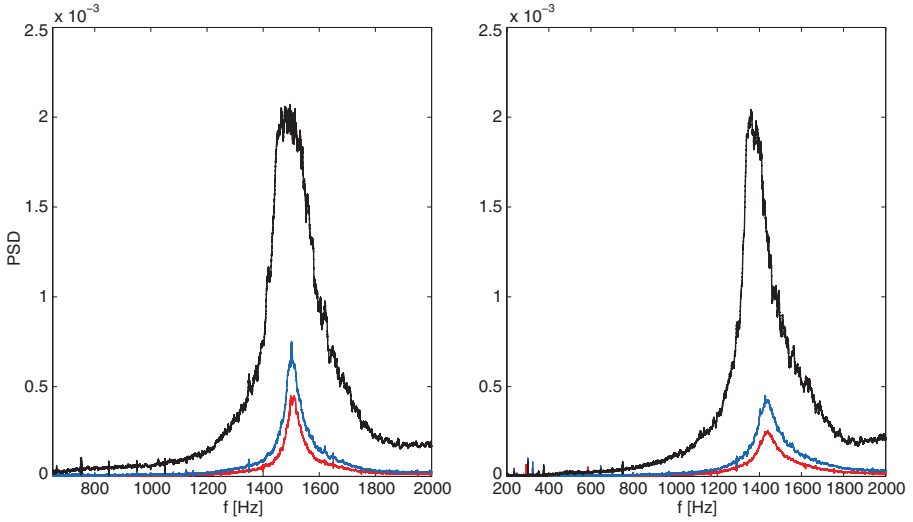

Fig. 5 Experimental PSD monitoring of the aluminum 1 actuator; $V_a = 0.8$ V (red curve), $V_a = 1.4$ V (blue curve), $V_a = 9$ V (black curve): a) $H = 3$ mm, and b) $H = 8$ mm.

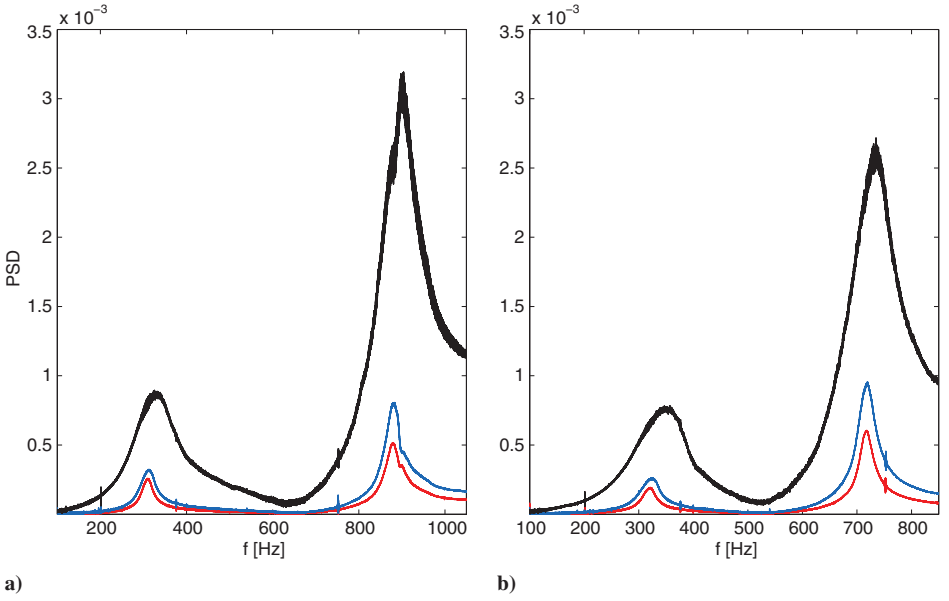

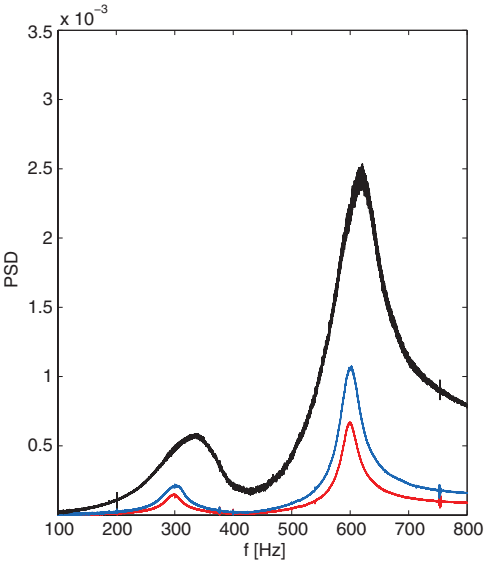

Fig. 6 Experimental PSD monitoring of the aluminum 2 actuator; $V_a = 0.8$ V (red curve), $V_a = 1.4$ V (blue curve), $V_a = 9$ V (black curve): a) $H = 4$ mm, b) $H = 7$ mm, and c) $H = 11$ mm.

frequencies, while the average width of such a band is of 10% for the peak velocities. Note that the influence of the uncertainty on l_e is expected to be relatively stronger because the effective orifice length influences directly the nominal Helmholtz's frequency and the nonlinear damping coefficient. Indeed, we will present numerical simulations showing that the membrane peak displacement at the Helmholtz's frequency is reduced by an amount of about 50% in case that the shorter value of l_e is considered in the computation.

V. Experimental Approach

To verify the analytical developments reported before, as well as to validate the numerical code, systematic experimental tests have been carried out on three different synthetic jet actuators designed to the purpose. The basic characteristics of such actuators are summarized in Table 1. The actuator with the membrane in brass and the two in aluminum are reported in Fig. 1, with the brass one on the left and the aluminum ones on the right. They have been designed essentially to obtain different values of the coupling ratio, ranging from about zero to 1.88. The schematic of the devices is shown in Fig. 2 highlighting their modular structure, which permits independent variations of cavity diameter and height, orifice diameter, and piezoelectric diaphragm. The brass actuator is a commercially available piezoelectric ceramic disk bonded to a thin brass metal plate fabricated by Murata Manufacturing Co. The aluminum membranes were built in-house by gluing a LZT piezoceramic disk (manufactured by PIEZO Inc.) on a thin aluminum foil.

In Table 1, geometrical and mechanical properties, as well as nominal characteristic frequencies of the tested devices, listed on the basis of the shim material, are summarized. The frequencies reported in Table 1 have been calculated by means of the analytical model illustrated before. For the sake of clarity, let us remember that f_w and f_h denote the (uncoupled) first-mode structural and Helmholtz natural frequencies, respectively, defined through Eqs. (3) and (15), respectively; f_1 and f_2 are the frequencies of the two coupled oscillators, i.e., the modified first-mode structural and Helmholtz resonance frequencies, defined by Eq. (28); f_{1P} and f_{2P} are the modified frequencies evaluated by employing the Persoons formulas

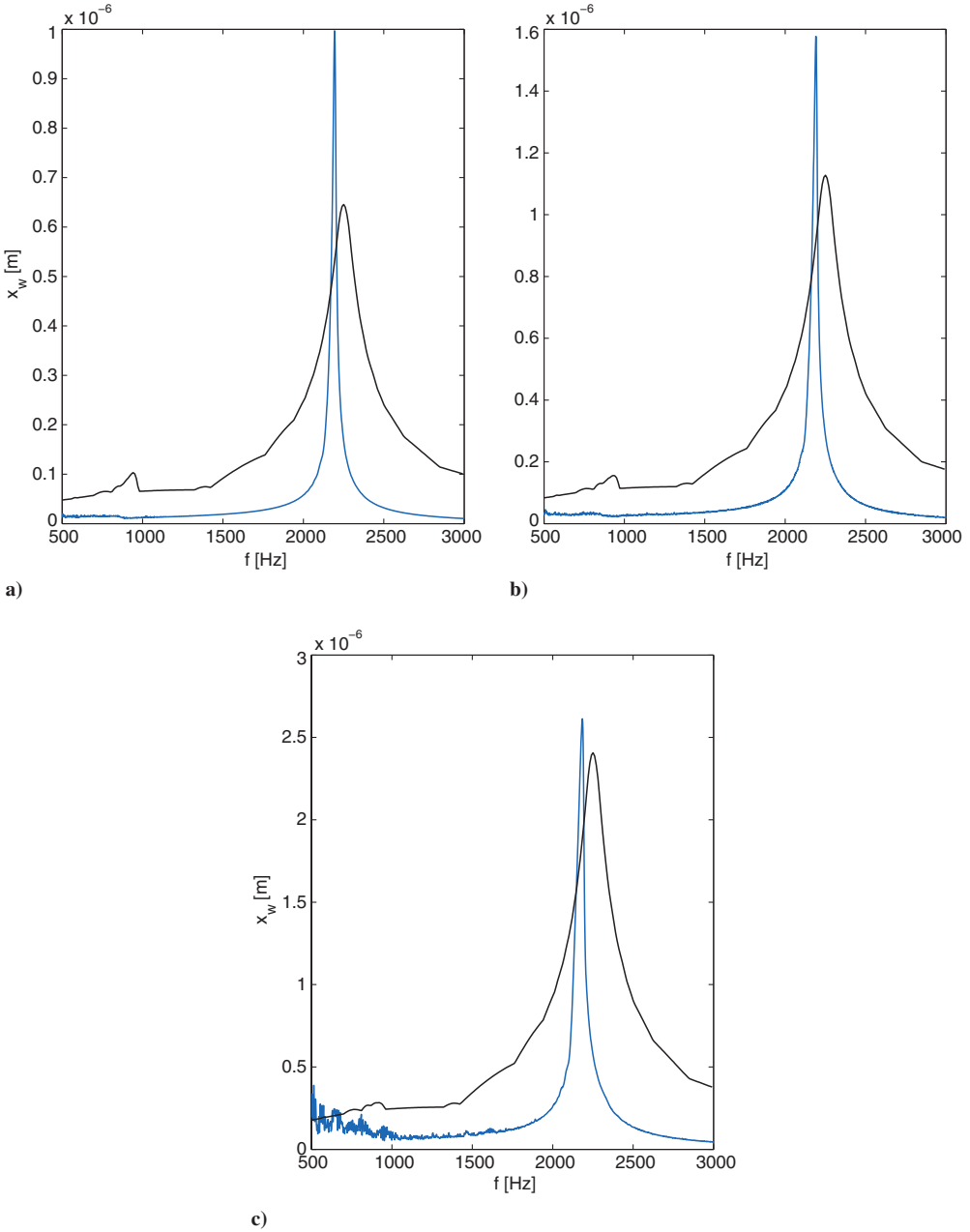

Fig. 7 Numerical–experimental comparison of membrane displacements for the brass actuator (with $H = 3$ mm); black curves represent the numerical solution, and blue curves represent the vibrometer monitoring: a) $V_a = 0.8$ V, b) $V_a = 1.4$ V, and c) $V_a = 3$ V.

[12]; and f_{1d} and f_{2d} take into account linear damping effects and arise from the eigenvalues problem of Eqs. (25) and (26). The coupling ratio CR introduced by Eq. (23) is reported in the last line.

As shown in Table 1, the nominal structural frequency of the brass devices is very close to the value predicted by the model of the coupled oscillators, evaluated both including damping effects (on the first oscillator) and neglecting them; in fact, we find also $f_1 \cong f_{1d}$. As a general trend, on the grounds of Eq. (27), the coupling effect increases the structural resonance frequency and lowers the Helmholtz resonance frequency. Furthermore, the coupling ratio CR is higher as the cavity height decreases. However, because for the aluminum 2 device the nominal structural frequency is less than the Helmholtz one, the situation is reversed in the sense that the coupling of the oscillators lowers f_1 and f_{1d} and raises f_2 and f_{2d}. Note that the Persoons relationships seem do not work well for the aluminum 2 actuator, for which the Helmholtz frequency is greater than the membrane one.

For the brass device, it results that also the Helmholtz frequency (i.e., the natural frequency of the acoustic oscillator) is almost coincident with the value predicted by means of the coupling model; furthermore, we have $f_2 = f_{2d}$. The quasi coincidence between the uncoupled natural structural and Helmholtz frequencies and the corresponding values of $\omega_{1,2}$, observed for the brass actuator, is much more weak for the aluminum 1 and totally disappears for the aluminum 2 actuator, which exhibits the strongest coupling effect.

A brief description of the experimental setup (depicted in Fig. 3) is reported in the following. The devices have been electrically excited with a sine signal generated in MATLAB environment through the routine *chirp* and then transmitted via a USB Instruments DS1M12 "Stingray" data-acquisition system to a linear-gain amplifier (typical gain factor is 5); an oscilloscope has been also employed to set the voltage amplitude V_a with a higher accuracy. The frequency of the signal has been varied typically over the range from 0 to 3000 Hz.

To the aim of detecting the frequency response of the actuators, the first technique is based on the measurement of the pressure disturbances produced by the motion of the diaphragm into the anechoic atmospheric environment, carried out by using a commercial digital microphone connected to the audio board of the PC; the power

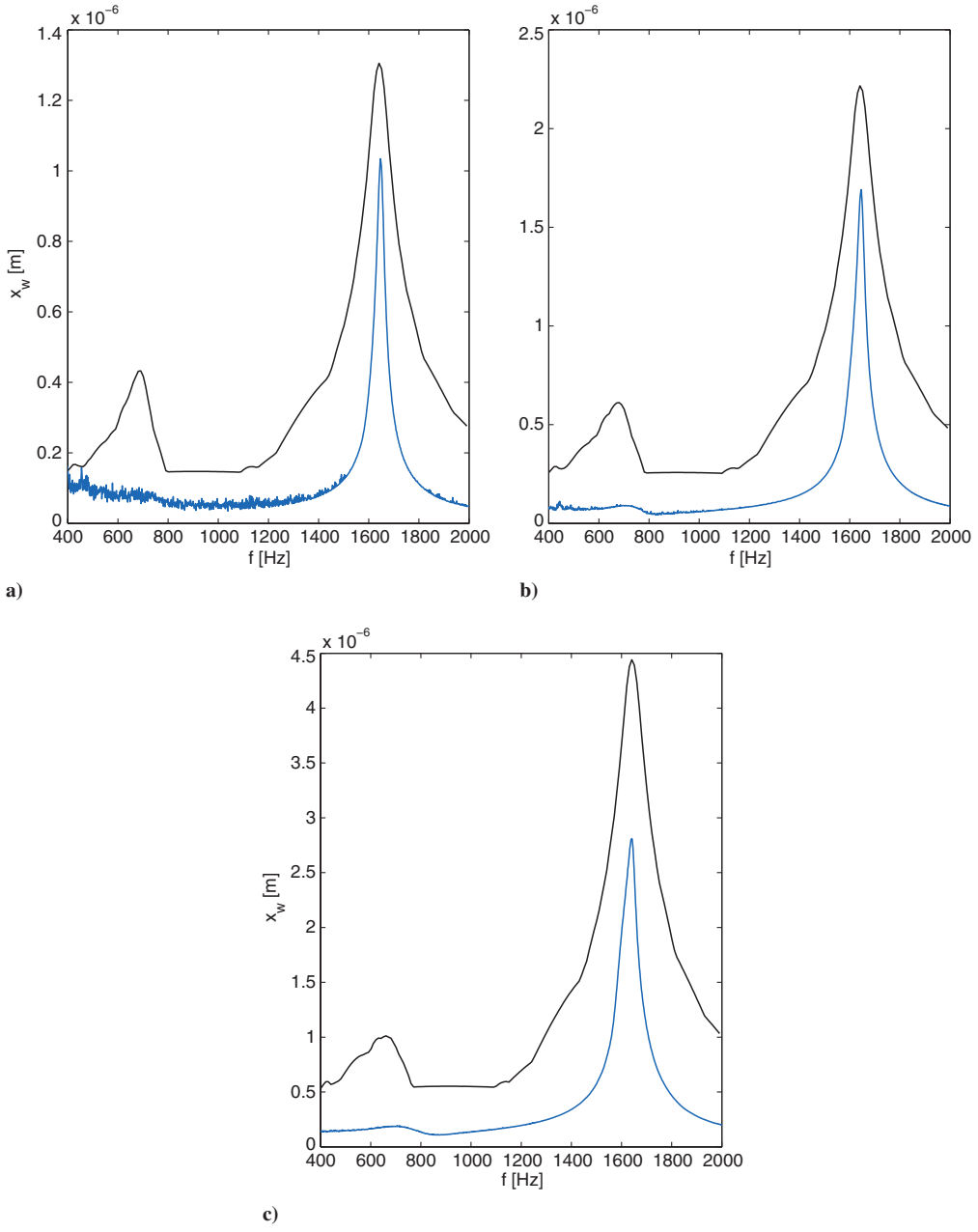

Fig. 8 Numerical–experimental comparison of membrane displacements for the aluminum 1 actuator (with $H = 3$ mm); black curves represent the numerical solution, and blue curves represent the vibrometer monitoring: a) $V_a = 0.8$ V, b) $V_a = 1.4$ V, and c) $V_a = 3$ V.

spectral density (PSD) of the pressure data has been calculated by using a standard fast Fourier transform algorithm.

The deflection of the composite membrane has been measured as well by means of a Polytec laser scanning vibrometer PSV400-H4 that integrates in the frequency domain the measured diaphragm velocity to obtain the displacement.

The experimental study of the frequency response of the three devices has been completed through a further testing session where the flow exit velocity has been measured in the external ambient at a station located on the jet axis approximately one orifice diameter downstream of the exit section. For these measurements, a standard Kanomax mini pitot tube, 1/8 in. in diameter and 6 in. in length, has been employed in connection with a Mouser/All Sensor pressure transducer, whose output signal is acquired by means of the same Data Acquisition unit and phase locked to the actuator excitation signal. The output signals are phase-averaged over typically 10 periods to obtain an uncertainty estimate of the jet velocity of 5%, calculated with the standard procedures of literature.

VI. Comparison of Experimental, Numerical, and Analytical Results

The resonance peak frequencies detected through the PSD analysis of the microphone data are listed in Table 2, together with values recorded by means of the vibrometer.

The influence of the supply voltage (which is kept rather low in this kind of test) is generally weak, but it is not clear why, in the case of the aluminum 2 device, the voltage slightly increases the resonance frequencies, whereas for the other devices, the trend is reversed. It should be noted that previous measurements made by Gomes et al. [17] for a wider voltage range showed that the resonance frequency tends to decrease with increasing in voltage. The spread between microphone and vibrometer data is 9% maximum, but for the brass actuator, it is much lower. Another general feature of these experimental data is that the aluminum 2 device shows two resonance peaks within the frequency range of testing. For the other two actuators, both microphone and vibrometer measurements revealed the upper peak only.

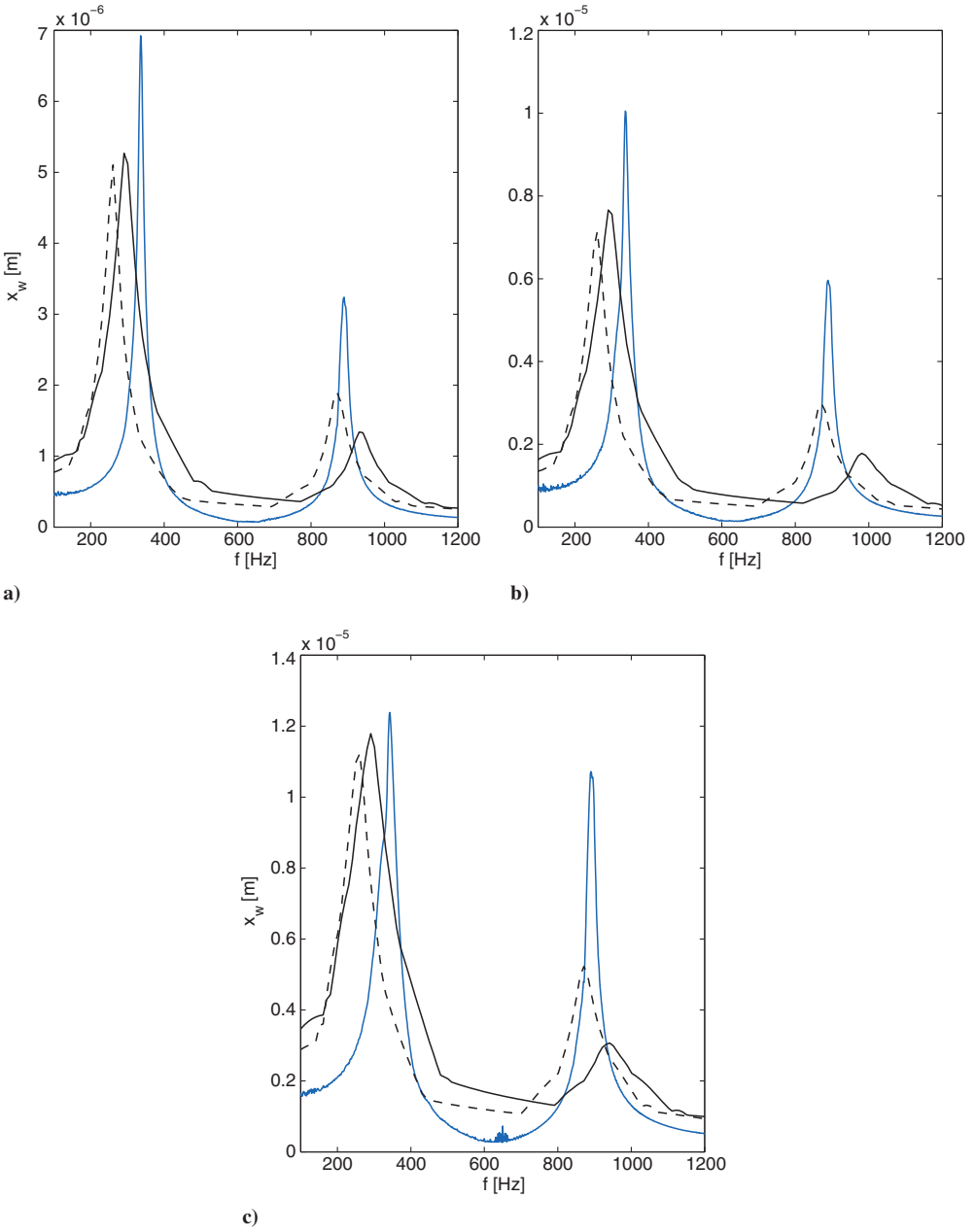

Fig. 9 Numerical–experimental comparison of membrane displacements for the aluminum 2 actuator (with $H = 4$ mm); black curves represent the numerical solution, the continuous line is for $\Delta l_e = 0.62$, the dashed line is for $\Delta l_e = 1.42$, and blue curves represent the vibrometer monitoring: a) $V_a = 0.8$ V, b) $V_a = 1.4$ V, and c) $V_a = 3$ V.

The experimental PSD findings for the brass actuator are illustrated in Fig. 4, for cavity heights of 3 and 5 mm; for each device, data have been reported for different voltage amplitudes. It is clearly evident that the voltage practically does not influence the peak position, but as expected, the PSD level increases with increasing the voltage. For $H = 3$ mm, a resonance peak at about 2250 Hz is well visible, which corresponds to the first mode of structural vibration of the system; in fact, note that this resonance frequency strictly agrees with the analytical prediction $f_1 = 2256$ Hz in Table 1 that, in this case, is weakly influenced by coupling effects ($f_w = 2176$ Hz). It is worth to point out that the PSD plots do not show any significant peak in correspondence of the Helmholtz frequency, namely at about 1000 Hz. Note also that the presence of higher-order structural modes is not always visible on the PSD tracings (and therefore the PSD scale range does not include them) because the distorted shim shape vibrating at natural frequencies higher than its fundamental produces little net displacement of the surrounding air. The PSD trend detected for the brass actuator of $H = 5$ mm is qualitatively the same. Again, there is a satisfactory agreement between the frequency f_1 and the corresponding experimental one of Table 2 equal to about 2379 Hz.

Data for the aluminum 1 actuator are depicted in Fig. 5. As for the previous case, there is a good agreement between the analytical prediction, which provides $f_1 = 1632$ and 1462 Hz for the cavity heights of 3 and 8 mm, respectively, and the experiments, which give a resonance peak around 1510 and 1443 Hz, respectively. Note that, in Table 2, the vibrometer measurements appear closer to the theoretical predictions. In any case, the coupling effects are more significant for this device because the structural resonance frequency of free-oscillator is 1376 Hz. No peak is visible at the Helmholtz frequency because of the reduced influence of the off-diagonal term $k_{12}U$ of Eq. (21), which scales with $(d_o/d_w)^2$, on the dynamics of the membrane oscillator and, more importantly, of the nonlinear damping term affecting the dynamics of the acoustic oscillator.

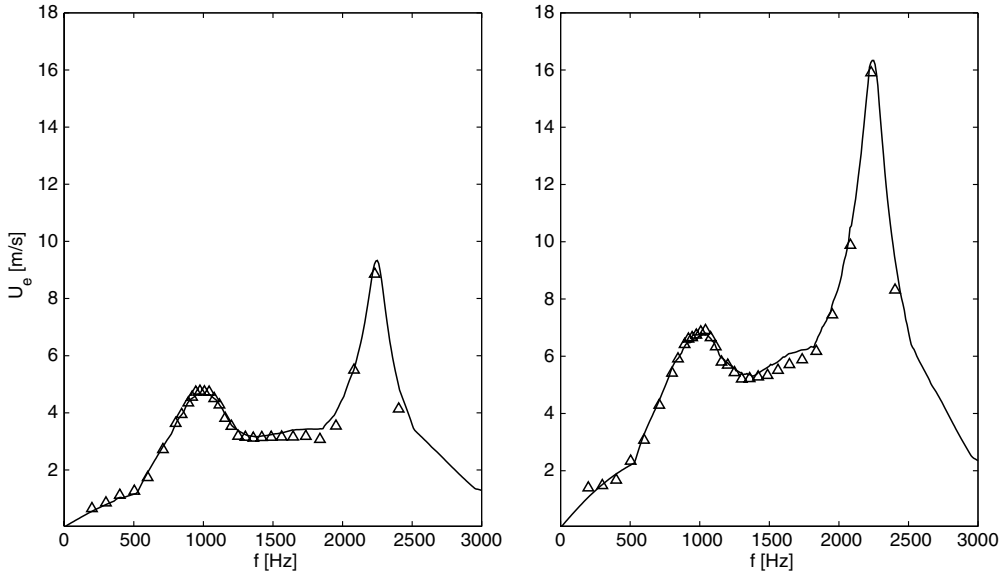

Fig. 10 Numerical–experimental comparison of average exit flow velocity frequency response for the brass actuator ($H = 3$ mm); triangles represent the experimental measurements, and black curves represent the numerical solution: a) $V_a = 35$ V, and b) $V_a = 70$ V.

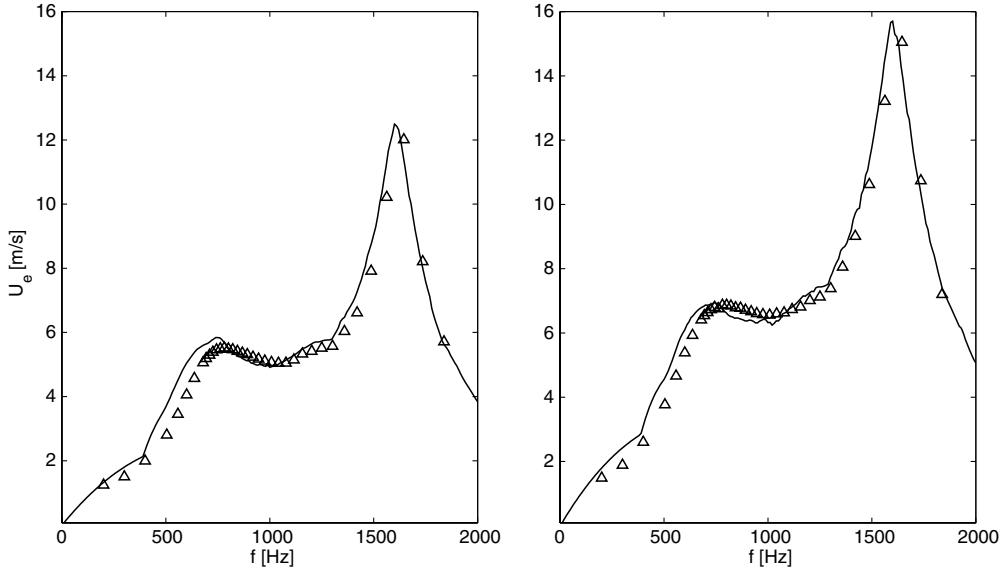

Fig. 11 Numerical–experimental comparison of average exit flow velocity frequency response for the aluminum 1 actuator ($H = 3$ mm); black curves represent the numerical solution, and triangles represent the experimental measures: a) $V_a = 25$ V, and b) $V_a = 35$ V.

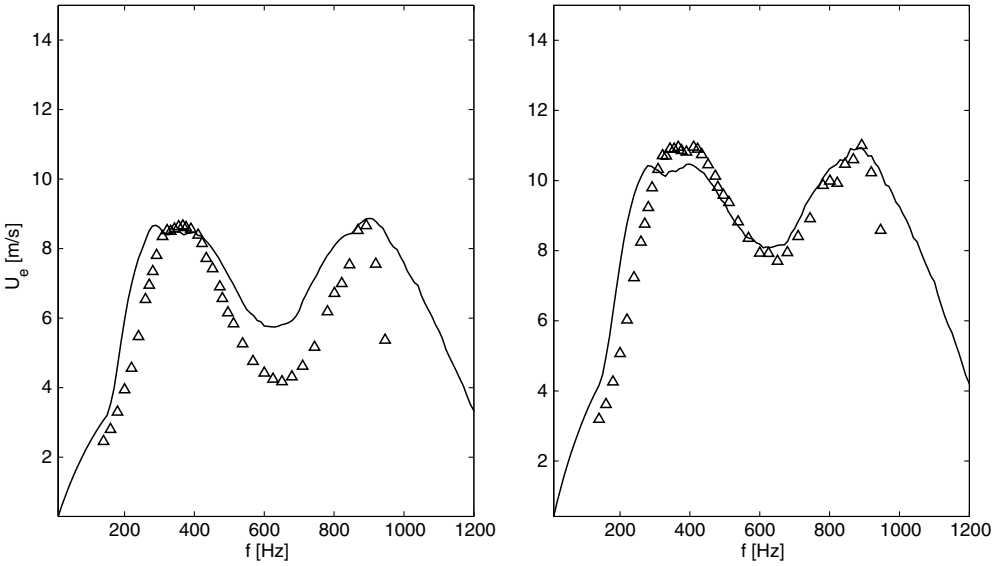

Fig. 12 Numerical–experimental comparison of average exit flow velocity frequency response for the aluminum 2 actuator ($H = 4$ mm); triangles represent the experimental measures, and black curves represent the numerical solution: a) $V_a = 35$ V, and b) $V_a = 50$ V.

For the third tested device (i.e., the aluminum 2), on the contrary, the PSD graphs of Fig. 6 show two peaks; the lower corresponds to the strongly coupled structural frequency (ranging from about 310 to 340 Hz), while the higher one (located at about 903, 735, and 620 Hz for cavity heights of 4, 7, and 11 mm, respectively, and voltage amplitude $V_a = 9$ V) corresponds to the modified frequency of the Helmholtz oscillator. The coupling effects of this actuator are very strong because the two nominal resonance frequencies are significantly modified. Note also the presence of a well marked displacement peak at the Helmholtz frequency, which is confirmed by vibrometer data (when available) reported in Table 2. This peculiar behavior is attributed to a reduced influence of the nonlinear damping term, as will be further discussed when comparing experimental and numerical results.

Table 3 Numerical resonance frequencies at $V_a = 35$ V

H, mm	Modified Helmholtz frequency, Hz	Modified structural frequency, Hz
	Brass	
3	960	2260
5	760	2210
	Aluminum 1	
3	770	1630
8	490	1480
	Aluminum 2	
4	900	290
7	690	320
11	570	330

Table 4 Experimental resonance frequencies from pitot tube

V_a, V	Modified Helmholtz frequency, Hz	Modified structural frequency, Hz
	Brass ($H = 3$ mm)	
35	976	2232
70	1042	2232
	Aluminum 1 ($H = 3$ mm)	
25	781	1645
35	801	1645
	Aluminum 2 ($H = 4$ mm)	
35	892	367
50	892	367

To have another basis of comparison of the dynamic response of the three devices, in Figs. 7–9, the membrane displacements detected by means of the laser vibrometer are compared to the corresponding findings of direct numerical simulations, for various supply voltages and cavity height of 3 mm, for the brass and the aluminum 1 actuators, and of 4 mm, for the aluminum 2 actuator. For this last actuator, numerical trends are shown for values of the additive constant of the effective orifice length, introduced in Eq. (14), of 0.62 (continuous line) and 1.42 (dashed line). These plots confirm qualitatively all the main features of the experimental results reported previously. Numerical data show for the first two actuators a relatively small peak at the lower frequency (which is more evident for the aluminum 1 device, also from vibrometer data) and a reduced (in comparison with experimental data) peak at the higher frequency for the aluminum 2 device. These discrepancies between experimental and numerical values are attributed to nonlinear damping effects that, in the numerical code, seem to be too small for the second actuator as well as too large for the third one. This finding will be discussed further when presenting jet velocity measurements. Remember that the numerical code has been, in general, calibrated on jet velocity data by using $K = 1.14$ and $\Delta l_e = 0.62$, but it is evident that $\Delta l_e = 1.42$ works better in predicting the membrane displacement for the aluminum 2 device.

Plots showing the frequency response of the actuators in terms of the downstream-directed velocity U_e measured by means of the pitot tube, at a point one orifice diameter downstream of the orifice exit, and therefore approximately corresponding to the saddle point, are reported in Figs. 10–12. Following the basic definitions and findings of literature (e.g., Smith and Glezer [18] and Smith and Swift [19]), the saddle point velocity is roughly 1.1 times the stroke length velocity U_o, namely the time average of the orifice blowing velocity over the entire period. Thus, to compare experimental measurements of U_e to numerical computations of the peak value $U_{\max}$ of the exit velocity U, the following relationship is used: $U_e \cong (1.1/\pi)U_{\max} = U_{\max}/2.85$.

Note that, during this testing session, the supply voltage has been adjusted to values of practical applications (i.e., well above the values reported in Table 2). Data points of Figs. 10–12 are compared to the corresponding numerical values obtained by integrating numerically the complete governing equations. Typical values of the electroacoustic transduction coefficient ϕ_a that best fit the continuous numerical curves to the velocity measurements are 105, 133, and 47.7

for brass, aluminum 1, and aluminum 2 actuators, respectively. As reported previously, we performed the numerical simulations with the basic values of $K = 1.14$ and $\Delta l_e = 0.62$, with the aim of optimizing the prediction capability of the numerical code in terms of jet-flow velocity.

Table 3 reports the resonance frequencies calculated numerically for each device at $V_a = 35$ V. This table should be compared to Table 4, showing analogous experimental findings to appreciate the data agreement. Data spread is generally less than 4%, except for the value of the modified structural frequency of aluminum 2 actuator, for which it appears to be about 26%. However, it should be noted that computer simulations of Fig. 12 show a rather wide plateau around this peak frequency, whereas the data spread of 26% refers exactly to the peak value. Of course, for a more general comparison including analytical, numerical, and experimental (from microphone, vibrometer, and pitot tube) results, one should glance at Tables 1–4 simultaneously.

VII. Further Numerical Insights

The results illustrated in the previous section exhibit a quite satisfactory agreement between the (fully nonlinear) numerical simulations of the frequency response of the resonant actuators considered in this work and the experimental and analytical findings. Thus, once the prediction capability of the numerical code has been established, it has been used to determine many other features of frequency response, very useful for design purposes. The maximum cavity pressure and membrane displacement and the jet-flow exit velocity as a function of the operation frequency are depicted in Figs. 13–15 for the three tested devices and for various cavity heights. The supply voltage V_a is equal to 35 V in all these simulations.

As a general comment, one should note that, in basic agreement with the experimental measurements (carried out basically at lower voltages), the membrane displacement exhibits an almost unimodal behavior for the brass and aluminum 1 devices, especially for higher cavity heights. The peak frequency is the structural one, weakly modified by the coupling effects; for both actuators and for $H/d_o = 0.5$, another smaller peak appears at the Helmholtz frequency. Moreover, note that the membrane displacement increases with increasing the cavity height; the cavity pressure influence on the membrane dynamics vanishing at high cavity height. Under the practical point of view, it is still more interesting to note that the behavior of exit flow velocity is different because of the occurrence of another peak corresponding to the lower Helmholtz frequency, again slightly modified by the coupling effects. The Helmholtz peak is

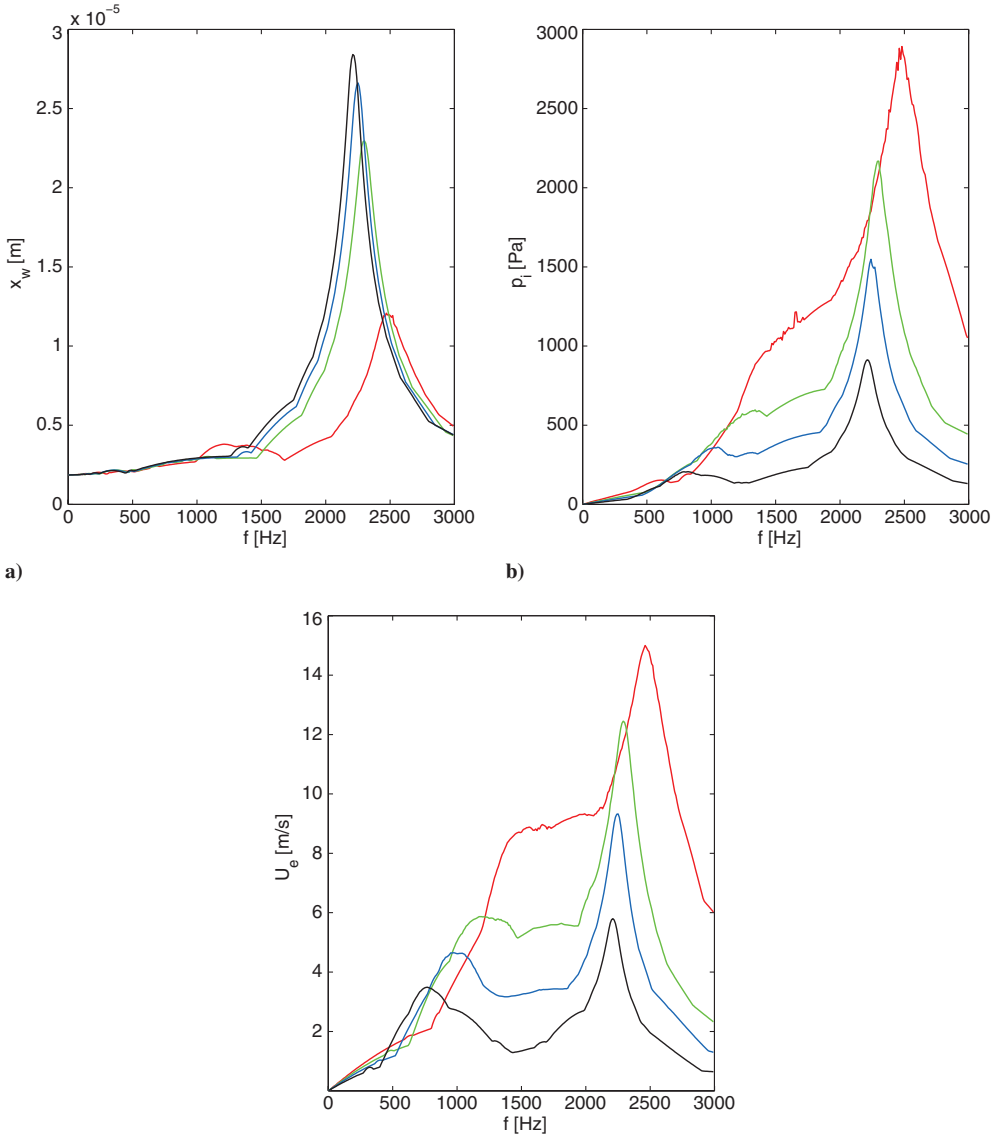

Fig. 13 Frequency response of a) maximum membrane displacement, b) maximum cavity pressure, and c) average exit flow velocity for the brass actuator at $V_a = 35$ V; the red line is for $H/d_o = 0.5$, green is $H/d_o = 1$, blue is $H/d_o = 1.5$, and black is $H/d_o = 2.5$.

lower than the structural one. For the brass device, the velocity peak increases with decreasing the cavity height, while for the aluminum 1 one, the trend is that the velocity peak reaches a plateau for intermediate values of H/d_o, and then it decreases at the largest height. For the brass actuator, the distance between the two resonance frequencies slightly increases with increasing H/d_0, in agreement with experimental results of Gomes et al. [17] obtained for $l_o/d_o > 1$, while for the aluminum 1, such a distance slightly decreases. Note that the experimental findings of Gomes et al. [17] show also that the resonance frequencies distance becomes practically constant as H/d_0 increases, in agreement with our analytical prediction in the case of $\omega_w \gg \omega_h$.

The velocity peak at the Helmholtz frequency strongly depends on the nonlinear damping term (present in the unsteady Bernoulli's equation), as already noted and discussed in the past by various authors, among others Gallas et al. [7], Sharma [8], and Persoons [12]. They found that one of the two expected peak frequencies can be missing due to the strong nonlinear damping. Additional simulations (not reported herein) confirmed their viewpoint, showing that the Helmholtz peak increases dramatically and overshoots the structural one when the fluid dynamic nonlinear damping is suppressed (i.e., $K = 0$). Remember also that the magnitude of this damping term, according to the Eq. (13), depends linearly on the head loss coefficient and is inversely proportional to the effective length of the orifice. Another feature of these two actuators is that the cavity pressure exhibits the same qualitative frequency response as the jet velocity.

The aluminum 2 device behaves in a different way. First of all, as already stressed, the two nominal Helmholtz and structural frequencies, which for this actuator are reversed, are remarkably modified by the high coupling ratio. The membrane displacement decreases with increasing the cavity height at the structural resonance frequency, whereas it increases with increasing H/d_o at the Helmholtz resonance frequency. The same behavior is exhibited by the frequency response of the jet velocity, with the result that the maximum peak is reached at the Helmholtz frequency for the highest simulated cavity height. This particular finding agrees with the theoretical prediction of Sec. III that, if $\omega_w \ll \omega_h$, then the distance between the two eigenvalues $|\omega_1^2 - \omega_2^2|/\omega_h^2$ does not depends on the cavity height H/d_o, and therefore $|\omega_1^2 - \omega_2^2| \simeq 1/(H/d_o)$. The quasi coincidence of the two resonance frequencies justifies that the maximum peak is reached for the highest cavity height.

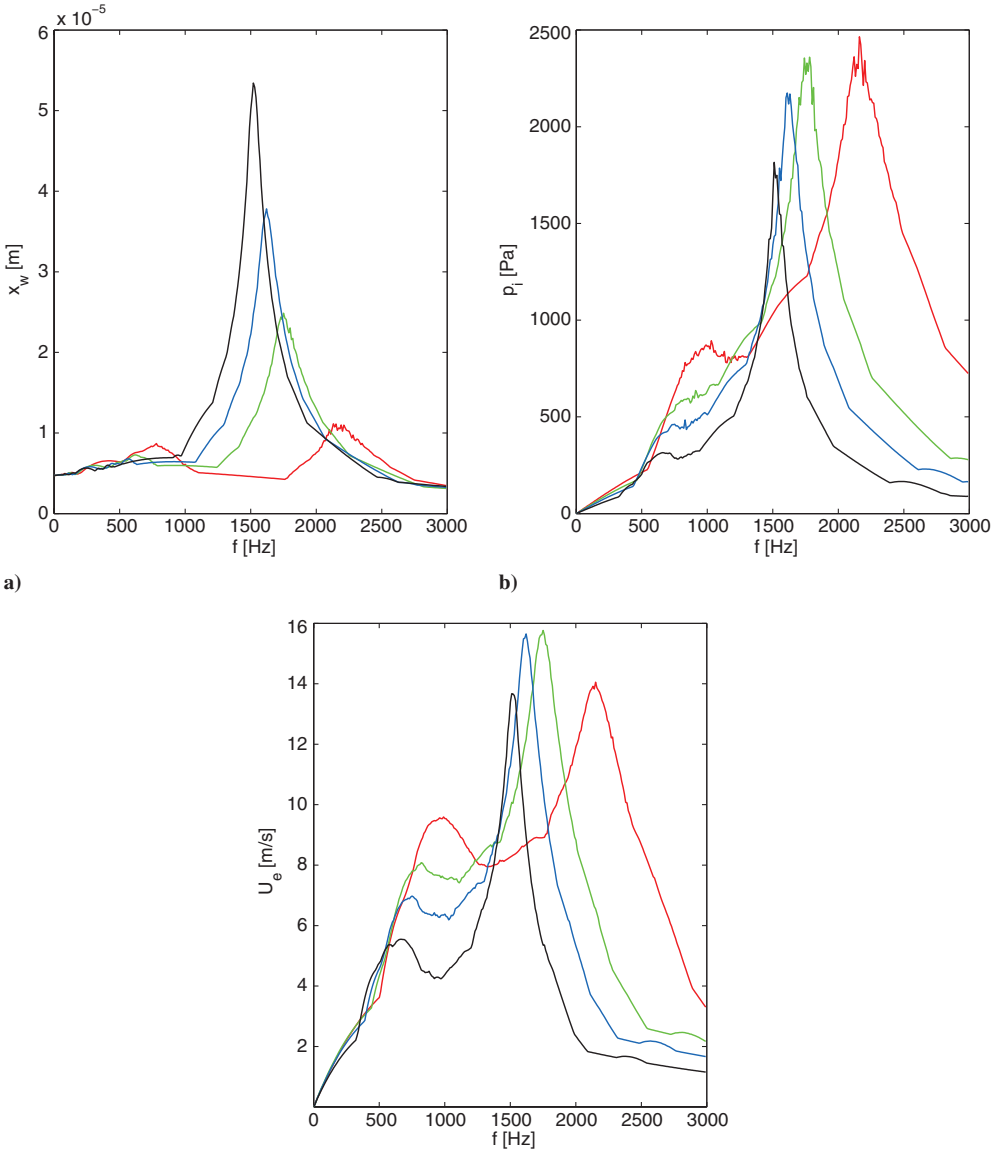

Fig. 14 Frequency response of a) maximum membrane displacement, b) maximum cavity pressure, and c) average exit flow velocity for the aluminum 1 actuator at $V_a = 35$ V; the red line is for $H/d_o = 0.5$, green is $H/d_o = 1$, blue is $H/d_o = 1.5$, and black is $H/d_o = 2.5$.

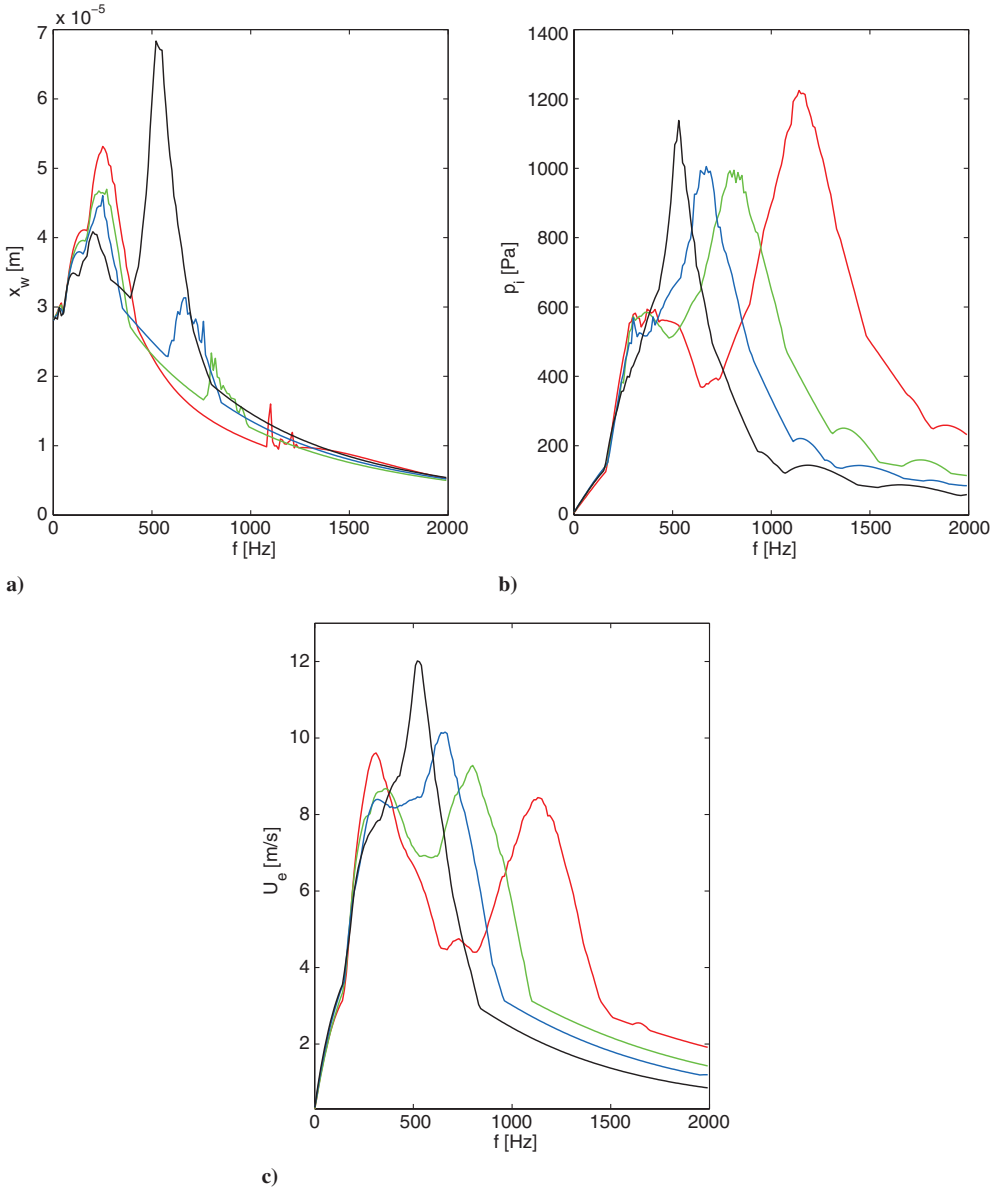

Fig. 15 Frequency response of a) maximum membrane displacement, b) maximum cavity pressure, and c) average exit flow velocity for the aluminum 2 actuator at $V_a = 35$ V; the red line is for $H/d_o = 0.5$, green is $H/d_o = 1$, blue is $H/d_o = 1.5$, and black is $H/d_o = 2.5$.

VIII. Conclusions

This paper has been aimed to yield insights on the frequency response of synthetic jet actuators driven by piezoelectric thin elements by using a lumped-element mathematical model. The model is fluid-dynamics based, and although its genesis is inspired by an analogous model of previous literature, it is innovative because it needs in input just electromechanical properties easily available from the commercial data sheet of the materials. For a certain class of devices, a numerical fitting parameter only is required, namely the electroacoustic transduction coefficient ϕ_a, which is the ratio of the effective acoustic piezoelectric coefficient to the acoustic compliance. From this viewpoint, the proposed model represents a practical tool for the overall design of the actuator. Among other quantities, the model can yield the frequency response characteristics of synthetic jet devices in terms of membrane displacement, pressure cavity, and exit jet-flow velocity. The computer code has been validated via comparisons with both analytical and experimental parallel investigations.

In the analytical study, the actuator has been idealized as an acoustic-mechanical system of two-coupled oscillators, and simple but rather accurate relationships have been given to predict the two peak frequencies, corresponding to the modified Helmholtz and first-mode structural resonance frequencies. Scaling laws of the distance between the two resonance frequencies as a function of the nondimensional cavity height H/d_o have been yielded. It is found that the role of the coupling effects is twofold; on one hand, they modify the nominal Helmholtz and structural resonance frequencies, and on the other hand, they introduce crossed linear reaction terms driving mutually the oscillators. The system suffers a nonlinear damping due to entrance head losses, which are proportional to the head loss coefficient and inversely proportional to the effective orifice length.

To perform comparisons with experimental data, various measurement campaigns have been carried out on three different actuators especially designed and manufactured to the purpose. The devices make use of brass or aluminum shims and standard piezoelectric disks driven by a sine input voltage. They have been designed essentially to achieve an increasing coupling ratio. The membrane displacements have been monitored indirectly by measuring pressure disturbances in the ambient atmosphere and directly by employing a digital laser vibrometer. A digitized pitot probe has been also used to measure the jet velocity in the external field at a location approximately coincident with the saddle-point (i.e., about one orifice diameter downstream of the exit section).

In the opinion of the present authors, the overall comparison among numerical and analytical as well as experimental findings is quite satisfactory. In particular, the predictions of the peak frequencies made by using the simple analytical relationships are confirmed by both the numerical computations and the various measurements. For the device exhibiting the strongest coupling, a perhaps not expected result is that the jet velocity peak occurs for the highest cavity height. The present study has confirmed the crucial role played by the nonlinear damping term on the acoustic (Helmholtz) oscillator of the model in reducing or suppressing the corresponding resonance peak. The numerical code has been, in general, calibrated on jet velocity data by using $K = 1.14$ and $\Delta l_e = 0.62$, but it is evident that, for the aluminum 2 actuator, the effective orifice length (namely, the air volume of the acoustic oscillator) is not fully adequate for predicting correctly the membrane displacement response. Hence, a more detailed analysis of the flow around the orifice is strongly needed to improve the overall prediction capabilities of the lumped-element model.

In future work, further experimental tests are planned to perform pressure measurements inside the cavity so as to give insights on the phase angles between internal pressure and orifice velocity, which have not been addressed here, although numerical evaluations are already available.

Acknowledgments

The work described in this paper has been basically funded by Compagnia di San Paolo and Polo delle Scienze e delle Tecnologie of the University of Naples Federico II, within the Finanziamento per l'Avvio di Ricerche Originali (F.A.R.O.) projects 2009 and 2012. The first author is indebted to Luigi Mongibello who produced the basic version of the Matlab code. The experimental part of the work is the result of a cooperative effort of various people of the Department of Industrial Engineering, Aerospace Sector. Many thanks are due to Claudio Leone for his continuous assistance in solving all the technological issues. Annagrazia Orazzo, Miriam Basile, and Gianluca Padula tested the devices during the very first testing session, while Andrea Renno and Concetta Rocco contributed to the subsequent velocity measurements. The laser vibrometer employed to detect the membrane displacement belongs to the Laboratory for Promoting Experiences in Aeronautical Structures and Acoustics, and the kind willingness of Leonardo Lecce is acknowledged accordingly. The support of Gennaro Cardone and Carlo Greco has been essential for their overall assistance in using laboratory facilities.

References

[1] Glezer, A., and Amitay, M., "Synthetic Jets," *Annual Review of Fluid Mechanics*, Vol. 34, 2002, pp. 503–529. doi:10.1146/annurev.fluid.34.090501.094913

[2] Cattafesta, L. N. III, and Sheplak, M., "Actuators for Active Flow Control," *Annual Review of Fluid Mechanics*, Vol. 43, 2011, pp. 247–272. doi:10.1146/annurev-fluid-122109-160634

[3] Mongibello, L., Rocco, G., Coppola, G., and de Luca, L., "Numerical Investigation of Two Adjacent Synthetic Jets for Flow Control," *Proceedings of the 2nd European Conference for Aero-Space Sciences (EUCASS)* [CD-ROM], Université Libre de Bruxelles, Brussels, Paper 02-06-08, 2007.

[4] Monaco, G., Mongibello, L., and de Luca, L., "Impingement Heat Transfer by Means of Synthetic Jets," *Proceedings of the ASME-ATI-UIT 2010 Conference on Thermal and Environmental Issues in Energy Systems*, Vol. 2, Edizioni ETS, Pisa, Italy, May 2010, pp. 1413–1417.

[5] Prasad, S. A. N., "Two-Port Electroacoustic Model of Piezoelectric Composite Circular Plate," M.S. Thesis, Dept. of Aerospace Engineering, Mechanics, and Engineering Sciences, Univ. of Florida, Gainesville, FL, 2002.

[6] Prasad, S. A. N., Gallas, Q., Horowitz, S., Homeijer, B., Sankar, B. V., Cattafesta, L. N., and Sheplak, M., "Analytical Electroacoustic Model of a Piezoelectric Composite Circular Plate," *AIAA Journal*, Vol. 44, No. 10, 2006, pp. 2311–2318. doi:10.2514/1.19855

[7] Gallas, Q., Holman, R., Nishida, T., Carroll, B., Sheplak, M., and Cattafesta, L., "Lumped Element Modeling of Piezoelectric-Driven Synthetic Jet Actuators," *AIAA Journal*, Vol. 41, No. 2, 2003, pp. 240–247. doi:10.2514/2.1936

[8] Sharma, R. N., "Fluid Dynamics Based Analytical Model for Synthetic Jet Actuation," *AIAA Journal*, Vol. 45, No. 8, Aug. 2007, pp. 1841–1847. doi:10.2514/1.25427

[9] Chaudhari, M., Verma, G., Puranik, B., and Agrawal, A., "Frequency Response of a Synthetic Jet Cavity," *Experimental Thermal and Fluid Science*, Vol. 33, No. 3, 2009, pp. 439–448. doi:10.1016/j.expthermflusci.2008.10.008

[10] Krishnan, G., and Mohseni, K., "Axisymmetric Synthetic Jets: An Experimental and Theoretical Examination," *AIAA Journal*, Vol. 47, No. 10, 2009, pp. 2273–2283. doi:10.2514/1.42967

[11] Seeley, C., Utturkar, Y., Arik, M., and Icoz, T., "Fluid–Structure Interaction Model for Low-Frequency Synthetic Jets," *AIAA Journal*, Vol. 49, No. 2, 2011, pp. 316–323. doi:10.2514/1.J050433

[12] Persoons, T., "General Reduced-Order Model to Design and Operate Synthetic Jet Actuators," *AIAA Journal*, Vol. 50, No. 4, 2012, pp. 916–927. doi:10.2514/1.J051381

[13] Kinsler, L. E., Frey, A. R., Coppens, A. B., and Sanders, J. V., *Fundamentals of acoustics*, 4th ed., Wiley, New York, 2000, pp. 107–108.

[14] Rathnasingham, R., and Breuer, K. S., "Coupled Fluid–Structural Characteristics of Actuators for Flow Control," *AIAA Journal*, Vol. 35, No. 5, 1997, pp. 832–837. doi:10.2514/2.7454

[15] Raju, R., Gallas, Q., Mittal, R., and Cattafesta, L., "Scaling of Pressure Drop for Oscillatory Flow Through a Slot," *Physics of Fluids*, Vol. 19, No. 7, 2007, Paper 078107. doi:10.1063/1.2749814

[16] Kooijman, G., and Ouweltjes, O., "Finite Difference Time Domain Electroacoustic Model for Synthetic Jet Actuators Including Nonlinear Flow Resistance," *Journal of the Acoustical Society of America*, Vol. 125, No. 4, 2009, pp. 1911–1918. doi:10.1121/1.3081514

[17] Gomes, L. D., Crowther, W. J., and Wood, N. J., "Towards a Practical Piezoceramic Diaphragm Based Synthetic Jet Actuator for High Subsonic Applications—Effect of Chamber and Orifice Depth on Actuator Peak Velocity," *3rd AIAA Flow Control Conference*, AIAA Paper 2006-2859, June 2006.

[18] Smith, B.L., and Glezer, A., "The Formation and Evolution of Synthetic Jets," *Physics of Fluids*, Vol. 10, No. 9, 1998, pp. 2281–2297. doi:10.1063/1.869828

[19] Smith, B. L., and Swift, G.W., "A Comparison Between Synthetic Jets and Continuous Jets," *Experiments in Fluids*, Vol. 34, No. 4, 2003, pp. 467–472. doi:10.1007/s00348-002-0577-6

F. Alvi
Associate Editor

Layout: T1 Standard Unicode | Book ID: 311437_1_En | Book ISBN: 978-3-319-09712-1
Chapter No.: 6 | Date: 9-10-2014 | Time: 7:06 pm | Page: 101/118

Characterization of Synthetic Jet Resonant Cavities

Luigi de Luca, Michele Girfoglio, Matteo Chiatto and Gennaro Coppola

Abstract The acoustic properties of piezo-electric driven resonant cavities usually employed to generate the so-called synthetic jets are analytically and numerically investigated in order to characterize the performances of such devices. It is shown that the actuator behaves as a two-coupled oscillators system and the dimensionless form of the governing equations allows one to identify various particular operating conditions. The theoretical predictions are validated through experimental tests carried out on devices having different mechanical and geometrical characteristics, designed in order to achieve an increasing coupling strength. Practical design implementations are discussed as well.

1 Introduction

The literature concerned with the synthetic jet actuators is huge and includes a wide field of applications such as flow control (perhaps the original one), heat transfer from small size surfaces, overall enhancement of mixing between fluid currents, generation of micro-thrust for propulsion or attitude control of Micro Aerial Vehicle (MAV). We limit to cite here the review papers of Glezer and Amitay [1] and Cattafesta and Sheplak [2]. Regarding present authors, previous contributions dealt with the direct numerical simulation of jet vectoring, as described by Mongibello et al. [3], a design procedure of synthetic jet actuator to be employed as heat transfer device, as reported by Monaco et al. [4], and the formulation and the experimental validation of a lumped element physical model of the operation of the actuator devoted to the prediction of its frequency response, by de Luca et al. [5].

L. de Luca (✉) · M. Girfoglio · G. Coppola
Department of Industrial Engineering—Aerospace Sect., Universita' degli Studi di Napoli, P.le Tecchio 80, 80125 Naples, Italy
e-mail: luigi.deluca@unina.it

M. Chiatto
Von Karman Institute, 1640 Rhode-St-Genese, Belgium

E. Ciappi et al. (eds.), *Flinovia - Flow Induced Noise and Vibration Issues and Aspects*, DOI 10.1007/978-3-319-09713-8_6

Layout: T1 Standard Unicode | Book ID: 311437_1_En | Book ISBN: 978-3-319-09712-1
Chapter No.: 6 | Date: 9-10-2014 | Time: 7:06 pm | Page: 102/118

The overall design of the actuator needs practical modeling tools, which are generally based on reduced order, lumped element physical models. A significant lumped element model of a piezoelectric-driven synthetic jet device is described by Prasad [6] and Prasad et al. [7], who gave detailed relationships for the transverse deflection of the inner and outer regions of the composite membrane in the simultaneous presence of applied voltage and pressure load. They resorted to the approach based on the equivalent electric circuit. Following the same approach, Gallas et al. [8] noted that in a lumped model one may use the acoustic compliance of the shim only reduced by a proper factor depending on the ratio of the radius, thickness and Young's modulus of the piezoceramic and shim materials. Later on, Sharma [9] proposed a different model directly based on the equations of fluid dynamics, where the oscillating membrane is considered as a single-degree-of-freedom mechanical system, while the cavity and the orifice are described by means of proper forms of the continuity and Bernoulli's unsteady equations, respectively. Sharma [9] validated his model on the very same experimental data of Gallas et al. [8].

Chaudhari et al. [10] carried out systematic measurements about the effects of the excitation frequency on the ejection and suction velocities, by varying the geometrical parameters of the cavity. Krishnan and Mohseni [11] studied the characteristics of the flow field produced by a round synthetic jet by using detailed numerical simulations of the turbulent Navier-Stokes equations. Seeley et al. [12] described a simplified fluid-structure interaction model based on the implementation of commercial Finite Elements codes, and proved its validity at relatively low frequency, namely well below the Helmholtz frequency. Persoons [13] proposed a low-order model of prediction of the frequency response of synthetic jet actuators driven by electromagnetic or piezoelectric supply. Based on the equivalent circuit approach, its model yields analytical expressions for the two resonance frequencies, as a function of the structural and Helmholtz resonance frequencies.

Recently de Luca et al. [5] presented a fluidic type lumped element modeling, that has been inspired by the Sharma's work [9], yielding the frequency response of the resonant cavity in terms of pressure disturbances, membrane displacement and external jet velocity. The model, validated against systematic experimental measurements, gave also simple but accurate analytical relationships for the two resonance frequencies characterizing the overall system response. The present contribution is a follow-up inspection of the previous investigation and is devoted to gain new insights on the fluid-structure interaction occurring during the operation of a typical piezoelectric-driven resonant cavity. The analysis hereafter presented is based on the dimensionless form of the equations governing the behavior of the two-coupled oscillators, the membrane and the Helmholtz one.

2 Model Formulation

The model described hereafter is essentially the same as the one presented by de Luca et al. [5], in turn inspired by the Sharma's work [9]. It refers to the three basic elements of the actuator: the oscillating membrane (diaphragm or wall, constituted

Layout: T1 Standard Unicode | Book ID: 311437_1_En | Book ISBN: 978-3-319-09712-1
Chapter No.: 6 | Date: 9-10-2014 | Time: 7:06 pm | Page: 103/118

by a thin round metal shim on which a smaller diameter piezoceramic disk is bonded), the cavity, the orifice.

For the sake of convenience, the three differential equations which describe the dynamics of the actuator are summarized below

$$\ddot{x}_w + 2\zeta_w \omega_w \dot{x}_w + \omega_w^2 x_w = \omega_w^2 \Delta x_w \sin \omega t - \frac{p_i A_w}{m_{wt}} \tag{1}$$

$$\frac{V_c}{\gamma p_o}\frac{\mathrm{d}p_i}{\mathrm{d}t} - A_w \dot{x}_w = -A_o U \tag{2}$$

$$\ddot{U} + \frac{K}{l_e}|U|\dot{U} + \omega_h^2 U = \frac{A_w}{A_o}\omega_h^2 \dot{x}_w \tag{3}$$

The dynamics of the membrane is described through the motion equation of a one-degree of freedom forced-damped spring-mass system, Eq. (1), where x_w is the (average) membrane displacement, t is time, p_i is the cavity (internal) differential pressure, m_{wt} is the diaphragm total mass, including shim, piezo-element and air added mass, ω_w is the natural frequency of membrane, ω is the operating frequency, Δx_w is the average linear membrane displacement due to the application of a certain voltage to the piezo-element, A_w is the membrane surface area, ζ_w is the diaphragm damping ratio, dot denotes time derivative; the second equation of the model is the conservation of mass in the cavity under the assumption of zero-dimensional (lumped) system, Eq. (2). By relating the density and pressure variations by means of an isentropic compression/expansion transformation, the continuity equation can be formulated as above written, where V_c is the cavity volume, p_o is the ambient pressure, γ is the specific heat ratio, U is the instantaneous orifice jet-flow velocity, A_o is the orifice area; the application of the unsteady Bernoulli's equation between a point inside the cavity where the flow velocity is practically null and a point, just outside the cavity, representing the location where the pressure matches the unperturbed external ambient value, yields the third equation of the model, Eq. (3), where ω_h is the natural Helmholtz frequency, K is the head loss coefficient.

In particular, the (first mode) structural circular frequency of the membrane is given by

$$\omega_w = \sqrt{\frac{k_w}{m_{wt}}} \tag{4}$$

and represents the uncoupled natural frequency of the membrane oscillator, where k_w is the equivalent spring stiffness of the membrane. This last can be obtained as

$$k_w = m_w (2\pi \widetilde{f}_w)^2 \tag{5}$$

where $\widetilde{f}_w$ is the frequency of the principal mode of vibration of a rigidly clamped disk. Although the presence of the piezoceramic element bonded to the metal shim

Layout: T1 Standard Unicode | Book ID: 311437_1_En | Book ISBN: 978-3-319-09712-1
Chapter No.: 6 | Date: 9-10-2014 | Time: 7:06 pm | Page: 104/118

enhances the flexural rigidity of the membrane (and in principle the very thin layer of glue should be taken into account as well), for standard operating conditions $\widetilde{f}_w$ can be referred to the first fundamental mode of the shim only (that is the membrane structural element actually clamped) and calculated by using the standard formula reported in many textbooks (de Luca et al. [5]). Here m_w is the diaphragm mass taking into account both shim and piezoceramic disk, but not including the dynamic contribution of the air added mass.

The uncoupled natural frequency of the acoustic oscillator is the so called Helmholtz frequency ω_h, which is usually recognized to be:

$$\omega_h = \sqrt{\frac{\gamma A_o^2 p_o / V_c}{\rho_a l_e A_o}} = \sqrt{\frac{k_a}{M_a}} \tag{6}$$

where k_a and M_a are, respectively, the equivalent stiffness of the air inside the cavity, $k_a = \gamma A_o^2 p_o / V_c$, and the effective mass of the air at the orifice, $M_a = \rho_a l_e A_o$.

It is worth to stress that the membrane dynamics is forced by the acoustic oscillator via the cavity pressure term as well as by the piezoelectric effect due to the applied sine voltage. The amplitude of this forcing, F_o, is expressed conveniently as

$$F_o = \frac{\omega_w^2 d_A V_a}{A_w} = \omega_w^2 \Delta x_w \tag{7}$$

where d_A is the effective acoustic piezoelectric coefficient that represents the ratio between the cavity volume variation ΔV and the applied voltage V_a, when the driving differential pressure is equal to zero [7]. Note that in the previous Eq. (7) the cavity volume variation $\Delta V = d_A V_a$ is divided by the membrane area A_w in order to obtain the average linear membrane displacement Δx_w (to be multiplied by k_w in order to obtain the driving force).

$$\Delta x_w = \frac{d_A V_a}{A_w} \tag{8}$$

The coefficient d_A could be evaluated analytically by means the distribution of the transverse displacement of the composite diaphragm, as made by Prasad [6] and Prasad et al. [7]. This procedure is not practical due to the difficulty of determining the required coefficients. An alternative way consists in determining the acoustic compliance of the membrane C_{ac} which, through a dual definition of d_A, is given by the ratio of the volume variation ΔV to a uniformly distributed pressure load p, in condition of electrical short-circuit [7]. Of course the evaluation of C_{ac} would require the same difficulties. However, one can refer to the acoustic compliance of a homogeneous circular plate (namely, having the properties of the piezoceramic disk) that yields insight into the scaling behavior of the diaphragm, and ultimately obtain d_A by means of the relationship

Layout: T1 Standard Unicode | Book ID: 311437_1_En | Book ISBN: 978-3-319-09712-1
Chapter No.: 6 | Date: 9-10-2014 | Time: 7:06 pm | Page: 105/118

$$d_A = C_{ac}\phi_a \tag{9}$$

in which ϕ_a is the electroacoustic transduction coefficient [7]. As introduced by de Luca et al. [5], the electroacoustic transduction coefficient is assumed to be a fitting parameter of the computer code.

In summary, the behavior of the synthetic jet actuator can be described by the dynamics of two mutually coupled oscillators: the first one, describing the membrane displacement x_w, is characterized by its uncoupled natural frequency ω_w, while the second one, acoustic oscillator, describing the dynamics of the mass of air at the orifice, M_a, through its velocity U, is characterized by the its natural frequency ω_h. The system of Eqs. (1–3) shows that both the dynamics of the membrane and of the orifice air mass are forced by the cavity pressure which couples them by means of the continuity Eq. (2). An external forcing due to the supply power also acts on the membrane dynamics. In order to investigate in more detail the coupling of the two oscillators, it is convenient to reformulate the equations.

By taking the time derivative of Eq. (1), and by eliminating the pressure derivative by means of Eq. (2), one obtains:

$$\ddot{V}_w + 2\zeta_w\omega_w\dot{V}_w + (\omega_w^2 + \omega_{wc}^2)V_w - \frac{A_o}{A_w}\omega_{wc}^2 U = (\omega\Delta x_w)\omega_w^2\cos\omega t \tag{10}$$

which is coupled with the Eq. (3). Note that another characteristic frequency ω_{wc} is introduced in Eq. (10), defined as

$$\omega_{wc} = \sqrt{\frac{\gamma A_w^2 p_o/V_c}{m_w}} = \sqrt{\frac{\gamma A_w p_o}{m_w H}} \tag{11}$$

which, according to Sharma [9], may be interpreted as the natural frequency of the pneumatic spring made of the air enclosed within the cavity of volume V_c and of the diaphragm mass m_w. Note that the height of the cavity, H, is explicitly introduced.

3 Dimensionless Form of the Equations

In order to give more insight to the problem physics, it is worth recasting the governing equations into a convenient dimensionless form. As far as the acoustic oscillator is concerned, proper choices of the reference quantities for time, length and velocity are the reciprocal of the operating frequency $1/\omega$, the cavity height H and the speed of sound of air c, respectively. The dimensionless form of the dynamics of the acoustic oscillator accordingly is:

Layout: T1 Standard Unicode | Book ID: 311437_1_En | Book ISBN: 978-3-319-09712-1
Chapter No.: 6 | Date: 9-10-2014 | Time: 7:06 pm | Page: 106/118

$$St^2 \frac{\mathrm{d}^2 U^*}{\mathrm{d}t^{*2}} + St\left(K\sqrt{\frac{H}{l_e}}|U^*|\right)\frac{\mathrm{d}U^*}{\mathrm{d}t^*} = V_w^* - \frac{A_o}{A_w}U^* \tag{12}$$

where the Strouhal number is defined as

$$St = \frac{\omega H}{c}\sqrt{\frac{l_e}{H}} \tag{13}$$

The condition corresponding to $St \ll 1$ is physically relevant. Apart from the scaling factor represented by the factor $\sqrt{l_e/H}$, this situation represents the case of acoustically thin cavity, the traveling time of a small pressure disturbance over the distance H being much smaller than the reference time $1/\omega$; in other terms, the air inside the cavity behaves as an incompressible medium (i.e., the air stiffness is infinite). By inspecting Eq. (12), it is evident that this equation reduces to the dimensional relationship:

$$A_w V_w = A_o U \tag{14}$$

namely, the volume rate entering the cavity as a consequence of the membrane displacement equals the volume rate of air expelled through the orifice. On the other hand, the Eq. (1) of the membrane dynamics shows that this last is decoupled from that of the acoustic oscillator. When $St \ll 1$, once the air velocity at the orifice has been obtained from Eq. (14), the cavity pressure may be evaluated by using the unsteady form of the Bernoulli's equation.

The physical situation of $St \gg 1$ also corresponds to decoupled membrane dynamics. In this case, however, the air stiffness is vanishing (the pressure field inside the cavity is practically unperturbed), so that the air jet velocity U is vanishing too.

The equation of motion of the membrane is made dimensionless with the aid of different time and velocity scales, a convenient choice being $1/\omega_w$ and $\omega \Delta x_w$, respectively. The non-dimensional form of such an equations is

$$\ddot{V}_w^* + 2\zeta_w \dot{V}_w^* + V_w^* + CF\left(V_w^* - \frac{A_o}{A_w}U^*\right) = \cos \omega t \tag{15}$$

where the coupling factor is defined as

$$CF = \frac{\omega_{wc}^2}{\omega_w^2} \tag{16}$$

It is straightforward to observe that under the condition for which $CF \ll 1$ (which means that the air stiffness is negligible in comparison with the membrane stiffness) the membrane dynamics is decoupled from the acoustic oscillator one. In this case the jet velocity and the cavity pressure are determined via the continuity and the

Layout: T1 Standard Unicode | Book ID: 311437_1_En | Book ISBN: 978-3-319-09712-1
Chapter No.: 6 | Date: 9-10-2014 | Time: 7:06 pm | Page: 107/118

unsteady Bernoulli's equations. Another aspect of this decoupling is that the modified structural and Helmholtz's frequencies tend to coincide with the corresponding uncoupled frequencies, as one may verify by inspecting the relationship yielding the eigenvalues of governing system under the assumption that any damping effects is negligible (de Luca et al. [5]):

$$\frac{\omega_{1,2}^2}{\omega_w^2} = \frac{-(1+\frac{\omega_{wc}^2}{\omega_w^2}+\frac{\omega_h^2}{\omega_w^2}) \pm \sqrt{(1+\frac{\omega_{wc}^2}{\omega_w^2}+\frac{\omega_h^2}{\omega_w^2})^2 - 4\frac{\omega_h^2}{\omega_w^2}}}{2} \tag{17}$$

Following de Luca et al. [5], the modified (i.e. coupled) natural frequencies are

$$f_{1,2} = \omega_{i1,2}/(2\pi), \tag{18}$$

$\omega_{i1,2}$ being the imaginary coefficients of the eigenvalues.

4 Validation of the Theory Against Experimental and Numerical Data

The theoretical issues developed before have been verified by means of both experimental measurements as well as numerical simulations of the governing Eqs. (1–3). The basic experimental validation of the physical model as well as of the related computer code has been already presented in a previous paper by de Luca et al. [5]. Hereafter we will refer to the coupling effects of the two oscillators and to the conditions governing them. Moreover, it has to be stressed that, in general, the coupling effects represented by the CF parameter refer to a certain device and may be neglected on the basis of design characteristics of the actuator, whatever is the operating condition. On the contrary, the conditions of decoupling occurring for $St \ll 1$ and $St \gg 1$ depend essentially on the operating condition and they may occur for any device.

4.1 Effect of CF

Experimental tests have been carried out on three different synthetic jet actuators (one with the membrane in brass and the other two in aluminum) designed to the purpose. The basic characteristics of such actuators are summarized in Table 1. They have been designed essentially in order to obtain different values of the coupling factor, ranging from about 0 to 1.88. The schematic of the devices is shown in Fig. 1 highlighting their modular structure, which permits independent variations of cavity diameter and height, orifice diameter, and piezoelectric diaphragm.

Layout: T1 Standard Unicode | Book ID: 311437_1_En | Book ISBN: 978-3-319-09712-1
Chapter No.: 6 | Date: 9-10-2014 | Time: 7:06 pm | Page: 108/118

Table 1 Features of the tested devices predicted analytically

	Property	Brass	Aluminum 1	Aluminum 2
Geometry	Shim diameter (mm)	35	42	80
	Shim thickness (mm)	0.4	0.24	0.25
	Piezoelectric diameter (mm)	23	31.8	63.5
	Piezoelectric thickness (mm)	0.23	0.191	0.191
	Cavity diameter (mm)	35	42	80
	Cavity height (mm)	3–5	3–8	4–7–11
	Orifice diameter (mm)	2	2	5
	Orifice length (mm)	2	2	2
	H/d_o	1.5–2.5	1.5–4	0.8–1.4–2.2
	l_e/d_o	1	1	0.4
Shim	Young's module (Pa)	9.7×10^{10}	7.31×10^{10}	7.31×10^{10}
	Poisson's module	0.36	0.31	0.31
	Density (kg/m^3)	8,490	2,780	2,780
Piezoelectric	Young's module (Pa)	6.7×10^{10}	6.6×10^{10}	6.6×10^{10}
	Poisson's module	0.31	0.31	0.31
	Density (kg/m^3)	8,000	7,800	7,800
Frequency response	f_w (Hz)	2,176	1,376	401
	f_1 (Hz)	2,256–2,221	1,632–1,462	307–297–283
	f_h (Hz)	1,000–775	833–510	723–547–436
	f_2 (Hz)	964–759	702–480	944–737–617
	CF	0.06–0.04	0.30–0.11	1.88–1.08–0.68

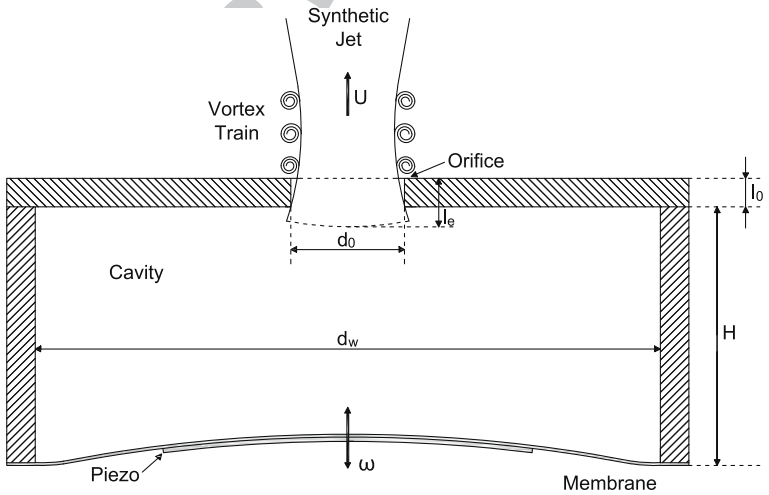

Fig. 1 Sketch of a typical device

Layout: T1 Standard Unicode | Book ID: 311437_1_En | Book ISBN: 978-3-319-09712-1
Chapter No.: 6 | Date: 9-10-2014 | Time: 7:06 pm | Page: 109/118

The brass actuator is a commercially available piezoelectric ceramic disk bonded to a thin brass metal plate fabricated by Murata Manufacturing Co. The aluminum membranes were built in-house by gluing a LZT piezoceramic disk (manufactured by PIEZO Inc.) on a thin aluminum foil.

In Table 1 geometrical and mechanical properties, as well as nominal characteristic frequencies of the tested devices, listed on the basis of the shim material, are summarized. The frequencies reported in Table 1 have been calculated by means of the analytical model illustrated before. f_w and f_h denote the (uncoupled) first-mode structural and Helmholtz natural frequencies, respectively, defined through Eqs. (4) and (6), respectively; f_1 and f_2 are the frequencies of the two coupled oscillators, i.e. the modified first-mode structural and Helmholtz resonance frequencies, defined by Eq. (18); the coupling factor CF introduced by Eq. (16) is reported in the last line.

As a general trend, on the grounds of Eq. (17) the coupling effect increases the structural resonance frequency and lowers the Helmholtz resonance frequency. Furthermore, the coupling factor CF is higher as the cavity height decreases. However, since for the aluminum 2 device the nominal structural frequency is less than the Helmholtz one, the situation is reversed in the sense that the coupling of the oscillators lowers f_1 and raises f_2.

As shown in Table 1, the nominal structural frequency of the brass devices is very close to the value predicted by the model of the coupled oscillators. For the brass device it results that also the Helmholtz frequency (i.e., the natural frequency of the acoustic oscillator) is almost coincident with the value predicted by means of the coupling model. The quasi-coincidence between the uncoupled natural structural and Helmholtz frequencies and the corresponding values of $\omega_{1,2}$, observed for the brass actuator, is much more weak for the aluminum 1 and totally disappears for the aluminum 2 actuator which exhibits the strongest coupling effect.

As already pointed out before, the model has been validated against systematic experimental tests whose findings have been already published in a previous paper by de Luca et al. [5]. Here we limit to remember that we made measurements of pressure disturbances produced by the motion of the membrane into the external ambient, deflection of the (composite) membrane by means of a laser scanning vibrometer, and jet exit velocity (by using a standard Pitot tube) in the external ambient at a station located on the jet axis just downstream of the stagnation point (the so called saddle point) separating near and far fields.

Plots showing the frequency response of the actuators in terms of the downstream-directed velocity U_e measured by means of the Pitot tube just downstream of the saddle point (i.e. at a point one orifice diameter downstream of the orifice exit), are reported in Figs. 2, 3 and 4. Following the basic definitions and findings of literature (e.g., [14, 15]), the saddle point velocity is roughly 1.1 times the stroke length velocity, U_o, namely the time-average of the orifice blowing velocity over the entire period. Thus, in order to compare experimental measurements of U_e to numerical computations of the peak value $U_{\max}$ of the exit velocity U, the relationship is used $U_e \cong (1.1/\pi)U_{\max} = U_{\max}/2.85$.

Layout: T1 Standard Unicode | Book ID: 311437_1_En | Book ISBN: 978-3-319-09712-1
Chapter No.: 6 | Date: 9-10-2014 Time: 7:06 pm | Page: 110/118

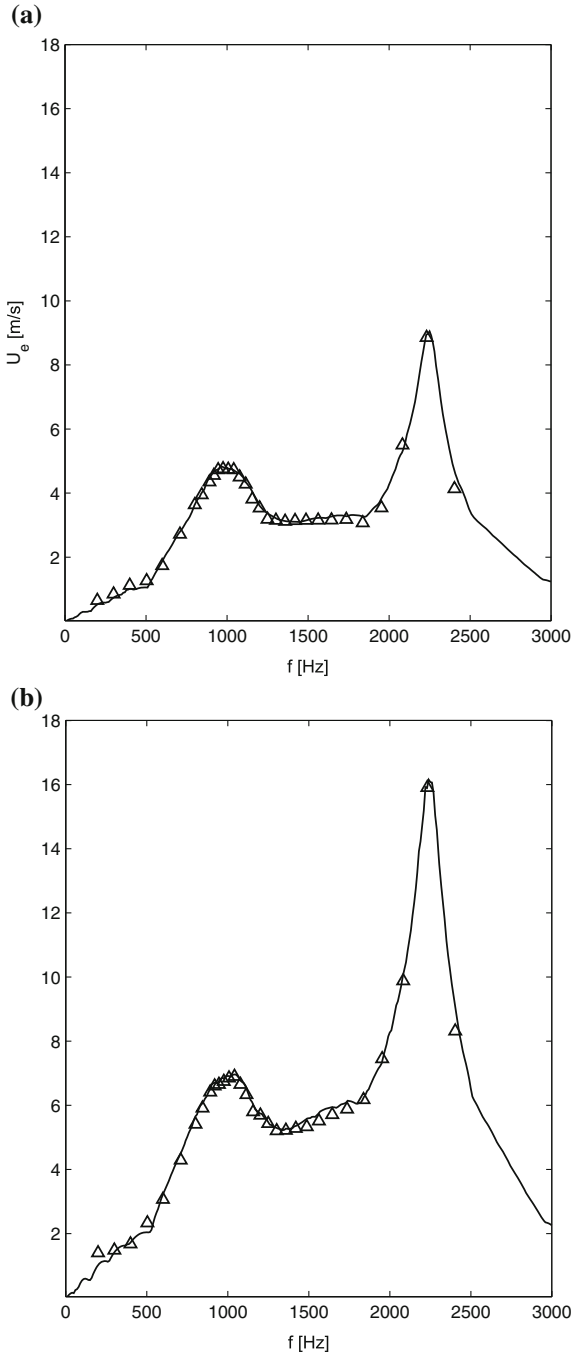

Fig. 2 Numerical-experimental comparison of average exit flow velocity frequency response for the brass actuator ($\boldsymbol{H} = \mathbf{3}$ mm); *triangles* represent the experimental measurements, *black curves* represent the numerical solution; **a** $\boldsymbol{V_a} = \mathbf{35}$ V, **b** $\boldsymbol{V_a} = \mathbf{70}$ V

Layout: T1 Standard Unicode | Book ID: 311437_1_En | Book ISBN: 978-3-319-09712-1
Chapter No.: 6 | Date: 9-10-2014 Time: 7:06 pm | Page: 111/118

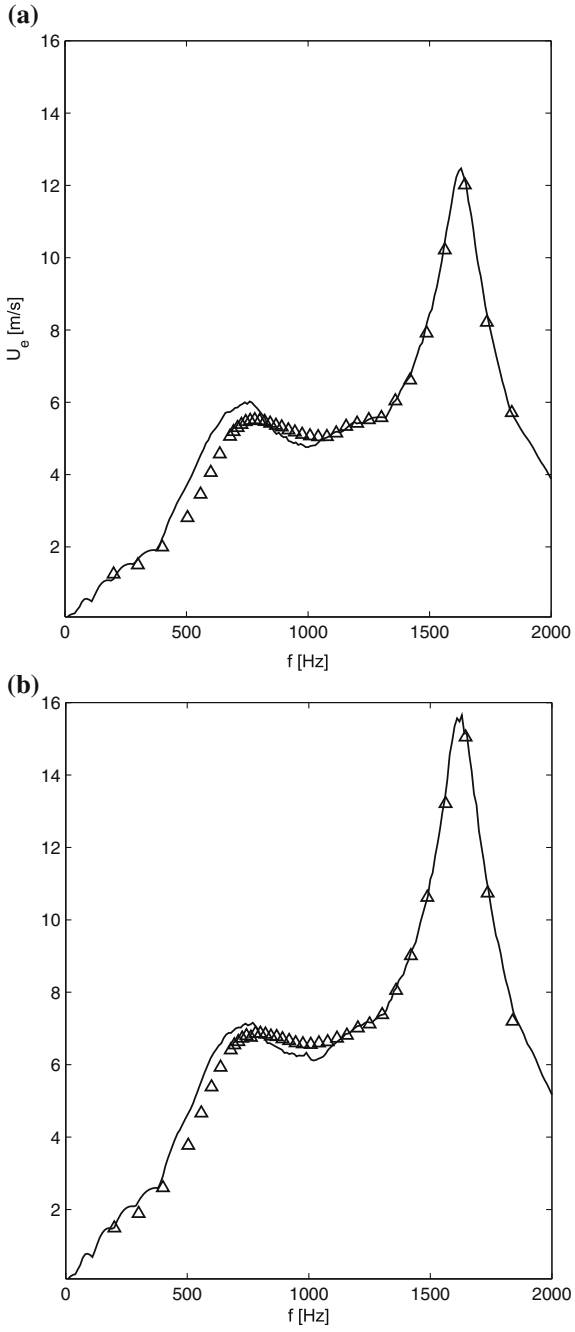

Fig. 3 Numerical-experimental comparison of average exit flow velocity frequency response for the aluminum 1 actuator ($\boldsymbol{H} = \mathbf{3}$ mm); *black curves* represent the numerical solution, *triangles* represent the experimental measures; **a** $\boldsymbol{V_a} = \mathbf{25}$ V, **b** $\boldsymbol{V_a} = \mathbf{35}$ V

Layout: T1 Standard Unicode | Book ID: 311437_1_En | Book ISBN: 978-3-319-09712-1
Chapter No.: 6 | Date: 9-10-2014 | Time: 7:06 pm | Page: 112/118

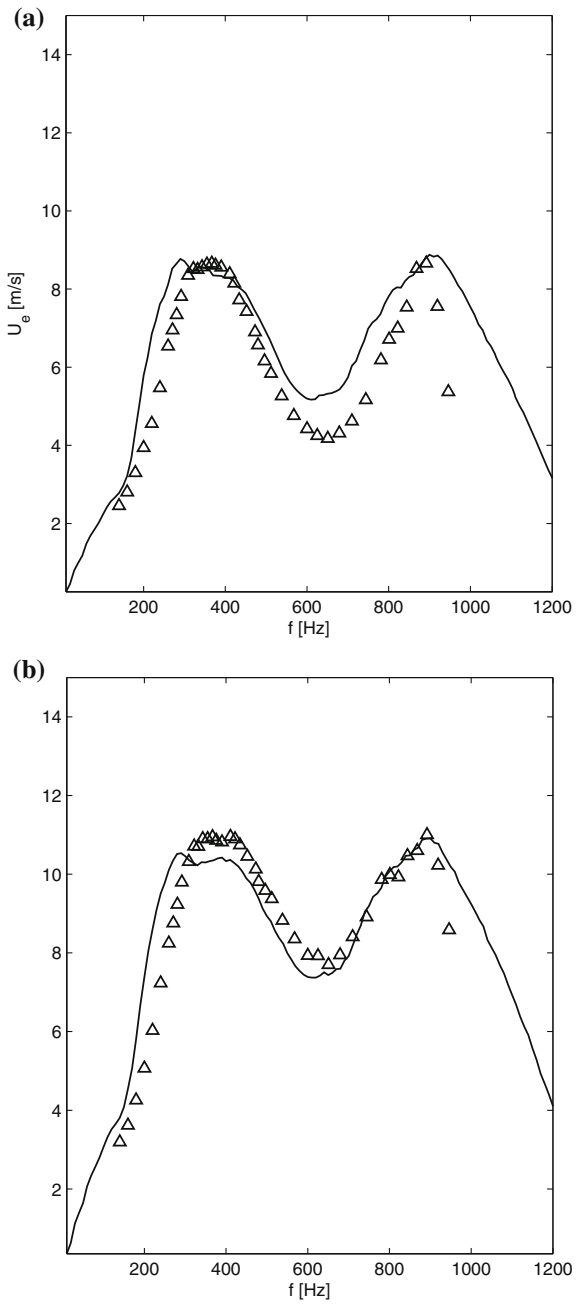

Fig. 4 Numerical-experimental comparison of average exit flow velocity frequency response for the aluminum 2 actuator ($\boldsymbol{H} = \mathbf{4}$ mm); *triangles* represent the experimental measures; *black curves* represent the numerical solution; **a** $\boldsymbol{V_a} = \mathbf{35}$ V, **b** $\boldsymbol{V_a} = \mathbf{50}$ V

Layout: T1 Standard Unicode | Book ID: 311437_1_En | Book ISBN: 978-3-319-09712-1
Chapter No.: 6 | Date: 9-10-2014 | Time: 7:06 pm | Page: 113/118

Data points of Figs. 2, 3 and 4 are compared to the corresponding numerical values obtained by integrating numerically the complete governing Eqs. (1–3). The numerical simulations have been carried out by means of a standard fourth order Runge-Kutta method in MATLAB environment with *ode45* routine. Initial conditions of $x_w = 0$, $\dot{x}_w = 0$, $p_i = 0$, and $U = 0$ have been assumed for all the computations; it has been observed that the quasi-steady oscillatory solution is generally reached in about 20–30 cycles. Typical values of the electroacoustic transduction coefficient ϕ_a that best fit the continuous numerical curves to the velocity measurements are 105, 133, 47.7 for brass, aluminum 1, aluminum 2 actuators, respectively.

Table 2 reports the resonance frequencies calculated numerically for each device at $V_a = 35$ V. This table should be compared to Table 3 showing analogous experimental findings in order to appreciate the data agreement. For the sake of convenience, data to be compared are reported in bold type in both tables. Data spread is generally less than 4 % except for the value of the modified structural frequency of aluminum 2 actuator, for which it appears to be about 26 %. However, it should be noted that computer simulations of Fig. 4 show a rather wide plateau around this peak frequency, whereas the the data spread of 26 % refers exactly to the peak value. For a more general comparison including analytical, numerical and experimental velocity results, one should glance at Tables 1, 2 and 3 simultaneously.

Table 2 Numerical resonance frequencies at $V_a = 35$ V

	H (mm)	Modified Helmholtz frequency (Hz)	Modified structural frequency (Hz)
Brass	3	**960**	**2,260**
	5	760	2,210
Aluminum 1	3	**770**	**1,630**
	8	490	1,480
Aluminum 2	4	**900**	**290**
	7	690	320
	11	570	330

Table 3 Experimental resonance frequencies from Pitot tube

	V_a (V)	Modified Helmholtz frequency (Hz)	Modified structural frequency (Hz)
Brass (H = 3 mm)	35	**976**	**2,232**
	70	1,042	2,232
Aluminum 1 (H = 3 mm)	25	781	1,645
	35	**801**	**1,645**
Aluminum 2 (H = 4 mm)	35	**892**	**367**
	50	892	367

Layout: T1 Standard Unicode | Book ID: 311437_1_En | Book ISBN: 978-3-319-09712-1
Chapter No.: 6 | Date: 9-10-2014 | Time: 7:06 pm | Page: 114/118

4.2 Effect of Strouhal Number

The effect of the Strouhal number can be appreciated by focusing the attention on particular operating conditions; for a given device, in particular, the conditions of $St \ll 1$ and $St \gg 1$, that are achieved for relatively low and high values of operation frequency, respectively, will be analyzed hereafter. Of course, one has to keep in mind that more in general the conditions of $St \ll 1$ and $St \gg 1$ correspond to situations of acoustically thin and thick resonant cavity, respectively, as before observed. This effect will be analyzed numerically with particular reference to the frequency response in terms of exit velocity of the three devices mentioned in the previous sections.

The maximum jet-flow exit velocity trends as functions of the operation frequency are depicted in Figs. 5, 6 and 7 for the three tested devices and for various dimensionless cavity heights H/d_o. The supply voltage V_a is equal to 35 V in all these simulations.

For all the devices two velocity peaks corresponding to the two resonance frequencies are clearly evident. For the brass device both the velocity peaks increase with decreasing the cavity height, whilst for the aluminum 1 one the trend is that the velocity peak of the structural resonance reaches a plateau for intermediate values of H/d_o and then it decreases at the largest height. For the brass actuator the distance between the two resonance frequencies slightly increases with increasing H/d_o, in agreement with experimental results of Gomes et al. [16] obtained for $l_o/d_o > 1$, while for the aluminum 1 such a distance slightly decreases.

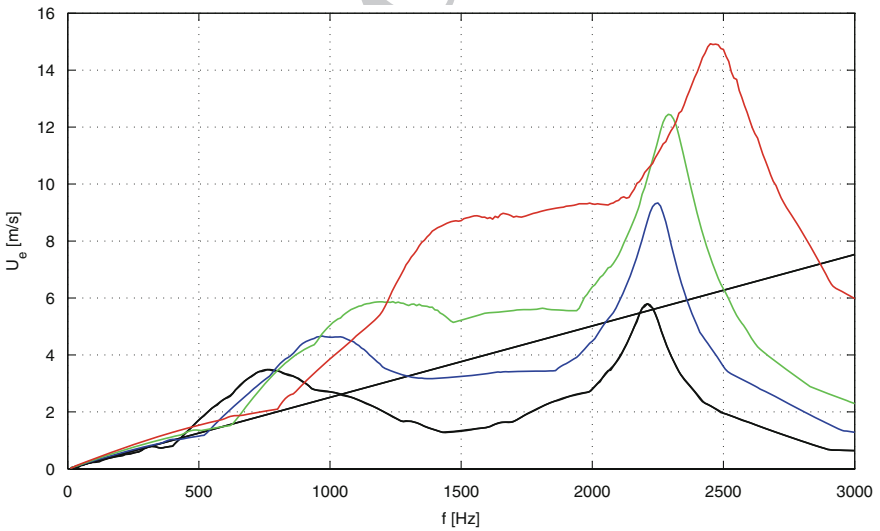

Fig. 5 Frequency response of average exit flow velocity for the brass actuator at $V_a = 35$ V; *red line* is for $H/d_o = 0.5$, *green* $H/d_o = 1$, *blue* $H/d_o = 1.5$, *black* $H/d_o = 2.5$. The *straight line* refers to Eq. (14)

Layout: T1 Standard Unicode | Book ID: 311437_1_En | Book ISBN: 978-3-319-09712-1
Chapter No.: 6 | Date: 9-10-2014 | Time: 7:06 pm | Page: 115/118

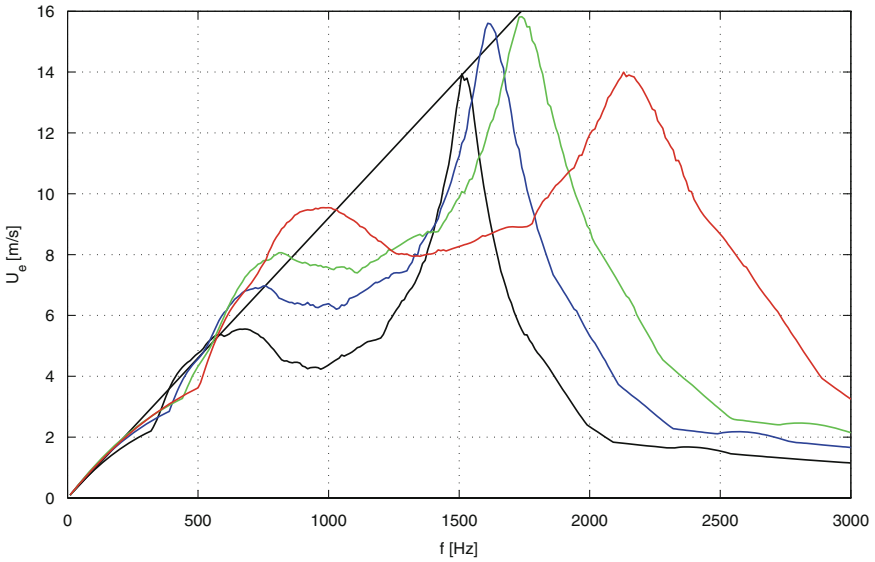

Fig. 6 Frequency response of average exit flow velocity for the aluminum 1 actuator at $V_a = 35$ V; *red line* is for $H/d_o = 0.5$, *green* $H/d_o = 1$, *blue* $H/d_o = 1.5$, *black* $H/d_o = 2.5$. The *straight line* refers to Eq. (14)

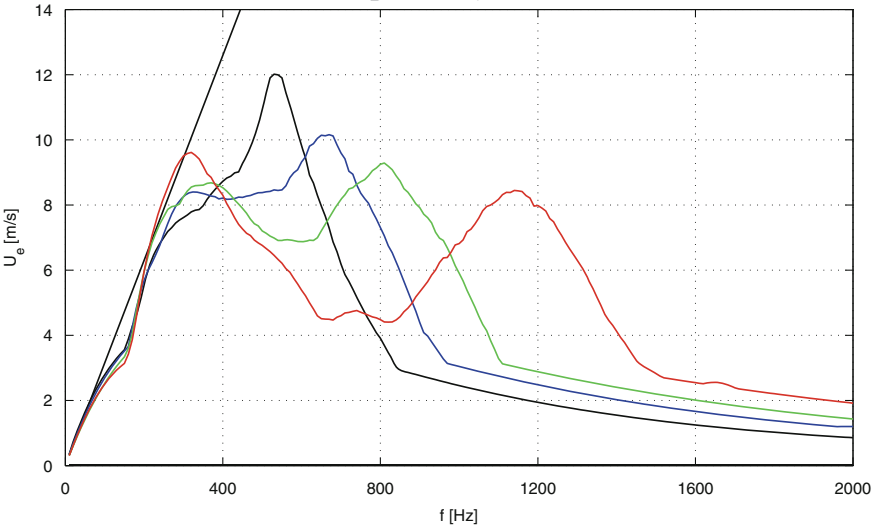

Fig. 7 Frequency response of average exit flow velocity for the aluminum 2 actuator at $V_a = 35$ V; *red line* is for $H/d_o = 0.5$, *green* $H/d_o = 1$, *blue* $H/d_o = 1.5$, *black* $H/d_o = 2.5$. The *straight line* refers to Eq. (14)

Layout: T1 Standard Unicode | Book ID: 311437_1_En | Book ISBN: 978-3-319-09712-1
Chapter No.: 6 | Date: 9-10-2014 Time: 7:06 pm | Page: 116/118

Note that the experimental findings of Gomes et al. [16] show also that the resonance frequencies distance becomes practically constant as H/d_o further increases, in agreement with the analytical prediction of de Luca et al. [5] valid in the case of $\omega_w \gg \omega_h$.

The straight lines present in the plots of Figs. 5, 6 and 7 refer to the linear dependance of the jet velocity upon the operating frequency given by the incompressible model described by the Eq. (14). For the brass and the aluminum 1 and 2 actuators it is clearly evident that such a simplified model closely agrees with the simulations of the complete model at low frequencies, the frequencies range of such an agreement widening for the smaller cavity heights, as predicted by the theory for $St \ll 1$. Note also that for this range of frequencies the response in terms of jet velocity is the same whatever is the cavity height, thus confirming that the membrane dynamics is decoupled from the acoustic oscillator one. These figures show that the uncoupled behavior is recovered also for relatively high frequencies, i.e. $St \gg 1$, where the expected response is of vanishing U_e, anticipated at lower frequencies for the highest cavity heights.

In order to complete the discussion about the behavior of the aluminum 2 device, note that the two nominal Helmholtz and structural frequencies, which for this actuator are reversed, are remarkably modified by the high coupling ratio. The jet velocity decreases with increasing the cavity height at the structural resonance frequency, whereas it increases with increasing H/d_o at the Helmholtz resonance frequency, with the result that the maximum peak is reached at the Helmholtz frequency for the highest simulated cavity height. This particular finding agrees with the theoretical prediction of de Luca et al. [5] that if $\omega_w \ll \omega_h$ then the distance between the two eigenvalues $|\omega_1^2 - \omega_2^2|/\omega_h^2$ does not depends on the cavity height H/d_o and therefore $|\omega_1^2 - \omega_2^2| \simeq 1/(H/d_o)$. The quasi-coincidence of the two resonance frequencies justifies that the maximum peak is reached for the highest cavity height.

5 Conclusions

Basic properties of resonant cavities driven by piezo-electric thin elements, typically employed in order to produce the so-called synthetic jets, have been analyzed by means of a lumped-element physical model. The model is fluid-dynamics based and, although his genesis is inspired by an analogous model of previous literature, it is innovative because it needs in input just electro-mechanical properties easily available from commercial data sheet of the materials. The synthetic jet devices are usually employed to control fluid flows. They are also used to cool locally reduced-size surfaces, as well as to enhance the mixing between fluid currents.

In these frameworks, the proposed model represents a practical tool for the overall design of the actuator. This has been idealized as an acoustic-mechanical system of two-coupled oscillators, the membrane one (i.e., the structural element)

Layout: T1 Standard Unicode | Book ID: 311437_1_En | Book ISBN: 978-3-319-09712-1
Chapter No.: 6 | Date: 9-10-2014 Time: 7:06 pm | Page: 117/118

and the Helmholtz's one (i.e., the acoustic one). Simplified, but rather accurate relationships have been given in order to predict the two modified (coupled) resonance frequencies, as a function of the decoupled natural frequencies of the two basic oscillators. The analytical investigation has been completed through an inspection of the dimensionless form of the governing equations, which introduce two characteristic parameters: the frequencies coupling factor and the Strouhal number. The study showed that the acoustic oscillator is always driven by the membrane dynamics, while there are conditions under which the membrane behavior is decoupled from the Helmholtz oscillator.

The fully nonlinear governing equations have been integrated numerically in MATLAB environment. In order to validate the computer code, various experimental campaigns have been carried out on three different actuators especially designed and manufactured to the purpose of obtaining an increasing coupling factor. In this paper, the comparison of the frequency response predicted numerically against experimental findings has been presented with reference in particular to the external jet velocity.

The theoretical and experimental results show that when the coupling factor is very small the two oscillators are decoupled, in the sense that the two modified resonance frequencies tend to the corresponding nominal values, yielded by simplified but accurate relationships.

The case of $St \ll 1$ is very interesting too. It physically corresponds to acoustically thin cavity and, for a given device, occurs at relatively low operating frequencies. In this decoupled regime it has also been found that the behavior of the actuator is well described by the so called incompressible model, where the air volume rate entering the cavity as a consequence of the membrane displacement equals the air volume rate leaving the cavity through the orifice.

A detailed numerical investigation about the influence of the cavity height has been also carried out. An interesting but perhaps not expected result is that for the device exhibiting the strongest coupling the jet velocity peak occurs for the highest investigated cavity.

Acknowledgments This work has been funded by Compagnia di S. Paolo and Polo delle Scienze e delle Tecnologie of Universita' degli Studi di Napoli Federico II, within the F.A.R.O. projects 2009 and 2012.

References

1. A. Glezer, M. Amitay, Synthetic jets. Annu. Rev. Fluid Mech. **34**, 503–529 (2002). doi:10.1146/annurev.fluid.34.090501.094913
2. L.N. Cattafesta III, M. Sheplak, Actuators for active flow control. Annu. Rev. Fluid Mech. **43**, 247–272 (2011). doi:10.1146/annurev-fluid-122109-160634
3. L. Mongibello, G. Rocco, G. Coppola, L. de Luca, Numerical investigation of two adjacent synthetic jets for flow control, in *2nd European Conference for Aero-Space Sciences (EUCASS),* Brussels, CD proceedings, paper 02-06-08

Layout: T1 Standard Unicode | Book ID: 311437_1_En | Book ISBN: 978-3-319-09712-1
Chapter No.: 6 | Date: 9-10-2014 | Time: 7:06 pm | Page: 118/118

4. G. Monaco, L. Mongibello, L. de Luca, Impingement heat transfer by means of synthetic jets, in *Proceedings of ASME-ATI-UIT 2010 Conference on Thermal and Environmental Issues in Energy Systems, Edizioni ETS, PISA*, vol. II, Sorrento, 16–19 May 2010, pp. 1413–1417. ISBN 978-884672659-9
5. L. de Luca, M. Girfoglio, G. Coppola, Modeling and experimental validation of the frequency response of synthetic jet actuators. AIAA J. (in press, 2014). doi:10.2514/1.J052674 AQ2
6. S.A.N. Prasad, Two-port electroacoustic model of piezoelectric composite circular plate, M.S. thesis, Department of Aerospace Engineering, Mechanics, and Engineering Sciences, University of Florida, Gainesville, 2002, pp. 1–166
7. S.A.N. Prasad, Q. Gallas, S. Horowitz, B. Homeijer, B.V. Sankar, L.N. Cattafesta, M. Sheplak, Analytical electroacoustic model of a piezoelectric composite circular plate. AIAA J. **44**(10), 2311–2318 (2006). doi:10.2514/1.19855
8. Q. Gallas, R. Holman, T. Nishida, B. Carroll, M. Sheplak, L. Cattafesta, Lumped element modeling of piezoelectric-driven synthetic jet actuators. AIAA J. **41**(2), 240–247 (2003). doi:10.2514/2.1936
9. R.N. Sharma, Fluid dynamics based analytical model for synthetic jet actuation. AIAA J. **45** (8), 1841–1847 (2007). doi:10.2514/1.25427
10. M. Chaudhari, G. Verma, B. Puranik, A. Agrawal, Frequency response of a synthetic jet cavity. Exp. Thermal Fluid Sci. **33**, 439–448 (2009). doi:10.1016/j.expthermflusci.2008.10.008
11. G. Krishnan, K. Mohseni, Axisymmetric synthetic jets: an experimental and theoretical examination. AIAA J. **47**(10), 2273–2283 (2009). doi:10.2514/1.42967
12. C. Seeley, Y. Utturkar, M. Arik, T. Icoz, Fluid-structure interaction model for low-frequency synthetic jets. AIAA J. **49**(2), 316–323 (2011). doi:10.2514/1.53408
13. T. Persoons, General reduced-order model to design and operate synthetic jet Actuators. AIAA J. **50**(4), 916–927 (2012). doi:10.2514/1.J051381
14. B.L. Smith, A. Glezer, The formation and evolution of synthetic jets. Phys. Fluids **10**(9), 2281–2297 (1998)
15. B.L. Smith, G.W. Swift, A comparison between synthetic jets and continuous jets. Exp. Fluids **34**(4), 467–472 (2003). doi:10.1007/800348-002-0577-6
16. L.D. Gomes, W.J. Crowther, N.J. Wood, Towards a practical piezoceramic diaphragm based synthetic jet actuator for high subsonic applications—effect of chamber and orifice depth on actuator peak velocity, in *3rd AIAA Flow Control Conference,* 5–8 June 2006, San Francisco, AIAA paper 2006–2859
17. L.E. Kinsler, A.R. Frey, A.B. Coppens, J.V. Sanders, *Fundamentals of acoustics*, 4th edn. (Wiley, New York, 2000), pp. 107–108 AQ3
18. R. Rathnasingham, K.S. Breuer, Coupled fluid-structural characteristics of actuators for flow control. AIAA J. **35**(5), 832–837 (1997). doi:10.2514/2.7454
19. R. Raju, Q. Gallas, R. Mittal, L. Cattafesta, Scaling of pressure drop for oscillatory flow through a slot. Phys. Fluids **19**(7) 2007. doi: 10.1063/1.2749814 (paper 078107)
20. G. Kooijman, O. Ouweltjes, Finite difference time domain electroacoustic model for synthetic jet actuators including nonlinear flow resistance. J. Acoust. Soc. Am. **125**(4), 1911–1918 (2009). doi:10.1121/1.3081514

Modelling of efficiency of synthetic jet actuators

Michele Girfoglio, Carlo Salvatore Greco, Luigi de Luca[a,b,c]

[a] *PhD student, Department of Industrial Engineering, Aerospace sect., Università di Napoli Federico II, Italy.*
[b] *PhD student, Department of Industrial Engineering, Aerospace sect., Università di Napoli Federico II, Italy.*
[c] *Professor, Department of Industrial Engineering, Aerospace sect., Università di Napoli Federico II, Italy.*

Abstract

A comprehensive and detailed modelling to evaluate the efficiency of energy conversion of piezo-electric actuators driving synthetic jets is developed. The contribution is original because the analysis is based on the energy equations of the two coupled oscillators, the membrane and the acoustic one, which are directly derived from the corresponding motion equations. The modelling is validated against numerical as well as experimental investigations carried out on a home-made actuator having an aluminum shim on which the piezo-disk is bonded. A major result is that for the actuator under investigation the global efficiency (representing the conversion of input Joule power to kinetic power) decreases with increasing the applied voltage. Considerations are reported to relate the theoretical orifice efficiency to the practical jet efficiency issuing in the external field.

Keywords:
efficiency, synthetic jet, piezo-electric

1. Introduction

Continuous and pulsed jets are nowadays quite largely used as devices for flow control (e.g., Glezer and Amitay [1], Cattafesta and Sheplak [2]) and heat transfer applications (e.g., Chaudhari et al. [3], Valiorgue et al. [4], Greco et al. [5]). The continuous request for a size reduction of such systems has led researchers to focus their efforts on the design of new technology devices. Synthetic jet actuators well fit this need because they produce jets with zero-net mass flux synthesized directly from the fluid system in which

the device itself is embedded (Smith and Glezer [6]), avoiding the need for an external input piping and making them ideal for reduced-space and low-weight applications. A synthetic jet is generated by a membrane oscillation (generally driven by a piezo-ceramic element) in a relatively small cavity, which produces a periodic cavity volume change and thus pressure variation. As the membrane oscillates, fluid is periodically entrained into- and expelled out from an orifice connecting the cavity with the external ambient (to be controlled). During the expulsion phase of the cycle, due to the flow separation, a vortex ring forms near the orifice exit section which, under favorable operating conditions (Holman et al. [7]), convects away towards the far field and breaks up due to the viscous dissipation eventually "synthesizing" a turbulent jet always directed downstream (Smith and Glezer [6]).

Since the jet formation depends on the ability of the vortex ring to escape to the subsequent ingestion phase, following Smith and Glezer [6], a basic parameter characterizing the jet strength is the so called stroke length $\bar{L}$, namely the integral of the (spatially averaged) velocity at the orifice exit over the ejection phase only of the cycle:

$$\bar{L} = \int_0^{T/2} U(t)dt \tag{1}$$

where T is the actuation period and $U(t)$ is the fluid velocity at the exit section. The stroke length can also be expressed conveniently as the product $\bar{L} = \bar{U}T$, where $\bar{U}$ is a proper reference velocity defined as:

$$\bar{U} = \frac{\int_0^{T/2} U(t)dt}{T} \tag{2}$$

Therefore, it is natural to expect that the jet is formed or not according to whether the parameter $\bar{L}/d_o$ is greater or less than 0.16π, with d_o being the orifice diameter. In the literature the parameter $\bar{L}/d_o$ is generally referred to as the reciprocal of the Strouhal number (Cater and Soria [8]).

The importance of the stroke length, or of the average velocity $\bar{U}$, lies in the fact that to compare the performance of a synthetic jet with that of a continuous jet, it is usual to refer to a Reynolds number based on the velocity $\bar{U}$, i.e.:

$$Re = \frac{\rho \bar{U} d_o}{\mu} \tag{3}$$

where ρ is air density, μ is air dynamic viscosity.

Although such a topic has been so widely explored only few studies on the synthetic jet efficiency have been carried out. One of the first works on the efficiency of synthetic jet was undertaken by Tesar and Zhong [9] who based their definition of efficiency on the capability of jet generation rather than on energy conversion considerations. They found experimentally a constant efficiency value equal to 7.2% for several values of Reynolds number (ranging from 4000 to 8000) and for two values of dimensionless stroke length $\overline{L}/d_o$ (equal to 223.9 and 527.8). They also compared their experimental evaluation with a numerical prediction made by using the commercial code FLUENT, and found that this last is twice the experimental one.

Subsequently Crowther and Gomes [10] studied the system costs associated with the application of flow control system to civil transport aircraft based on the use of electrically powered synthetic jet actuators. They defined the efficiency of the actuator as fluid power (scaling with the cube of the exit velocity) divided by absorbed electrical power, and analyzed it as a function of the operating conditions and actuator geometry, which were chosen reasonably close to those expected for industrial applications. For this reason the experiments were carried out basically with a chamber depth to orifice diameter ratio equal to 0.56 and an orifice depth to diameter ratio equal to 2.1. By resorting to the energy balance principle, Crowther and Gomes [10] considered that the difference between the supplied electrical power and the gained fluid power was lost because of electrical impedance (ascribed to the piezo-electric actuator), mechanical impedance (related to the diaphragm dynamics) and acoustic impedance (due to the fluid-acoustic coupling of the flow within the cavity and though the orifice), however without accurately quantifying each term of the balance. They showed their experimental findings in terms of a map of the electric-fluidic conversion efficiency, where such an efficiency was reported as a function of excitation voltage amplitude (for peak-to-peak excitation voltage up to 250V) and actuation frequency (up to 4000Hz). They found that the efficiency attains a maximum equal to about 14% and noted that it did not correspond to the condition of maximum exit velocity because of the dielectric saturation effect affecting the commercial piezo-electric patch (i.e., the piezo-element bonded to the brass shim).

A more recent work, focusing specifically on the energy conversion efficiency of synthetic jets devices, was presented by Li et al. [11] who tried to express on an analytical basis every term contributing to the energy rate balance. They argued that once the synthetic jet has received electric en-

ergy input, due to the capacitance of the piezo-electric actuator, a part of the energy is stored as electric potential energy while the rest of the energy is converted to mechanical energy accompanied by energy dissipation. The mechanical energy includes vibration of piezo-electric actuators and kinetic energy of air flow. For piezo-electric actuators two forms of energy, i.e. strain energy and kinetic energy, are temporarily stored by the vibrating structure. Energy dissipation (namely energy loss) occurs in piezo-electric actuators due to the deflection dynamics, as well as in the air flow motion (i.e., the head losses) when traversing the jet orifice. The synthetic jet device efficiency is defined as the ratio of the kinetic power of the air flow to the input electric energy. The authors carried out experiments on two slot synthetic jets having orifice length of 4mm and 15mm, for two values of voltage amplitude (80V and 100V) and actuation frequency ranging from 200Hz to 1100Hz. Li et al. [11] found that the efficiency of energy conversion is dependent on the orifice size and on the operating conditions (namely, voltage and frequency) showing a peak (of about 40% for the 15mm orifice) close to the mechanical resonance frequency of the actuator. They claim that the uncertainty of their experimental evaluation was of about 34%.

The aim of the present paper is to assess a rigorous and comprehensive physical approach to the evaluation of the efficiency of piezo-electrically driven synthetic jet actuators, based on a rather detailed modelling of the actuator dynamics, already developed by two of the authors, de Luca et al. [12], in the past. The peculiarity of the present approach is that the energy balance equation, properly averaged over the actuation period, is derived directly from the equations governing the dynamics of the actuator. The advantage is that the presence of each term of the resulting energy balance draws its justification from the corresponding dynamics term and, in principle, there is no need to perform experimental measurements to evaluate the actuator efficiency at the orifice exit section. Since the physical model mentioned above has been already tested and calibrated against a systematic experimental campaign, the uncertainty of the efficiency estimation should be reduced.

The paper is organized as follows: section 2 reports the basic equations governing the dynamics of the actuator, whilst section 3 is devoted to the development of the energy balance, directly derived from the dynamics equations. The experimental validation and calibration of the proposed model are discussed in section 4, and, finally, conclusions are drawn in section 5.

2. Governing equations system

In this section a short description of the motion equations governing the dynamics of a typical piezo-electrically driven synthetic jet actuator will be given. Details regarding the physical modelling can be found in the original paper of de Luca et al. [12]. It should be pointed out that the approach followed by the present authors is fluid-dynamics based, and was inspired by the previous original paper of Sharma [13].

The membrane behavior is modelled as a one-degree of freedom forced mass-spring-damper system

$$m_{wt}\ddot{x}_w + c_{wt}\dot{x}_w + k_w x_w = F - p_i A_w \tag{4}$$

where m_{wt} is the diaphragm total mass (including shim, piezo-element and air added mass), x_w is the membrane displacement at a generic time instant t, c_{wt} is the total damping coefficient (including the structural damping coefficient and a further damping coefficient due to the interaction with the external air), k_w is the equivalent stiffness of the membrane, F is the electrodynamic force, p_i is the cavity (internal) differential pressure, A_w is the membrane area.

The electrodynamic force F is related to the piezo-electric effect due to the applied sine voltage and is given by

$$F = F_0 \sin \omega t = \frac{k_w d_A V_a}{A_w} \sin \omega t = k_w \Delta x_w \sin \omega t \tag{5}$$

where F_0 is the forcing magnitude, d_A is the effective acoustic piezo-electric coefficient, V_a is the voltage amplitude, $\omega = 2\pi f$ is the operating angular frequency (with f being the natural frequency, $f = 1/T$) and Δx_w is the (average) linear "static" displacement of the membrane due to the piezo-electric effect.

The application of the unsteady Bernoulli's equation between a point inside the cavity where the flow velocity is practically null and a point, just outside the cavity, representing the location where the pressure matches the unperturbed external ambient value, yields

$$M_a \frac{dU}{dt} = p_i A_o - \frac{1}{2} K \rho_a A_o U|U| \tag{6}$$

in which A_o is the orifice area, K is the head loss coefficient, ρ_a is the air density, $M_a = \rho_a l_e A_o$ is the mass of air oscillating inside the orifice (Helmholtz

oscillator), with l_e being the effective length of the orifice (i.e., the distance between the two locations of application of the Bernoulli's equation) and U being is the instantaneous orifice jet-flow velocity, as already defined in section 1.

The equation of evolution of the third unknown, the cavity pressure p_i, is obtained by enforcing the conservation of air mass in the cavity; by relating the density and pressure variations by means of an isentropic compression/expansion transformation, the continuity equation can be formulated in the following way

$$\frac{V_c}{\gamma p_0}\frac{dp_i}{dt} = A_w\dot{x}_w - A_oU \tag{7}$$

where V_c is the cavity volume, p_0 is the ambient pressure, γ is the specific heat ratio.

3. Derivation of the energy balance equation and definition of efficiency

Multiplying the equation (4) by the membrane velocity $\dot{x}_w$, yields:

$$\frac{dE_w}{dt} = F\dot{x}_w - p_iA_w\dot{x}_w - c_w\dot{x}_w^2 \tag{8}$$

where E_w is the diaphragm energy defined as

$$E_w = \frac{1}{2}m_w\dot{x}_w^2 + \frac{1}{2}k_w{x_w}^2 \tag{9}$$

that takes into account both kinetic and elastic strain contributions.

Similarly, the product between the equation (6) and the jet exit velocity U yields

$$\frac{dE_o}{dt} = p_iA_oU - \frac{1}{2}K\rho_aA_o|U|^3 \tag{10}$$

where E_o is given by

$$E_o = \frac{1}{2}M_aU^2 \tag{11}$$

and represents the kinetic energy flow rate of the air mass through the orifice.

The (instantaneous) energy balance equation of the actuator system can be obtained by summing the equations (8) and (10). Moreover, since we are interested in characterizing the actuator behavior over an operating cycle, it

is convenient to apply the time average operator on the resulting equation, defined as

$$\bar{\varphi} = \frac{1}{T}\int_0^T \varphi dt \tag{12}$$

where φ is the generic time-dependent variable.

The energy balance equation averaged over an actuation cycle (i.e., over a time equal to the period T) is given by

$$\underbrace{\frac{1}{T}\int_0^T d(E_w + E_o)}_{\overline{\Delta E}} = \underbrace{\frac{1}{T}\int_0^T F\dot{x}_w dt}_{\bar{P}_e} + \underbrace{\frac{1}{T}\int_0^T p_i(A_o U - A_w \dot{x}_w)dt}_{\bar{P}_m}$$
$$- \underbrace{\frac{1}{T}\int_0^T c_{wt}\dot{x}_w^2 dt}_{\bar{D}_s} - \underbrace{\frac{1}{T}\int_0^T \frac{1}{2}(K-1)\rho_a A_o |U|^3 dt}_{\bar{D}_f} - \underbrace{\frac{1}{T}\int_0^T \frac{1}{2}\rho_a A_0 |U|^3 dt}_{\bar{P}_k} \tag{13}$$

An accurate description of the various contributions of equation (13) is reported hereafter:

- $\overline{\Delta E}$ is the total energy variation. Note that this term is null because, for each cycle, there is no change for E_w and E_o.
- $\bar{P}_e$ is the electrodynamic power provided to the membrane by the applied voltage.
- $\bar{P_m}$ is the mechanical power due to the work done by the differential pressure p_i which acts on the wall surface A_w and on the orifice surface A_o. By using the equation (7), it can be shown that this term is proportional to $\frac{1}{2}({p_i}^2(T) - {p_i}^2(0))$ and, therefore, it does not give any contribution because p_i assumes the same value at the beginning and end of each cycle. One can reach the same result by observing that the pressure work is conservative by definition.
- $\bar{D}_s$ is the power dissipation due to the structural damping effects of the membrane.
- $\bar{D}_f$ is the power dissipation due to the head loss of fluid dynamics type at the orifice.

- $\bar{P}_k$ is the kinetic power of air flow at the orifice. Note explicitly that the kinetic power here refers by definition to the entire cycle, i.e. the suction phase included. We will continue this discussion in the last section 4.

Then, by deleting $\overline{\Delta E}$ and $\bar{P_m}$ terms, the equation (13) becomes

$$\bar{P}_e - \bar{D}_s - \bar{D}_f - \bar{P}_k = 0 \tag{14}$$

and, once defined the kinetic efficiency η_c as the ratio of the kinetic power of the exit flow $\bar{P}_k$ to the electrodynamic power $\bar{P}_e$, one obtains

$$\eta_k = \frac{\bar{P}_k}{\bar{P}_e} = 1 - \frac{\bar{D}_s + \bar{D}_f}{\bar{P}_e} \tag{15}$$

It is worthwhile to stress that in practice the global efficiency of an actuator has to quantify the amount of Joule power provided to the system $\bar{P}_j$ that is actually converted in $\bar{P}_e$. This can be done by introducing the electrodynamic transduction efficiency η_e

$$\eta_e = \frac{\bar{P}_e}{\bar{P}_j} \tag{16}$$

Hence, finally, one can define the (global) efficiency of the actuator η as the product of η_k by η_e

$$\eta = \eta_k \eta_e = \frac{\bar{P}_k}{\bar{P}_j} \tag{17}$$

where the external Joule power supply $\bar{P}_j$ provided to the actuator is calculated as

$$\bar{P}_j = \frac{1}{T} \int_0^T V I dt \tag{18}$$

with $V = V_a \sin \omega t$ being the applied voltage and I the electric current flowing through the piezo-electric element.

The rate of $\bar{P}_j$ not turned into $\bar{P}_e$ is converted into a variation of internal energy $\dot{Q}$ of the air inside the cavity (heat generation per unit time), which is transferred in part to the external ambient through a natural convection mechanism, and, in part, into enthalpy flow rate of the air leaving the orifice

$$\bar{P}_j - \bar{P}_e = \dot{Q} \equiv h A_e \Delta T + \dot{m} c_p \Delta T \tag{19}$$

where h is the convective heat transfer coefficient by natural convection, A_e is the exchange surface (which depends on the relevant geometry of actuator), ΔT is the average-per-cycle temperature difference between the system and the colder surrounding external air, $\dot{m} = \rho_a \bar{U} A_o$ and we remember that $\bar{U}$ is the average velocity associated to the stroke length (eq. 2), and c_p is the specific heat coefficient at constant pressure. For the sake of simplicity we assumed that the air inside the cavity is isothermal with the device case.

From equation (19) one obtains also

$$\eta_e = 1 - \frac{\dot{Q}}{\bar{P}_j} \tag{20}$$

4. Validation of the model and results

For fixed values of the geometrical and electro-mechanical parameters of a typical synthetic jet actuator, the modeling developed before has been employed to estimate the various contributions of the energy budget equations (13, 14) by carrying out direct numerical simulations of the governing equations (4, 6, 7). For a proper operating frequency f, the time trends of the relevant quantities, in practice the membrane velocity and the air velocity at the orifice exit, have been used to evaluate, ultimately, the energy conversion efficiencies (15, 16, 17). Numerical integration has been performed by means of a standard 4th order Runge-Kutta method in MATLAB environment with *ode45* routine. Initial conditions of $x_w = 0$, $\dot{x}_w = 0$, $p_i = 0$, and $U = 0$ have been assumed for all the computations and it has been observed that the quasi-steady oscillatory solution is generally reached in about 20 cycles (de Luca et al. [12]). The time averages here performed refer typically to the 23^{th} cycle.

The uncertainty errors of the numerical data have been evaluated especially with respect to variations of the values of the head loss coefficient as well as of the effective orifice length (de Luca et al. [12]). For K varying in the range $1 < K < 1.46$ the variations of the resonance frequencies are restricted within a maximum of 2%, while the corresponding variations of the air velocity peaks are generally of the order of 10%. The uncertainty of data of l_e is reflected on the peak frequencies which vary within a corresponding uncertainty band of 5% which may grow up to a maximum of 10% for relatively low frequencies, while the average width of such a band is of 10% for the peak exit velocities.

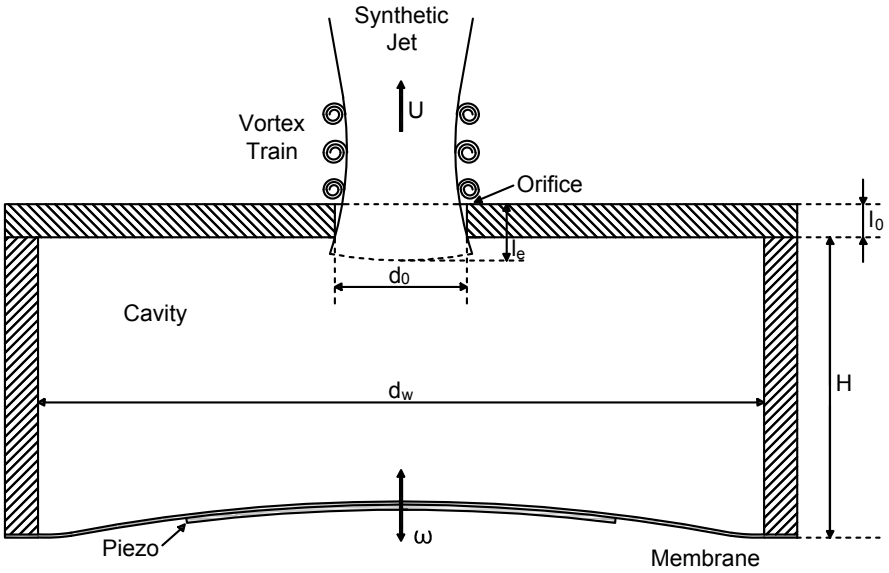

Figure 1: Modular structure of the actuator (de Luca et al. [12])

To validate the modeling, numerical values of efficiency have been compared with measured data for a typical synthetic jet actuator, the characteristics of which are summarized in Table 1. The membrane was built in-house by gluing a LZT piezo-ceramic disk (manufactured by PIEZO System inc.) on a thin aluminum foil. The schematic of the device is also shown in Fig. 1 highlighting its modular structure, which permits independent variations of cavity diameter and height, orifice diameter, and piezo-electric diaphragm (de Luca et al. [12]). Here we adopted the value $K = 1.14$ for the head loss coefficient, while the effective length of the orifice l_e, was basically evaluated according to the description of Sharma [13], namely $l_e/d_0 = l_0/d_0 + \Delta l_e$, with Δl_e=0.71.

For a given operating voltage, the evaluation of the Joule power supply (equation (18)) needs the knowledge of the current intensity. This has been done by means of the theoretical relationship

$$I_t = 2\pi f C V_a \tag{21}$$

where I_t denotes the theoretical current intensity peak, and C is the electric capacitance of the piezo-ceramic disk (furnished by the manufacturer). To verify this estimation, the current intensity peak has been also measured directly by means of the experimental apparatus sketched in Fig. 2. A wave-

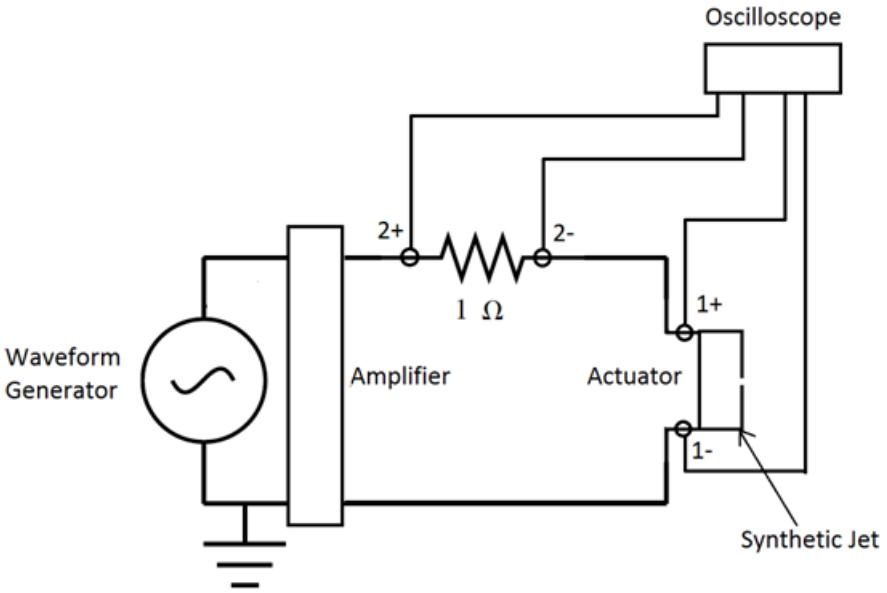

Figure 2: Sketch of the experimental setup.

Table 1: Features of the tested device

Property		
Geometry	Shim diameter (mm)	80
	Shim thickness (mm)	0.25
	Piezo-electric diameter (mm)	63.5
	Piezo-electric thickness (mm)	0.191
	Cavity diameter (mm)	80
	Cavity height (mm)	4
	Orifice diameter (mm)	5
	Orifice length (mm)	2
Shim	Young's Module (Pa)	$7.31 \text{x} 10^{10}$
	Poisson's Module	0.31
	Density (Kg/m^3)	2780
Piezo-electric	Young's Module (Pa)	$6.6 \text{x} 10^{10}$
	Poisson's Module	0.31
	Density (Kg/m^3)	7800
	Capacitance (nF)	265

form generator (Wavetek model 164) creates an electrical sinusoidal signal which is amplified (by EPA 104 PIEZO System inc. unit) and sent to the synthetic jet device. Voltage and current are acquired by a two channels oscilloscope (Tektronix tds 2024).

In Table 2, experimental measurements of the electric current peak I_e are compared to the corresponding theoretical values I_t. The data spread is generally less than 9% except for $V_a = 50V$, for which it appears to be about 13%.

The efficiency values computed for the tested device at the modified Helmholtz resonance frequency (which is of 900Hz, as reported by de Luca et al. [12]) are listed in Table 3, together with the two power dissipation terms. Here we limit to remember that the modified Helmholtz (circular) frequency, ω_{mh} can be estimated to a good approximation by the relationship:

$$\frac{\omega_{mh}^2}{\omega_w^2} = \frac{-(1 + \frac{\omega_{wc}^2}{\omega_w^2} + \frac{\omega_h^2}{\omega_w^2}) + \sqrt{(1 + \frac{\omega_{wc}^2}{\omega_w^2} + \frac{\omega_h^2}{\omega_w^2})^2 - 4\frac{\omega_h^2}{\omega_w^2}}}{2} \tag{22}$$

where the (first mode) structural frequency of the membrane is given by

Table 2: Comparison of theoretical current peak with measured data (Ampere)

$V_a(V)$	$I_t(A)$	$I_e(A)$
25	0.038	0.036
30	0.045	0.044
35	0.052	0.054
40	0.059	0.056
45	0.066	0.060
50	0.073	0.064
55	0.079	0.074
60	0.085	0.080
65	0.093	0.086
70	0.099	0.094
75	0.106	0.104

$$\omega_w = \sqrt{\frac{k_w}{m_{wt}}}, \tag{23}$$

the uncoupled Helmholtz frequency is

$$\omega_h = \sqrt{\frac{\gamma A_o^2 p_o / V_c}{\rho_a l_e A_o}} = \sqrt{\frac{k_a}{M_a}}, \tag{24}$$

and the coupling frequency is defined as

$$\omega_{wc} = \sqrt{\frac{\gamma A_w^2 p_o / V_c}{m_w}} = \sqrt{\frac{\gamma A_w p_o}{m_w H}} \tag{25}$$

which, following Sharma [13], may be interpreted as the frequency of the pneumatic spring made of the air enclosed within the cavity of volume V_c and of the diaphragm mass m_w. Note that the height of the cavity, H, is explicitly introduced.

As one can observe (Table 3), the influence of the driving voltage is rather weak for η_k, $\bar{D}_f/\bar{P}_e$ and $\bar{D}_s/\bar{P}_e$; conversely, η_e decreases with increasing V_a, thus determining the same trend for the global efficiency η. For the sake of completeness, to give the reader the possibility to check the calculations, the following additional parameters have been considered, according to the complete description of the actuator under examination made by de Luca et

Table 3: Efficiencies and dissipation terms at modified Helmholtz frequency

$V_a(V)$	$\eta_k(\%)$	$\eta_e(\%)$	$\eta(\%)$	$\bar{D}_f/\bar{P}_e(\%)$	$\bar{D}_s/\bar{P}_e(\%)$
25	79.6	90.7	72.2	11.1	9.3
30	79.8	85.4	68.1	11.2	8.7
35	79.5	79.6	63.3	11.1	8.7
40	79.3	74.8	59.3	11.1	8.8
45	80.2	69.6	55.8	11.2	7.9
50	79.6	66.8	53.2	11.1	8.1
55	81.3	64.2	52.2	11.4	7.8
60	81.7	59.1	48.3	11.4	7.2
65	80.8	58.8	47.5	11.3	7.8
70	79.7	54.6	43.5	11.2	7.7
75	80.8	51.5	44	11.3	7.8

al. [12]: $\rho_a = 1.205\ Kg/m^3$; $k_w = 9.48 \cdot 10^4\ N/m$; $d_A = 4.01 \cdot 10^{-9}\ m^3/V$; $c_{wt} = 2.75\ Ns/m$, evaluated at the frequency of 900Hz.

Hereafter we will show that the trends against voltage of the quantities shown in Table 3 are well fitted by simple power laws which, in turn, can be justified on the basis of scaling theoretical considerations.

From the numerical integration of the governing equations we found that the variations of exit kinetic power and electrodynamic power follow the following trends

$$\bar{P}_k \approx {V_a}^{1.8} \tag{26}$$

$$\bar{P}_e \approx {V_a}^{1.8} \tag{27}$$

as is depicted in Figs. 3 and 4, respectively, where circle symbols refer to computed data e continuous lines refer to the analytical relationships. Therefore, being η_k given by the ratio between two quantities both proportional to ${V_a}^{1.8}$, it does not depend on V_a. Since one expects that $\bar{D}_f$ has the same scaling law as $\bar{P}_k$, the fluid dynamic dissipation rate $\bar{D}_f/\bar{P}_e$ is constant too. Indeed, according to their definitions in equation (13), $\bar{P}_k$ and $\bar{D}_f$ vary as U_0^3 and $\bar{P}_e$ as $F_0\dot{x}_{w0}$ (with U_0 and $\dot{x}_{w0}$ being the fluid and membrane peak velocities, respectively), and therefore one could expect that they scale as V_a^3 and V_a^2, respectively. However, due to the complex coupling between the two oscillators, the membrane and the acoustic one, in the presence of significant non linear damping acting on the acoustic one, such theoretical laws are re-

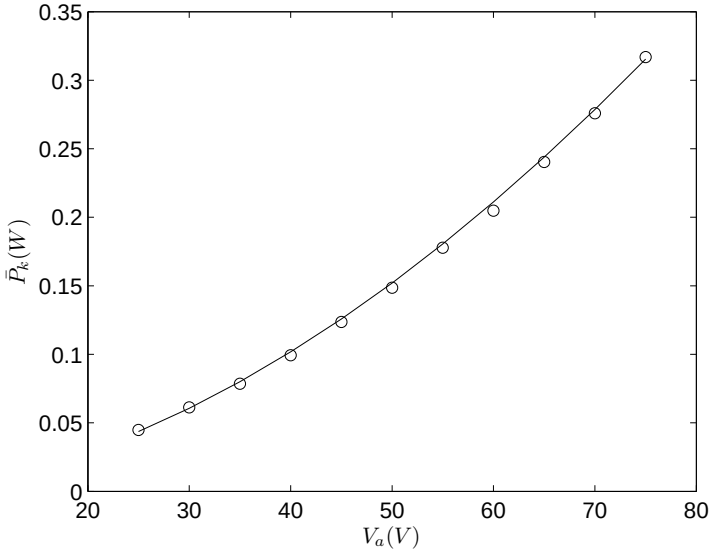

Figure 3: Kinetic power at orifice exit versus voltage. Circle symbols are computed data, continuous line represents eq. (26)

markably modified, as discussed in detail by de Luca et al. [12] and de Luca et al. [14]. Here we found that $U_0 \approx {V_a}^{0.6}$ and $\dot{x}_{w0} \approx {V_a}^{0.8}$. Since F_0 scales with V_a, the scaling relationships of equations (26) and (27) are justified.

Fig. 5 shows that the Joule power, evaluated experimentally, increases with increasing the voltage amplitude following a power law of the kind

$$\bar{P}_j \approx {V_a}^{2.3} \tag{28}$$

Note that if the behavior of the piezo-ceramic element was governed perfectly by the Ohm's law, i.e. if the capacitance was constant, $\bar{P}_j$ would be directly proportional to ${V_a}^2$. In effect, the relationship (28) tells us that the piezo-element capacitance varies as a function of the voltage and, furthermore, that the output instantaneous current is a distorted sine wave.

Finally, as depicted in Fig. 6, the behavior of the transduction coefficient η_e defined by equation (16) and relating the Joule power to the electrodynamic one, taking into account also the relationship (27), is well fitted by a power law of the following type

$$\eta_e \approx {V_a}^{-0.5} \tag{29}$$

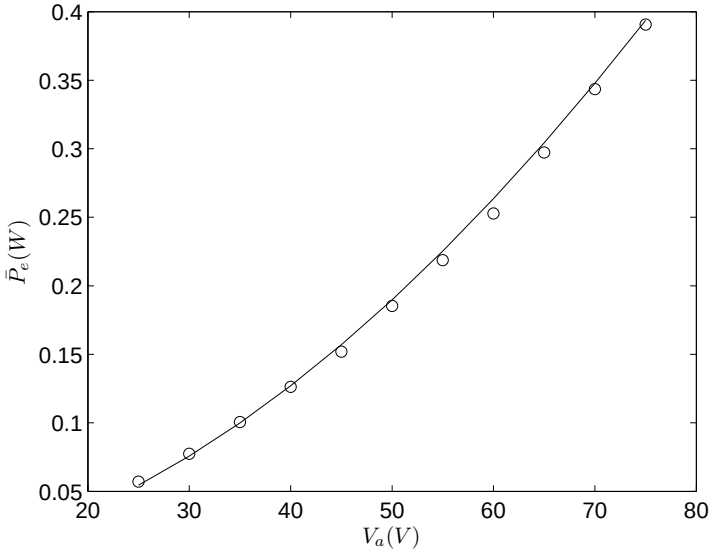

Figure 4: Electrodynamic power versus voltage. Circle symbols are computed data, continuous line represents eq. (27)

A similar trend holds for the global efficiency η (equation (17)).

Hereafter we will end this section with some practical remarks. Remember that the kinetic power defined by equation (13), and the related kinetic efficiency of equation (15), refer by definition to the entire cycle, i.e. the suction phase included. In effect, in some specific applications where, for instance, the final goal is to obtain a proper trust linked to the downstream momentum flux, or in heat transfer situations where the goal is to achieve a proper jet Reynolds number based on the stroke length velocity of equation (2), the kinetic power should be referred to the ejection phase only and evaluated just downstream of the so called saddle point, namely the stagnation point along the jet axis separating, during the suction phase, the ingestion near field and the ejection far field. Of course, an accurate evaluation of the time variation of the jet velocity at the saddle point could be made by proper measurements (e.g., by means of PIV techniques) or by detailed CFD computations. However, according to the experimental findings of Smith and Glezer [6], one can admit that the jet velocity peak is about the same as the air velocity peak at the orifice; thus, under the assumption of sine temporal variation of the jet velocity just downstream of the saddle point during the

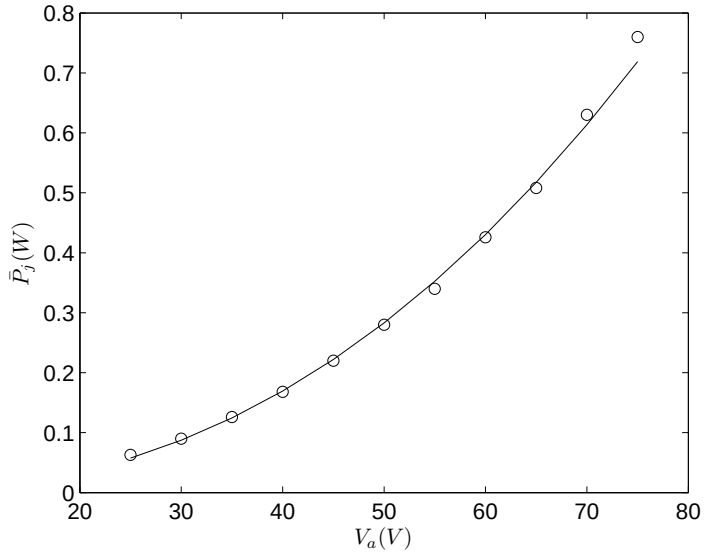

Figure 5: Measured Joule power versus voltage. Circle symbols are experimental data, continuous line represents eq. (28)

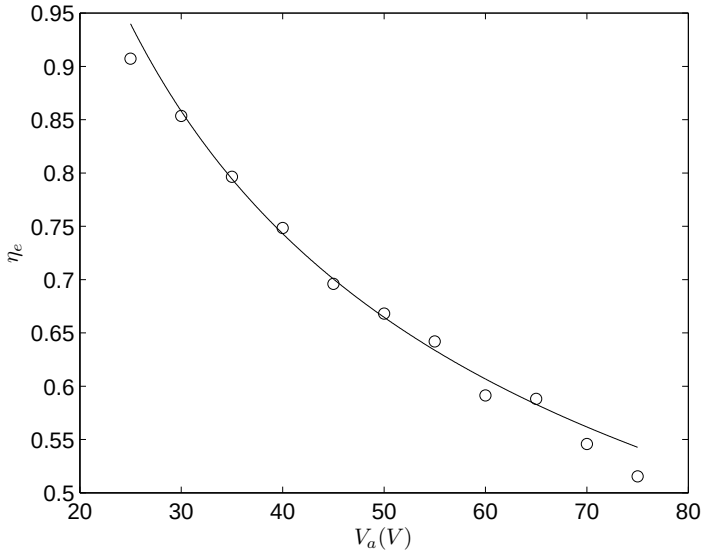

Figure 6: Electrodynamic efficiency versus voltage. Circle symbols are measured data, continuous line represents eq. (29)

ejection phase, one could conclude that the kinetic power is roughly speaking the half of the quantity estimated by equation (13). In practice, due both to a temporal distortion of the velocity signal from the sine trend, and to addition fluid dynamic dissipations in the external air field, the kinetic power can lower down to about 1/3 of the quantity defined in equation (13). Thus, the values of efficiency reported in Table 3 should be reduced by a factor ranging from 1/2 to 1/3 accordingly. For instance, the global efficiency of 44% corresponding to the voltage of $V_a = 75V$ would be reduced down to about 15%.

Moreover, when a numerical modelling is not available to estimate the electrodynamic power, the electric efficiency can be evaluated through the equivalent relationship (20), which requires essentially the measurement of the mass flow rate of air at the orifice, the Joule power and the average-per-cycle temperature difference between the system and the colder surrounding external air ΔT introduced in equation (19). Here equation (19) has been employed within a reverse procedure to estimate ΔT. If we assume $h = 10W/m^2$, which is a typical value in natural convection, for the standard value of the specific heat coefficient at constant pressure at ambient temperature, ΔT ranges from $0.02°C$ (corresponding to the lower voltage) to $0.78°C$.

5. Conclusions

In this paper we presented a comprehensive and detailed physical modelling to evaluate the efficiency of synthetic jet actuators, driven by piezoelectric effect. To the knowledge of present authors this approach is original because is based on relevant energy equations written for both the membrane and acoustic oscillators, which are derived from the corresponding motion equations.

It has been shown that the global efficiency, which is defined as the ratio of the useful kinetic power to the input Joule power, can be expressed as the product of the electrodynamic efficiency (defining the conversion of Joule power to electrodynamic power) and the kinetic efficiency (defining the conversion of electrodynamic power to kinetic energy). Both the efficiency can be also estimated in terms of the relevant dissipation terms. In particular, the electrodynamic efficiency is related to the variation of internal energy of air inside the cavity, or heat generation, which is dissipated towards the external ambient both by natural convection on the walls of the actuator case, and

through the enthalpy flow rate traversing the orifice. On the contrary, the kinetic efficiency is produced by fluid dynamics and structural dissipations.

The physical model has been validated against experimental measurements carried out on a built-in-house device having the piezo-ceramic disk glued on an aluminum shim. Combined numerical and experimental investigations allowed us to find that, for the particular actuator under examination, analyzed at modified Helmholtz frequency, the kinetic efficiency does not vary with applied voltage, whereas the electrodynamic efficiency scales with the reciprocal of the voltage square root. These trends have been also justified according to theoretical scaling laws discussed for each relevant power term.

A discussion has been made on the connection between the energy conversion efficiency at orifice (which is the base subject of the present paper) and the corresponding efficiency in the external jet field, estimated approximately at the stagnation point (or saddle point) separating, during the suction phase, the ingestion near field from the ejection far field. It has been argued that the saddle point efficiency is lower than the orifice efficiency by a factor that can range from 1/2 to 1/3.

Finally, it has been shown that the electrodynamic efficiency can be conveniently evaluated by measuring, among other standard quantities, the average-per-cycle temperature difference between the air inside the cavity and the external ambient. In the present application a reverse procedure allowed us to evaluate such a temperature difference, which is limited to a maximum of almost one degree centigrade.

References

[1] Glezer, A., and Amitay, M., "Synthetic jets", *Annual Review of Fluid Mechanics*, Vol. 34, 2002, pp. 503-529. doi: 10.1146/annurev.fluid.34.090501.094913.

[2] Cattafesta, L. N. III, and Sheplak, M., "Actuators for Active Flow Control", *Annual Review of Fluid Mechanics*, Vol. 43, 2011, pp. 247-272. doi: 10.1146/annurev-fluid-122109-160634.

[3] Chaudhari, M., Puranik, B., and Agrawal, A., "Heat transfer characteristics of synthetic jet impingement cooling", *Int. J. Heat Mass Tran.*, Vol. 53, No. 5, 2010, pp. 1057-1069.

[4] Valiorgue, P., Persoons, T., McGuinn, A., and Murray, D.B., "Heat transfer mechanisms in an impinging synthetic jet for small jet-to-surface spacing", *Experimental Thermal and Fluid Science*, Vol. 33, No. 4, 2009, pp. 597-603.

[5] Greco, C.S., Ianiro, A. and Cardone, G., "Time and phase average heat transfer in single and twin circular synthetic impinging air jets", *International Journal of Heat and Mass Transfer*, Vol. 73, 2014, pp. 776-788.

[6] Smith, B.L., and Glezer, A., "The formation end evolution of synthetic jets", *Phys.Fluids*, Vol. 10, No. 9, 1998, pp. 2281-2297.

[7] Holman, R., Utturkar, Y., Mittal, R., Smith, B.L., and Cattafesta, L., "Formation criterion for synthetic jets", *AIAA J.*, Vol. 43, No. 10, 2005, pp. 2110-2116.

[8] Cater, J.E., and Soria, J., "The evolution of round zero-net-mass-flux jets", *Journal of Fluid Mechanics*, Vol. 472, 2002, pp. 167-200.

[9] Tesar, V. and Zhong, S., "Efficiency of generating the synthetic jets", *Transactions of Aeronautical and Astronautical Society of the Republic of China*, Vol. 35, No. 1, 2003, pp. 45-53.

[10] Crowther, W. J., and L. T. Gomes. "An evaluation of the mass and power scaling of synthetic jet actuator flow control technology for civil transport aircraft applications", *Proceedings of the Institution of Mechanical Engineers, Part I: Journal of Systems and Control Engineering* 222.5 (2008), pp. 357-372.

[11] Li, Ri, Rajdeep Sharma, and Mehmet Arik. "Energy conversion efficiency of synthetic jets", ASME 2011 Pacific Rim Technical Conference and Exhibition on Packaging and Integration of Electronic and Photonic Systems. American Society of Mechanical Engineers, 2011.

[12] de Luca, L., Girfoglio, M., and Coppola, G., "Modeling and experimental validation of the frequency response of synthetic jet actuators", *AIAA J.*, Vol. 52, No. 8, 2014, pp. 1733-1748. doi: 10.2514/1.J052674

[13] Sharma, R., "Fluid Dynamics Based Analytical Model for Synthetic Jet Actuation", *AIAA Journal*, Vol. 45, No. 8, 2007, pp. 1841-1847.

[14] de Luca, L., Girfoglio, M., Chiatto, M., and Coppola, G., "Characterization of synthetic jet resonant cavities", Springer International Publishing Switzerland 2015, E. Ciappi et al. (eds.), *Flinovia - Flow Induced Noise and Vibration Issues and Aspects*, pp. 101-118, Book ISBN: 978-3-319-09712-1. doi: 10.1007/978-3-319-09713-8_6

Università degli studi di Napoli Federico II
Dipartimento di Ingegneria Industriale

Dottorato di Ricerca in Ingegneria Aerospaziale, Navale e della Qualità - XXVII ciclo

PhD Thesis

Volume B

Unsteady gravitational liquid sheet flows

MICHELE GIRFOGLIO

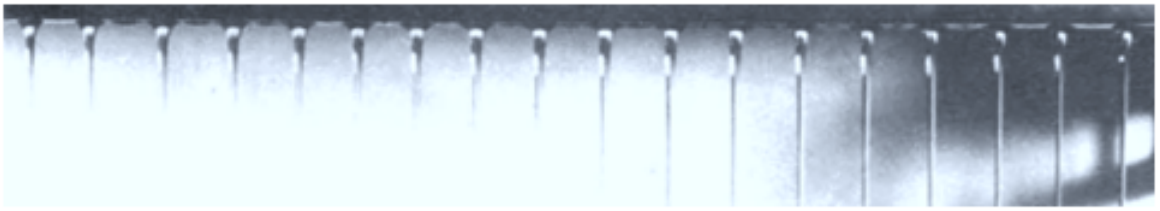

Supervisor:
Luigi de Luca

Coordinator:
Luigi de Luca

March 2015

Preface

My research activity has been focused on two topics very different from each other. For this reason, the present PhD thesis consists of two volumes:

- The volume A deals with the modeling and the experimental validation of the frequency response and the energy conversion efficiency of a synthetic jet actuator driven by a thin piezoelectric disk.
- The volume B deals with the global dynamics of gravitational liquid sheet flows subjected to surface tension.

Results showed in this volume have been published in the following journal/conference papers:

1. M. Girfoglio, F. De Rosa, G. Coppola, L. de Luca, "Unsteady transonic liquid sheet flows", 35 pp., to be submitted to Journal of Fluid Mechanics, 2015.
2. F. De Rosa, M. Girfoglio, L. de Luca, "Global dynamics analysis of nappe oscillation", Physics of Fluids, vol. 26; pp. 122109-1-122109-24, 2014. ISSN: 1070-6631, doi: 10.1063/1.4904752
3. M. Girfoglio, F. De Rosa, G. Coppola, L. de Luca, "Global dynamics of transonic gravitational liquid sheet flows", In: EFMC10 – European Fluid Mechanics Conference 10. Lyngby, Copenhagen, 15-18 september 2014.
4. M. Girfoglio, F. De Rosa, G. Coppola, L. de Luca, "Global eigenmodes of free-interface vertical liquid sheet flows", Wit Transactions on Engineering Sciences, vol. 1, pp. 285-295, 2013. ISSN: 1743-3533, doi: 10.2495/MPF130241
5. F. De Rosa, M. Girfoglio, G. Coppola, L. de Luca, "Global dynamics of gravitational liquid sheet flows", In: AIDAA Napoli XXII, pp. 1-12. Napoli, 9-12 september 2013. Italian Association of Aeronautics and Astronautics. ISBN: 9788890648427

Abstract

The unsteady global dynamics of a gravitational liquid sheet interacting with a one-sided adjacent air enclosure, typically referred to as nappe oscillation, is addressed, under the assumptions of potential flow and both in absence and in presence of surface tension effects.

To the purpose of shedding physical insights, the investigation is carried out from both the dynamics and the energy aspects. An interesting re-formulation of the problem consists of recasting the nappe global behavior as a driven damped spring-mass oscillator, where the inertial effects are linked to the liquid sheet mass and the spring is represented by the equivalent stiffness of the air enclosure acting on the average displacement of the compliant nappe centerline. The investigation is carried out by means of modal (i.e. time asymptotic) linear approach, which is corroborated by direct numerical simulations of the governing equation.

In absence of surface tension effects, the modal analysis shows that the flow system is characterized by low-frequency and high-frequency oscillations, the former related to the crossing time of the perturbations over the whole domain, the latter related to the spring-mass oscillator. The low-frequency oscillations, observed in real life systems, are produced by the (linear) combination of multiple modes. The flow system is characterized by short-time energy amplifications even in asymptotically stable configurations, that are confirmed by numerical simulations and justified by energy budget considerations. Strong analogies with the edge tones problem are encountered, in particular the *integer-plus-one-quarter* resonance criterion is uncovered, where the basic frequency to be multiplied by $n + \frac{1}{4}$ is just the one related to the spacing among the imaginary parts of the eigenvalues.

In presence of surface tension effects, it is known that the basic nature of the global dynamics of gravitational liquid sheet flows depends crucially on the inlet Weber number $We = \rho_\mathrm{l} U_\mathrm{in}^{\star 2} H_\mathrm{in}^\star / 2\sigma$, where ρ_l is the liquid density, $U_\mathrm{in}^\star$ the inlet liquid velocity, $H_\mathrm{in}^\star$ the initial thickness of the sheet, σ the air-liquid surface tension. When $We > 1$, the local Weber number too, $We_l = U^2/c^2$ (with U and $c = \sqrt{\sigma/\rho_\mathrm{l} H}$ being the local flow and

capillary waves velocity, respectively), is greater than unity at each streamwise location, so that the flow can be defined *supersonic*-like everywhere. When $We < 1$, there exists an initial region where the sheet flow is *subsonic*, up to the *transonic* location, downstream of which the flow becomes *supersonic*. From the theoretical viewpoint the problem is not straightforward, because it is known that the equation governing the evolution of small disturbances exhibits a singularity just at the *transonic* station, although the solution to the problem is not yet yielded. Thus, the present work is aimed at developing a theoretical/numerical procedure to fill up this lack of information.

Preliminary physical insights of the sheet centerline sinuous modes show that the nappe dynamics features the propagation of two wave fronts both directed downstream or one downstream and the other one upstream depending on whether the flow is supersonic or subsonic, respectively. In every situation the inlet section is considered as a perfectly reflecting boundary. As regards the other boundary condition, in supersonic flow it is of null centerline slope at the inlet; in subsonic regime it is imposed just at the singularity station, by enforcing the boundedness of the sheet slope there. An additional analytical investigation on the nature of the singularity, based on the Frobenius theory, predicts that the flow is unconditionally stable for any $We < 1$ and that the disturbance time growth rate results to be bounded above.

The findings of the eigenvalues spectral analysis confirm all the theoretical predictions discussed above. They in turn closely agree with direct numerical simulations of the partial differential equation governing in the space-time domain the global evolution of the disturbances, starting from an initial gaussian-like shape, with particular attention to *transonic* and high Weber number regimes.

Acknowledgements

First and foremost, I would like to thank my mother and my father (God bless you!) for their constant and unconditional affection.

I would like to thank my friends, in particular Mario and Ivan, and my colleagues, Fortunato, Matteo, Annagrazia and Armandojanni, for their emotional support.

A special acknowledgment goes to Prof. Gennaro Cardone, who gave me the possibility to became a PhD student.

The support and the guidance of my project advisor, Prof. Luigi de Luca, has been crucial for the most critical aspects of my research activity.

Finally, I would like to acknowledge my girlfriend, Giusy: thanks for being what you are, for all that you mean to me, I don't know how I could have lived if you had never existed or if we had never met.

Contents

List of Figures

Chapter 1

Introduction

1.1 Motivation and objectives

The investigation of the unsteady dynamics of gravitational liquid sheet flows is of great importance in many engineering applications. It is well known that the control of the break up of liquid jets (both plane and annular) plays a key role in several industrial processes, such atomization and spray processes in which high-speed flows are vaporized in order to increase the efficiency of the combustors. Liquid sprays are used in these processes (to inject the fuel into the burner of furnaces, turbines, internal combustion engines, rockets, etc.) as well as in agriculture, medicine, cooling systems. At reduced velocities, when the effect of the gravity is crucial, several technological processes require the control of the evolution dynamics of such liquid jets, such as coating and paper-making processes.

The basic ideas explaining the physical mechanisms leading to the jet rupture (break up) seem well established, even though the attempt to recast such a level of knowledge within the framework of modern approaches of fluid dynamics instability is a current subject of research. As an example, a known experimental evidence is that the plane jet breaks up when the flow Weber number is lowered below unity [2], though, at present time there is no theory able to predict the actual value of Weber number of rupture. On the other hand, other recent experimental findings [3] showed that the sheet rupture seems do not be caused by amplification of single modal waves.

The aim of the present contribution is to investigate the global dynamics of gravitational liquid sheet flows by taking into account the effects of the surface tension.

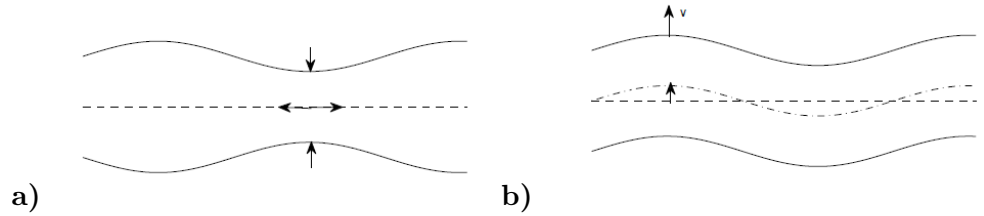

FIGURE 1.1: Qualitative depiction of the two fundamental oscillation modes of a plane liquid sheet: a) *varicose* mode, b) *sinuous* mode.

1.2 Stability analysis: literature review

Squire [4] and Hagerty and Shea [5] have carried out early relevant works related to the stability analysis of a liquid jet. They focused on the problem of a liquid sheet interacting with an inviscid steady external gas and identified the two fundamental oscillation modes of a plane liquid sheet; a symmetric oscillation mode (*varicose* mode) and an antisymmetric oscillation mode (*sinuous* mode), both showed in Fig. 1.1. Furthermore, they found that the instability was generated by aerodynamic effects, related to the velocity difference between the air and the external gas, and that the surface tension played a stabilizing role.

Later on, such temporal stability analysis was extended to the viscous case by [6]. They found two different instability mechanisms: a not viscous aerodynamic instability, not depending on the flux Reynolds number, and an instability of viscous nature, strongly depending on the flux Reynolds number, which represented the dominant mechanism for low flux Weber numbers (≈ 1). Conversely, for high Weber numbers ($\gg 1$), when the aerodynamic instability is crucial, they found that the viscosity had a stabilizing effect on the flow system, by moving the onset of the instability towards higher wave lengths.

Lin et al. [7] carried out the first relevant absolute instability analysis of a viscous liquid sheet interacting with an inviscid gas. They found a pseudo-absolute instability for the *sinuous* mode, when the Weber number is lowered below unity. An analogous behaviour has been found by [8] who studied the impulse response for an inviscid gravitational liquid sheet, by obtaining the same critical Weber number. In summary, the results of such investigations have allowed to conclude that the liquid sheet is characterized by a pseudo-absolute instability for Weber numbers less than unity, otherwise it results to be convectively unstable. Anyway, the spatial stability analysis did not confirm the presence of the two different peaks found by [6] by means of a temporal analysis for low Weber numbers since the viscous mode was characterized by a too low spatial amplification.

Later on, de Luca [2] experimentally studied the break up of a gravitational liquid sheet characterized by an uniform velocity profile in the inlet section. The author observed

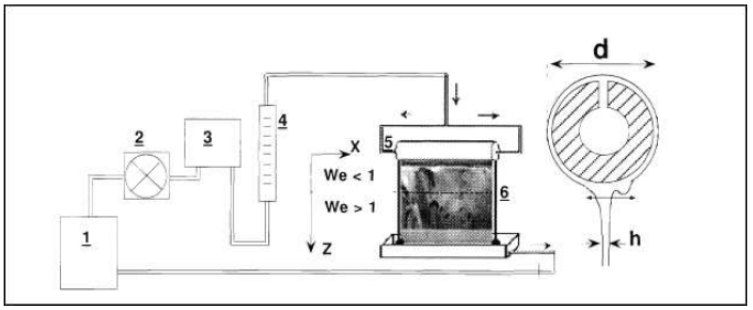

FIGURE 1.2: Experimental set-up used by [1] in order to visualize the flow structure

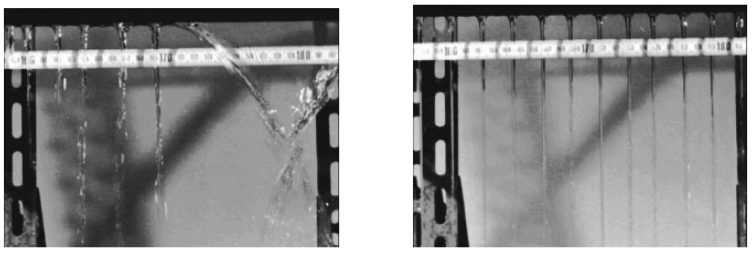

FIGURE 1.3: Experimental visualization of the sheet break up [2]

that the sheet was subjected to rupture exclusively for Weber numbers less than unity, with a value depending on the non-parallelism factor. This result suggested that the break up phenomenon was related to a global instability mechanism.

Schmid and Henningson [9] studied the global instability of a plane gravitational liquid sheet by using a perturbative method based on the *slender* sheet approach, applied to a mathematical model previously developed by [10]. They investigated the interaction with an air cushion located on one side of the sheet by considering an isentropic transformation of the air. By means of a non modal analysis of the low frequency modes, they found that the flow system was unstable, in good agreement with the experimental measurements. It is worth to stress that in [9] both viscous and surface tension effects were neglected.

In addition to the contributions cited above, a lot of experimental investigations have been carried out in order to explain the physical mechanisms related to the sheet break up. Fig. 1.2 shows an experimental set-up recently used to visualize the flow structure. As depicted in Fig. 1.3, the sheet rupture is characterized by the formation of discrete filaments which, later on, break up into drops.

1.3 Thesis layout

This thesis is presented in four chapters followed by a conclusion and an appendix. In Chapter 1 an overview is given, together with the motivation and the objectives of

the research. In Chapter 2 the development of the mathematical model is reported. Chapter 3 and Chapter 4 show the most relevant results obtained in absence and in presence of surface tension effects, respectively. The appendix collects the most relevant conference/journal papers published during the research activity.

Chapter 2

Physical modeling

To derive a physical model for the unsteady evolution of an inviscid gravitational liquid sheet, the assumptions of thin curtain and plug flow are adopted [10–12].

It has been considered the boundary pressure field produced by the curtain compliant interface within a two-dimensional air enclosure delimited by the sheet itself, rigid walls and a lower basin, namely it has been addressed the unsteady behavior of the configuration generally referred to as nappe oscillation. Splashing effects are neglected. Furthermore, the investigation will be restricted to the occurrence of one-dimensional surface wave-patterns. One can expect that oblique waves (i.e., developing along the spanwise direction) occur when extending the study to three-dimensional configurations, as already found experimentally by Le Grand-Pitera et al. [1] in the case of symmetrical semi-infinite boundary air environments.

Figure 2.1 shows the schematic of the geometrical configuration under consideration. In the unperturbed condition the liquid flows along the vertical x-direction with a steady velocity and two symmetrical free interfaces. The definitions of unsteady centerline location ℓ and thickness h of the sheet are given, in terms of the interface positions $y^{\pm}$, as follows

$$\begin{aligned} \ell^{\star}(x^{\star},t^{\star}) &= \frac{y^{\star+}(x^{\star},t^{\star})+y^{\star-}(x^{\star},t^{\star})}{2} \\ h^{\star}(x^{\star},t^{\star}) &= y^{\star+}(x^{\star},t^{\star})-y^{\star-}(x^{\star},t^{\star}) \end{aligned}$$

where superscripts $\pm$ refer to right and left interfaces, respectively, and t^* is the time. Here as elsewhere star denotes dimensional quantities. Furthermore, the general definition $\varphi^{\star\pm}(x^{\star},t^{\star}) = \varphi^{\star}(x^{\star},y^{\star\pm},t^{\star})$ will be adopted in the following, φ being any of the

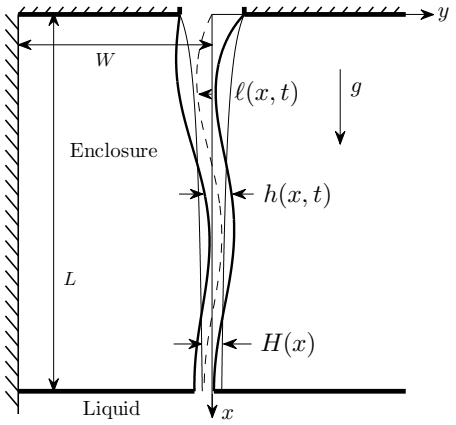

FIGURE 2.1: Sketch of the model configuration

flow variables u, v and p (where u and v are the streamwise and lateral liquid velocity components, respectively, and p is liquid pressure)

2.1 Governing equations

The starting mathematical framework is given by the two-dimensional Euler equations in which gravity is retained, closed by the kinematic and dynamic conditions imposed at the free interfaces.

The assumption of a thin sheet with respect to the wavelength of a disturbance allows one to consider local plug-type velocity profiles for u and v across the nappe thickness. To derive the governing equations the following procedure is adopted: the mass and x-momentum balances are formulated over a generic slice of the curtain of length dx; the y-momentum equation is integrated along the lateral coordinate y; the unsteady quantities can be considered as the sum of a steady contribution and a fluctuation (i.e. perturbation)

$$u^* = U^* + u'^* \tag{2.1}$$

$$v^* = V^* + v'^* \tag{2.2}$$

$$p^* = P^* + p'^* \tag{2.3}$$

$$h^* = H^* + h'^* \tag{2.4}$$

$$y^{*\pm} = Y^{*\pm} + y'^{*\pm} \tag{2.5}$$

where capital letters (here as elsewhere) denotes basic (steady) quantities and prime the corresponding fluctuations. Under the assumption of small perturbations, the linearized forms of the continuity, x-momentum and y-momentum equations are written, respectively:

$$\frac{\partial h'^\star}{\partial t^\star} + \frac{\partial}{\partial x^\star}\left(U^\star h'^\star + H^\star u'^\star\right) = 0 \tag{2.6}$$

$$\frac{\partial u'^\star}{\partial t^\star} + \frac{\partial}{\partial x^\star}\left(U^\star u'^\star\right) = -\frac{1}{\rho_\mathrm{l}}\frac{\partial p'^\star}{\partial x^\star} \tag{2.7}$$

$$\frac{\partial v'^\star}{\partial t^\star} + U^\star\frac{\partial v'^\star}{\partial x^\star} = -\frac{1}{\rho_\mathrm{l} H^\star}\left(p'^{\star+} - p'^{\star-}\right) \tag{2.8}$$

where ρ_l is the liquid density.

The boundary conditions are:

$$v^{\star\pm} = \frac{\partial y^{\star\pm}}{\partial t^\star} + u^{\star\pm}\frac{\partial y^{\star\pm}}{\partial x^\star} \tag{2.9}$$

$$p^{\star\pm} = p_\mathrm{a}^{\star\pm} \mp \sigma\frac{\partial^2 y^{\star\pm}}{\partial x^{\star 2}}\left[1 + \left(\frac{\partial y^{\star\pm}}{\partial x^\star}\right)^2\right]^{-\frac{3}{2}} \tag{2.10}$$

where $p_\mathrm{a}^{\star\pm}(x^\star, t^\star)$ is the local value of the external ambient pressure and σ is the surface tension coefficient.

The difference between the boundary fluctuating pressures of eq. (2.8) can be expressed in terms of perturbations of ambient pressure and interface locations by linearizing the dynamic boundary condition (2.10):

$$p'^{\star\pm} = p'^{\star\pm}_\mathrm{a} \mp \sigma\left[1 + \left(\frac{dY^{\star\pm}}{dx^\star}\right)^2\right]^{-\frac{3}{2}} \cdot \left\{\frac{\partial^2 y'^{\star\pm}}{\partial x^{\star 2}} - 3\frac{\frac{d^2Y^{\star\pm}}{dx^{\star 2}}\frac{dY^{\star\pm}}{dx^\star}\frac{\partial y'^{\star\pm}}{\partial x^\star}}{1 + \left(\frac{dY^{\star\pm}}{dx^\star}\right)^2}\right\} \tag{2.11}$$

The result can be recast in the form:

$$p'^{\star+} - p'^{\star-} = \widetilde{p}'^\star_\mathrm{a} - 2\sigma\frac{\partial}{\partial x^\star}\left[F^\star\frac{\partial \ell'^\star}{\partial x^\star}\right] \tag{2.12}$$

with $F^\star = \left[1 + \frac{1}{4}\left(\frac{dH^\star}{dx^\star}\right)^2\right]^{-\frac{3}{2}}$, and $\widetilde{p}^\star_\mathrm{a} = p^{\star+}_\mathrm{a} - p^{\star-}_\mathrm{a}$. Note also that $|Y^{*\pm}| = \frac{H^*}{2}$.

Eq. (2.8) has to be coupled with the linearized kinematic boundary condition, which can be properly expressed in terms of the centerline deflection only:

$$v'^{\star} = \frac{\partial \ell'^{\star}}{\partial t^{\star}} + U^{\star}\frac{\partial \ell'^{\star}}{\partial x^{\star}}. \tag{2.13}$$

Eqs. (2.8) and (2.13) constitute a closed system for the unknown lateral velocity and centerline perturbations, namely representing the so called skew-symmetric *sinuous* solution of the unsteady perturbed field.

It is straightforward to observe that eqs. (2.6) and (2.7) represent, on the other hand, the symmetric, or *varicose*, solution for the perturbed longitudinal velocity and sheet thickness. In fact, the liquid pressure (which is constant in this symmetric case, i.e. $p'^{\star} = p'^{\star +} = p'^{\star -}$) can be eliminated by taking the half sum of the right hand side of eq. (2.11) so as to obtain

$$p'^{\star} = \overline{p}_{\mathrm{a}}'^{\star} - \frac{\sigma}{2}\frac{\partial}{\partial x^{\star}}\left[F^{\star}\frac{\partial h'^{\star}}{\partial x^{\star}}\right] \tag{2.14}$$

where

$$\overline{p}_{\mathrm{a}}^{\star} = \frac{p_{\mathrm{a}}^{\star +} + p_{\mathrm{a}}^{\star -}}{2}.$$

To close the two systems of coupled equations (2.6-2.7) and (2.8-2.13) expressions for the ambient gas pressure terms $\overline{p}_{\mathrm{a}}'^{\star}$ and $\widetilde{p}_{\mathrm{a}}'^{\star}$ as functions of the perturbations of the sheet are required.

The infinitesimal variation of the enclosure volume, resulting from the sheet fluctuation, is given by

$$\mathcal{V}_{\mathrm{a}}'^{\star} = \int_0^{L^{\star}} \ell'^{\star}(x^{\star})dx^{\star} - \frac{1}{2}\int_0^{L^{\star}} h'^{\star}(x^{\star})dx^{\star}$$

If one hypothesizes that the air within the enclosure encompasses compression/expansion isoentropic thermodynamic transformations, it is possible to give explicit expressions for the external pressure terms of the eqs. (2.12) and (2.14), for the two different oscillating modes of the sheet, respectively, as follows:

$$\widetilde{p}_{\mathrm{a}}'^{\star} = \gamma \frac{P_{\mathrm{a}}^{\star}}{\mathcal{V}_{\mathrm{a}}^{\star}} \int_0^{L^{\star}} \ell'^{\star}(x^{\star}) dx^{\star} \tag{2.15}$$

$$\overline{p}_{\mathrm{a}}'^{\star} = \frac{\gamma}{4} \frac{P_{\mathrm{a}}^{\star}}{\mathcal{V}_{\mathrm{a}}^{\star}} \int_0^{L^{\star}} h'^{\star}(x^{\star}) dx^{\star} \tag{2.16}$$

where γ is the specific heat ratio, $P_{\mathrm{a}}^{\star}$ is the unperturbed gas pressure into the enclosure and $\mathcal{V}_{\mathrm{a}}^{\star} = L^{\star}W^{\star} - \frac{1}{2}\int_0^{L^{\star}} H^{\star}(x^{\star})dx^{\star}$ is the corresponding volume in the configuration shown in Figure 2.1.

Substituting the above relationships of the pressure difference and of the average pressure into the streamwise and lateral momentum equations (2.7, 2.8) eventually yields, respectively:

$$\frac{\partial u'^{\star}}{\partial t^{\star}} + \frac{\partial}{\partial x^{\star}}\left(U^{\star}u'^{\star}\right) = \frac{\sigma}{2\rho_{\mathrm{l}}} \frac{\partial^2}{\partial x^{\star 2}} \left[F^{\star} \frac{\partial h'^{\star}}{\partial x^{\star}}\right] \tag{2.17}$$

$$\frac{\partial v'^{\star}}{\partial t^{\star}} + U^{\star}\frac{\partial v'^{\star}}{\partial x^{\star}} = \frac{2\sigma}{\rho_{\mathrm{l}} H^{\star}} \frac{\partial}{\partial x^{\star}} \left[F^{\star} \frac{\partial \ell'^{\star}}{\partial x^{\star}}\right] - \frac{\gamma}{\rho_{\mathrm{l}} H^{\star}} \frac{P_{\mathrm{a}}^{\star}}{\mathcal{V}_{\mathrm{a}}^{\star}} \int_0^{L^{\star}} \ell'^{\star}(x^{\star}) dx^{\star} \tag{2.18}$$

It is worth noting that in deriving eq. (2.17) it is implicitly assumed that the pressure fluctuation inside the air enclosure does not vary in space, according to the model of a lumped reaction of the cushion.

The set of two systems of coupled equations (2.6-2.17) and (2.13-2.18), already derived in Girfoglio et al. [13] (see Appendix), can be rigorously derived by using the theory and the methods of perturbations [14]

2.2 Non-dimensional equations and slender sheet approximation

The governing equations can be conveniently made dimensionless by employing the reference quantities

$$L_{\mathrm{r}}^{\star} = L^{\star}, \quad \ell_{\mathrm{r}}^{\star} = H_{\mathrm{in}}^{\star},$$
$$u_{\mathrm{r}}^{\star} = U_{\mathrm{in}}^{\star}, \quad v_{\mathrm{r}}^{\star} = \varepsilon U_{\mathrm{in}}^{\star},$$
$$t_{\mathrm{r}}^{\star} = L^{\star}/U_{\mathrm{in}}^{\star}, \quad p_{\mathrm{r}}^{\star} = \rho_{\mathrm{l}} U_{\mathrm{in}}^{\star 2}$$

with $\varepsilon = \ell_{\mathrm{r}}^{\star}/L_{\mathrm{r}}^{\star}$ denoting the *slenderness* parameter (tiny according to the assumptions made in deriving the model). The non-dimensional form results

$$\frac{\partial \ell}{\partial t} + U\frac{\partial \ell}{\partial x} = v \tag{2.19}$$

$$\frac{\partial v}{\partial t} + U\frac{\partial v}{\partial x} = \frac{1}{\mathrm{We}H}\frac{\partial}{\partial x}\left[F\frac{\partial \ell}{\partial x}\right] - \frac{\gamma}{H}\frac{P_{\mathrm{a}}\int_0^1 \ell(x)dx}{\varepsilon\left(\frac{W^{\star}}{L^{\star}} - \frac{\varepsilon}{2}\int_0^1 H dx\right)} \tag{2.20}$$

$$\frac{\partial h}{\partial t} + \frac{\partial}{\partial x}\left(Uh + Hu\right) = 0 \tag{2.21}$$

$$\frac{\partial u}{\partial t} + \frac{\partial}{\partial x}\left(Uu\right) = \frac{\varepsilon^2}{4\mathrm{We}}\frac{\partial^2}{\partial x^2}\left[F\frac{\partial h}{\partial x}\right] \tag{2.22}$$

where $\mathrm{We} = \frac{\rho_{\mathrm{l}} {U_{\mathrm{in}}^{\star}}^2 H_{\mathrm{in}}^{\star}}{2\sigma}$ is the Weber number and $F = \left[1 + \frac{\varepsilon^2}{4}\left(\frac{dH}{dx}\right)^2\right]^{-\frac{3}{2}}$.

As extensively discussed in Coppola et al. [11], in the absence of viscosity, an analytical solution for the steady (base) flow of sheet thickness and streamwise liquid velocity can be obtained by performing a parameter-type expansion in the small ratio ε^2 of the unperturbed governing equations. At the zerotth order expansion, the following non-dimensional Torricelli's free-fall solution for the steady main flow results:

$$UH = 1 \quad \text{and} \quad U = \sqrt{1 + 2\mathrm{Fr}\ x} \tag{2.23}$$

where $\mathrm{Fr} = gL^{\star}/{U_{\mathrm{in}}^{\star}}^2$ denotes the Froude number.

Accordingly, the corresponding lowest order expansion to the eqs. (2.19-2.22) leads to the *slender* sheet approximation:

sinuous mode

$$\begin{cases} \dfrac{\partial \ell}{\partial t} + U\dfrac{\partial \ell}{\partial x} = v & (2.24) \\ \dfrac{\partial v}{\partial t} + U\dfrac{\partial v}{\partial x} = \dfrac{1}{\mathrm{We}H}\dfrac{\partial^2 \ell}{\partial x^2} - \dfrac{\mathcal{K}}{H}\bar{\ell} & (2.25) \end{cases}$$

varicose mode

$$\begin{cases} \dfrac{\partial h}{\partial t} + \dfrac{\partial}{\partial x}\left(Uh + Hu\right) = 0 & (2.26) \\ \dfrac{\partial u}{\partial t} + \dfrac{\partial}{\partial x}\left(Uu\right) = 0 & (2.27) \end{cases}$$

with $\mathcal{K} = \gamma\frac{P_{\mathrm{a}}}{\varepsilon\frac{W^{\star}}{L^{\star}}}$ and

$$\bar{\ell} = \int_0^1 \ell\ dx$$

denoting the average sinuous deflection of the sheet.

In summary, three independent dimensionless parameters for the problem under study have to be considered: the Weber number We, the Froude number Fr and the equivalent air stiffness $\mathcal{K}$. Note explicitly that in the present analysis the air stiffness includes simultaneously the effects of the undisturbed pressure within the enclosure, of the enclosure width and of the slenderness ratio $\varepsilon = H^{\star}_{\text{in}}/L^{\star}$, which in principle have to be taken into account separately.

Note that eqs. (2.26-2.27) governing the evolution of the varicose modes are not able to sustain any oscillating wave pattern in the configuration here adopted, reducing to simple advection equations. Therefore, the attention will be focused hereinafter on the sinuous disturbances (eqs. (2.24-2.25)) only.

Chapter 3

Nappe oscillation in absence of surface tension

In this chapter, the nappe oscillation in absence of surface tension effects will be investigated. To the purpose of shedding physical insights, the study will examine both the dynamics and the energy aspects. The analysis is carried out through a modal (i.e., time asymptotic) linear approach, which is corroborated by direct numerical simulations of the governing equations.

Note that the complete treatment, further supported by a non-modal (i.e., short-time transient) linear approach, can be found in [12] (see Appendix), from which the results reported hereafter are arisen.

3.1 Theoretical insight on the nappe global dynamics

The equations for sinuous disturbances (2.24-2.25), in absence of surface tension (We $= \infty$), became

$$\begin{cases} \dfrac{\partial \ell}{\partial t} + U \dfrac{\partial \ell}{\partial x} = v & (3.1) \\ \dfrac{\partial v}{\partial t} + U \dfrac{\partial v}{\partial x} = -\dfrac{\mathcal{K}}{H} \bar{\ell} & (3.2) \end{cases}$$

Due to the hyperbolic nature of the governing equations, they are equipped with two boundary conditions prescribed at the inlet location, $x = 0$, namely, $\ell(0) = v(0) = 0$.

In order to give more physical insight on the fluid system under study, the equations for sinuous disturbances (focus of the present analysis) can be properly rearranged by taking into account integral quantities depending on the sheet extension as a whole. Hereafter it will be seen that it is globally modeled as a lumped one-degree-of-freedom spring-mass system, in which the role of the spring is played by the air into the enclosure and the mass is that of the liquid sheet itself.

Let's start to reconsider the system of equations (3.1-3.2) in terms of a single second order partial integro-differential equation

$$\frac{D^2\ell}{Dt^2} = -\frac{\mathcal{K}}{H}\bar{\ell} \tag{3.3}$$

where $\frac{D}{Dt}$ is the substantial derivative. Such an equation governs the linear inviscid evolution of a generic disturbance subjected to an integral reaction term. The role played by the air stiffness $\mathcal{K} \geq 0$ is crucial in characterizing the dynamics of the self-sustained wave-patterns evolving into the curtain. If $\mathcal{K} = 0$ the equation is trivial, reducing to the simple advection equation with variable mean velocity given by eq. (2.23). Then, if no input is introduced at the left boundary, after a finite time any solution vanishes, with the disturbance being continually expelled at the outlet of the domain.

Conversely, the presence of the reaction term in the form of an integral changes things in such a way that the temporal evolution of the disturbance is by no means identically null after a finite time. As it will be shown in the subsequent investigations, depending on the stiffness of the air chamber adjacent to the sheet, the system dynamics exhibits different features in terms of both stability properties and energy time evolution.

After expressing the substantial derivative in explicit form, integrating eq. (3.3) over the whole length of the sheet yields:

$$\frac{d^2}{dt^2}\left[\int_0^1 H\ell \; dx\right] + \mathcal{K}\bar{\ell} = -\left.\frac{\partial \ell}{\partial t}\right|_1 - v_1 \tag{3.4}$$

where the boundary conditions at the inlet location, $\ell(0) = 0$ and $v(0) = 0$, have been considered, and quantities at the outlet boundary are denoted with the subscript 1. This notation will be used hereafter for all the quantities at the right boundary.

The integral at left hand side of eq. (3.4) can be conveniently expressed as:

$$\int_0^1 H(x)\ell(x) \; dx = \bar{H}\bar{\ell} + \int_0^1 H'(x)\ell'(x) \; dx \tag{3.5}$$

where $H'(x)$ and $\ell'(x)$ into the covariance term on the right side of the above equation represent the local deviations of sheet thickness and centreline position from their average

values, $\bar{H}$ and $\bar{\ell}$, respectively, and with the following position being also made:

$$\bar{H} = \int_0^1 H \, dx.$$

The adopted hypotheses of small sheet thickness and perturbations assure that the covariance term is small so that it can be neglected into eq. (3.5) and the analogy with an elastic oscillator holds, as it appears hereafter:

$$\bar{H}\frac{d^2\bar{\ell}}{dt^2} + \mathcal{K}\bar{\ell} = -\left(2\frac{\partial \ell}{\partial t}\bigg|_1 + U\frac{\partial \ell}{\partial x}\bigg|_1\right) \tag{3.6}$$

where $\bar{H}$ denotes the mass of the liquid sheet and $\mathcal{K}$ is the equivalent spring stiffness of the enclosure air, whilst the righthand side has been written by considering eq. (3.1). It's worth noting that in absence of gravity effects (i.e. parallel flow) eq. (3.6) is obtained without any approximation from eq. (3.4) and the above analogy is exact. Then, the righthand side of eq. (3.6) can be further manipulated in order to extract a damping term, that is to say:

$$\bar{H}\frac{d^2\bar{\ell}}{dt^2} + 2\frac{d\bar{\ell}}{dt} + \mathcal{K}\bar{\ell} = \underbrace{-2\frac{d}{dt}\int_0^1 x\frac{\partial \ell}{\partial x}dx - U\frac{\partial \ell}{\partial x}\bigg|_1}_{f_\mathrm{i}} \tag{3.7}$$

where f_i represents the self-induced forcing acting on the elastic oscillator.

In summary, the global dynamics of the nappe consists of the mutual interaction of the centerline local deflection with the compliant air chamber which behaves as a spring acting on the average sheet deflection. Eq. (3.3) shows that the local deflection is forced by the global reaction term of the spring, whilst the dynamics of the global spring-mass oscillator is driven by a combination of local sheet displacement values, as described by eq. (3.7). In the following part of the chapter, it will be correlated such a mutual forcing to special features of the eigenvalues spectrum; the spectrum uncovers the natural mode (possibly unstable) of the spring-mass system and the peculiar oscillating behavior of the nappe described not just by single modes, but by the superposition of a number of modes to be ascribed essentially to Eq. (3.3) and physically connected to another characteristic frequency linked to the typical crossing (or falling) time.

Here it is useful to introduce the following ansatz: the system is stable if the crossing time is less than the period of the spring-mass oscillator, $\mathcal{T}$. In the opposite situation the self-forcing establishes, leading to instability. Of course, since the oscillator works in the driven regime, the oscillation period does not correspond to the natural frequency of oscillation and in general it cannot be determined in analytical closed form. It should be stressed that this ansatz includes the gravity effects, in the sense that in the presence

of gravity effects a shorter crossing time is expected, as well as a higher $\mathcal{K}$ threshold of instability. Such predictions will be confirmed by the subsequent spectral analysis. In analogy with the classic acoustic phenomenon of edge tones, it will be showed that resonance occurs at frequencies one-plus-one-fourth times the instability onset frequency. It is worth to remember that the edge tones phenomenon refers to the acoustic tones produced when a jet of air strikes a wedge shaped edge, whereas resonance occurs at frequencies one-integer-plus-one-quarter times the frequency given by the ratio of the jet velocity to the distance between the jet exit section and the wedge apex. In other physical terms, Curle [15] explained that the jet wavelength w and the edge to nozzle distance d are related by the relationship $d = (n + 1/4)w$, where n is an integer.

3.2 Disturbance energy evolution

In order to investigate some features of the solutions of eqs. (3.3) and (3.7), it is useful to examine the mechanisms of perturbation growth (or decay) by considering also the time behavior of the system's energy E. For sinuous disturbances the energy balance equation can be easily derived by multiplying eq. (3.2) by the lateral velocity fluctuation v, and then by integrating it over the whole volume (per unit length in transversal direction) of the sheet, thus obtaining:

$$\frac{dE_\mathrm{k}}{dt} + \frac{v_1^2}{2} = -\left(\mathcal{K}\bar{\ell}\right)\int_0^1 v\ dx \tag{3.8}$$

where the kinetic energy E_k is defined as

$$E_\mathrm{k} = \frac{1}{2}\int_0^1 Hv^2\ dx \tag{3.9}$$

and the energy terms are made dimensionless with respect to the reference energy $E_\mathrm{r}^\star = \rho_\mathrm{l}\ell_\mathrm{r}^\star L_\mathrm{r}^\star v_\mathrm{r}^{\star 2}$.

Apart from the presence of the convective exchange term of kinetic energy at the lower end of the domain, the righthand side of eq. (3.8) shows that a single mechanism contributes to the rate of change of kinetic energy, that is to say the pressure (i.e., the term in between the parentheses) work per unit time exchanged during the isentropic compression/expansion of the air enclosure. By looking at the analogy with the elastic oscillator, one expects that the pressure work has a time oscillating trend driven by the frequency of the self-induced forcing acting on the spring-mass model (3.7); since the pressure work can assume both positive and negative values, no conclusion may be drawn about the large time asymptotic behavior.

It is worthwhile to further rearrange Eq. (3.8) by eliminating the lateral velocity v with the aid of eq. (3.1), where the convective term is integrated by parts. The result is:

$$\frac{dE}{dt} + \frac{v_1^2}{2} = -\mathcal{K}\bar{\ell}U_1\ell_1 + \mathcal{K}\bar{\ell}\int_0^1 \frac{dU}{dx}\ell \, dx \tag{3.10}$$

with $E = E_\mathrm{k} + E_\mathrm{e}$, where the elastic energy of the enclosure air is

$$E_\mathrm{e} = \frac{1}{2}\mathcal{K}\,\bar{\ell}^2. \tag{3.11}$$

By making considerations analogous to those already discussed for eq. (3.5), eq. (3.10) can be written as

$$\frac{dE}{dt} + \frac{v_1^2}{2} = -\mathcal{K}\bar{\ell}U_1\ell_1 + \mathcal{K}\bar{\ell}^2\overline{\left(\frac{dU}{dx}\right)} \tag{3.12}$$

where

$$\overline{\left(\frac{dU}{dx}\right)} = Fr \cdot t_\mathrm{cross} \tag{3.13}$$

t_cross being the marching time needed by the perturbation to cross the entire domain.

Note that $-\mathcal{K}\bar{\ell}U_1\ell_1$ represents the convective exchange of elastic energy at the outlet (namely, the work flux related to the pressure), whilst the term $\mathcal{K}\bar{\ell}^2\overline{\left(\frac{dU}{dx}\right)}$ can be interpreted as a production of disturbances total energy extracted from the stretching (i.e. non parallel) basic flow. Since the basic flow, driven by the gravity field, accelerates along the streamwise direction, this last term is always positive (it is null if $Fr = 0$), contributing to increase the disturbance energy. As observed before for the kinetic energy, one cannot infer any conclusions about the asymptotic behavior of the total energy; nevertheless, due to the positive gravitational production term, one can expect a short time growth also in asymptotically stable situations. It will be seen that this is possible even when the gravitation effects are negligible.

Furthermore, a close-up inspection of the term $-\mathcal{K}\bar{\ell}U_1\ell_1$ allows one to predict, in no-gravity configurations, asymptotic stability depending on the phase lag ϕ existing between the signals $\bar{\ell}$ and ℓ_1: a perfect phase synchronization (ϕ =0) leads the system's energy to asymptotically decrease from its initial value; when the signals have a phase lag $0 < \phi \leq \pi$ the temporal behavior of the system's energy assumes an oscillating, nonmonotonic trend and the phase quadrature ($\phi = \frac{\pi}{2}$) among $\bar{\ell}$, ℓ_1 spots the critical threshold for the large time stability interval ($0 < \phi < \frac{\pi}{2}$), while no conclusions can be inferred for a phase lag $\frac{\pi}{2} < \phi \leq \pi$. Once again, when gravity effects are retained it is not possible to predict the system's energy trend over the long times through the phase lag ϕ, because asymptotic growing or decaying behaviors depend on whether the production term overwhelms the kinetic and elastic convective exchanges. These theoretical

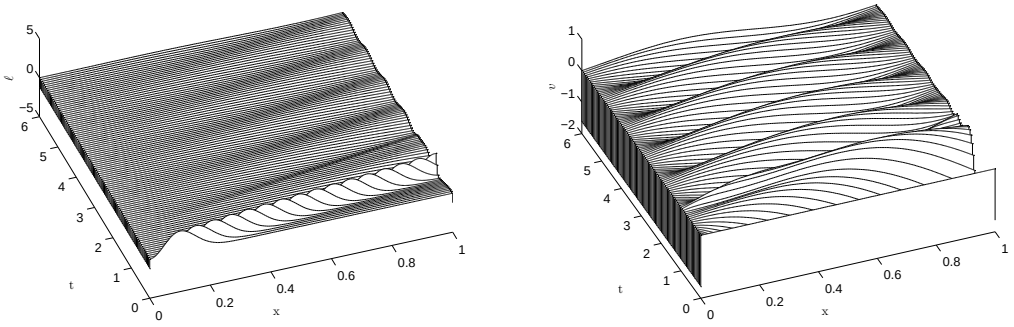

FIGURE 3.1: Spatio-temporal evolution of ℓ and v disturbances in absence of gravitational effects for $\mathcal{K} = 18$.

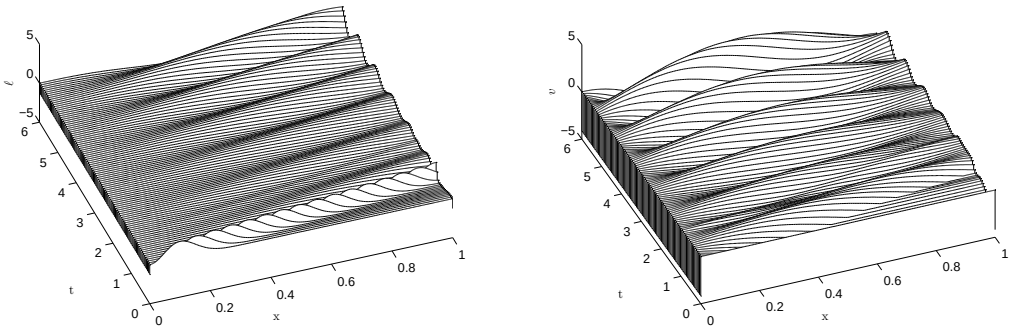

FIGURE 3.2: Spatio-temporal evolution of ℓ and v disturbances in absence of gravitational effects for $\mathcal{K} = 30$.

predictions will be confirmed hereafter by means of both direct numerical simulations and linear stability analysis.

3.3 Spatio-temporal characteristics via direct numerical simulations

The time evolution of an initially localized disturbance for spotted values of the chamber stiffness inducing totally different asymptotic behaviors of the system will be analyzed; both the case when gravity is neglected and retained will be examined by means of direct numerical simulation of the governing equation (3.3).

Let's start to analyze the simplified condition of parallel main flow, in which gravity is neglected. The spatio-temporal representation of numerically computed solutions to eq. (3.3), in terms of centreline deflection ℓ and lateral velocity v, evaluated for $\mathcal{K}$ values

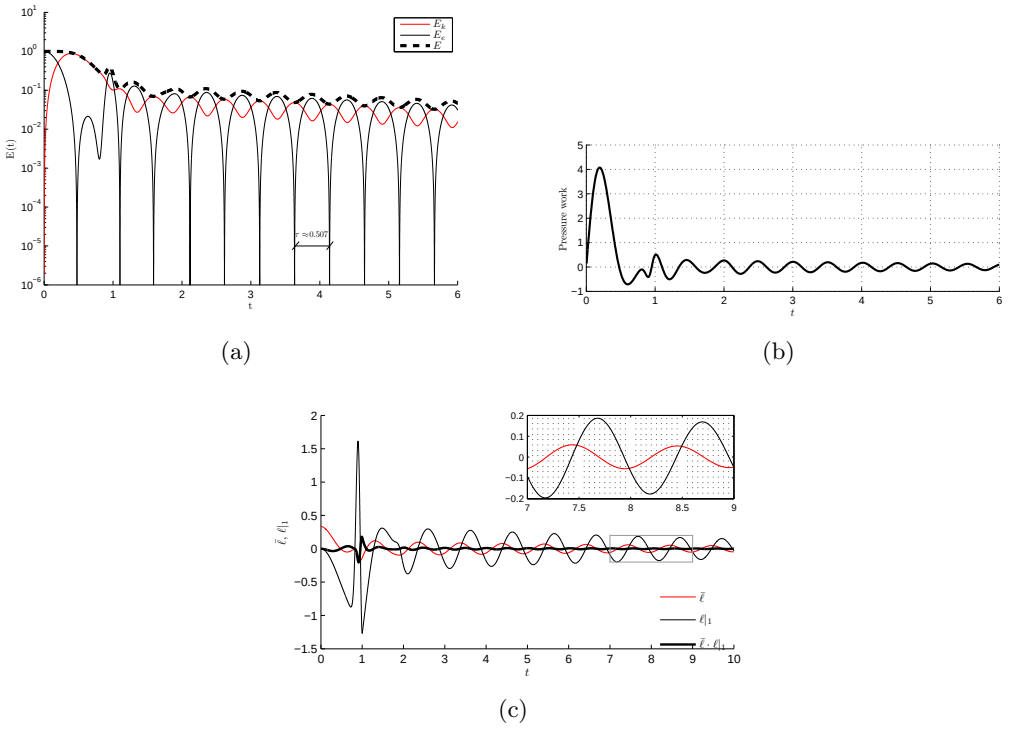

FIGURE 3.3: Temporal evolution of the disturbance energy (a), pressure work (b) and normalized outlet E_e convective exchange (c), for $\mathcal{K} = 18$ and Fr =0

inducing a different asymptotic behavior of the energy norm, are reported in Figures 3.1 and 3.2. The initial condition of the simulations is constituted by a compact support function satisfying the prescribed boundary conditions, i.e. a Gaussian-like pulse for the perturbed centreline deflection ℓ, localized near the upper boundary; no perturbation in lateral velocity fluctuation v is considered here.

As can be observed from the simulations, the centreline pulse, initially localized near the upper boundary, travels without significantly modifying its own structure until it reaches the opposite boundary. However, immediately the velocity disturbance is forced to assume non-null finite values, with a non-zero integral average over the domain. This is due to the momentum equation (3.2), in which the transport of v is governed by the global reaction of the air enclosure, which depends in turn by the centreline fluctuation ℓ. For relatively small $\mathcal{K}$ values the ℓ transport equation, eq. (3.1), behaves practically as a pure advection model, with the forcing (represented by the lateral velocity v) becoming insignificant, as can be clearly observed in simulations of Figure 3.1, carried out for a $\mathcal{K}$ value close to the marginally stable critical value in absence of gravity. A different scenario is found as $\mathcal{K}$ increases, due to the enhancing of the mutual influence of the disturbances that induces the original pulse to lose its compact support while it travels towards the outlet boundary. Such a deviation from its original structure becomes increasingly important as $\mathcal{K}$ increases giving rise to a wave-packet generation,

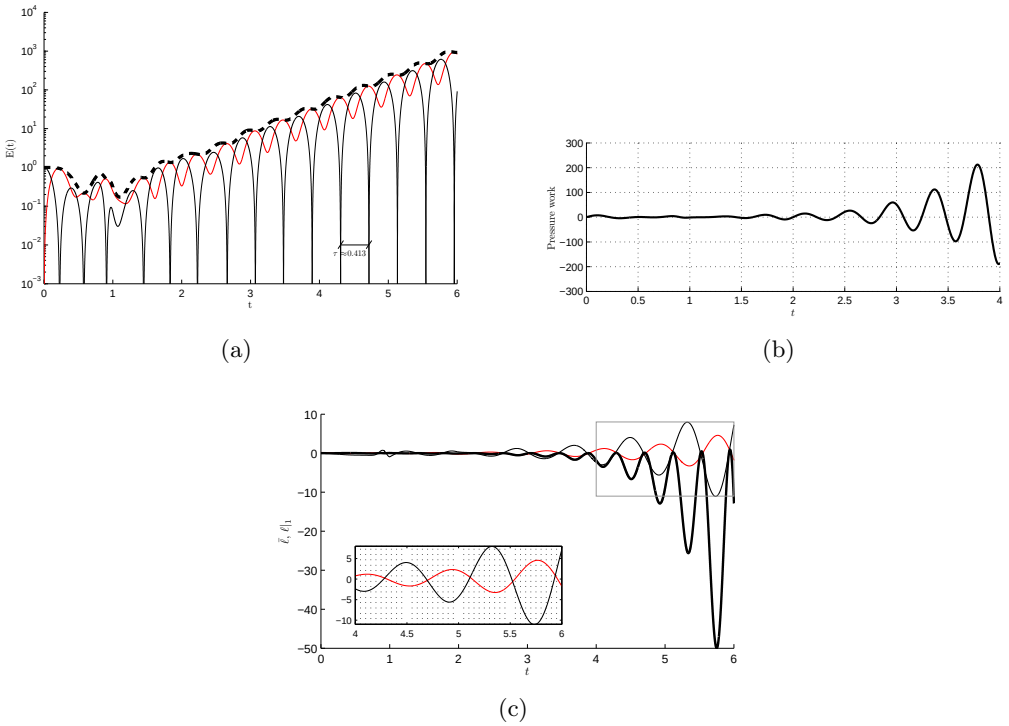

FIGURE 3.4: Temporal evolution of the disturbance energy (a), pressure work (b) and normalized outlet E_e convective exchange (c), for $\mathcal{K} = 58.87$ and $Fr = 0$

placed behind the Gaussian bump, the structure of which is enhanced with increasing air stiffness parameter. More remarkable, numerical simulations show that after the initial transient, whose duration, $t = 1$, represents the marching time at constant velocity of the pulse disturbance over the entire domain, a continuous generation of new pulses, affecting the entire length of the sheet, is induced due to the action of the air chamber over the compliant sheet. The continuous triggering of pulses gives rise to an asymptotic regime where the time-depending behavior of the perturbation experiences an oscillating trend with a constant period that is determined by the parameter $\mathcal{K}$, in both stable and unstable situations.

Such typical transient behaviors can be better appreciated in Figures 3.3-3.4, referring to stable and unstable cases, respectively, in the absence of gravity, and in Figures 3.5-3.6, corresponding to stable and unstable, respectively, gravitational cases. Each figure depicts the time variation of total energy of the disturbance, including the kinetic and elastic components, in frame (a); the pressure work per unit time introduced at the righthand side of eq. (3.8), in frame (b); the contribution to the rate of change of the total energy yielded by the convective exchange of elastic energy at the outlet in eq. (3.12), scaled by the constant $-\mathcal{K}U_1$, together with the single trends of $\bar{\ell}$ and ℓ_1, in frame (c). All energy terms are scaled with respect to the initial elastic energy E_e of the original pulse.

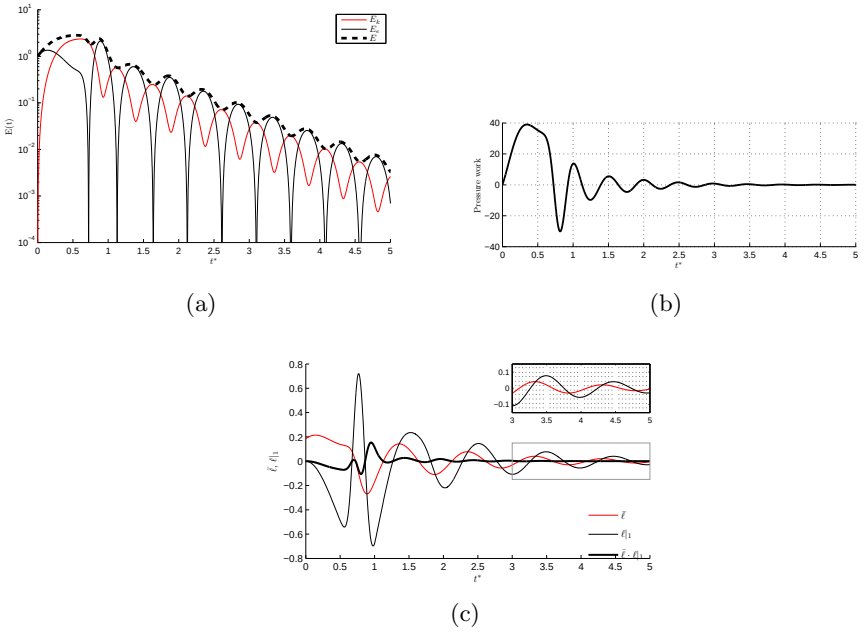

(a) (b)

(c)

FIGURE 3.5: Temporal evolution of the disturbance energy (a), its time derivative (b) and normalized outlet E_e convective exchange (c), for $\mathcal{K} = 58.87$ and $Fr = 20$

In both cases of $Fr = 0$, Figures 3.3 and 3.4 show that, after an initial transient where the total energy does not exhibit any short time amplification, all the energy contributions follow a perfectly regular time oscillating trend. The period τ of such oscillations matches that of the pressure work exchanged with the air chamber, represented in frame (b) of the figures, as well as that of the convective exchange of elastic energy (thick line) in

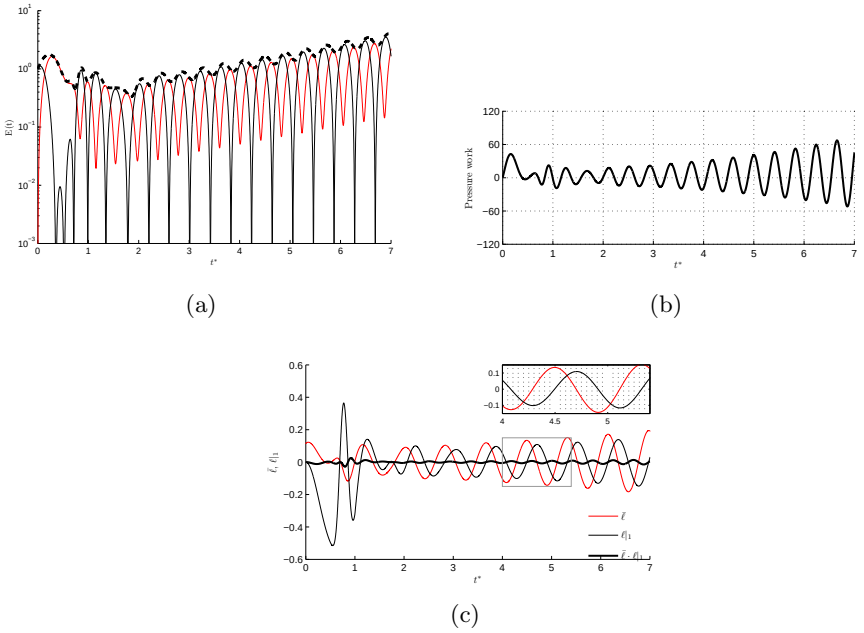

(a) (b)

(c)

FIGURE 3.6: Temporal evolution of the disturbance energy (a), its time derivative (b) and normalized outlet E_e convective exchange (c), for $\mathcal{K} = 160$ and $Fr = 20$

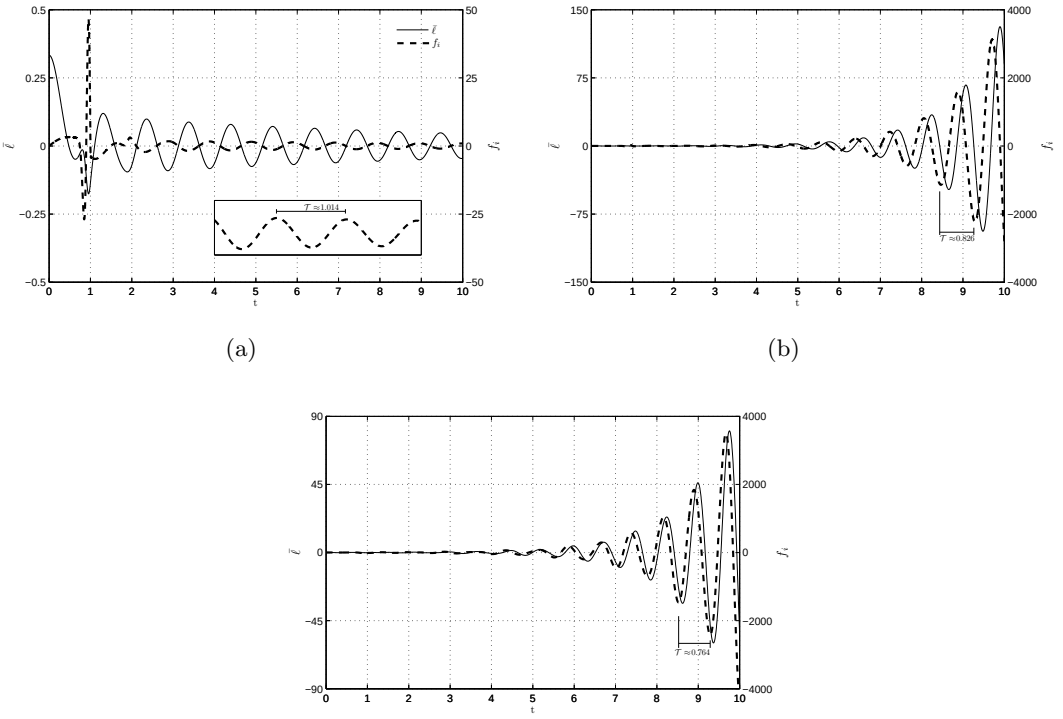

FIGURE 3.7: Temporal evolution of $\bar{\ell}$ and self-induced forcing f_i for (a) $\mathcal{K} = 18$, (b) $\mathcal{K} = 58.87$ and (c) $\mathcal{K} = 100$.

frame (c). Of course the period shown in figures is half of that of the nappe centerline displacement $\mathcal{T}$. Note also that in the unstable case $\bar{\ell}$ and ℓ_1 are almost in phase opposition, coherently with findings suggested in the previous section, while in the stable one they are close to the phase quadrature. The gravitational cases with $Fr = 20$ of Figures 3.5-3.6 (where, for the sake of convenience, the dimensionless time t^* over the crossing time is introduced) feature basically the same characteristic results. Note that the value of $\mathcal{K}$ ≈59, here stable, represented an unstable situation in the absence of gravity, in agreement with the theoretical prediction that when gravity is relevant the falling time is reduced and the instability threshold, $\mathcal{T} = t_\mathrm{cross}$, moves $\mathcal{K}$ towards higher values. However, although gravity plays an asymptotic stabilizing role, Figures 3.5 and 3.6 clearly show that the total energy exhibits a short time growth due to the production term present at righthand side of eq. (3.12).

Other considerations about the asymptotic behavior of the system can be also inferred from the dynamical point of view, specifically by bearing in mind the lumped system of eq. (3.7). The self-induced forcing f_i is implicitly dependent on the value of the parameter $\mathcal{K}$; in general, it is found that it amplifies or decays asymptotically in time depending on whether the disturbances total energy amplifies or decays. Although it is not possible to determine in closed form the time trend of f_i as a function of $\mathcal{K}$, similar

to the standard driven damped spring-mass oscillators, the phase lag between forcing and system response depends on the relative values of forcing frequency and oscillator natural frequency. Here, for the simplified case of no gravity, from eq. (3.7) one can deduce that the natural frequency is $\lambda_N = \sqrt{\mathcal{K} - 1}$. Depending on the assumed frequency of f_i with respect to λ_N three different scenarios are possible. Figure 3.7 shows a comparison between the time evolution of the average sheet displacement $\bar{\ell}$, i.e. the spring displacement, and the forcing f_i, i.e. the right hand side of eq. (3.7). In the frame (a), corresponding to the stable configuration for $\mathcal{K}$=18, it can be observed that, after the initial transient, $\bar{\ell}$ and f_i are almost in phase opposition, because the spring-mass motion is forced at a frequency (about equal to 6.19) greater than its natural frequency ($\lambda_N \approx$ 4.12). This is a general behavior, found for all the stable values of $\mathcal{K}$. Furthermore, the oscillation period $\mathcal{T}$ of f_i is exactly twice the oscillation period τ of the system's energy, as can be observed by comparing the inset of frame (a) and Figure 3.3a. The asymptotical stabilization of the system can be explained, from a dynamical point of view, by considering the effect of a continuously reducing forcing acting on a damped system. On the contrary, frames (b) and (c) correspond to unstable configurations. As will be clarified by the subsequent stability analysis, unstable configurations offer different scenarios in which, as $\mathcal{K}$ increases, the driving term f_i can result in phase, phase quadrature and phase opposition with respect to the spring displacement $\bar{\ell}$ (e.g., see Figure 3.12b). This is clearly confirmed in simulations of Figure 3.7 showing, in frame (b), the phase quadrature between $\bar{\ell}$ and f_i corresponding to the resonance condition for $\mathcal{K}$=58.87 and, in frame (c), the circumstance that $\bar{\ell}$ and its forcing term are almost in phase, with the frequency of f_i being lower than the natural one ($\lambda_N \approx 9.95$). Of course, also in unstable configurations the system's energy oscillates with a period exactly matching the semi-period of the self-induced forcing, as can be observed for the resonance case depicted in Figures 3.4a and 3.7b.

3.4 Spectral stability analysis

A comprehensive methodology to analyze the problem governed by eq. (3.3) consists of formulating a boundary value eigenvalues problem. The standard approach to obtain global solutions consists of separating the variables and assuming the following form of the disturbance: $\ell(x,t) = \hat{\ell}(x) \cdot e^{\lambda t}$. This leads to the eigenvalue problem:

$$\lambda^2 \hat{\ell} + (2\lambda U + F_r)\, D\hat{\ell} + U^2 D^2 \hat{\ell} = -\frac{\mathcal{K}}{H}\hat{\bar{\ell}} \tag{3.14}$$

with D denoting spatial derivative along x direction, $\hat{\ell}$ the eigenfunction and λ the complex eigenvalue.

3.4.1 Analytical approach in no-gravity case

In the special case of no-gravity, $Fr = 0$, it is straightforward to obtain the characteristic eigenvalue equation in closed form. By integrating the above equation over the whole length of the nappe and by employing the relevant boundary conditions, $\hat{\ell}_0 = D\hat{\ell}_0 = 0$, one obtains that the average sheet deflection is a linear combination of $\hat{\ell}_1$ and $D\hat{\ell}_1$:

$$\hat{\bar{\ell}} = -\frac{2\lambda\hat{\ell}(1) + D\hat{\ell}(1)}{\lambda^2 + \mathcal{K}} \tag{3.15}$$

and hence:

$$D^2\hat{\ell} + 2\lambda D\hat{\ell} + \lambda^2\hat{\ell} = \frac{2\lambda\hat{\ell}(1) + D\hat{\ell}(1)}{1 + \frac{\lambda^2}{\mathcal{K}}}.$$

Integrating the above equation produces:

$$\hat{\ell} = \frac{\mathcal{K}\hat{\bar{\ell}}}{\lambda^2}\left[(1 + \lambda x)\, e^{-\lambda x} - 1\right]$$

and, as a consequence of eq. (3.1),

$$\hat{v} = \frac{\mathcal{K}\hat{\bar{\ell}}}{\lambda}\left[(1 + \lambda x)\, e^{-\lambda x} - 1\right] - \mathcal{K}\hat{\bar{\ell}} x e^{-\lambda x}$$

from which, by taking into account eq. (3.15), eigenvalues λ can be obtained as complex solutions of the characteristic eigenvalue equation

$$\frac{\mathcal{K}}{\mathcal{K} + \lambda^2}\left[\left(\frac{2}{\lambda} + 1\right) e^{-\lambda} - \frac{2}{\lambda}\right] + 1 = 0 \tag{3.16}$$

which, in agreement with a previous statement, does not admit a solution for $\mathcal{K} = 0$.

Apart from the trivial solution $\lambda = 0$, which is not an eigenvalue, eq. (3.16) does not admit any real solution for $\mathcal{K} > 0$, in agreement with the physical considerations requiring that the disturbance has always an oscillating nature due to the driving mechanism of the air chamber. Conversely, complex solutions of eq. (3.16) lie, in the complex plane, along a single branch since the 2^{nd} order partial differential equation (3.3) admits just a single characteristic along which disturbances propagate, namely $\frac{dx}{dt} = U$.

A straightforward manipulation of eq. (3.16), consisting in separating its real and imaginary parts, yields the critical value $\mathcal{K}_{\text{cr}}$ of the air cushion stiffness corresponding to the transition from stable to unstable configurations. Frequencies of the marginally stable disturbances ($\lambda_{\text{r}} = 0$) can be graphically obtained by searching for the contact points

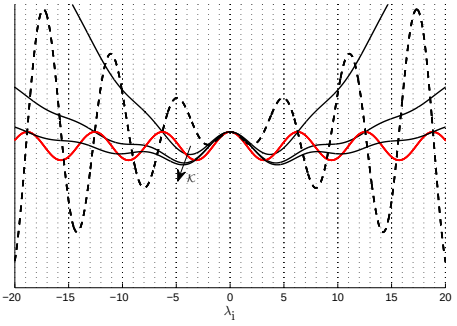

FIGURE 3.8: Functions plot (a) $\cos\lambda_i$ (–), (b) $1-\frac{\lambda_i}{2}\sin\lambda_i$ (- -) and (c) $2\frac{\sin\lambda_i}{\lambda_i}+\frac{\lambda_i^2}{\mathcal{K}}-1$ (–) for $\mathcal{K} = (19.74; 78.96; 177.65)$.

among the functions arising from the complex manipulation of eq. (3.16):

$$\begin{cases} \cos\lambda_i = 1-\dfrac{\lambda_i}{2}\sin\lambda_i \\ \cos\lambda_i = 2\dfrac{\sin\lambda_i}{\lambda_i}+\dfrac{\lambda_i^2}{\mathcal{K}}-1 \end{cases} \tag{3.17}$$

Solutions depend on the value of the $\mathcal{K}$ parameter, however the first contact point (corresponding to $\mathcal{K} = 19.74$) represents a triple point since there is a change in the stability for the solutions of the model equation. Note that the frequency of the first couple of marginally stable modes corresponds to a period matching the required crossing time t_{cross} so that the disturbances can be expelled into the sheet basin, in agreement with the ansatz of section 3.1.

3.4.2 Numerical approach

In the general case the eigenvalue problem (3.14) can be conveniently reformulated starting from eqs. (3.1-3.2) and enforcing the global temporal modes position, so as to recast the governing equations into the following compact matrical form

$$\lambda\begin{pmatrix}\hat{\ell}\\ \hat{v}\end{pmatrix} = \mathcal{A}\begin{pmatrix}\hat{\ell}\\ \hat{v}\end{pmatrix} \tag{3.18}$$

where the spatial operator is

$$\mathcal{A} \equiv \begin{pmatrix} -U\cdot\mathcal{D} & -\mathcal{I} \\ -\dfrac{\mathcal{K}}{H}\displaystyle\int_0^1 dx & -U\cdot\mathcal{D} \end{pmatrix}$$

with $\mathcal{I}$ denoting the identity operator.

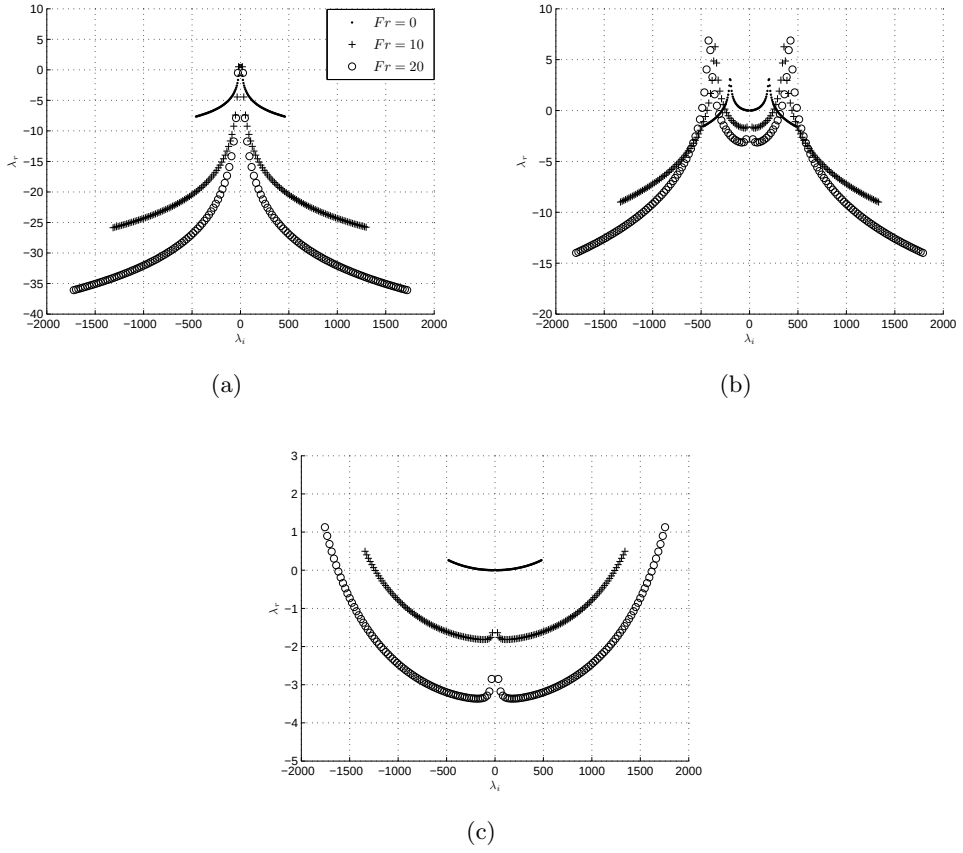

(a) (b)

(c)

FIGURE 3.9: Spectra obtained by varying gravity effects [Fr=0 (·), Fr=10 (+) and Fr=20 (o)] for (a) $\mathcal{K} = 100$, (b) $\mathcal{K} = 4 \cdot 10^4$ and (c) $\mathcal{K} = 10^6$.

For values of $Fr \neq 0$ (and $\mathcal{K} > 0$), eigenvalues and eigenfunctions are numerically computed by means of a Chebyshev collocation method, with both differential and integral terms being spectrally accurate. Figure 3.9 depicts the spectra obtained for various Froude numbers, evaluated for three typical values of stiffness of the air chamber inducing different shapes of distribution of the eigenvalues in the complex plane. The spectra are generally constituted of two symmetric branches with respect to the imaginary axis, each made of infinitely many eigenvalues, whose spreading rate is continuously varying with the gravity effect. The shape of the branches depends on the value assumed by the parameter $\mathcal{K}$ and results to be of three different possible configurations over the entire semi-infinite interval of positive $\mathcal{K}$ values. The major characteristic of the spectra, whatever the equivalent stiffness $\mathcal{K}$, is that each branch exhibits eigenvalues almost equally spaced in imaginary parts. Thus, two characteristic frequencies can be recognized, one related to the constant spacing of imaginary parts $\Delta\lambda_\mathrm{i}$ and the other one to the imaginary part of the leading (i.e. most unstable) modes pair. The latter corresponds to the frequency at which the damped spring-mass system (3.7) oscillates driven by the

self-induced forcing f_{i}, whilst the former is related to the crossing time

$$t_{\mathrm{cross}} = \int_0^1 \frac{dx}{\sqrt{1 + 2Fr\ x}} \tag{3.19}$$

so that, by varying the Froude number, it always results in $\Delta\lambda_{\mathrm{i}} \approx \frac{2\pi}{t_{\mathrm{cross}}}$.

The different configurations assumed by the spectrum as $\mathcal{K}$ is varied are strictly linked to the frequency assumed by the leading mode pair which, in turn, is correlated to the oscillation frequency of the spring-mass oscillator (3.7). For stiffness values of the enclosure air small enough (e.g., see frame (a) of Figure 3.9) the leading mode pair is also the lowest frequency eigenvalues pair of the spectrum; as $\mathcal{K}$ increases, the frequency of the fluid oscillator (3.7) increases accordingly and the leading modes shift outwards to higher frequencies, giving rise to a cascade of "inner" eigenvalue pairs having lower frequency in the neighborhood of the imaginary axis, as displayed in the typical configuration of frame (b); finally, for even higher $\mathcal{K}$ values the oscillation frequency of the spring-mass system can result greater than the numerically computable highest frequency of the spectrum, leading to the shape depicted in frame (c).

As expected, gravity certainly plays a role in determining the shape of the spectrum for a given stiffness $\mathcal{K}$. This is clearly showed in Figure 3.10 in which, for the same air chamber stiffness value as Figure 3.9c, the spectra computed for three different Froude numbers are reported. The initial parabola shaped spectrum represented also in Figure 3.9c changes as Fr increases and becomes analogous in shape to those of Figure 3.9b, so that a typical configuration can be similarly obtained by properly choosing the couple of parameters Fr and $\mathcal{K}$. The reason for this characteristic behavior lies in the mutual role played by gravity and stiffness in influencing the oscillation frequency of the righthand side of eq. (3.7). As the Froude number increases, the crossing time t_{cross} reduces correspondingly; the spacing $\Delta\lambda_{\mathrm{i}}$ among the eigenvalues increases so that the oscillation period $\mathcal{T}$ of the spring-mass system results rapidly higher than the maximum period included into the spectrum computed at the lowest Froude number. As a consequence, the corresponding frequency, initially higher than that of most unstable modes at $Fr = 10$, appears into the "spreading" part of the spectra evaluated at higher Froude numbers, and moves inward as Fr goes up.

The overall stabilizing role played by gravity is clearly confirmed in each frame of Figure 3.9 and Figure 3.10. As the Froude number increases the entire spectrum spreads in the complex plane moving the bulk of its eigenvalues towards even more stable regions. We stress once again that this is a consequence of the reduction of the crossing time acting as a stabilizing effect competing against the forcing mechanism due to the air chamber, according to the ansatz of section 3.1.

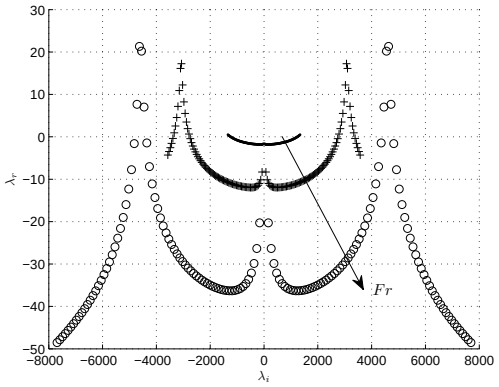

FIGURE 3.10: Spectra obtained by varying gravity effects [Fr=10 (·), Fr=100 (+) and Fr=500 (o)] for $\mathcal{K} = 10^6$.

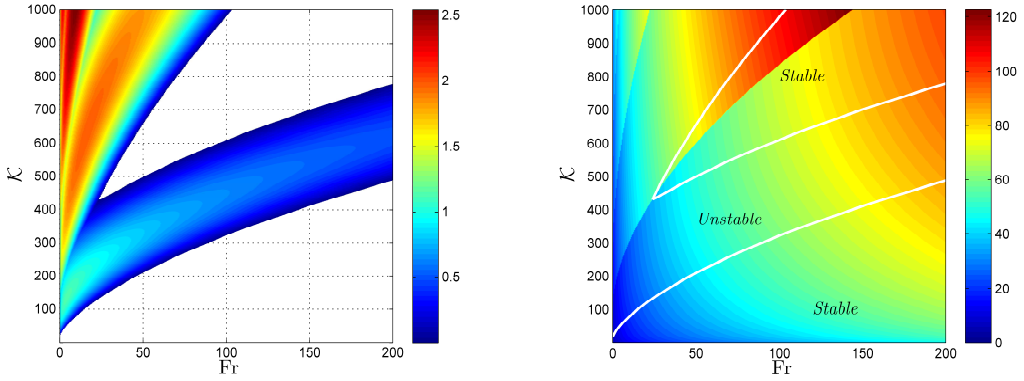

(a) (b)

FIGURE 3.11: Color maps of modal global behavior for a selected range of Froude number and $\mathcal{K}$ values. (a) is growth rate, (b) is frequency. White regions in frame (a) correspond to stable configurations.

Figure **3.11** shows a map of the modal stability/instability regions associated with the leading mode complex pair of the spectrum, obtained for a selected range of $\mathcal{K}$ values and by varying the Froude number from no-gravity case to sufficiently high gravity effects. Growth rates of disturbances are depicted in frame (a), where the color regions represent iso-level positive growth-rates (with stable configurations spotted by blank regions), while in frame (b) the corresponding frequencies of the fluid oscillator (3.7) are reported (the white lines represent the marginal modal curves).

The stabilizing effect induced by gravity on the asymptotic behavior of the system, driven by the leading mode, is clearly illustrated in Figure **3.11**. The stability region in frame (a), already existing in the no-gravity case for values of $\mathcal{K} < 19.74$ (e.g. see Figure 3.8) broadens as described by the marginal stability curve roughly following the trend given by $\mathcal{K} = 26\sqrt{Fr} + 0.6Fr$. However, note that for higher $\mathcal{K}$ values a further stable region occurs, which assumes a wedge-shaped conformation at its lower side and

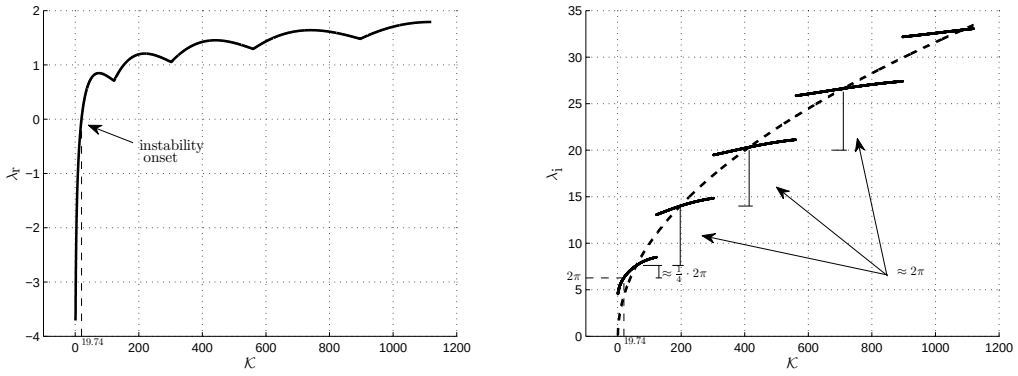

(a) (b)

FIGURE 3.12: Parametric trend with $\mathcal{K}$ of a) growth-rate and b) frequency of the leading mode pair, evaluated at $Fr = 0$. Dashed line in frame (b) represents the natural frequency variation of the lumped system (3.7).

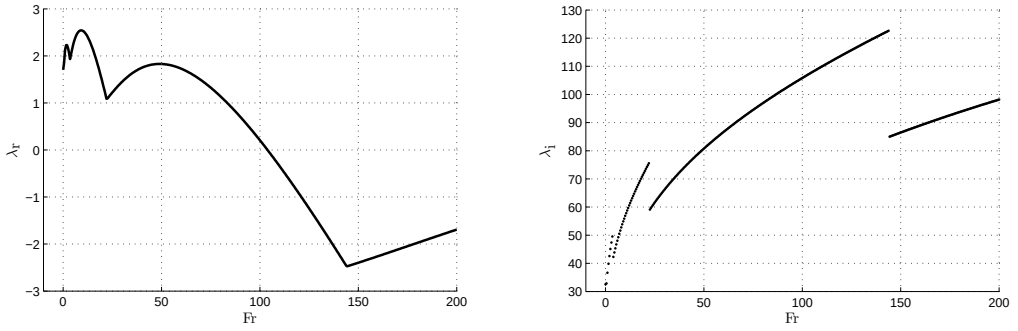

(a) (b)

FIGURE 3.13: Parametric trend with Fr of a) growth rate and b) frequency of the leading mode pair, evaluated at $\mathcal{K} = 1000$.

exhibits for higher Fr values the same trend as the marginal curve underlying. This typical behavior reproduces cyclically as $\mathcal{K}$ grows within the range of $(\mathcal{K}, Fr)$ values inspected (not shown herein). Thus, the map of growth-rate presents a periodic series of wedge-shaped stability regions as $\mathcal{K}$ increases, whose edges continuously shift towards higher Froude numbers. Figure 3.11b shows that in general the oscillation frequency of the leading mode increases with increasing Froude numbers. Moreover, a discontinuous trend with $\mathcal{K}$ is observed at any fixed Fr due to the jump of the leading mode pair of the spectrum, giving rise to the characteristic onion structure depicted in Figure 3.11b.

Such a typical modal behavior with $\mathcal{K}$ and Fr can be better appreciated by looking at Figures 3.12 and 3.13, showing parametric curves obtained by sectioning the maps of Figure 3.11 at fixed Fr and $\mathcal{K}$, respectively. Frames (a) and (b) of Figure 3.12 exhibit growth rate and frequency evolutions with $\mathcal{K}$ when gravity is neglected. Note, in

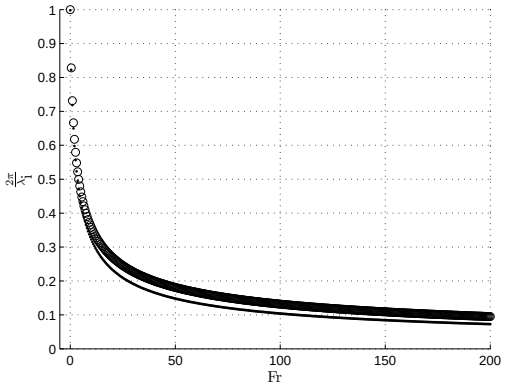

FIGURE 3.14: Deviation with Froude number of the oscillation period $\mathcal{T}$ of the spring-mass system corresponding to the critical transition configurations ($\cdot$) from the analytical predictions (o) of eq. (4.41).

particular, that the frequency plot (b) is piecewise discontinuous due to the presence of additional leading modes in the spectrum at discrete values of $\mathcal{K}$. The dashed line also present in plot (b) refers to the natural frequency variation of the lumped system (3.7). The thin dashed segment in plot (a) marks the marginal value $\mathcal{K}$=19.74 of null growth rate, to which the frequency of λ_i=6.28 corresponds. In other terms, in the absence of gravity, the frequency of the marginal mode is related to the falling time, thus confirming the ansatz of section 3.1. Note also that this is not a resonance frequency, whose values are given by the intersections of the dashed line with the piecewise discontinuous line of Figure 3.12(b). As can be seen inspecting the plot (b), the first value of the resonance frequency is found to be 7.61, with 7.61/6.28=1.21, thus uncovering the *one-plus-one-quarter* criterion of the edge tones problem to a good accuracy. Furthermore, all other higher values are evenly spaced by 6.28. This very interesting result uncovers the theoretical considerations of Schwartz [16] and the experimental findings of Sato et al. [17], which in turn resemble a major characteristic of the edge tone phenomenon [15]. In fact, the possible resonance frequencies are given by the relationship $2\pi(n+\frac{1}{4})$, where n is an integer. At the same time Figure 3.13 reports the growth-rate (frame a) and frequency (frame b) trends obtained by varying the Froude number for the highest $\mathcal{K}$ value depicted in Figure 3.11. The unusual parabolic trend of Figure 3.12a, assumed by the growth-rate of each leading mode pair before being overwhelmed by the adjoining eigenvalue, is basically confirmed in the presence of gravity together with the stretching of the range of a single leading mode as Froude number goes up. Conversely, although gravity enhances the growth-rate of the unstable modes, it plays a stabilizing role because it moves the marginal $\mathcal{K}$ values upwards. Furthermore, the frequency curves of Figure 3.13b, as Fr grows, move along segments having different slopes associated with each leading mode and the corresponding jumps in frequency follow a spreading trend consistent with the frequency associated to the crossing time, $\Delta\lambda_i$, whose negative

amplitude is a result of the parametric behavior shown in Figure 3.10.

It should be pointed out that the perfect agreement found at $Fr = 0$ between the frequency of the marginally stable leading mode pair and the one linked to the spacing $\Delta\lambda_{\mathrm{i}}$ is slightly lost in the presence of gravity, with an increasing discrepancy as the gravitational influence becomes more relevant. This can be observed in Figure 3.14 showing the analytical trend with the Froude number of t_{cross} together with the numerically computed period $\mathcal{T}$ of the spring-mass oscillator, associated with the leading mode. In the presence of a spatially developing base flow, the neutral stability criterion is fulfilled for oscillation periods $\mathcal{T}$ smaller than the corresponding crossing time t_{cross} .

Chapter 4

Surface tension effects

In this chapter, the effects of surface tension on the global dynamics of nappe oscillation will be investigated.

The introduction of the *local* Weber number, based on the local liquid velocity $U(x)$ and local sheet thickness $H(x)$ (eq. 2.23)

$$We_l = \frac{\rho_1 U(x)^2 H(x)}{2\sigma} \tag{4.1}$$

i.e. also,

$$We_l = \frac{U^2(x)}{c^2(x)} \tag{4.2}$$

where

$$c(x) = \sqrt{\frac{2\sigma}{\rho_1 H(x)}} \tag{4.3}$$

with c being the wave velocity of sinuous disturbances (de Luca and Costa [18]), allows one to affirm that if $We > 1$, then $We_l > 1$ at each location, and the flow can be considered *supersonic*-like for the wave-patterns evolution. On the contrary, if the inlet Weber number is less than unit (i.e., *subsonic*), since the local Weber number is increasing along the downstream direction, a *transonic* location inside the sheet separates an initially *subsonic* region from a downstream *supersonic* region. Note that the relationship holds too

$$We_l = We\frac{H^*_{\text{in}}}{H(x)} = We\frac{U(x)}{U^*_{\text{in}}} \tag{4.4}$$

Since the experimental evidence is that generally the sheet can break up for $We < 1$, the analysis of the transonic flow regime (i.e., initially subsonic) is a crucial topic. From the theoretical viewpoint the problem is not straightforward, because the governing equation exhibits a singularity just at the transonic station (where $We_l = 1$), as documented also by the previous literature (Finnicum et al. [19], Weinstein et al. [20], Ramos [21, 22]). All these authors evidence and analyze the nature of the singularity, although no one solved definitely the time-dependent equations governing the shape of the subsonic nappe. The present chapter is aimed at developing a theoretical/numerical procedure to fill up this lack of information.

Note that the treatment reported hereafter can be found in [23].

4.1 Overall insight on the nappe dynamics

In order to give more physical insight on the fluid system under study, the equations for sinuous disturbances (focus of the present analysis) can be properly rearranged by taking into account integral quantities depending on the sheet extension as a whole. As already showed in the previous chapter, it is globally modeled as a lumped one-degree-of-freedom spring-mass system, in which the role of the spring is played by the air into the enclosure and the mass is that of the liquid sheet itself.

Let's start to reconsider the system of equations (2.24-2.25) in terms of a single second order integro-differential equation

$$\frac{D^2\ell}{Dt^2} - \frac{U}{We}\frac{\partial^2\ell}{\partial x^2} = -\frac{\mathcal{K}}{H}\bar{\ell} \tag{4.5}$$

where $\frac{D}{Dt}$ is the substantial derivative. Such an equation governs the linear inviscid evolution of a generic disturbance subjected to the integral reaction term of the right hand side. The role played by the air stiffness $\mathcal{K} \geq 0$ is crucial in characterizing the dynamics of the self-sustained wave-patterns evolving into the curtain. If $\mathcal{K} = 0$ the equation is trivial, reducing to the simple wave equation with velocity $\pm\sqrt{U/We}$ relative to that of the basic flow U, basically equipped with a perfectly reflecting boundary condition at inlet, $\ell(0) = 0$, and free-outflow condition at outlet. In the fixed reference frame the wave velocity is

$$U \pm \sqrt{\frac{U}{We}} \tag{4.6}$$

which can also be recast in the form

$$U\left(1 \pm \sqrt{\frac{1}{We_l}}\right) \tag{4.7}$$

On the other hand, it is straightforward to verify that in the absence of reaction the wave equation admits solutions of the kind

$$\ell = Ae^{ik(x-at)} \tag{4.8}$$

where $a = U\left(1 \pm \sqrt{\frac{1}{We_l}}\right)$, k is any real wavenumber and A is a constant.

Particular attention has to be paid to enforce the boundary conditions depending on whether the inlet Weber number is supersonic or subsonic. In fact, in the first case two boundary conditions are prescribed at the inlet location, $x = 0$, namely $\ell(0) = 0$ and $\frac{\partial \ell}{\partial x}(0) = 0$ (which in turn means $v(0) = 0$), whilst in the latter case the condition, $\ell(0) = 0$, has to be retained at the inlet section, and another one has to be considered at a downstream location. It will be discussed that the second condition, indeed, is employed to remove the singularity of the equation and is enforced just at the singularity location.

In the absence of the reaction term, one has to expect that any compact support disturbance introduced in the field splits in two parts: in supersonic conditions the one traveling on the left direction, after reflection at the inlet boundary, is eventually expelled through the right boundary as the other one, initially travelling on the right direction, does too; in subsonic local conditions both perturbations produced by the initial splitting travel towards the outlet and are expelled. Thus, if no input is introduced at the left boundary, after a finite time any solution vanishes, with the disturbance being continually expelled at the outlet of the domain. Conversely, the presence of the reaction term in the form of an integral changes things in such a way that the temporal evolution of the disturbance is by no means identically null after a finite time. As will be shown in the subsequent investigations, depending on the stiffness of the air chamber adjacent to the sheet, the system dynamics exhibits different features in terms of both stability properties and energy time evolution.

A major conjecture is that, due to the perfect reflecting character of the left boundary, at very large times the upstream characteristics is nihil potent in the sense any disturbance propagating towards the left direction will be only reflected and thus its asymptotic

behavior will be the same as that the disturbances propagating on the right direction. In summary, one has to expect two-branches spectra in supersonic cases and just one branch in subsonic cases. Moreover, bearing in mind the ansatz stated in the section 3.1, i.e. the system is stable if the crossing time of a disturbance over the entire domain length is less than the period of the spring-mass oscillator, another conjecture is that the subsonic case is generally less stable than the supersonic one, both tending to the behavior in the absence of surface tension when We number tends to infinity. As found by previous contributions (Schmid & Henningson [9], de Rosa et al. [12]), the integral reaction term contributes to *separate* the single modes in such a way that the corresponding eigenvalues of the spectrum have different real coefficient (and almost evenly spaced imaginary coefficients, with the distance among them corresponding to the crossing time). Under this aspect, the reaction term acts similarly to the boundary damping term of the example n. 4 of Trefethen [24]. The result is that at large times one has to expect the emergence of an unstable o less stable single mode which corresponds, as will be seen hereafter, to the response of the system behaving as a forced-damped oscillator. Of course, since the oscillator works in the driven regime, the oscillation period does not correspond to the natural frequency of oscillation and in general it cannot be determined in analytical closed form. It should be stressed that this ansatz includes the gravity effects, in the sense that in the presence of gravity effects a shorter crossing time is expected, as well as a higher $\mathcal{K}$ threshold of instability. Moreover, surface tension should have a stabilizing influence in subsonic situations (the downstream travelling modes are faster), while one can expect that the upstream directed modes of supersonic conditions are less stable. In transonic regime, when passing from subsonic to supersonic conditions, the slower branch of the spectrum is expected to appear abruptly, whilst the faster branch should be continuous. Such predictions will be confirmed by the subsequent spectral analysis, which will be further corroborated by direct numerical simulations.

After expressing the substantial derivative in explicit form, integrating eq. (4.5) over the whole length of the sheet yields:

$$\bar{H}\frac{d^2\bar{\ell}}{dt^2} + 2\frac{d\bar{\ell}}{dt} + \mathcal{K}\bar{\ell} = \underbrace{-2\frac{d}{dt}\int_0^1 x\frac{\partial \ell}{\partial x}dx - \left[\left(U - \frac{1}{We}\right)\frac{\partial \ell}{\partial x}\right]_0^1}_{f_\mathrm{i}} \tag{4.9}$$

where f_i represents the self-induced forcing acting on the elastic oscillator and the boundary condition at the inlet location, $\ell(0) = 0$, has been considered. Eq. (4.9) exhibits a strict analogy with the motion equation of an elastic oscillator, where $\bar{H}$ denotes the mass of the liquid sheet and $\mathcal{K}$ is the equivalent spring stiffness of the enclosure air. A proper manipulation allowed one to extract a damping term. Of course, in supersonic regime it results $\left.\dfrac{\partial \ell}{\partial x}\right|_0 = 0$.

In summary, the global dynamics of the nappe consists of the mutual interaction of the centerline local deflection with the compliant air chamber which behaves as a spring acting on the average sheet deflection. Eq. (4.5) shows that the local deflection is forced by the global reaction term of the spring, whilst the dynamics of the global spring-mass oscillator is driven by a combination of local sheet displacement values, as described by eq. (4.9). In the following part of the chapter it will be correlated such a mutual forcing to special features of the eigenvalues spectrum; the spectrum uncovers the natural mode (possibly unstable) of the spring-mass system and the peculiar oscillating behavior of the nappe described not just by single modes, but by the superposition of a number of modes to be ascribed essentially to Eq. (4.5) and physically connected to another characteristic frequency linked to the typical crossing (or falling) time.

4.2 Disturbance energy evolution

In order to investigate some features of the solutions of eqs. (4.5) and (4.9), it is useful to examine the mechanisms of perturbation growth (or decay) by considering also the time behavior of the system's energy E. For sinuous disturbances the energy balance equation can be derived by multiplying eq. (2.25) by the lateral velocity fluctuation v, and then by integrating it over the whole volume (per unit length in transversal direction) of the sheet. Eliminating the lateral velocity v with the aid of eq. (2.24), where the convective term is integrated by parts, as made in the previous chapter, one can obtain:

$$\frac{d}{dt}(E_\mathrm{k}+E_\sigma+E_e)+\frac{v^2}{2}\bigg|_0^1+\frac{1}{2We}\left(\frac{\partial \ell}{\partial x}\right)^2\bigg|_0^1=-\mathcal{K}\bar{\ell}U_1\ell_1+\frac{1}{We}v\frac{\partial \ell}{\partial x}\bigg|_0^1+ \tag{4.10}$$

$$+\mathcal{K}\bar{\ell}\int_0^1\frac{dU}{dx}\ell\,dx-\frac{1}{2We}\int_0^1\frac{\partial U}{\partial x}\left(\frac{\partial \ell}{\partial x}\right)^2\,dx \tag{4.11}$$

where the kinetic energy E_k, the surface tension energy E_σ, and the elastic energy E_e of the enclosure air are defined respectively as

$$E_\mathrm{k}=\frac{1}{2}\int_0^1 Hv^2\,dx \tag{4.12}$$

$$E_\sigma=\frac{1}{2We}\int_0^1\left(\frac{\partial \ell}{\partial x}\right)^2\,dx \tag{4.13}$$

$$E_\mathrm{e}=\frac{1}{2}\mathcal{K}\,\bar{\ell}^2. \tag{4.14}$$

and the energy terms are made dimensionless with respect to the reference energy $E_{\mathrm{r}}^{\star} = \rho_{\mathrm{l}} \ell_{\mathrm{r}}^{\star} L_{\mathrm{r}}^{\star} v_{\mathrm{r}}^{\star 2}$.

Of course the sum under derivative at left hand side of eq. (4.11) represents the total energy defined as

$$E = E_{\mathrm{k}} + E_{\sigma} + E_{\mathrm{e}} \tag{4.15}$$

By making considerations analogous to those already discussed in the previous chapter to evaluate the averaged value of a product of *small* quantities (the sheet thickness slope and perturbations are small), the energy balance can be written as

$$\frac{dE}{dt} + \frac{v^2}{2}\bigg|_0^1 + \frac{1}{2We}\left(\frac{\partial \ell}{\partial x}\right)^2\bigg|_0^1 = -\mathcal{K}\bar{\ell}U_1\ell_1 + \frac{1}{We}v\frac{\partial \ell}{\partial x}\bigg|_0^1 + \mathcal{K}\bar{\ell}^2\overline{\left(\frac{dU}{dx}\right)} - \frac{1}{2We}\overline{\left(\frac{d\ell}{dx}\right)^2}\overline{\left(\frac{dU}{dx}\right)} \tag{4.16}$$

where it holds also

$$\overline{\left(\frac{dU}{dx}\right)} = Fr \cdot t_{\mathrm{cross}} \tag{4.17}$$

with t_{cross} being the marching time needed by the perturbation to cross the entire domain.

Note that $\frac{v^2}{2}\Big|_0^1$ and $\frac{1}{2We}\left(\frac{\partial \ell}{\partial x}\right)^2\Big|_0^1$ represent the convective exchange terms of kinetic and surface tension energy, respectively, at the ends of the domain; $-\mathcal{K}\bar{\ell}U_1\ell_1$ and $\frac{1}{We}v\frac{\partial \ell}{\partial x}\Big|_0^1$ are the convective exchange of elastic energy at the outlet (namely, the work flux related to the pressure) and the analogous work flux related to the surface tension, respectively; $\mathcal{K}\bar{\ell}^2\overline{\left(\frac{dU}{dx}\right)}$ and $-\frac{1}{2We}\overline{\left(\frac{d\ell}{dx}\right)^2}\overline{\left(\frac{dU}{dx}\right)}$ can be interpreted as two production terms of disturbances total energy extracted from the stretching (i.e. non parallel) basic flow, the former directly related to the pressure field inside the chamber, the latter to the surface tension. Since the basic flow, driven by the gravity field, accelerates along the streamwise direction, the production term due to the external pressure is always positive, whilst that due to the surface tension is always negative. As already observed in the previous chapter, one cannot infer any conclusions about the asymptotic behavior of the total energy; nevertheless, due to the positive gravity production term, one can expect a short time growth also in asymptotically stable situations and this is possible even when the gravitational effects are negligible. On the contrary, surface tension plays in any case

a stabilizing role (some numerical results obtained via direct numerical simulations are showed in [25], see Appendix).

These theoretical predictions will be confirmed hereafter by means of the linear stability analysis.

4.3 Linear stability analysis

A comprehensive methodology to analyze the asymptotic global behavior of the nappe dynamics consists of formulating a boundary value eigenvalues problem. This can be conveniently carried out starting from eqs. (2.24-2.25) and enforcing the global temporal modes position, i.e. by separating the variables and assuming the following form of the disturbances: $\ell(x,t) = \hat{\ell}(x) \cdot e^{\lambda t}$ and $v(x,t) = \hat{v}(x) \cdot e^{\lambda t}$, where $\hat{\ell}$ and $\hat{v}$ are the eigenfunction and λ is the complex eigenvalue. This permits one to recast the governing equations into the following compact matrical form

$$\lambda \begin{pmatrix} \hat{\ell} \\ \hat{v} \end{pmatrix} = \mathcal{A} \begin{pmatrix} \hat{\ell} \\ \hat{v} \end{pmatrix} \tag{4.18}$$

where the spatial operator is

$$\mathcal{A} \equiv \begin{pmatrix} -U \cdot \mathcal{D} & -\mathcal{I} \\ \frac{U}{We} \cdot \mathcal{D}^2 - \frac{\mathcal{K}}{H} \int_0^1 dx & -U \cdot \mathcal{D} \end{pmatrix}$$

with $\mathcal{I}$ denoting the identity operator, and $\mathcal{D}$ and $\mathcal{D}^2$ the first and the second spatial derivatives, respectively.

Eigenvalues and eigenfunctions are numerically computed by means of a Chebyshev collocation method in MATLAB environment, with both differential and integral terms being spectrally accurate.

As already anticipated before, for inlet supersonic conditions, $We > 1$, the two boundary conditions are both imposed at inlet section, i.e.

$$\hat{\ell}(0) = 0 \tag{4.19}$$

$$\left.\frac{\partial \hat{\ell}}{\partial x}\right|_0 = 0 \tag{4.20}$$

On the contrary, for inlet subsonic conditions, $We < 1$, due to the upstream directed wave characteristic velocity $U-a$, the perfectly reflecting conditions $\hat{\ell}(0) = 0$ only can be retained at the inlet boundary. On the other hand, as will be seen hereafter, for subsonic inlet at large times the eigenvalues equation becomes singular and just the condition to remove this singularity constitutes the required second boundary condition.

4.3.1 Singularity treatment

To highlight the presence of a singularity in the equation governing sinuous disturbances in subsonic flow conditions let us to reconsider the system of equations (2.24-2.25), where the kinematic condition is employed to substitute the lateral velocity v into the y-momentum balance equation. It is found

$$\frac{\partial}{\partial x}\left[\left(U-\frac{1}{We}\right)\frac{\partial \ell}{\partial x}\right]+2\frac{\partial}{\partial x}\left(\frac{\partial \ell}{\partial t}\right)+\frac{1}{U}\frac{\partial^2 \ell}{\partial t^2}=-\mathcal{K}\bar{\ell} \tag{4.21}$$

Enforcing the global temporal modes position yields the eigenvalue relationship

$$\frac{d}{dx}\left[\left(U-\frac{1}{We}\right)\frac{d\hat{\ell}}{dx}\right]+2\lambda\frac{d\hat{\ell}}{dx}+\lambda^2\frac{1}{U}\hat{\ell}=-\mathcal{K}\bar{\ell} \tag{4.22}$$

This is a Sturm-Liouville like eigenvalue integro-differential equation. It is singular since the second order term coefficient vanishes at the location where the flow, accelerating due to gravity, reaches a critical U velocity equating $1/We$. This singularity has been removed by developing the following procedure.

Integrating eq. (4.21) from the inlet location to the generic location x and resolving for $\frac{\partial \ell}{\partial x}$, yields

$$\frac{\partial \ell}{\partial x}=\frac{-\mathcal{K}x\bar{\ell}-2\frac{\partial \ell}{\partial t}-\frac{\partial^2}{\partial t^2}\int_0^1\frac{\ell}{U}\,dx+\left(1-\frac{1}{We}\right)\frac{\partial \ell}{\partial x}\Big|_0}{U-\frac{1}{We}} \tag{4.23}$$

Eliminating in a convenient way $\frac{\partial \ell}{\partial t}$ from the third addend of the numerator of the above equation by making use of the kinematic boundary condition, gives an expression for the local slope of the sheet centerline, which depends, in addition to the other terms, on the slope value at the inlet location.

$$\frac{\partial \ell}{\partial x} = \frac{-\mathcal{K} x \bar{\ell} - \frac{\partial \ell}{\partial t} - \frac{\partial}{\partial t}\int_0^1 \frac{v}{U}\, dx + \left(1 - \frac{1}{We}\right)\left.\frac{\partial \ell}{\partial x}\right|_0}{U - \frac{1}{We}} \tag{4.24}$$

It has been already stated that in supersonic conditions, since the perturbations do not travel upstream, it is generally assumed $\left.\frac{\partial \ell}{\partial x}\right|_0 = 0$, as observed also experimentally by Finnicum et al. [19] in the steady state situation. On the other hands, note that in supersonic regime the denominator never vanishes in any location. Things change dramatically in subsonic regime since at the critical station where the local Weber numer is unit, the denominator of eq. (4.24) vanishes. Since for inlet Weber numbers weakly less than unit the sheet can *survive* without rupture, one can hypothesize that the sheet assumes an initial slope such as to eliminate this singularity (Finnicum et al. [19]). The idea is to evaluate the initial slope $\left.\frac{\partial \ell}{\partial x}\right|_0 = 0$ which nullifies the numerator of eq. (4.24) and to substitute it into the equation itself, so as to obtain an undetermined ratio. It is found

$$\left.\frac{\partial \ell}{\partial x}\right|_0 = \frac{\mathcal{K} x_s \bar{\ell} + \frac{\partial \ell}{\partial t}(x_s) + \frac{\partial}{\partial t}\int_0^{x_s} \frac{v}{U}\, dx}{1 - \frac{1}{We}} \tag{4.25}$$

and the relationship of the slope at any generic station x assumes the form

$$\frac{\partial \ell}{\partial x} = \frac{\mathcal{K}(x_s - x)\bar{\ell} + \frac{\partial \ell}{\partial t}(x_s) - \frac{\partial \ell}{\partial t}(x) - \frac{\partial}{\partial t}\int_{x_s}^{x} \frac{v}{U}\, dx}{U - \frac{1}{We}} \tag{4.26}$$

where x_s is the location where $U = \frac{1}{We}$, namely where $We_l = 1$, given by

$$x_s = \frac{1 - We^2}{2 Fr We^2} \tag{4.27}$$

Applying De L'Hopital's rule allows one to calculate the singular limit as

$$\left.\frac{\partial \ell}{\partial x}\right|_{x_s} = \frac{-\mathcal{K}\bar{\ell} - \frac{\partial}{\partial t}\left[\left.\frac{\partial \ell}{\partial x}\right|_{x_s}\right] - We \left.\frac{\partial v}{\partial t}\right|_{x_s}}{Fr We} \tag{4.28}$$

or else, considering the asymptotic large time behavior of the eigenfunctions

$$\left.\frac{\partial \hat{\ell}}{\partial x}\right|_{x_s} = \frac{-\mathcal{K}\bar{\hat{\ell}} - \lambda We \cdot \hat{v}(x_s)}{\lambda + Fr We}. \tag{4.29}$$

In summary, for subsonic flow inlet, the boundary conditions to be enforced in solving the eigenvalue problem are expressed by eq. (4.29) together with $\hat{\ell}(0) = 0$.

An analytical study of the singularity has been developed in order to provide further insights on the modal behaviour of the system. Just some theoretical considerations useful to predict and confirm numerical results will be stressed although, as it will be seen, a complete analytical solution can be obtained, at least for certain values of the governing dimensionless parameters We and Fr. For our purposes, it will be neglected the pressure term in the equation (4.22), the presence of which does not influence the singularity features. Therefore, it will be made reference to the following equation (the first derivative which appears in the equation (4.22) has been developed)

$$\underbrace{U\left(U - \frac{1}{\mathrm{We}}\right)}_{P}\frac{d^2\hat{\ell}}{dx^2} + \underbrace{(2U\lambda + 1)}_{Q}\frac{d\hat{\ell}}{dx} + \underbrace{\lambda^2}_{R}\hat{\ell} = 0 \tag{4.30}$$

It is easy verify that the following conditions are satisfied:

$$P(x_s) = 0 \tag{4.31}$$

$$\lim_{x\to x_s}(x - x_s)\frac{Q}{P} = \frac{4We + 1}{Fr} \quad \text{(finite)} \tag{4.32}$$

$$\lim_{x\to x_s}(x - x_s)^2\frac{R}{P} = 0 \quad \text{(finite)} \tag{4.33}$$

Therefore, the singular abscissa can be classified as a regular singular point [26]. According to the basic Frobenius theory [27], the solution of the equation (4.30) around the singularity location can be expressed in the following way

$$\hat{\ell}(x, s) = (x - x_s)^\alpha \sum_{n=0}^{\infty} a_n (x - x_s)^n \tag{4.34}$$

Substituting the position above in the equation (4.30) and imposing the equality between similar terms, one obtains (for $n = 0$) the following indicial equation

$$a_0\left[\frac{1}{We}\alpha(\alpha - 1) + \left(\frac{1}{We} + \frac{2}{We^2}\lambda\right)\alpha\right] = 0 \tag{4.35}$$

By taking into account that $a_0 \neq 0$ by definition [27], the equation (4.35) yields

$$\alpha_1 = 0 \qquad \alpha_2 = -\frac{2\lambda}{WeFr} \tag{4.36}$$

Since $|\alpha_1 - \alpha_2| = \frac{2\lambda}{WeFr}$ is not an integer or null (by observing the formula structure it results to be a reasonable hypothesis), the solution is given by the linear combination of two Frobenius series [27]

$$\hat{\ell}(x,s) = C_1 \sum_{n=0}^{\infty} a_{n,1}(x - x_s)^n + C_2(x - x_s)^{-\frac{2\lambda}{WeFr}} \sum_{n=0}^{\infty} a_{n,2}(x - x_s)^n \tag{4.37}$$

where C_1 and C_2 are two constants to be determined in function of the boundary conditions. Note that, being $\alpha_1 = 0$, the first Frobenius series reduces to a standard power series expansion (Taylor series).

It is worth to analyze the convergence properties of the series expansion (4.37). The equation (4.30) shows another regular singular point at $U = 0$ ($\bar{x} = -\frac{1}{2Fr}$). According to [27], the radius of convergence of series (4.37) is greater than or equal to the distance between x_s and the nearest singular point ($\bar{x}$). Therefore, the series expansion (4.37) converges to the eigenvalues problem (4.30) solution at least at each station $x \in \left]-\frac{1}{2Fr}, -\frac{1}{2Fr} + \frac{1}{We^2 Fr}\right[$

Note that the physical domain extends from 0 to 1; therefore, it is possible to affirm that for $-\frac{1}{2Fr} + \frac{1}{We^2 Fr} > 1$ and, so, for

$$We < \sqrt{\frac{2}{2Fr + 1}} \tag{4.38}$$

the series (4.37) represents, in principle, the analytical solution of the singular eigenvalues problem (4.30). Unfortunately, the calculation of the series expansion coefficients results to be very costly. On the other hand, note that for $Fr = 1$ (the numerical results showed in the next sections will make reference to this value which represents the typical experimental order of magnitude), the constraint showed by the equation (4.38) becomes $We < 0.816$; the investigation of such values of We is not useful because, as just said previously, the sheet can survive without rupture for We weakly less than unit.

Of course, the singular location $\bar{x} = -\frac{1}{2Fr}$ is not physically interesting because it is located outside the sheet domain for each Fr and, therefore, it does not need special treatments.

By referring to the expansion (4.37), the boundedness condition of $\frac{d\hat{\ell}}{dx}$ in x_s can be formulated in the following way

$$\lim_{x \to x_s} (x - x_s)^{n-1-\frac{2\lambda}{WeFr}} < \infty \qquad \forall n \tag{4.39}$$

which yields

$$\lambda_r < -\frac{WeFr}{2} \tag{4.40}$$

It is possible to conclude that, in *transonic* regime, not only the spectrum is unconditionally stable for each We and Fr but it is subjected to a constraint on the maxim growth rate achievable; in other words, the growth rate results to be upper-bounded. As it will seen in the following sections, the numerical results will confirm this prediction.

4.3.2 Direct numerical simulation

To corroborate the asymptotic modal analysis, direct numerical simulations of the governing equations system (2.24-2.25) have been also carried out, by means of a Crank-Nicholson finite-difference scheme, for various values of the control parameters. The initial condition is constituted by a compact support function satisfying the prescribed boundary conditions, namely a Gaussian-like pulse for the perturbed centerline of nappe, properly localized upstream or downstream of the singularity station depending on the flow regime nature, subsonic or supersonic, respectively. No perturbation in lateral velocity fluctuation v is considered here. Among the various possibilities analysed during the numerical tests, the most convenient numerical procedure appeared that based on the direct integration of the system of equations (2.24-2.25). Bearing in mind the wave nature of the expected solution, formally it has been imposed just the reflecting condition, $\ell(0) = 0$, on eq. (2.24), the free-outflow condition at the right boundary being self-guaranteed. It should be stressed that, as a consequence, at the inlet station the equation (2.24) is implicitly enforced as $v = U\frac{\partial \ell}{\partial x}$. No particular treatment has been added for the specific subsonic or supersonic regimes.

It will be showed, in particular, that the direct numerical simulation of the spatio-temporal partial-derivative equations did not need any special trick for the presence of the singularity in subsonic regime. The comparison between the large time solution arising from the simulation usually agrees perfectly with the corresponding eigenfunction emerging from the modal analysis.

4.4 Analysis of transonic regime

Fig. 4.1 compares spectra obtained in subsonic ($We = 0.98$) and supersonic ($We = 1.02$) regimes for Fr=1 and various typical values of the air stiffness $\mathcal{K}$. It should be preliminarily noted that, as expected, the subsonic regimes (for $We = 0.98$ it corresponds $x_s = 0.021$) are characterized by one-branch only (associated to the faster travelling wave with velocity $U + \sqrt{\frac{U}{We}}$), constituted by two symmetrical parts. For the highest value of $\mathcal{K} = 10^6$ each of the two symmetrical parts of the branch exhibits an outer cusp-point maximum, as well as local maxima represented by the inner pair of eigenvalues. For the other values of $\mathcal{K}$ the branches follow a characteristic hyperbola-shape. All the situations reported in Fig. 4.1(a) are stable and note also that, as already extensively discussed in the previous chapter, according to the damped spring-mass model driven by the self-induced forcing f_{i} of eq. (4.9), the frequency of the less stable eigenvalue scales with $\sqrt{\mathcal{K}}$ (of course in driven regime it coincides with that of the forcing term). Another characteristic frequency is related to the constant spacing of imaginary parts $\Delta\lambda_{\mathrm{i}}$ of eigenvalues which is related to the crossing time [13]

$$t_{\mathrm{cross}} = \int_0^1 \frac{dx}{U \pm \sqrt{\frac{U}{We}}} \tag{4.41}$$

so that, by varying Froude and Weber numbers, it always results in $\Delta\lambda_{\mathrm{i}} \approx \frac{2\pi}{t_{\mathrm{cross}}}$. A further finding is the confirmation of the wave travelling feature of the solution; as will be discussed in a more quantitative detail later on, for each value of $\mathcal{K}$ here analyzed the wave velocity satisfies the relationship

$$U + a = \frac{\lambda_i}{2\pi k} \tag{4.42}$$

with λ_i indicating the disturbance circular frequency (i.e., the imaginary coefficient of eigenvalue) and k the wavenumber, which can be evaluated inspecting the eigenfunctions. This strict comparison will be carried out hereafter and will be also corroborated by direct numerical simulations.

Fig. 4.1(b) reports three spectra for $We = 1.02$ and the same values of $\mathcal{K}$ as the previous Fig. 4.1(a) referring to a Weber number only slightly less than 1.02. Thus, the analysis of the two spectra yields a picture of the things when traversing the transonic region. The major feature of the present spectra is that, from one hand one notes the presence of a type of branch representing the parametric continuation of the analogous branch found for $We = 0.98$, from the other a new *nucleus* of eigenvalues having growth rate

weakly less than zero clearly arises. The new nucleus of eigenvalues is to be ascribed to the travelling waves with velocity $U - \sqrt{\frac{U}{We}}$ and to their interference with another group of low frequency eigenvalues associated to the faster waves with velocity $U + \sqrt{\frac{U}{We}}$. This last finding can be better appreciated looking at Figs. 4.2(a) and (b), depicting the close-up views of the previous Figs. 4.1(a) and (b), respectively.

Fig. 4.2(a) shows a detail of the lowest frequency eigenvalues calculated for $We = 0.98$ (but not less stable eigenvalues for $\mathcal{K} = 10^6$), whilst Fig. 4.2(b) refers to the less stable supersonic ($We = 1.02$) eigenvalues, showing in a great detail the interference of modes. This interference appears rather weak for $\mathcal{K} = 10^2$ since the external branches, fast modes, are the continuation of those present for $We = 0.98$ and coherently are slightly less stable ($\lambda_{rmax} = -0.59$) than the subsonic case ($\lambda_{rmax} = -0.62$). The inner branches are to be attributed to slow modes. The situation is more complex for higher $\mathcal{K}$ because of the absence of clear fast modes; on the contrary, for both $\mathcal{K} = 10^4$ and 10^6 the leading modes appear to be slow modes. In summary, fast eigenmodes $U + a$ are continuous in transonic regime for $\mathcal{K} = 10^2$, whilst in any case slow eigenmodes $U - a$ appear abruptly. Note that, for $We = 0.98$, for any $\mathcal{K}$, the growth rate of the less stable eigenvalue is less than $\frac{-WeFr}{2} = 0.49$ (represented by the black straight line), according to the analytical prediction provided by eq. (4.40)

The previous findings featuring eigenvalues spectra are further highlighted by the shapes of the relevant eigenfunctions, for instance those presented in Fig. 4.3 for $\mathcal{K} = 10^2$, in Fig. 4.4 for $\mathcal{K} = 10^4$, in Fig. 4.5 for $\mathcal{K} = 10^6$. For all the plots it is $Fr = 1$ and frame (a) and (b) refer to subsonic ($We = 0.98$) and supersonic ($We = 1.02$) regimes, respectively.

Since the corresponding spectrum of Fig. 4.2(a) shows that the imaginary part of the leading mode is $\lambda_i = 13.22$, while from the eigenmode shape of Fig. 4.3 (a) one can read a characteristic wavenumber of about $k = 0.77$ (note that for this particular case the estimation of the wavenumber is particularly critical), a wave travelling velocity of $\frac{\lambda_i}{2\pi k} = 2.73$ can be deduced, which is in quite good agreement with the theoretical prediction of $U + a = U + \sqrt{\frac{U}{We}} = 2.62$. It should be pointed out that in this last relationship it has been referred to the mean flow velocity U, namely the flow velocity evaluated at the domain midpoint $x = 0.5$. The accuracy of this kind of comparison has been checked for a wide range of values of the governing parameters, and for instance verified by looking at Figs. 4.4 (a) and 4.5 (a). Of course the evaluation of the wavenumber is more accurate with increasing the value of the air equivalent stiffness. The results are that k is slightly greater than 7 for $\mathcal{K} = 10^4$ and slightly greater than 74 for $\mathcal{K} = 10^6$. It is worth to point out that this values scale with each other by a factor of order ten which is to be expected if one consider that the leading frequency λ_i scales by the same factor, which is roughly equal to the square root of $\mathcal{K}$. Moreover, note that the eigenmodes

computed via the present spectral analysis well agree also with the large time direct simulations of perturbed interface shapes and that the same wave travelling velocity has been estimated by following the spatio-temporal evolution of a fixed wave point, e.g. a crest. In any case, the precise comparison among spectral analysis and direct numerical simulation will be discussed hereafter.

Figs. 4.3(b), Fig. 4.4(b) and Fig. 4.5(b) depict the leading mode shapes for the usual three tested $\mathcal{K}$ values and a We number of 1.02, i.e. slightly supersonic. Thus, the comparison between every (a) and (b) frames of these figures gives a picture of typical findings obtained when traversing the transonic regime. The major result is that whilst for $\mathcal{K} = 10^2$ the leading modes of subsonic ($We = 0.98$) and supersonic ($We = 1.02$) regimes are both of fast type, for the higher $\mathcal{K}$ values the leading mode switches from the fast to the slow mode. The agreement of the wave travelling velocity estimated via spectral analysis and numerical simulation is not, however, strictly satisfactory. Whilst for $\mathcal{K} = 10^2$ the former method gives a value of about 2.72 to be compared with 2.59 obtained with the latter one, for both the higher $\mathcal{K}$ values the spectral analysis yields 0.14 against 0.24 of the direct simulation.

4.5 Details of direct numerical simulations

As asserted before, it has been made also systematic numerical simulations of the large time spatio-temporal evolution of the interface deflection during its transient, starting from an initial instant when a particular perturbation, typically a gaussian-like bump, was imposed to the interface shape. Generally it has not been considered any initial disturbance on the lateral velocity perturbation v. The frames reported in Fig. 4.6 refer to the evolution computed for the subsonic case of $We = 0.82$ with $\mathcal{K} = 10^4$, and to a bump disturbance initially located at $x = 0.1$, therefore located in the subsonic region $0 < x < x_s$, here resulting $x_s = 0.24$ (eq.(4.27)). Note also, however, that other simulations, not shown herein, revealed that the asymptotic deflection eventually reached by the sheet is not influenced by the initial position of the disturbance. The frames reported in Fig. 4.6 show an initial bump splitting into two parts, one travelling rightwards and being rapidly expelled, the other one travelling leftwards with the expected velocities. The reflection of the left part on the inlet boundary at $x = 0$ generates the temporary establishment of a low wavenumber mode which is rapidly characterized by the appearance of shorter wavelength ripples. At large times a travelling wave, exhibiting an almost regular structure with a wavenumber of about $k = 7$, eventually establishes.

A comparison of large time sheet centerline deflections between eigenmodes (frames (a)) and direct numerical simulations (frames (b)) is reported in Figs. 4.7, 4.8, 4.9, corresponding to $\mathcal{K}$ equal to 100, 10^4, 10^6, respectively.

The above comparisons appear quite satisfactory. In particular, one has to stress the perfect agreement of the two solutions near the singularity station $x_s = 0.24$, which confirms that the procedure of treatment of the singularity worked successfully in the spectral analysis. Furthermore, from these plots one can retrieve the same kind of information about the nature of the leading modes emerging at large times, as previously discussed in detail as far as the transonic regime is concerned.

4.6 Insight on supersonic regime

It is relevant to conclude the presentation of the results by yielding a look at the scenarios emerging in the fully supersonic regimes. Fig. 4.10 depicts eigenvalues spectra obtained for $Fr = 1$ and $\mathcal{K} = 10^4$ and for various Weber numbers increasing from the subsonic value of $We = 0.82$ to the supersonic one of $We = 2.5$. The continuity of the spectrum morphology when traversing the transonic regime is once again clearly depicted from these plots, which show also that starting from $We = 1.43$ the leading mode of supersonic regime is definitely the fast one having travelling velocity $U + a$.

A major peculiarity of the trends of the leading modes in the near supersonic field is the occurrence of characteristic high frequency ripples due to the interference of modes; such ripples structures are typically present with increasing the Weber number, as the leading mode evolves from a very low wavenumber to a moderate wavenumber compatible with the expected spring-mass frequency $\lambda_i = O\sqrt{\mathcal{K}}$ and fast travelling wave velocity $U + a$. The ripples disappear starting from about $We = 3.5$. Typical ripples structures are presented in plots of Fig. 4.11, illustrating both the leading mode shape (frame (a)) and its direct simulation (frame (b)). The numerical simulations show that the ripples form due to the bits among the faster modes that go back downstream the lower modes.

It is also very interesting to compare the spectra obtained for the subsonic regime of $We = 0.98$, hence near the threshold of the transonic value, and for very high supersonic Weber numbers, tending to infinity and simulating the absence of surface tension, as illustrated in Fig. 4.12.

The comparison shows clearly that the leading mode frequency in the two cases here considered is practically the same, namely $\lambda_i \cong 118$. However, while the subsonic regime features an evident stability, the supersonic one without effects of surface tension is remarkably unstable, since, as deeply discussed by De Rosa et al. [12] and in the previous

chapter, in latter case the falling time exceeds the mass-spring period of oscillation. Since for a given frequency, the wavenumber of the leading mode is inversely proportional to the wave velocity, such a characteristic is expected in comparing the large time behaviors of nappe centerline deflection, and indeed it is visible in Fig. 4.13 where frame (a) refers to the subsonic case and frame (b) to the no surface tension supersonic one. Note that the supersonic wavenumber, $k \cong 13.29$, is about twice the subsonic wavenumber, $k \cong 7.18$, according to the circumstance that the average wave velocity is about $U = \sqrt{2}$ in the former case, and about $U = 2.62$ in the latter one.

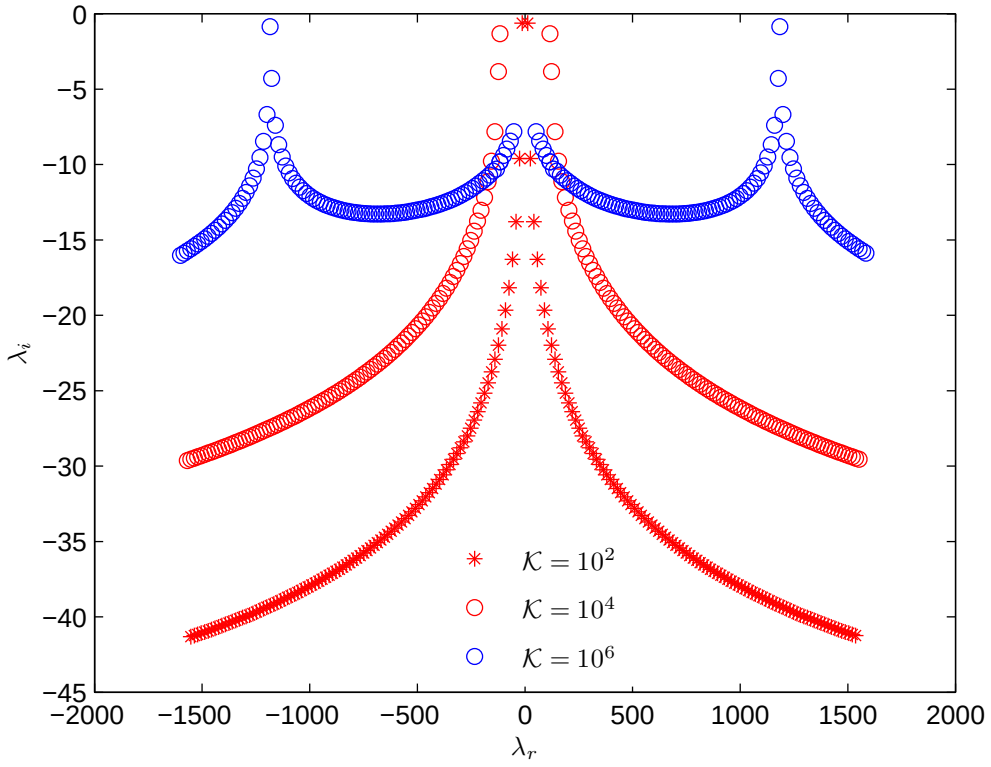

(a)

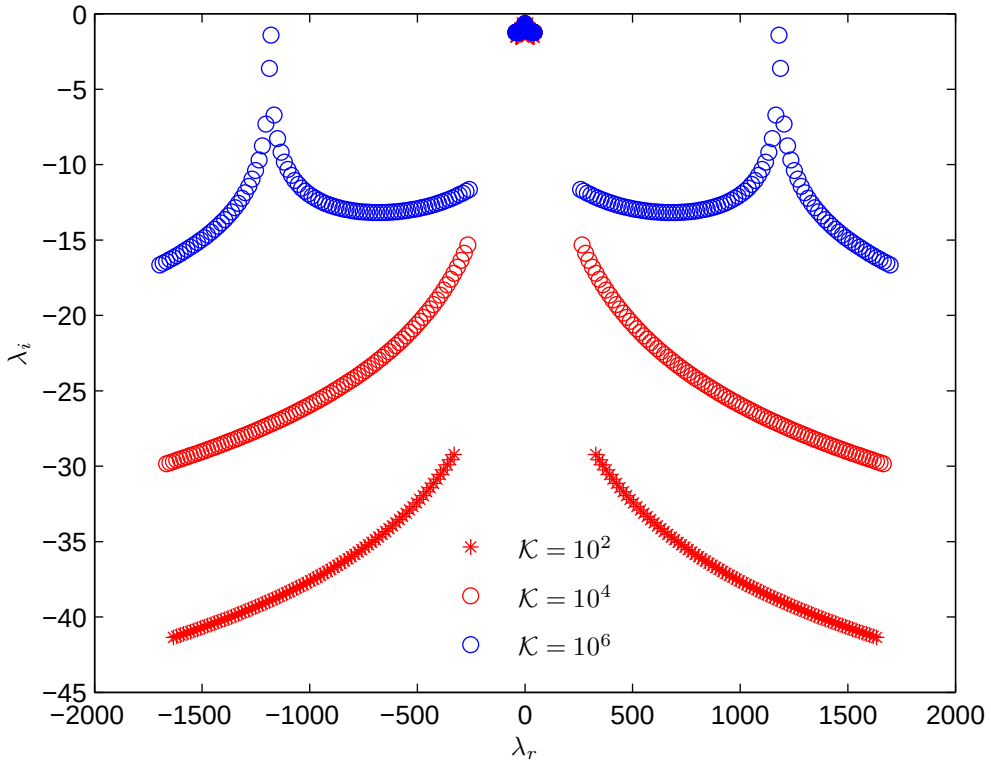

(b)

FIGURE 4.1: Spectra for $Fr = 1$ and selected $\mathcal{K}$ values. (a) $We = 0.98$, (b) $We = 1.02$.

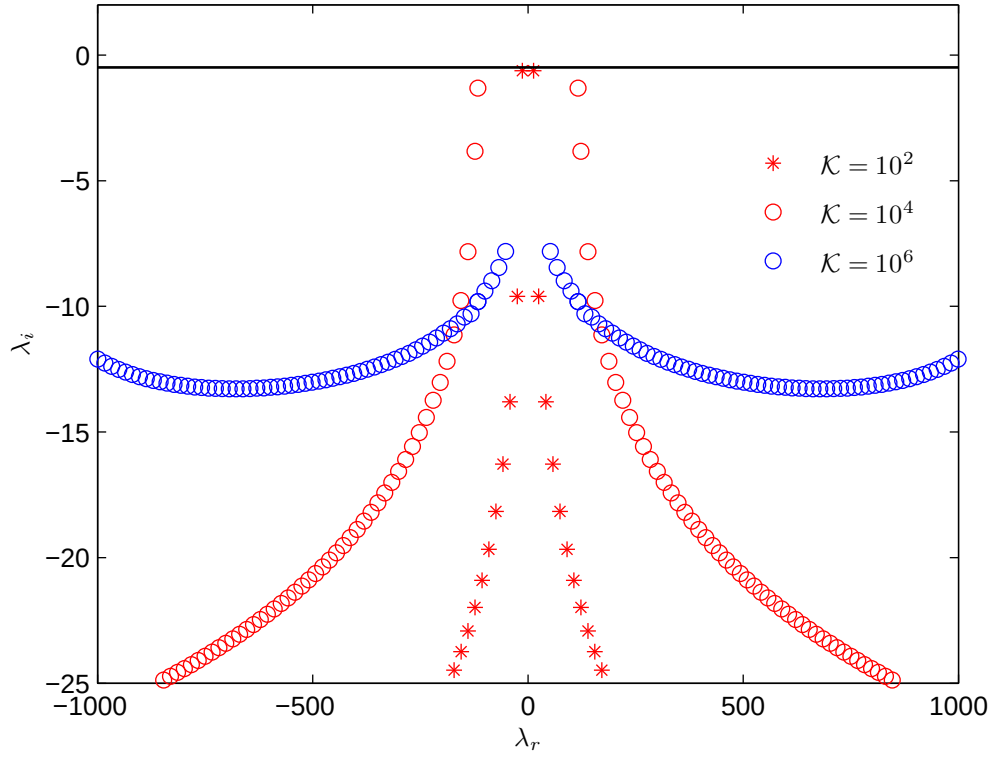

(a)

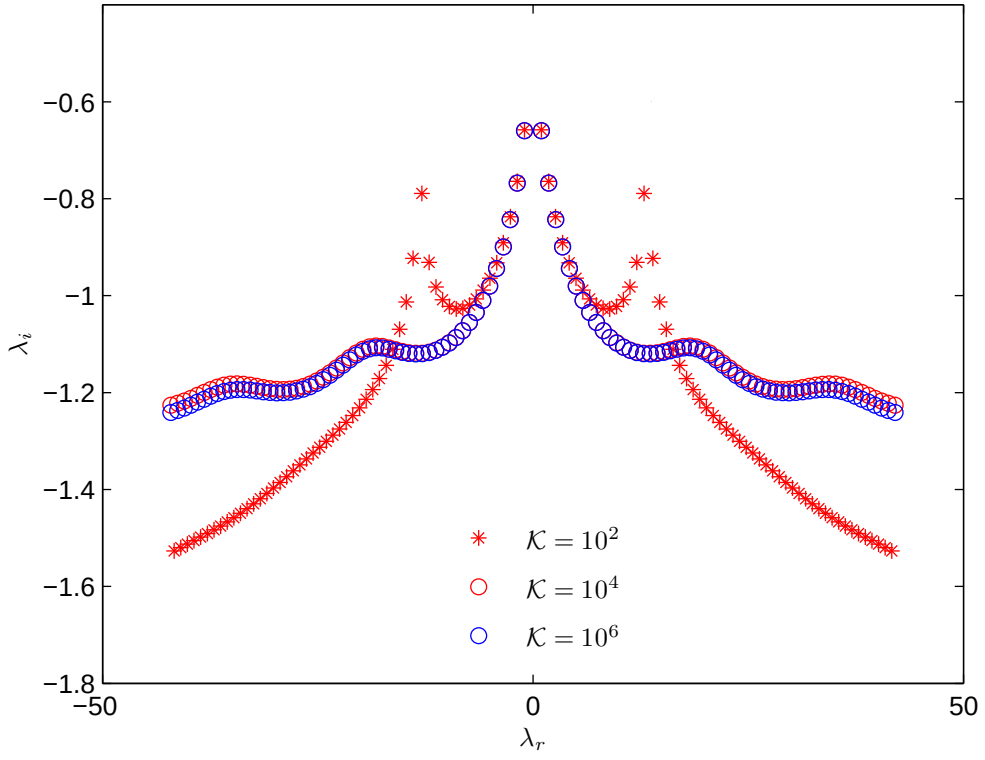

(b)

FIGURE 4.2: Less stable eigenvalues of spectra for $Fr = 1$ and selected $\mathcal{K}$ values. The black straight line in the frame (a) represents the theoretical boundary showed by eq. (4.40). (a) $We = 0.98$, (b) $We = 1.02$.

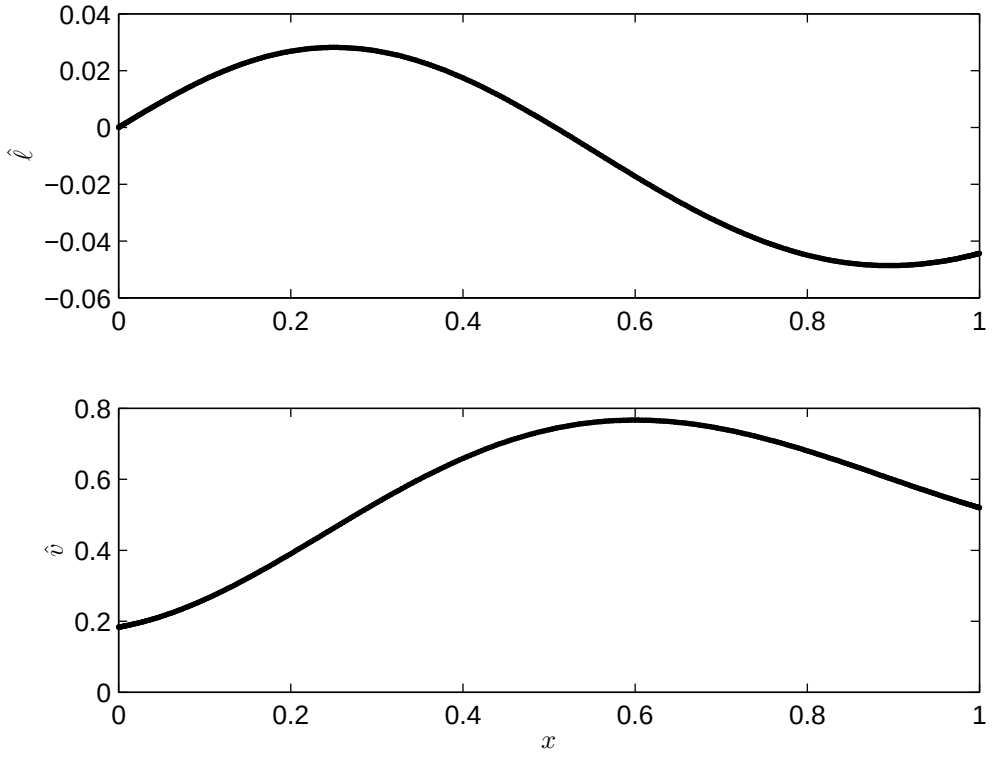

(a)

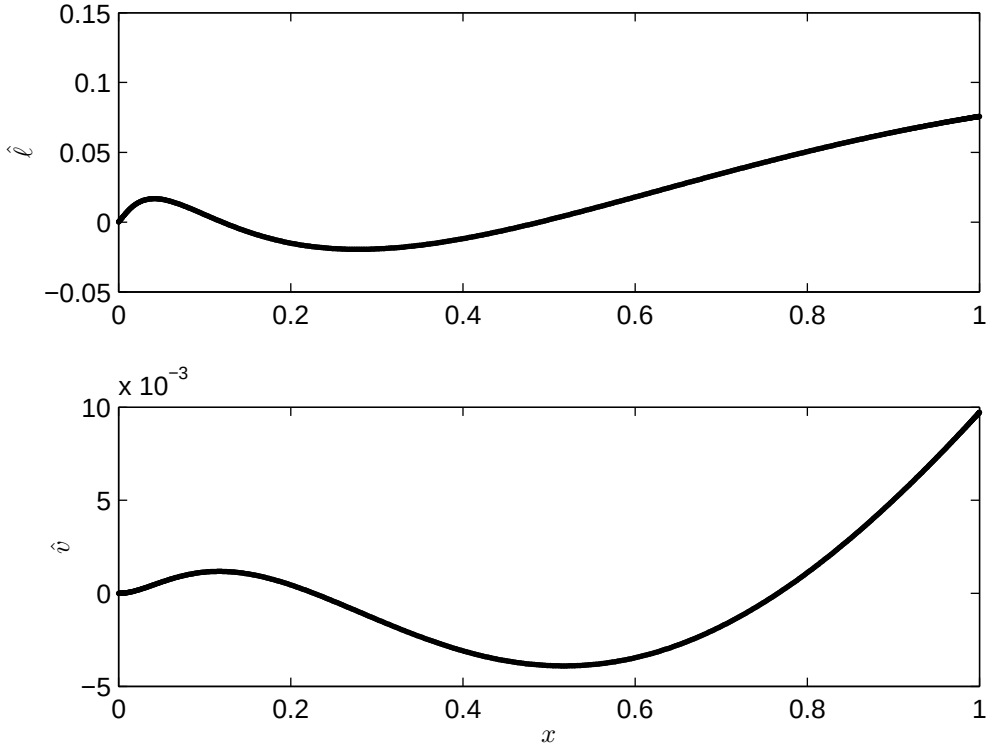

(b)

FIGURE 4.3: Leading eigenfunctions for $Fr = 1$ and $\mathcal{K} = 10^2$. (a) $We = 0.98$, (b) $We = 1.02$.

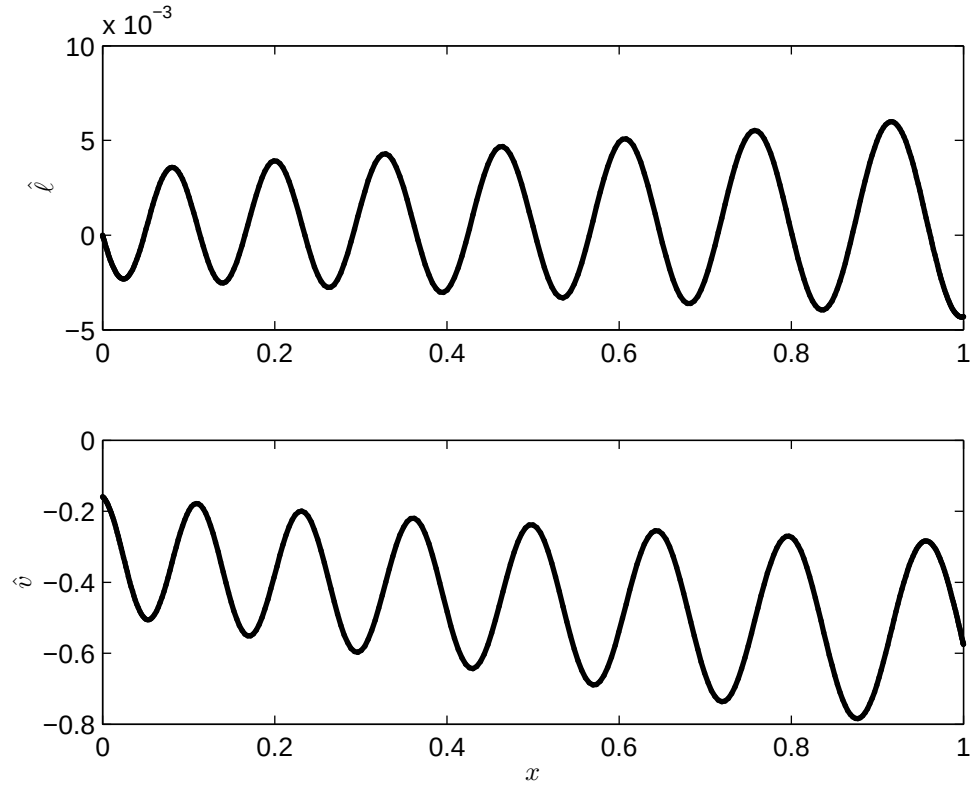

(a)

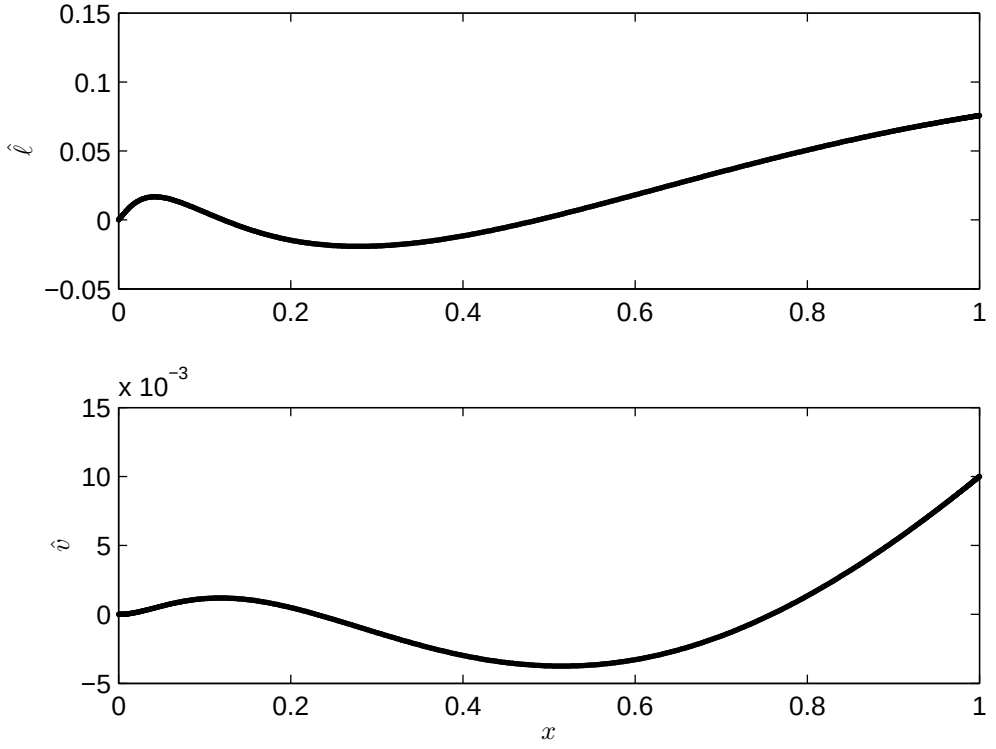

(b)

FIGURE 4.4: Leading eigenfunctions for $Fr = 1$ and $\mathcal{K} = 10^4$. (a) $We = 0.98$, (b) $We = 1.02$.

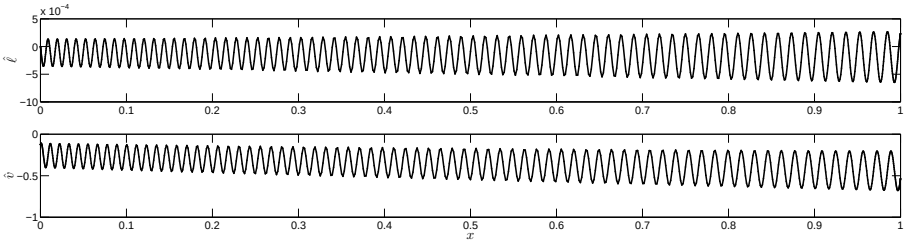

(a)

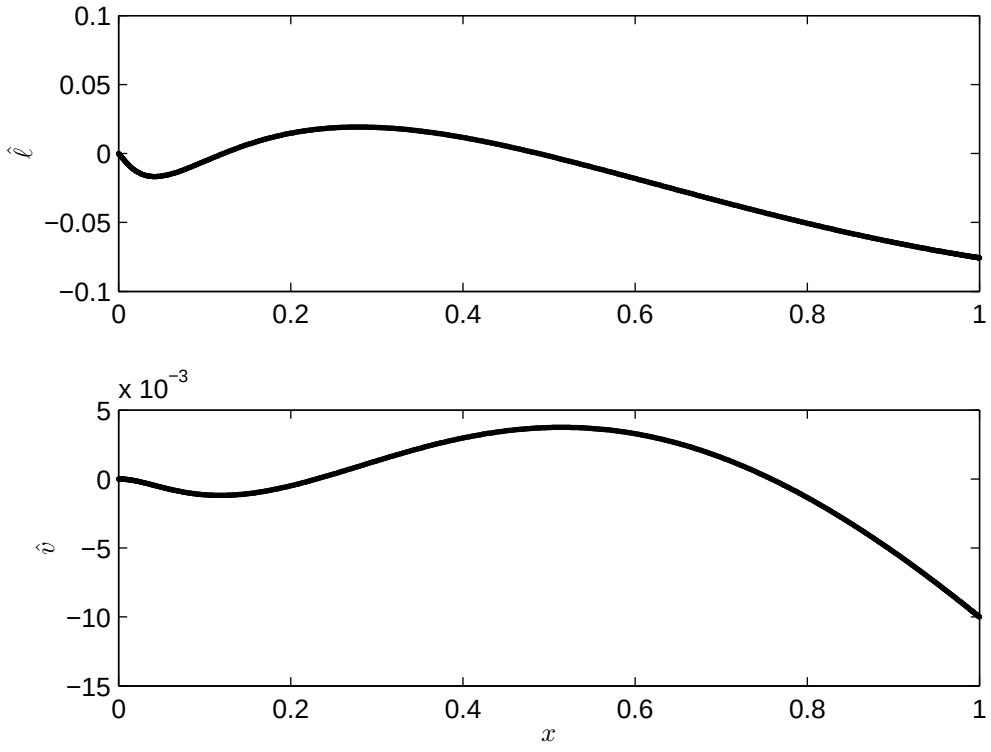

(b)

FIGURE 4.5: Leading eigenfunctions for $Fr = 1$ and $\mathcal{K} = 10^6$. (a) $We = 0.98$, (b) $We = 1.02$.

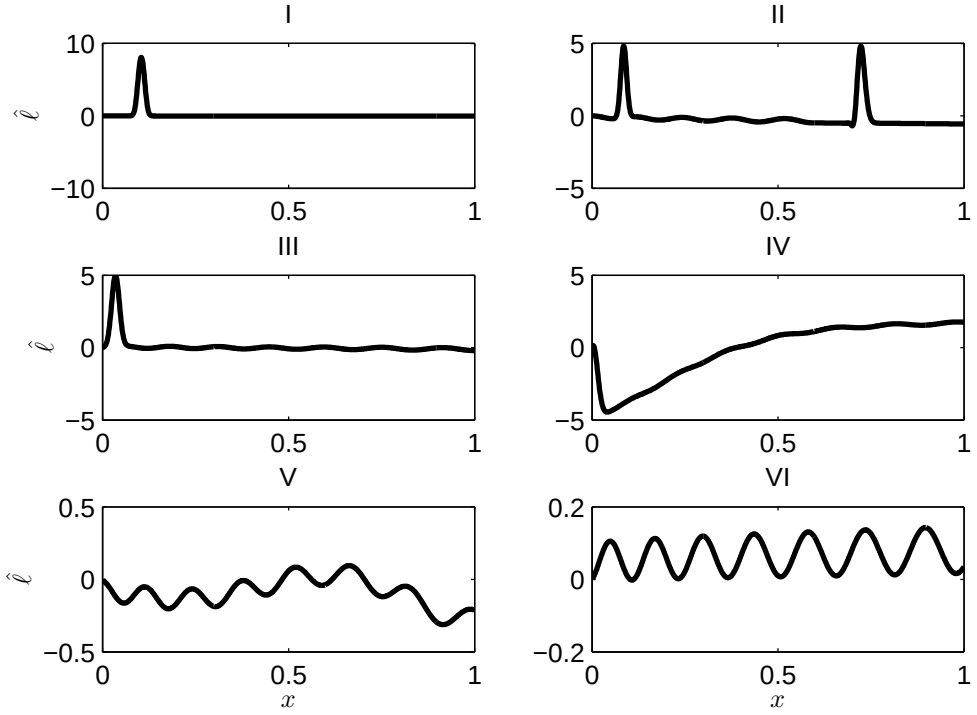

FIGURE 4.6: Frames related to the numerical simulation for $We = 0.82$, $Fr = 1$ and $\mathcal{K} = 10^4$.

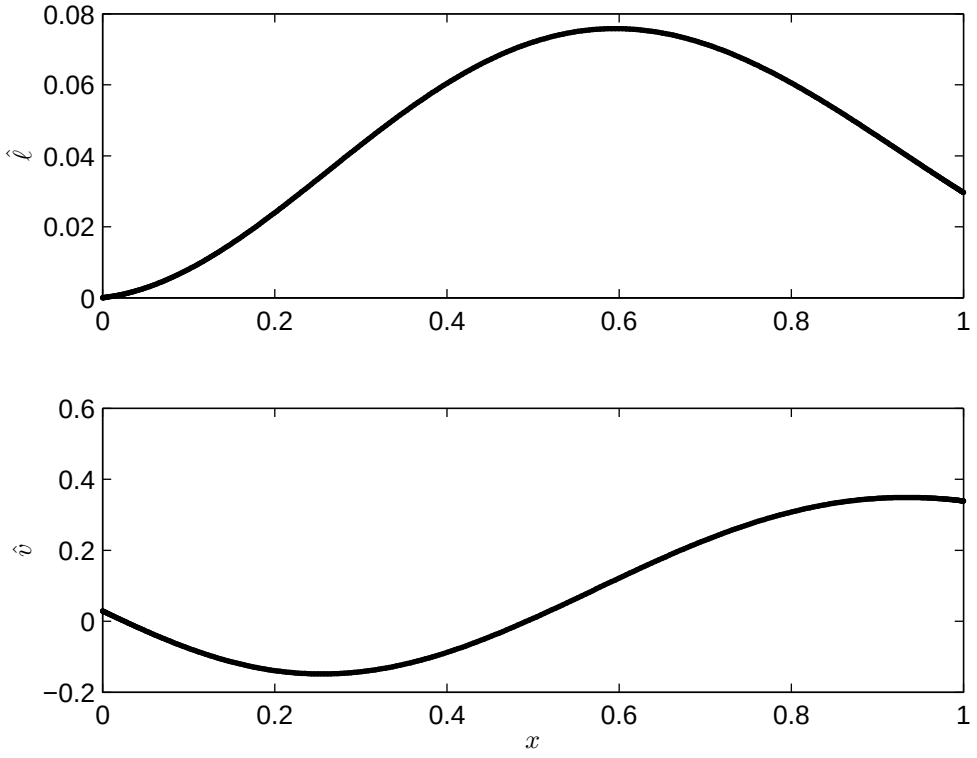

(a)

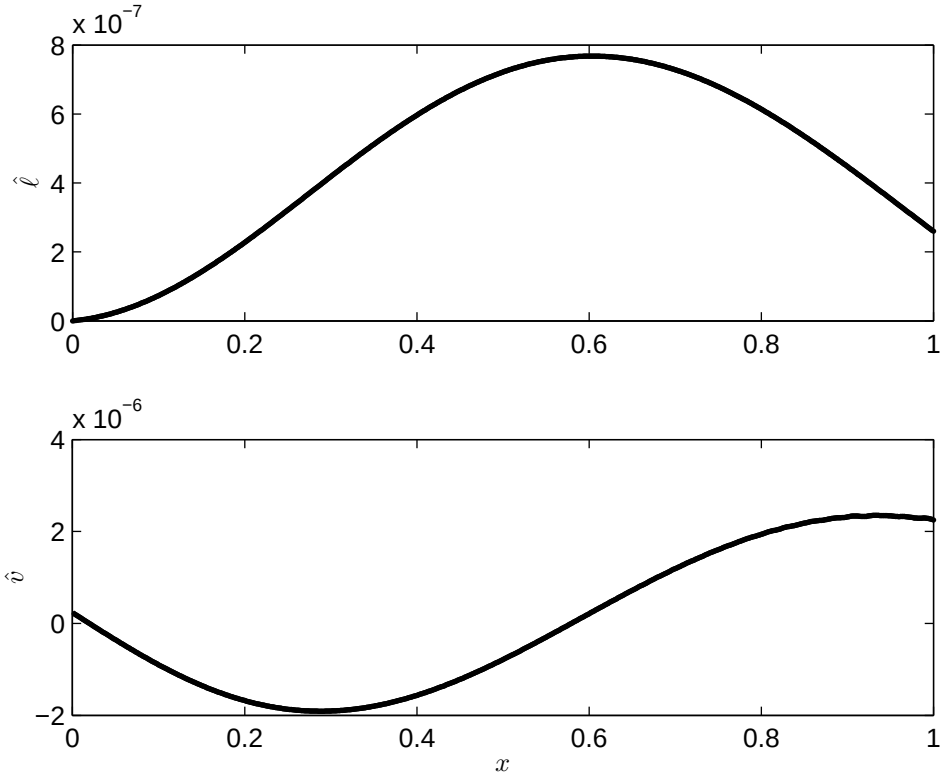

(b)

FIGURE 4.7: Comparison of eigenmode (a) and numerical simulation (b) for $We = 0.82$, $Fr = 1$ and $\mathcal{K} = 10^2$.

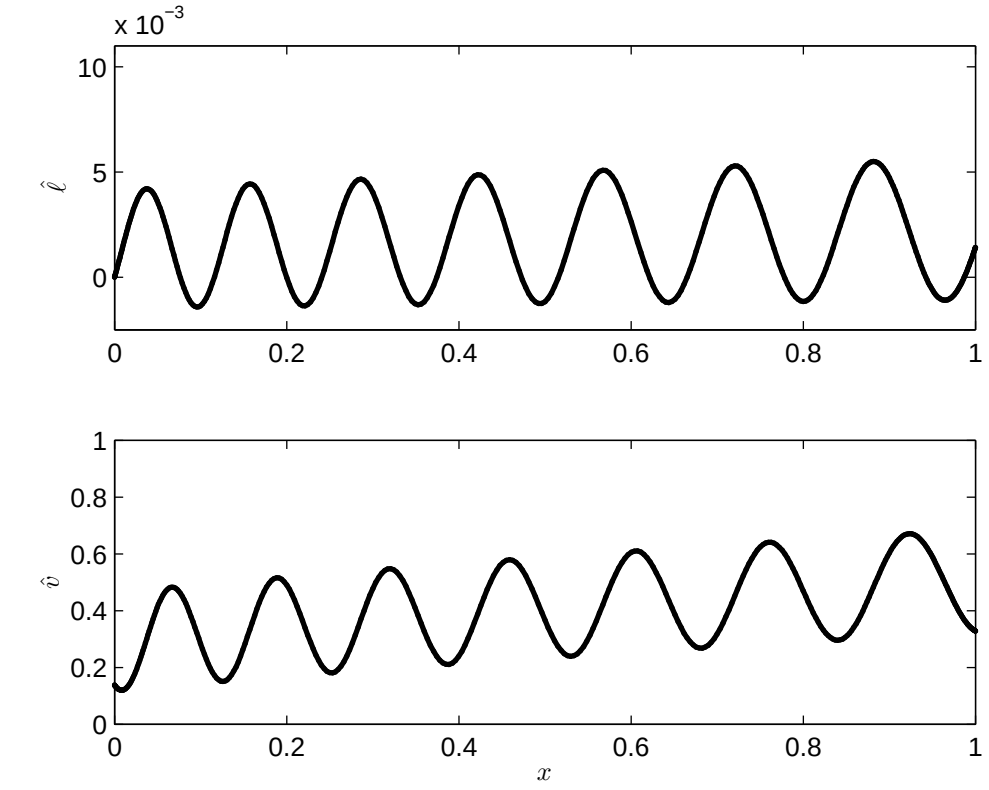

(a)

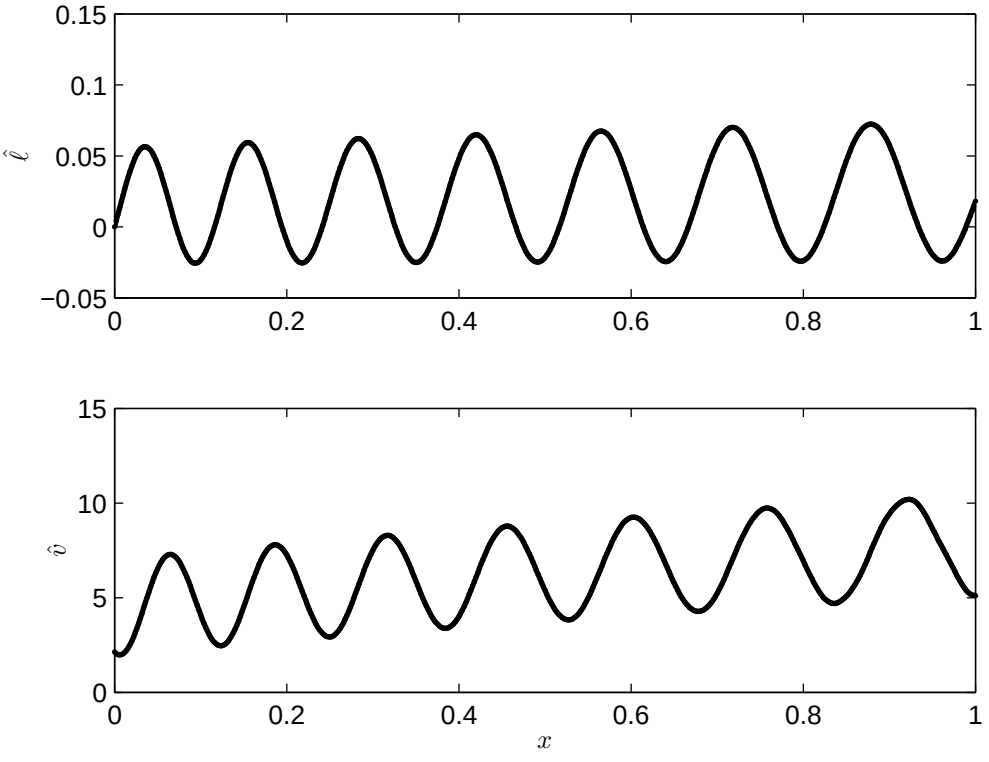

(b)

FIGURE 4.8: Comparison of eigenmode (a) and numerical simulation (b) for $We = 0.82$, $Fr = 1$ and $\mathcal{K} = 10^4$.

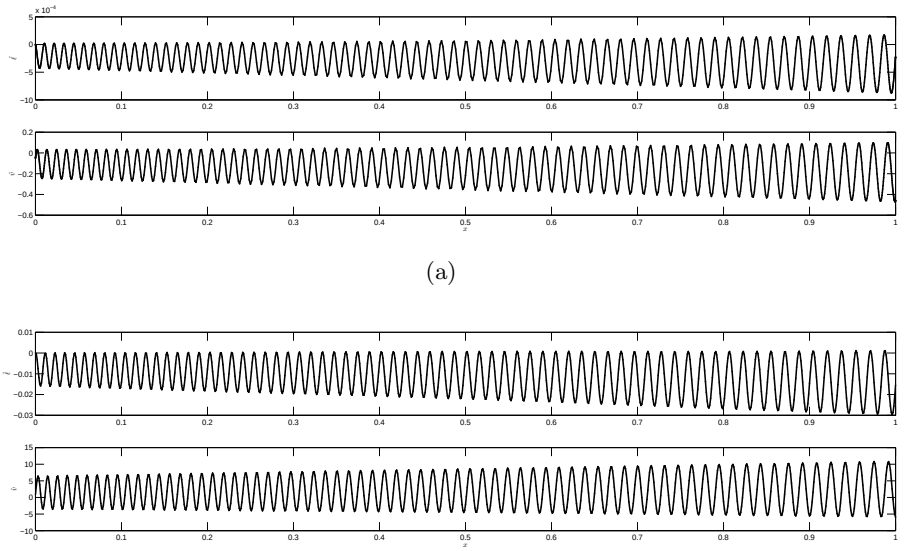

(a)

(b)

FIGURE 4.9: Comparison of eigenmode (a) and numerical simulation (b) for $We = 0.82$, $Fr = 1$ and $\mathcal{K} = 10^6$.

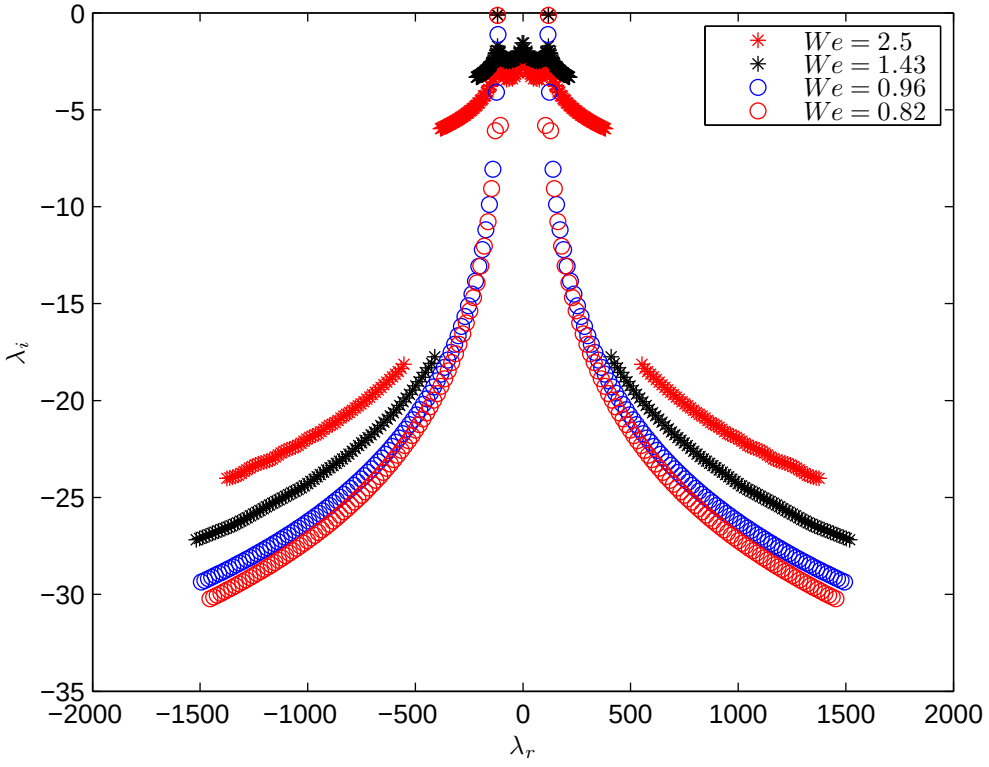

FIGURE 4.10: Evolution of spectra from subsonic to supersonic regimes for various Weber numbers, $Fr = 1$ and $\mathcal{K} = 10^4$.

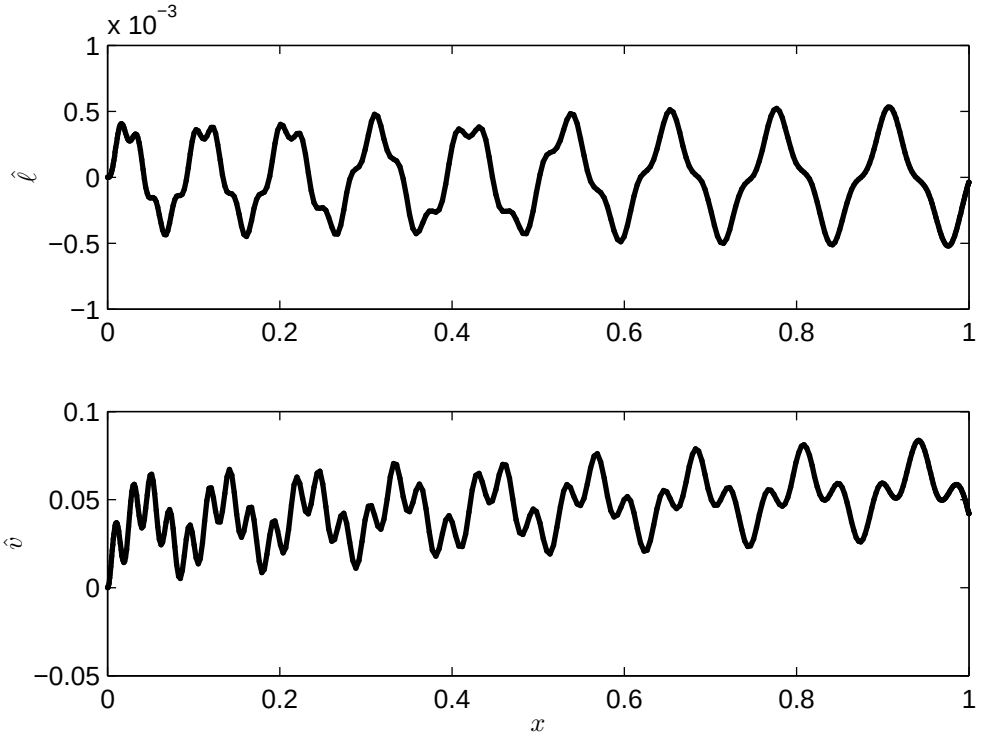

(a)

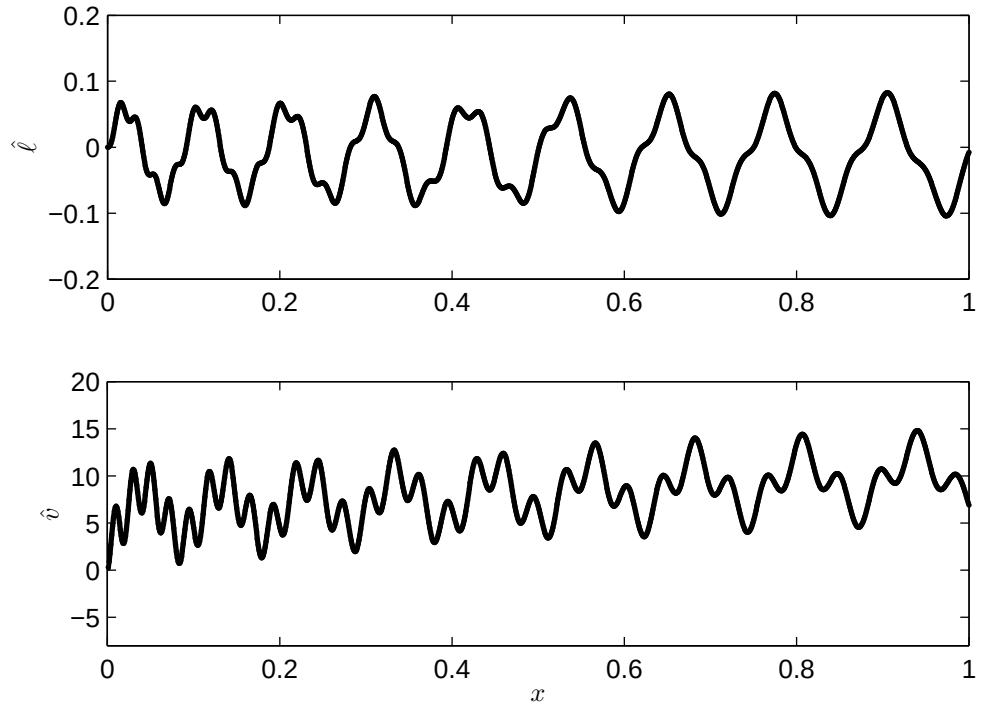

(b)

FIGURE 4.11: Leading eigenmodes (a) and direct simulations of large time behavior (b) for $We = 2.5$ and $Fr = 1$ and $\mathcal{K} = 10^4$.

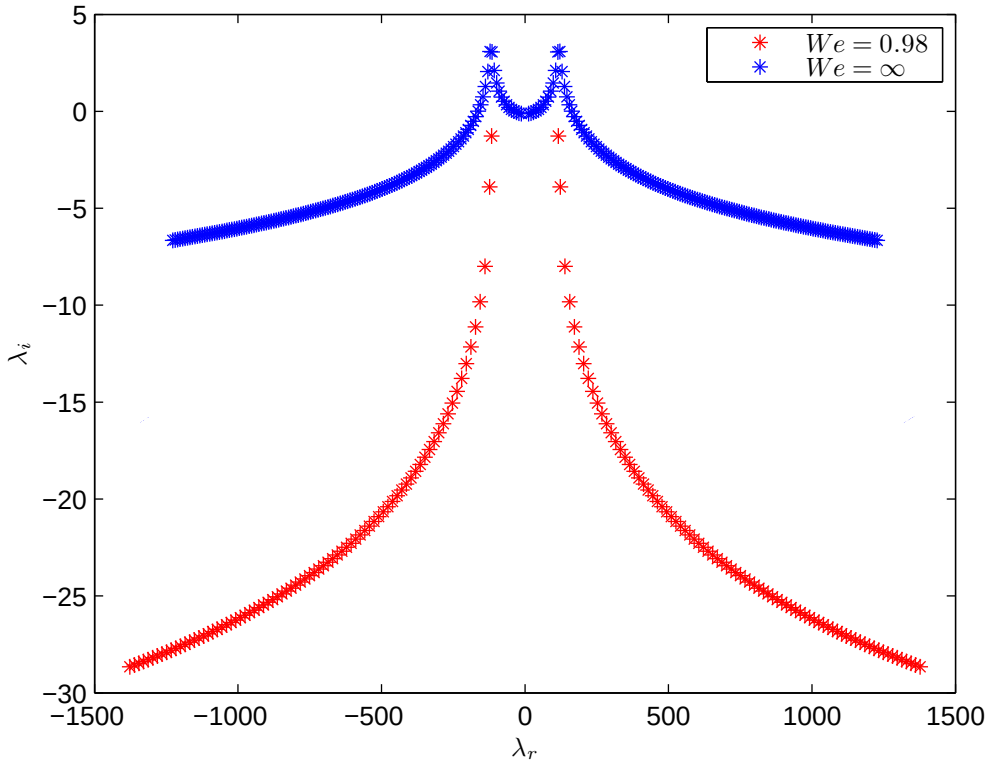

FIGURE 4.12: Comparison of spectra for $We = 0.98$ and $We = 10^6$; in both cases, $Fr = 1$ and $\mathcal{K} = 10^4$.

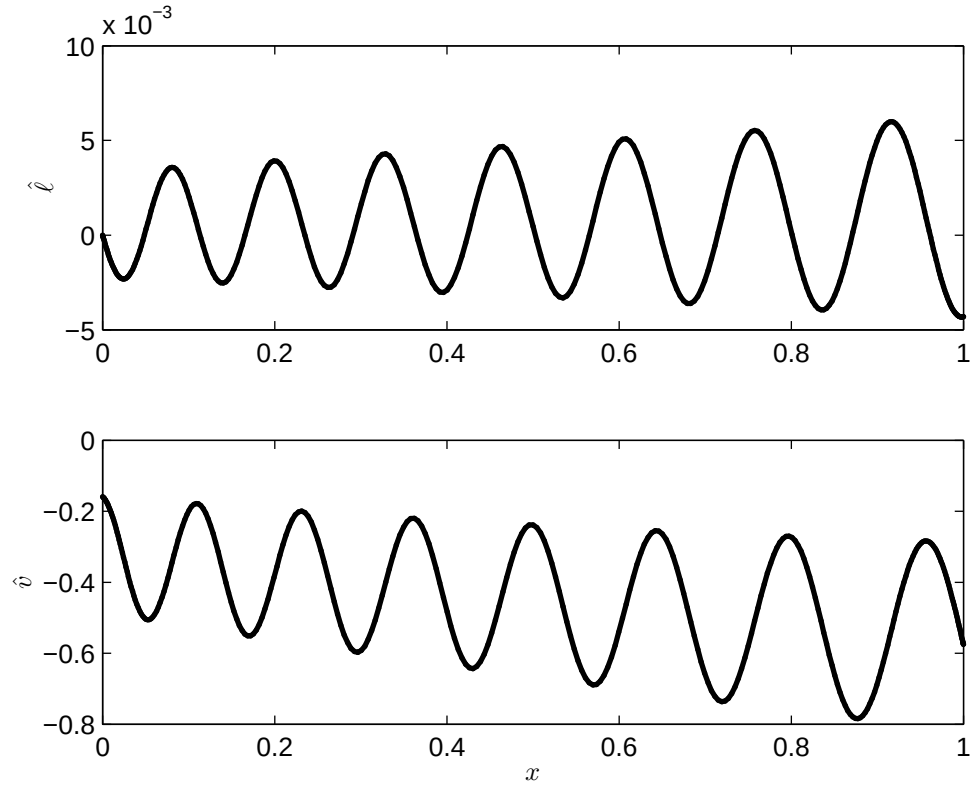

(a)

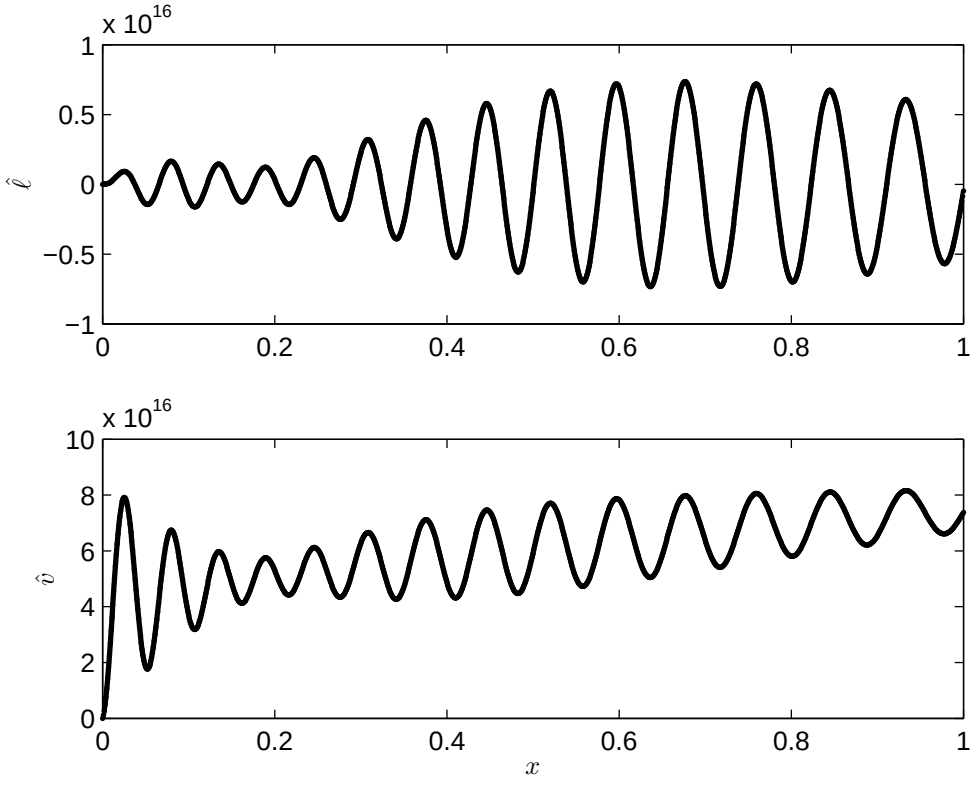

(b)

FIGURE 4.13: Direct simulations of large time behavior of leading eigenmodes for $Fr = 1$ and $\mathcal{K} = 10^4$. (a) $We = 0.98$, (b) $We = 10^6$.

Conclusions

The dynamic behavior of nappe oscillation has been revisited with reference to a physical model in which a thin liquid sheet interacts with an one-sided closed air chamber. The mutual influence of the air within the enclosure with the compliant nappe interface can produce self-induced forcing whose features have been widely investigated. The analysis has been carried out by developing a simplified inviscid one-dimensional physical model that arises, in the context of a linearized formulation of free-interface convection dominated systems, by assuming a coordinate-type expansion for the flow variables.

The present contribution represents a step ahead in the knowledge of the phenomenon in two ways: first, it analyzes more in detail the spectrum of the frequencies of the system, and indicates that the oscillations of low frequency are related to the quasi-constant spacing of the imaginary parts of the eigenvalues (already known); it also identifies clearly that the high frequency oscillations have to be related to a global spring-mass oscillator model whose mass is that of the liquid sheet and the equivalent stiffness $\mathcal{K}$ of the spring is that of the air inside the enclosure, which experiences compression/expansion thermodynamic transformations.

The investigation has been carried out by means of both a modal (i.e., time asymptotic) linear approach, which is corroborated by direct numerical simulations of the governing equation. With the aim of yielding various physical insights, the analysis has been carried out from both a dynamics and energy perspective.

In absence of surfaces tension effects, a major result is the determination of the instability onset based on the ansatz, fully confirmed by the numerical analysis, that the system is stable if the crossing time of a perturbation over the whole length of the domain is shorter than the period of the spring-mass oscillator. In the opposite situation the self-forcing establishes itself, leading to instability. It should be stressed that this ansatz includes the gravity effects, in the sense that in the presence of gravity a shorter crossing time is expected, and, accordingly, a higher $\mathcal{K}$ threshold of instability. Since the oscillator works in the driven regime, the oscillation period does not correspond to the natural frequency of oscillation and, in general, it cannot be determined in analytical closed

form. Moreover, in analogy with the acoustic phenomenon of edge tones, it is found that resonance occurs at frequencies *one integer-plus-one-fourth* times the instability onset frequency, where the basic frequency to be multiplied by $n + \frac{1}{4}$ is just the one related to the spacing among the imaginary parts of the eigenvalues.

In presence of surface tension effects, the unsteady dynamics can be described by means of a typical 2^{nd} order partial differential equation of hyperbolic type, showing two distinct characteristic curves. A relevant procedure has been employed in order to remove the singularity showed by the integro-differential operator for $We < 1$. An additional analytical investigation on the nature of the singularity, based on the Frobenius theory, predicts that the flow is unconditionally stable for any $We < 1$ and that the disturbance time growth rate results to be bounded above. The major feature showed by a typical spectrum for $We > 1$ is that, from one hand one notes the presence of a type of branch representing the parametric continuation of the analogous branch found for $We < 1$ (associated to the faster waves) from the other a new nucleus of eigenvalues having growth rate weakly less than zero clearly arises (associated to the lower waves). The comparison of large time sheet centerline defections between eigenmodes and direct numerical simulations appears quite satisfactory. A major peculiarity of the trends of the leading modes in the near supersonic field is the occurrence of characteristic high frequency ripples due to the interference of modes. The comparison between the spectra obtained for $We < 1$ and for very high supersonic Weber numbers, tending to infinity and simulating the absence of surface tension, shows clearly that the leading mode frequency is practically the same.

Bibliography

[1] N. Le Grand-Piteira, P. Brunet, L. Lebon, and L. Limat. Propagating wave pattern on a falling liquid curtain. *Phys. Rev. E*, 74:026305, 2006.

[2] L. de Luca. Experimental investigation of the global instability of plane sheet flows. *J. Fluid Mech.*, 399:355, 1999.

[3] J.S. Roche, N. Le Grand, P. Brunet, L. Lebon, and L. Limat. Perturbations on a liquid curtain near break-up: Wakes and free edges. *Physics of Fluids*, 18:082101, 2006.

[4] H.B. Squire. Investigation of the instability of a moving liquid film. *British Journal of Applied Physics*, 4:167, 1953.

[5] W.W. Hagerty and J.F. Shea. A study of the stability of plane liquid sheets. *J. of Appl. Mech.*, 22:509, 1955.

[6] X. Li and R.S. Tankin. On the temporal instability of a two-dimensional viscous liquid sheet. *J. Fluid Mech.*, 226:426, 1991.

[7] S.P. Lin, Z.W. Lian, and B.J. Creighton. Absolute and convective instability of a liquid sheet. *J. Fluid Mech.*, 220:673, 1990.

[8] L. de Luca and M. Costa. Two-dimensional flow of a liquid sheet under gravity. *Comput. Fluids*, 24:401, 1995.

[9] P.J. Schmid and D.S. Henningson. On the stability of a falling liquid curtain. *J. Fluid Mech.*, 463:163, 2002.

[10] C. Mehring and W.A. Sirignano. Nonlinear capillary wave distortion and disintegration of thin liquid sheets. *J. Fluid Mech.*, 388:69, 1999.

[11] G. Coppola, F. De Rosa, and L. de Luca. Surface tension effects on the motion of a free-falling liquid sheet. *Phys. Fluids*, 25(6):062103, 2013. doi:10.1063/1.4810751.

[12] F. De Rosa, M. Girfoglio, G. Coppola, and L. de Luca. Global dynamics analysis of nappe oscillation. *Phys. Fluids*, 26(12):122109, 2014. doi:10.1063/1.4904752.

[13] M. Girfoglio, F. De Rosa, G. Coppola, and L. de Luca. Global eigenmodes of free-interface vertical liquid sheet flows. *WIT Transactions Engineering Sciences*, 79: 285–295, 2013.

[14] Fortunato De Rosa. *Dinamiche instazionarie ed instabilità lineare globale di getti liquidi*. PhD thesis, Università degli studi di Napoli Federico II, 2013.

[15] N. Curle. The mechanics of edge-tones. *Proceedings of the Royal Society of London. Series A, Mathematical and Physical Sciences*, 216(1126):412–424, 1953.

[16] H. I. Schwartz. Nappe oscillation. *J. Hydraulics Div.*, 90(6):129–143, 1964.

[17] Y. Sato, S. Miura, T. Nagamine, S. Morii, and S. Ohkubo. Behavior of a falling water sheet. *J. of Environment and Engineering*, 2:394–406, 2007.

[18] L. de Luca and M. Costa. Stationary waves on plane liquid sheets falling vertically. *Eur. J. Mech. B Fluids*, 16(1):75–88, 1997.

[19] S. J. Weinstein D. S. Finnicum and K.J. Rushak. The effect of applied pressure on the shape of a two-dimensional liquid curtain falling under the influence of gravity. *J. Fluid Mech.*, 255:647–665, 1993.

[20] S. J. Weinstein, A. Clarke, A. G. Moon, and E. A. Simister. Time-dependent equations governing the shape of a two-dimensional liquid curtain, part 1: Theory. *Phys. Fluids*, 9:3625–3636, 1997.

[21] J. I. Ramos. Singularities and stability of inviscid, planar liquid membranes. *Int. J. Eng. Sci.*, 39:1935–1948, 2001.

[22] J. I. Ramos. Oscillatory dynamics of inviscid planar liquid sheets. *Appl. Math. Comput.*, 143:109–144, 2003.

[23] M. Girfoglio, F. De Rosa, G. Coppola, and L. de Luca. Unsteady transonic liquid sheet flows. *to be submitted to Journal of Fluid Mechanics*, 2015.

[24] L. N. Trefethen. Pseudospectra of linear operators. *SIAM Rev.*, 39(3):383–406, 1997.

[25] F. De Rosa, M. Girfoglio, G. Coppola, and L. de Luca. Global dynamics of gravitational liquid sheet flows. In *AIDAA Napoli XXII*, pages 1–12, 2013.

[26] W.E. Boyce and R.C. DiPrima. *Elementary Differential Equations and Boundary Value Problems*. Wiley, 2008.

[27] C.M. Bender and S.A. Orszag. *Advanced Mathematical Methods for Scientists and Engineers: Assymptotic Methods and Perturbation Theory*. Springer, 1999.

Appendix

The most relevant conference/journal papers published during the research activity are hereafter collected.

Global dynamics analysis of nappe oscillation

Fortunato De Rosa, Michele Girfoglio, and Luigi de Luca

Citation: Physics of Fluids (1994-present) **26**, 122109 (2014); doi: 10.1063/1.4904752
View online: http://dx.doi.org/10.1063/1.4904752
View Table of Contents: http://scitation.aip.org/content/aip/journal/pof2/26/12?ver=pdfcov
Published by the AIP Publishing

PHYSICS OF FLUIDS **26**, 122109 (2014)

Global dynamics analysis of nappe oscillation

Fortunato De Rosa,[a] Michele Girfoglio,[b] and Luigi de Luca[c]
Department of Industrial Engineering, Aerospace Sector, Università di Napoli "Federico II", Naples, Italy

(Received 24 June 2014; accepted 5 December 2014; published online 29 December 2014)

The unsteady global dynamics of a gravitational liquid sheet interacting with a one-sided adjacent air enclosure, typically referred to as nappe oscillation, is addressed, under the assumptions of potential flow and absence of surface tension effects. To the purpose of shedding physical insights, the investigation examines both the dynamics and the energy aspects. An interesting re-formulation of the problem consists of recasting the nappe global behavior as a driven damped spring-mass oscillator, where the inertial effects are linked to the liquid sheet mass and the spring is represented by the equivalent stiffness of the air enclosure acting on the average displacement of the compliant nappe centerline. The investigation is carried out through a modal (i.e., time asymptotic) and a non-modal (i.e., short-time transient) linear approach, which are corroborated by direct numerical simulations of the governing equation. The modal analysis shows that the flow system is characterized by low-frequency and high-frequency oscillations, the former related to the crossing time of the perturbations over the whole domain and the latter related to the spring-mass oscillator. The low-frequency oscillations, observed in real life systems, are produced by the (linear) combination of multiple modes. The non-normality of the operator is responsible for short-time energy amplifications even in asymptotically stable configurations, which are confirmed by numerical simulations and justified by energy budget considerations. Strong analogies with the edge-tone problem are encountered; in particular, the *integer-plus-one-quarter* resonance criterion is uncovered, where the basic frequency to be multiplied by $n + \frac{1}{4}$ is just the one related to the spacing among the imaginary parts of the eigenvalues. [http://dx.doi.org/10.1063/1.4904752]

I. INTRODUCTION

It is well known that a thin water sheet (curtain), flowing freely from a top opening, gives rise to strong low-frequency periodic oscillations when interacting with an air enclosure acting as a resonator. Such a behavior, commonly referred to as the nappe oscillation phenomenon,[1] is most pronounced as the volume of air is closed and arises from a mutually induced mechanism among the oscillations of the curtain and the pressure fluctuations in the air enclosure adjacent to one side of the sheet, with the other one being an unperturbed ambient.[2] The flow of waterfalls, naturally outpoured or generated by the overflow of water over long crests of dams or weirs, represents a typical example of such a configuration. The noise produced by the oscillation of the waterfall can be radiated far away from the source and may cause problems such as vibrations in door or windowpanes in buildings nearby, and even, structural damages to the dam itself.

Theoretically, the physical problem represents a typical configuration of a spatially developing fluid system able to sustain a variety of wave-patterns. Although the spatio-temporal evolution of planar free-falling liquid sheet flows has been widely discussed, mainly in the context of linear

[a] fortunato.derosa@unina.it
[b] michele.girfoglio@unina.it
[c] deluca@unina.it

stability analysis,[3–6] little attention has been paid to modeling the global coupling between advection and reaction effects (where the term global refers to the system as a whole) when the curtain interacts with a closed air chamber. Among previous experimental contributions about the nappe oscillation, most noticeable are the works of Sato and coauthors,[7,8] who found a strong correlation among the oscillation frequency of the water sheet and the pressure fluctuation in the air chamber behind it. They also performed a theoretical analysis to examine the modal stability of the sheet vibration by means of a complex eigenvalue problem, and compared the frequency at which unstable modes occur with the characteristic frequency of a one-degree-of-freedom spring-mass system, with the air into the enclosure being considered as a spring and the water sheet being modeled as a mass. However, the characteristic frequency of the most unstable mode is from 10- to 20-times larger than the frequency experimentally observed in visualizing the nappe oscillation phenomenon. Even the shape of the associate eigenfunction is completely different that characterizes the unsteady oscillating behavior of the nappe.

Le Grand-Piteira *et al*.[9] report theoretical as well as experimental findings on the characteristics of the global dynamics of liquid sheets, but their work is concerned with a different context, i.e., the case of symmetrical semi-infinite boundary air environments.

The nappe oscillation phenomenon has been theoretically addressed by Schmid and Henningson,[10] who formulated the linearized physical model governing the spatio-temporal evolution of disturbances in the form of an integro-differential system of equations over a finite length domain. Within the framework of the linear non-modal stability theory, they found time-periodic oscillations of the amplification of the disturbance energy, and correlated the period of such oscillations to the quasi-constant spacing among the imaginary part of the eigenvalues. They concluded that the phenomenon under study is governed not by a single mode but by the (linear) interaction of many (stable) modes. Such a *global* feature of the spectrum closely agrees with the low-frequency oscillations typically observed during the nappe oscillation. Since the role played by viscosity and surface tension should be important in stabilizing the spectrum, as argued by the authors themselves, they limited the analysis to some significant stable modes, focusing their interest on the global oscillations; no connection with parameters associated with single modes was inspected.

In the present work, the nappe oscillation problem is revisited from the linear global viewpoint. The entire eigenvalues spectrum is deeply analyzed, focusing on its unstable part (representing the single-mode sheet behavior, previously evidenced in the literature through the spring-mass model) and on the constant imaginary-spacing of stable eigenvalues (representing the global sheet behavior, previously evidenced through the nappe oscillation frequency). The spring-mass model describes the dynamics of the average displacement of the sheet centerline over its total length; we will show that such a dynamics is forced by the local dynamics of the lower end of the sheet. The study is based on a simplified one-dimensional unsteady model, already derived in the different context of the modeling of slender liquid sheets by means of a series expansion in the slenderness parameter for the unknown flow quantities.[4,11] The model is closed with the specification of the external pressure field, representing the reaction of an air enclosure located on one side of the sheet. The problem is investigated theoretically, by employing both modal and non-modal analysis, and numerically, by means of direct numerical simulation of the unsteady equations. In order to ascertain the basic physical mechanisms governing the phenomenon, the dynamics analysis is also corroborated by a parallel energy analysis, resorting to the so called energy budget methodology.

An interesting physical finding is the strong analogy between the present problem and that of the edge-tones (i.e., the acoustic tones produced when a jet of air strikes a wedge shaped edge), which regards a simple relationship for determining the dimensionless resonance frequencies, namely, the *integer-plus-one-quarter* criterion of Curle.[12]

II. THE PHYSICAL MODEL

To derive a physical model for the unsteady evolution of an inviscid gravitational liquid sheet, the assumptions of plug flow and thin curtain will be adopted.[13,14] The surface tension effects are neglected because most of the features of the present fluid system are not strictly related to the

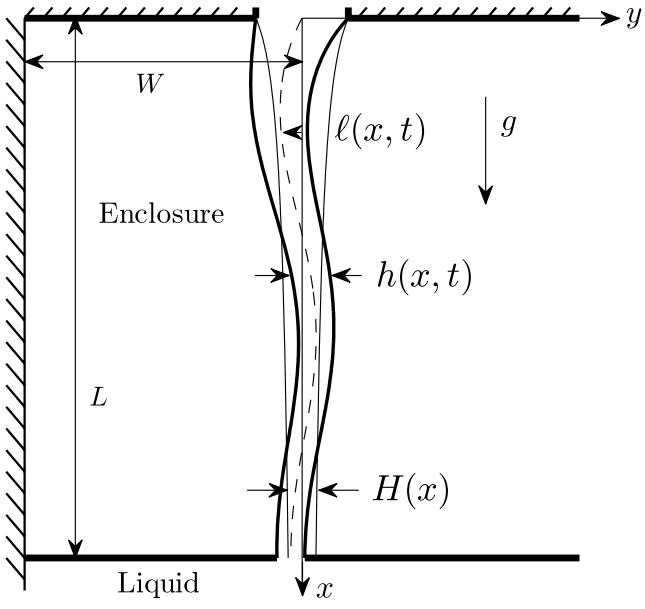

FIG. 1. Sketch of the model configuration.

surface tension, and also because in various real configurations, the convective effects prevail over those of the surface tension.

Although in principle, self-sustained periodic oscillations can be observed also in aerated air pockets,[15] here, we consider the pressure disturbances produced by the curtain compliant interface within a two-dimensional air enclosure delimited by the sheet itself, rigid walls, and a lower basin. Splashing effects are neglected. It has to be noticed that, in real situations such as that of a waterfall, the air cavity is not perfectly sealed, so that the present two-dimensional analysis well applies to physical situations with large aspect ratio values. Furthermore, the investigation will be restricted to the occurrence of one-dimensional surface wave-patterns. One can expect that oblique waves (i.e., developing along the spanwise direction) occur when extending the study to three-dimensional configurations, as already found experimentally by Le Grand-Piteira *et al.*[9] in the case of symmetrical semi-infinite boundary air environments.

Figure 1 shows the schematic of the geometrical configuration under consideration. In the unperturbed condition, the liquid flows along the vertical x-direction with a steady velocity and two symmetrical free interfaces. The expressions of centerline location ℓ and thickness h of the sheet are given, in terms of the interface positions $y^{\pm}$, as follows:

$$\ell^{\star}(x^{\star},t^{\star}) = \frac{y^{\star+}(x^{\star},t^{\star}) + y^{\star-}(x^{\star},t^{\star})}{2},$$
$$h^{\star}(x^{\star},t^{\star}) = y^{\star+}(x^{\star},t^{\star}) - y^{\star-}(x^{\star},t^{\star}),$$

where superscripts ± refer to right and left interface, respectively, and t^* is the time. Here, as elsewhere, star denotes dimensional quantities.

A. Governing equations

The starting mathematical framework is given by the two-dimensional Euler equations in which gravity is retained, closed by the kinematic and dynamic conditions imposed at the free interfaces

$$p^{\star\pm} = p_{\mathrm{a}}^{\star\pm},$$
$$v^{\star\pm} = \frac{\partial y^{\star\pm}}{\partial t^{\star}} + u^{\star\pm}\frac{\partial y^{\star\pm}}{\partial x^{\star}}.$$

In the above equations, $p_a^{\star\pm}(x^\star,t^\star)$ is the local value of the external ambient pressure and the general definition $\varphi^{\star\pm}(x^\star,t^\star) = \varphi^\star(x^\star, y^{\star\pm},t^\star)$ has been adopted, φ being any of the flow variables u, v, and p (where u and v are the streamwise and lateral velocity components, respectively).

The assumption of a thin sheet with respect to the wavelength of a disturbance allows us to reduce the problem to a one-dimensional unsteady formulation. Following Mehring and Sirignano,[13] a coordinate-type expansion in the lateral direction y, for all the flow variables involved, is introduced. Such a perturbative approach is valid for $y^\star \in (y^{\star-}, y^{\star+})$ and hence, the inequality

$$|y^\star - \ell^\star(x^\star,t^\star)| \le \frac{h^\star(x^\star,t^\star)}{2} \tag{1}$$

holds. By adapting the procedure employed in Girfoglio *et al.*,[16] the lowest order set of equations governing the unsteady evolution of the sheet is derived by retaining the zero-th order approximation for the momentum and continuity equations, coupled with interface conditions at first order; that is,

$$\frac{\partial h^\star}{\partial t^\star} + \frac{\partial (u^\star h^\star)}{\partial x^\star} = 0, \tag{2}$$

$$\frac{\partial \ell^\star}{\partial t^\star} + u^\star \frac{\partial \ell^\star}{\partial x^\star} - v^\star = 0, \tag{3}$$

$$\frac{\partial u^\star}{\partial t^\star} + u^\star \frac{\partial u^\star}{\partial x^\star} = g - \frac{1}{\rho_l}\left[\frac{\partial \overline{p}_a^\star}{\partial x^\star} - \frac{\overline{p}_a^\star}{h^\star}\frac{\partial \ell^\star}{\partial x^\star}\right], \tag{4}$$

$$\frac{\partial v^\star}{\partial t^\star} + u^\star \frac{\partial v^\star}{\partial x^\star} = -\frac{1}{\rho_l h^\star}\widetilde{p}_a^\star, \tag{5}$$

where ρ_l is the liquid density and any velocity component $u^\star$, $v^\star$ has to be considered as the zero-th order approximation of the power-series expansion in the small parameter $(y^\star - \ell^\star)$. In the momentum equations (4) and (5), the usual positions have also been made

$$\widetilde{p}_a^\star = p_a^{\star+} - p_a^{\star-}, \qquad \overline{p}_a^\star = \frac{p_a^{\star+} + p_a^{\star-}}{2}.$$

Under the assumption of small perturbations, the linearized set of equations is obtained by assuming symmetry conditions for the base problem[14]

$$\frac{\partial \ell'^\star}{\partial t^\star} + U^\star \frac{\partial \ell'^\star}{\partial x^\star} - v'^\star = 0, \tag{6}$$

$$\frac{\partial v'^\star}{\partial t^\star} + U^\star \frac{\partial v'^\star}{\partial x^\star} = -\frac{1}{\rho_l H^\star}\widetilde{p}_a'^\star, \tag{7}$$

$$\frac{\partial h'^\star}{\partial t^\star} + \frac{\partial}{\partial x^\star}\left(U^\star h'^\star + H^\star u'^\star\right) = 0, \tag{8}$$

$$\frac{\partial u'^\star}{\partial t^\star} + \frac{\partial}{\partial x^\star}\left(U^\star u'^\star\right) = -\frac{1}{\rho_l}\frac{\partial \overline{p}_a'^\star}{\partial x^\star} \tag{9}$$

with capital letters denoting basic (steady) quantities and primes the corresponding fluctuations. Note that Eqs. (6) and (7) govern the evolution of the so called sinuous modes (involving lateral velocity disturbance and displacement of the sheet centerline), while Eqs. (8) and (9) govern the so called varicose modes, involving vertical velocity disturbance and sheet thickness variation.

As extensively discussed in Coppola *et al.*,[14] in the absence of viscosity and surface tension, the steady solution of sheet thickness and streamwise liquid velocity is given by the analytical Torricelli's free-fall solution

$$U^\star = \sqrt{U_{in}^{\star 2} + 2gx^\star}, \qquad H^\star = \frac{U_{in}^\star H_{in}^\star}{U^\star}, \tag{10}$$

where $U_{in}^\star$ and $H_{in}^\star$ are the liquid velocity and the sheet thickness at the inlet section. To close the two systems of coupled equations (6) and (7) and (8) and (9), just an expression for the ambient gas pressure terms $(\overline{p}_a'^\star, \widetilde{p}_a'^\star)$ as functions of the deflection of the sheet is required.

B. Ambient gas pressure model and non-dimensional equations

By considering relation (1) for perturbed quantities, the infinitesimal variation of the enclosure volume, resulting from the sheet fluctuation, is given by

$$\mathcal{V}_{\mathrm{a}}'^{\star} = \int_0^{L^\star} \ell'^{\star}(x^\star)dx^\star - \frac{1}{2}\int_0^{L^\star} h'^{\star}(x^\star)dx^\star.$$

If we hypothesize that the air within the enclosure encompasses compression/expansion isoentropic thermodynamic transformations, we are able to give explicit expressions for the external pressure terms of Eqs. (7) and (9), for the two different oscillating modes of the sheet, respectively, as follows:

$$\widetilde{p}_{\mathrm{a}}'^{\star} = \gamma \frac{P_{\mathrm{a}}^\star}{\mathcal{V}_{\mathrm{a}}^\star}\int_0^{L^\star} \ell'^{\star}(x^\star)dx^\star, \tag{11}$$

$$\overline{p}_{\mathrm{a}}'^{\star} = \frac{\gamma}{4}\frac{P_{\mathrm{a}}^\star}{\mathcal{V}_{\mathrm{a}}^\star}\int_0^{L^\star} h'^{\star}(x^\star)dx^\star, \tag{12}$$

where γ is the specific heat ratio, $P_{\mathrm{a}}^\star$ is the unperturbed gas pressure into the enclosure, and $\mathcal{V}_{\mathrm{a}}^\star = L^\star W^\star - \frac{1}{2}\int_0^{L^\star} H^\star(x^\star)dx^\star$ is the corresponding volume in the configuration shown in Figure 1.

By employing the reference quantities

$$L_{\mathrm{r}}^\star = L^\star, \quad \ell_{\mathrm{r}}^\star = H_{\mathrm{in}}^\star,$$
$$u_{\mathrm{r}}^\star = U_{\mathrm{in}}^\star, \quad v_{\mathrm{r}}^\star = \varepsilon U_{\mathrm{in}}^\star,$$
$$t_{\mathrm{r}}^\star = L^\star/U_{\mathrm{in}}^\star, \quad p_{\mathrm{r}}^\star = \rho_{\mathrm{l}} U_{\mathrm{in}}^{\star 2}$$

with $\varepsilon = \ell_{\mathrm{r}}^\star/L_{\mathrm{r}}^\star$ denoting the *slenderness* parameter (tiny according to the assumptions made in deriving the model), the set of equations (6)–(9) is conveniently rewritten in non-dimensional form (by taking into account explicitly the fluctuations of the ambient pressure (11) and (12)) as follows:

sinuous mode

$$\begin{cases} \dfrac{\partial \ell}{\partial t} + U\dfrac{\partial \ell}{\partial x} = v, & (13) \\ \dfrac{\partial v}{\partial t} + U\dfrac{\partial v}{\partial x} = -\dfrac{\mathcal{K}}{H}\bar{\ell}, & (14) \end{cases}$$

varicose mode

$$\begin{cases} \dfrac{\partial h}{\partial t} + \dfrac{\partial}{\partial x}(Uh + Hu) = 0, & (15) \\ \dfrac{\partial u}{\partial t} + \dfrac{\partial}{\partial x}(Uu) = 0, & (16) \end{cases}$$

where

$$\mathcal{K} = \gamma \frac{P_{\mathrm{a}}}{\varepsilon\left(\frac{W^\star}{L^\star} - \frac{\varepsilon}{2}\int_0^1 H dx\right)} \tag{17}$$

is the equivalent stiffness of the enclosure air, and

$$\bar{\ell} = \int_0^1 \ell\, dx \tag{18}$$

denotes the average sinuous deflection of the sheet.

Accordingly, Eq. (10) for base solution takes the following non-dimensional form:

$$UH = 1 \quad \text{and} \quad U = \sqrt{1 + 2Fr\, x}, \tag{19}$$

where $Fr = gL^\star/U_{\mathrm{in}}^{\star 2}$ denotes the Froude number.

In summary, just two independent dimensionless parameters for the problem under study have to be considered: the Froude number Fr and the equivalent air stiffness $\mathcal{K}$. Note explicitly that in

the present analysis, the air stiffness includes simultaneously the effects of the undisturbed pressure within the enclosure, of the enclosure width and of the slenderness ratio $\varepsilon = H^{\star}_{\text{in}}/L^{\star}$, which in principle have to be taken into account separately.

Note that Eqs. (15) and (16) governing the evolution of the varicose modes are not able to sustain any oscillating wave-pattern in the configuration here adopted, reducing to simple advection equations. Therefore, the attention will be focused hereinafter on the sinuous disturbances (Eqs. (13) and (14)), through a modal and non-modal theoretical approach. In this last case, due to the hyperbolic nature of the governing equations, they are equipped with two boundary conditions prescribed at the inlet location, $x = 0$, namely, $\ell(0) = 0$ and $v(0) = 0$.

III. THEORETICAL INSIGHT ON THE NAPPE GLOBAL DYNAMICS

In order to give more physical insight on the fluid system under study, the equations for sinuous disturbances (focus of the present analysis) can be properly rearranged by taking into account integral quantities depending on the sheet extension as a whole. Hereafter, we will see that it is globally modeled as a lumped one-degree-of-freedom spring-mass system, in which the role of the spring is played by the air into the enclosure and the mass is that of the liquid sheet itself.

Let us start to reconsider the system of equations (13) and (14) in terms of a single second order partial integro-differential equation

$$\frac{D^2\ell}{Dt^2} = -\frac{\mathcal{K}}{H}\bar{\ell}, \tag{20}$$

where $\frac{D}{Dt}$ is the substantial derivative. Such an equation governs the linear inviscid evolution of a generic disturbance subjected to an integral reaction term. The role played by the air stiffness $\mathcal{K} \geq 0$ is crucial in characterizing the dynamics of the self-sustained wave-patterns evolving into the curtain. If $\mathcal{K} = 0$, the equation is trivial, reducing to the simple advection equation with variable mean velocity given by Eq. (19). Then, if no input is introduced at the left boundary, after a finite time any solution vanishes, with the disturbance being continually expelled at the outlet of the domain. Conversely, the presence of the reaction term in the form of an integral changes things in such a way that the temporal evolution of the disturbance is by no means identically null after a finite time. As it will be shown in the subsequent investigations, depending on the stiffness of the air chamber adjacent to the sheet, the system dynamics exhibits different features in terms of both stability properties and energy time evolution.

After expressing the substantial derivative in explicit form, integrating Eq. (20) over the whole length of the sheet yields

$$\frac{d^2}{dt^2}\left[\int_0^1 H\ell\, dx\right] + \mathcal{K}\bar{\ell} = -\left.\frac{\partial \ell}{\partial t}\right|_1 - v_1, \tag{21}$$

where the boundary conditions at the inlet location, $\ell(0) = 0$ and $v(0) = 0$, have been considered, and quantities at the outlet boundary are denoted with the subscript 1. This notation will be used hereafter for all the quantities at the right boundary.

The integral at left hand side of Eq. (21) can be conveniently expressed as

$$\int_0^1 H(x)\ell(x)\, dx = \bar{H}\bar{\ell} + \int_0^1 H'(x)\ell'(x)\, dx, \tag{22}$$

where $H'(x)$ and $\ell'(x)$ into the covariance term on the right side of the above equation represent the local deviations of sheet thickness and centreline position from their average values, $\bar{H}$ and $\bar{\ell}$, respectively, and with the following position being also made:

$$\bar{H} = \int_0^1 H\, dx.$$

The adopted hypotheses of small sheet thickness and perturbations assure that the covariance term is small so that it can be neglected into Eq. (22) and the analogy with an elastic oscillator

holds, as it appears hereafter

$$\bar{H}\frac{d^2\bar{\ell}}{dt^2} + \mathcal{K}\bar{\ell} = -\left(2\frac{\partial \ell}{\partial t}\Big|_1 + U\frac{\partial \ell}{\partial x}\Big|_1\right), \tag{23}$$

where $\bar{H}$ denotes the mass of the liquid sheet and $\mathcal{K}$ is the equivalent spring stiffness of the enclosure air, whilst the right hand side has been written by considering Eq. (13). It's worth noting that in absence of gravity effects (i.e., parallel flow), Eq. (23) is obtained without any approximation from Eq. (21) and the above analogy is exact. Then, the right hand side of Eq. (23) can be further manipulated in order to extract a damping term, that is to say

$$\bar{H}\frac{d^2\bar{\ell}}{dt^2} + 2\frac{d\bar{\ell}}{dt} + \mathcal{K}\bar{\ell} = \underbrace{-2\frac{d}{dt}\int_0^1 x\frac{\partial \ell}{\partial x}dx - U\frac{\partial \ell}{\partial x}\Big|_1}_{f_\mathrm{i}}, \tag{24}$$

where f_i represents the self-induced forcing acting on the elastic oscillator.

In summary, the global dynamics of the nappe consists of the mutual interaction of the centerline local deflection with the compliant air chamber which behaves as a spring acting on the average sheet deflection. Equation (20) shows that the local deflection is forced by the global reaction term of the spring, whilst the dynamics of the global spring-mass oscillator is driven by a combination of local sheet displacement values, as described by Eq. (24). In the following part of the paper, we will correlate such a mutual forcing to special features of the eigenvalues spectrum; the spectrum uncovers the natural mode (possibly unstable) of the spring-mass system and the peculiar oscillating behavior of the nappe described not just by single modes but by the superposition of a number of modes to be ascribed essentially to Eq. (20) and physically connected to another characteristic frequency linked to the typical crossing (or falling) time.

Here, we would like to introduce the following ansatz: the system is stable if the crossing time is less than the period of the spring-mass oscillator, $\mathcal{T}$. In the opposite situation, the self-forcing establishes, leading to instability. Of course, since the oscillator works in the driven regime, the oscillation period does not correspond to the natural frequency of oscillation and in general, it cannot be determined in analytical closed form. It should be stressed that this ansatz includes the gravity effects, in the sense that in the presence of gravity effects, a shorter crossing time is expected, as well as a higher $\mathcal{K}$ threshold of instability. Such predictions will be confirmed by the subsequent spectral analysis. In analogy with the classic acoustic phenomenon of edge tones, we will uncover that resonance occurs at frequencies one-plus-one-fourth times the instability onset frequency. Let us remember that the edge tones phenomenon refers to the acoustic tones produced when a jet of air strikes a wedge shaped edge, whereas resonance occurs at frequencies one-integer-plus-one-quarter times the frequency given by the ratio of the jet velocity to the distance between the jet exit section and the wedge apex. In other physical terms, Curle[12] explained that the jet wavelength w and the edge to nozzle distance d are related by the relationship $d = (n + 1/4)w$, where n is an integer.

IV. DISTURBANCE ENERGY EVOLUTION

In order to investigate some features of the solutions of Eqs. (20) and (24), it is useful to examine the mechanisms of perturbation growth (or decay) by considering also the time behavior of the system's energy E. For sinuous disturbances, the energy balance equation can be easily derived by multiplying Eq. (14) by the lateral velocity fluctuation v, and then by integrating it over the whole volume (per unit length in transversal direction) of the sheet, thus obtaining

$$\frac{dE_\mathrm{k}}{dt} + \frac{v_1^2}{2} = -\left(\mathcal{K}\bar{\ell}\right)\int_0^1 v\,dx, \tag{25}$$

where the kinetic energy E_k is defined as

$$E_k = \frac{1}{2}\int_0^1 H v^2\, dx \tag{26}$$

and the energy terms are made dimensionless with respect to the reference energy $E_r^\star = \rho_l \ell_r^\star L_r^\star v_r^{\star 2}$.

Apart from the presence of the convective exchange term of kinetic energy at the lower end of the domain, the right hand side of Eq. (25) shows that a single mechanism contributes to the rate of change of kinetic energy, that is to say the pressure (i.e., the term in between the parentheses) work per unit time exchanged during the isentropic compression/expansion of the air enclosure. By looking at the analogy with the elastic oscillator, one expects that the pressure work has a time oscillating trend driven by the frequency of the self-induced forcing acting on the spring-mass model (24); since the pressure work can assume both positive and negative values, no conclusion may be drawn about the large time asymptotic behavior.

It is worthwhile to further rearrange Eq. (25) by eliminating the lateral velocity v with the aid of Eq. (13), where the convective term is integrated by parts. The result is

$$\frac{dE}{dt} + \frac{v_1^2}{2} = -\mathcal{K}\bar{\ell}U_1\ell_1 + \mathcal{K}\bar{\ell}\int_0^1 \frac{dU}{dx}\ell\, dx \tag{27}$$

with $E = E_k + E_e$, where the elastic energy of the enclosure air is

$$E_e = \frac{1}{2}\mathcal{K}\,\bar{\ell}^2. \tag{28}$$

By making considerations analogous to those already discussed for Eq. (22), Eq. (27) can be written as

$$\frac{dE}{dt} + \frac{v_1^2}{2} = -\mathcal{K}\bar{\ell}U_1\ell_1 + \mathcal{K}\bar{\ell}^2\overline{\left(\frac{dU}{dx}\right)}, \tag{29}$$

where

$$\overline{\left(\frac{dU}{dx}\right)} = Fr \cdot t_{\text{cross}}, \tag{30}$$

t_{cross} being the marching time needed by the perturbation to cross the entire domain.

Note that $-\mathcal{K}\bar{\ell}U_1\ell_1$ represents the convective exchange of elastic energy at the outlet (namely, the work flux related to the pressure), whilst the term $\mathcal{K}\bar{\ell}^2\overline{\left(\frac{dU}{dx}\right)}$ can be interpreted as a production of disturbances total energy extracted from the stretching (i.e., non-parallel) basic flow. Since the basic flow, driven by the gravity field, accelerates along the streamwise direction, this last term is always positive (it is null if $Fr = 0$), contributing to increase the disturbance energy. As observed before for the kinetic energy, one cannot infer any conclusions about the asymptotic behavior of the total energy; nevertheless, due to the positive gravitational production term, one can expect a short time growth also in asymptotically stable situations. We will see that this is possible even when the gravitation effects are negligible.

Furthermore, a close-up inspection of the term $-\mathcal{K}\bar{\ell}U_1\ell_1$ allows one to predict, in no-gravity configurations, asymptotic stability depending on the phase lag ϕ existing between the signals $\bar{\ell}$ and ℓ_1: a perfect phase synchronization ($\phi = 0$) leads the system's energy to asymptotically decrease from its initial value; when the signals have a phase lag $0 < \phi \leq \pi$, the temporal behavior of the system's energy assumes an oscillating, nonmonotonic trend and the phase quadrature ($\phi = \frac{\pi}{2}$) among $\bar{\ell}$, ℓ_1 spots the critical threshold for the large time stability interval ($0 < \phi < \frac{\pi}{2}$), while no conclusions can be inferred for a phase lag $\frac{\pi}{2} < \phi \leq \pi$. Once again, when gravity effects are retained, it is not possible to predict the system's energy trend over the long times through the phase lag ϕ, because asymptotic growing or decaying behaviors depend on whether the production term overwhelms the kinetic and elastic convective exchanges. These theoretical predictions will be confirmed hereafter by means of both direct numerical simulations and linear stability analysis.

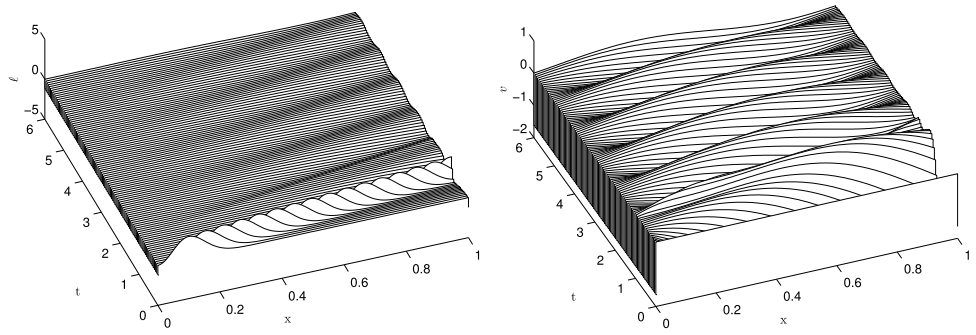

FIG. 2. Spatio-temporal evolution of ℓ and v disturbances in absence of gravitational effects for $\mathcal{K} = 18$.

V. SPATIO-TEMPORAL CHARACTERISTICS VIA DIRECT NUMERICAL SIMULATIONS

The time evolution of an initially localized disturbance for spotted values of the chamber stiffness inducing totally different asymptotic behaviors of the system will be analyzed; both the case when gravity is neglected and retained will be examined by means of direct numerical simulation of governing equation (20).

Let us start to analyze the simplified condition of parallel main flow, in which gravity is neglected. The spatio-temporal representation of numerically computed solutions to Eq. (20), in terms of centreline deflection ℓ and lateral velocity v, evaluated for $\mathcal{K}$ values inducing a different asymptotic behavior of the energy norm, are reported in Figures 2 and 3. The initial condition of the simulations is constituted by a compact support function satisfying the prescribed boundary conditions, i.e., a Gaussian-like pulse for the perturbed centreline deflection ℓ, localized near the upper boundary; no perturbation in lateral velocity fluctuation v is considered here.

As can be observed from the simulations, the centreline pulse, initially localized near the upper boundary, travels without significantly modifying its own structure until it reaches the opposite boundary. However, immediately the velocity disturbance is forced to assume non-null finite values, with a non-zero integral average over the domain. This is due to momentum equation (14), in which the transport of v is governed by the global reaction of the air enclosure, which depends in turn by the centreline fluctuation ℓ. For relatively small $\mathcal{K}$ values, the ℓ transport equation, Eq. (13), behaves practically as a pure advection model, with the forcing (represented by the lateral velocity v) becoming insignificant, as can be clearly observed in simulations of Figure 2, carried out for a $\mathcal{K}$ value close to the marginally stable critical value in absence of gravity. A different scenario is found as $\mathcal{K}$ increases, due to the enhancing of the mutual influence of the disturbances that induces the original pulse to lose its compact support while it travels towards the outlet boundary. Such a deviation from its original structure becomes increasingly important as $\mathcal{K}$ increases giving rise to a wave-packet generation, placed behind the Gaussian bump, the structure of which is enhanced with increasing air stiffness parameter. More remarkable, numerical simulations show that after

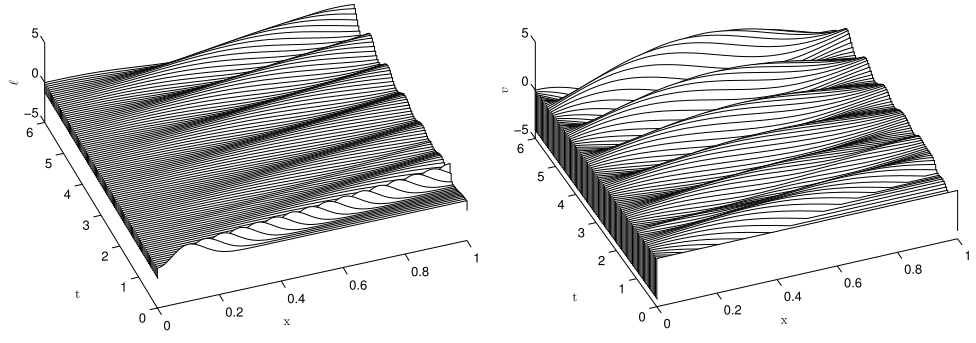

FIG. 3. Spatio-temporal evolution of ℓ and v disturbances in absence of gravitational effects for $\mathcal{K} = 30$.

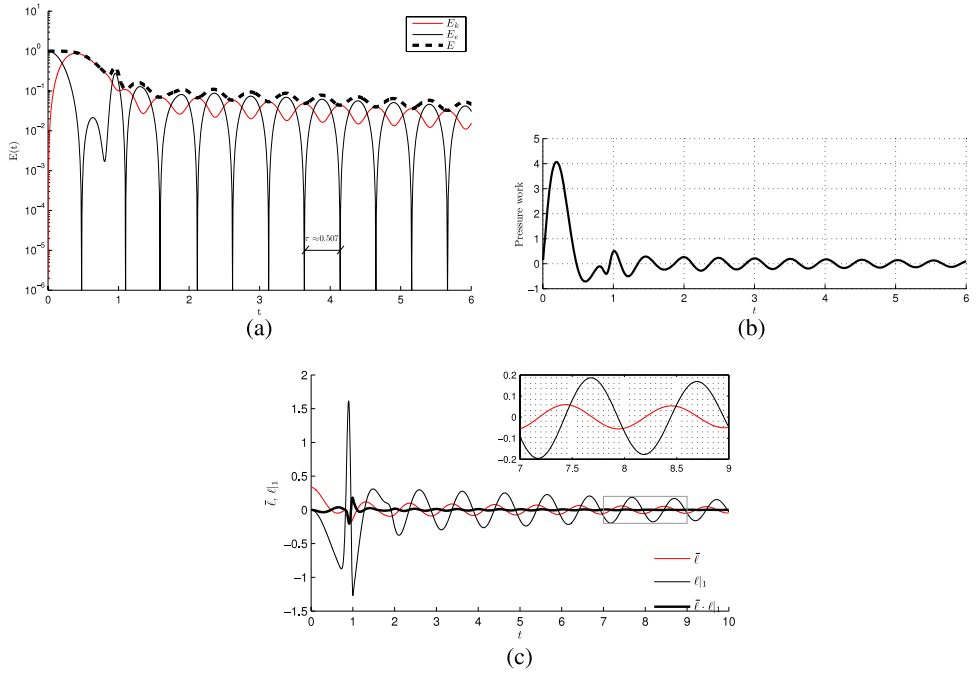

FIG. 4. Temporal evolution of the disturbance energy (a), pressure work (b), and normalized outlet E_e convective exchange (c), for $\mathcal{K} = 18$ and $Fr = 0$.

the initial transient, whose duration, $t = 1$, represents the marching time at constant velocity of the pulse disturbance over the entire domain, a continuous generation of new pulses, affecting the entire length of the sheet, is induced due to the action of the air chamber over the compliant sheet. The continuous triggering of pulses gives rise to an asymptotic regime where the time-depending behavior of the perturbation experiences an oscillating trend with a constant period that is determined by the parameter $\mathcal{K}$, in both stable and unstable situations.

Such typical transient behaviors can be better appreciated in Figures 4 and 5, referring to stable and unstable cases, respectively, in the absence of gravity, and in Figures 6 and 7, corresponding to stable and unstable, respectively, gravitational cases. Each figure depicts the time variation of total energy of the disturbance, including the kinetic and elastic components, in frame (a); the pressure work per unit time introduced at the right hand side of Eq. (25), in frame (b); the contribution to the rate of change of the total energy yielded by the convective exchange of elastic energy at the outlet in Eq. (29), scaled by the constant $-\mathcal{K}U_1$, together with the single trends of $\bar{\ell}$ and ℓ_1, in frame (c). All energy terms are scaled with respect to the initial elastic energy E_e of the original pulse.

In both cases of $Fr = 0$, Figures 4 and 5 show that, after an initial transient where the total energy does not exhibit any short time amplification, all the energy contributions follow a perfectly regular time oscillating trend. The period τ of such oscillations matches that of the pressure work exchanged with the air chamber, represented in frame (b) of the figures, as well as that of the convective exchange of elastic energy (thick line) in frame (c). Of course the period shown in figures is half of that of the nappe centerline displacement $\mathcal{T}$. Note also that in the unstable case, $\bar{\ell}$ and ℓ_1 are almost in phase opposition, coherently with findings suggested in Sec. IV, while in the stable one, they are close to the phase quadrature. The gravitational cases with $Fr = 20$ of Figures 6 and 7 (where, for the sake of convenience, the dimensionless time t^* over the crossing time is introduced) feature basically the same characteristic results. Note that the value of $\mathcal{K} \approx 59$, here stable, represented an unstable situation in the absence of gravity, in agreement with the theoretical prediction that when gravity is relevant, the falling time is reduced and the instability threshold, $\mathcal{T} = t_{\text{cross}}$, moves $\mathcal{K}$ towards higher values. However, although gravity plays an asymptotic stabilizing role, Figures 6 and 7 clearly show that the total energy exhibits a short time growth due to the production term present at right hand side of Eq. (29).

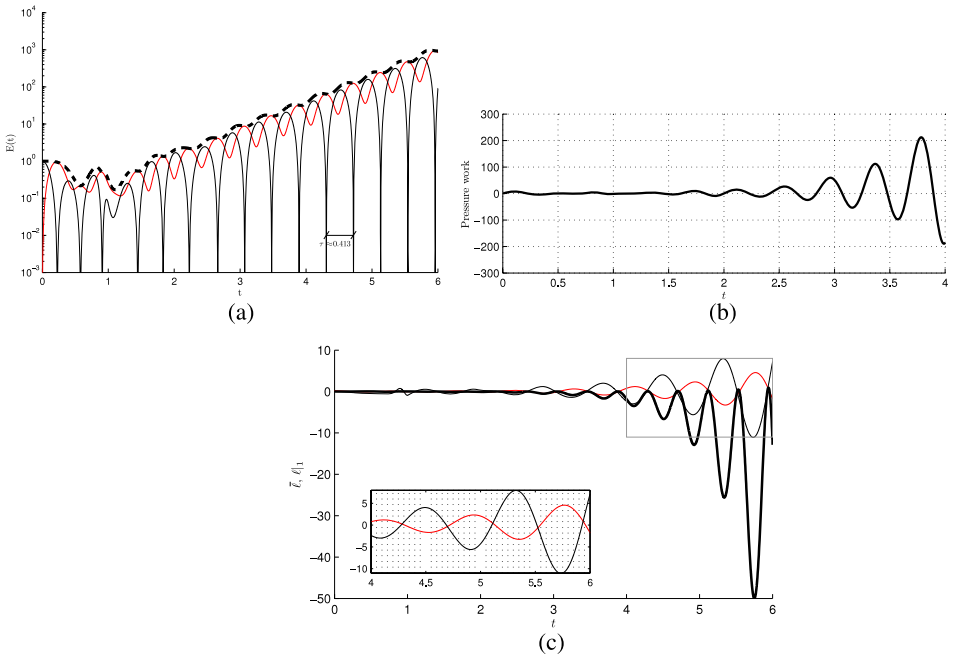

FIG. 5. Temporal evolution of the disturbance energy (a), pressure work (b), and normalized outlet E_e convective exchange (c), for $\mathcal{K} = 58.87$ and $Fr = 0$.

Other considerations about the asymptotic behavior of the system can be also inferred from the dynamical point of view, specifically by bearing in mind the lumped system of Eq. (24). The self-induced forcing f_i is implicitly dependent on the value of the parameter $\mathcal{K}$; in general, we found that it amplifies or decays asymptotically in time depending on whether the disturbances' total energy amplifies or decays. Although it is not possible to determine in closed form, the time

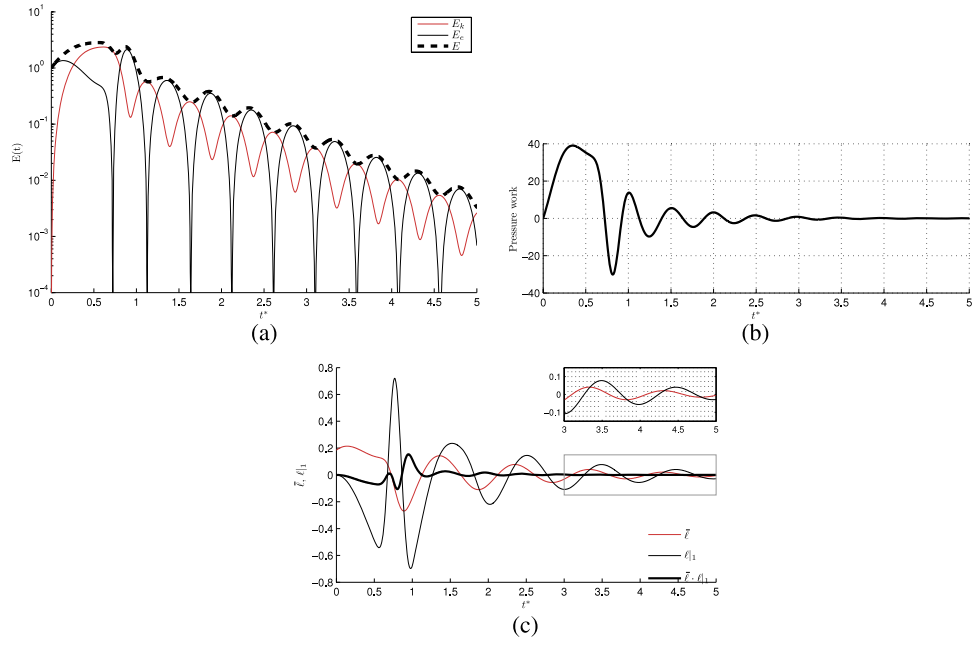

FIG. 6. Temporal evolution of the disturbance energy (a), its time derivative (b), and normalized outlet E_e convective exchange (c), for $\mathcal{K} = 58.87$ and $Fr = 20$.

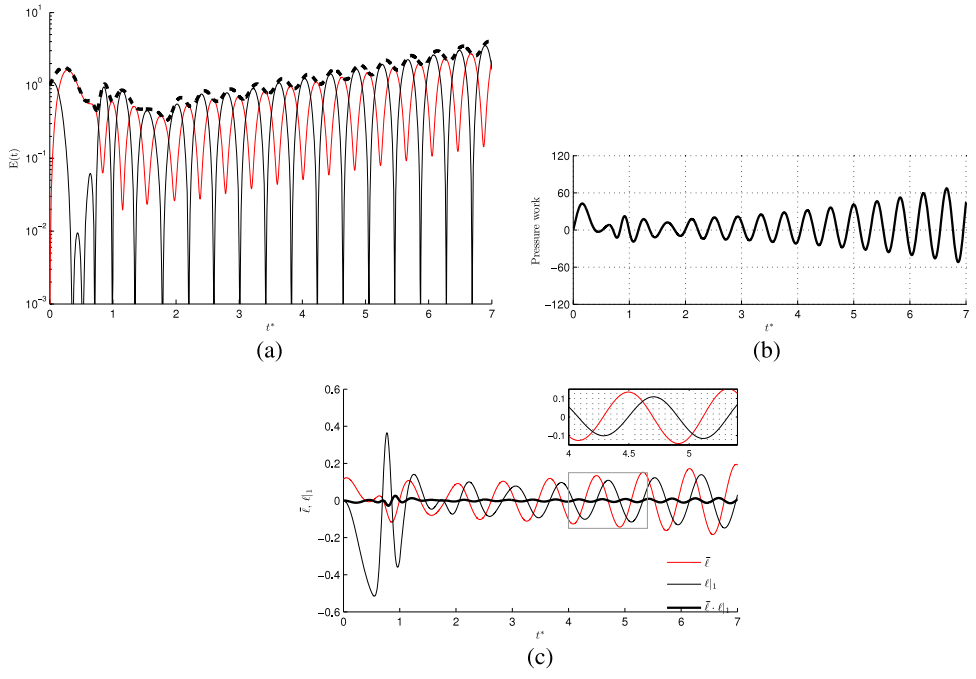

FIG. 7. Temporal evolution of the disturbance energy (a), its time derivative (b), and normalized outlet E_e convective exchange (c), for $\mathcal{K} = 160$ and $Fr = 20$.

trend of f_i as a function of $\mathcal{K}$, similar to the standard driven damped spring-mass oscillators, the phase lag between forcing and system response depends on the relative values of forcing frequency and oscillator natural frequency. Here, for the simplified case of no gravity, from Eq. (24), one can deduce that the natural frequency is $\lambda_N = \sqrt{\mathcal{K} - 1}$. Depending on the assumed frequency of f_i with respect to λ_N three different scenarios are possible. Figure 8 shows a comparison between the

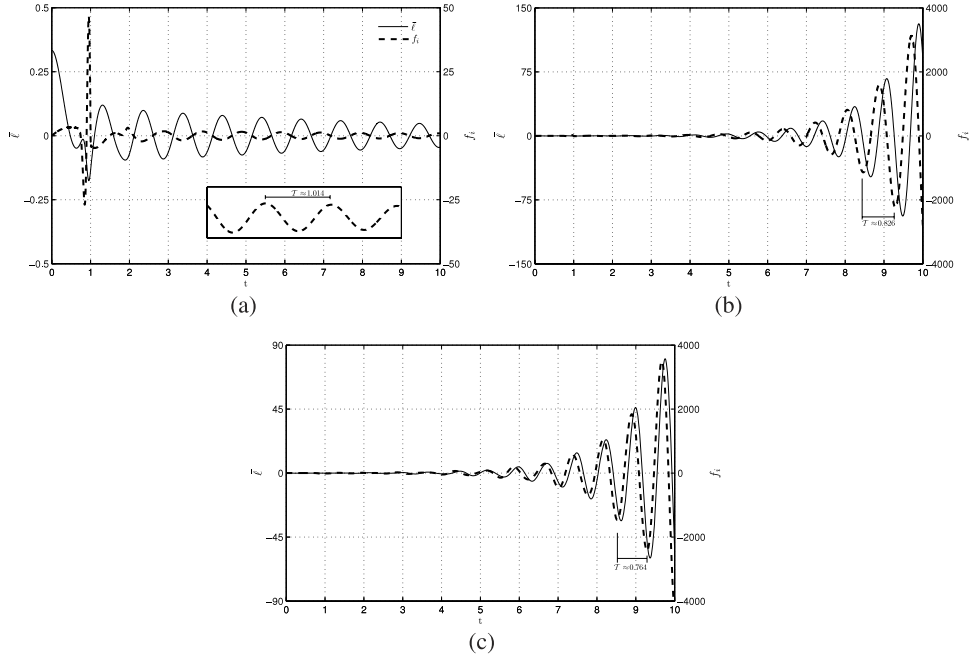

FIG. 8. Temporal evolution of $\bar{\ell}$ and self-induced forcing f_i for (a) $\mathcal{K} = 18$, (b) $\mathcal{K} = 58.87$, and (c) $\mathcal{K} = 100$.

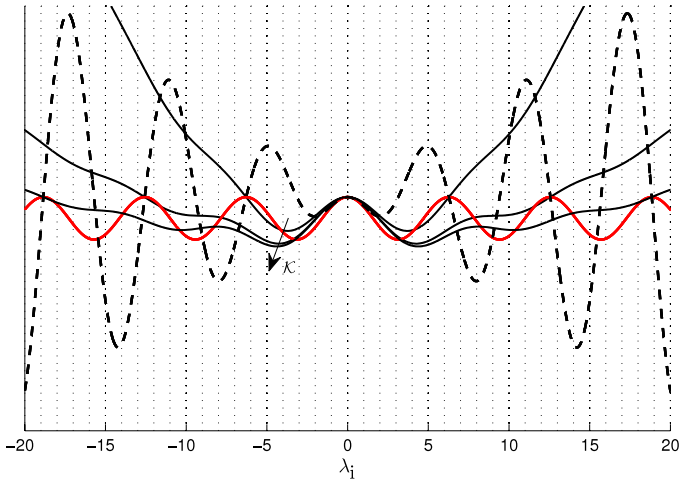

FIG. 9. Functions plot (a) $\cos\lambda_i$ (red solid line), (b) $1-\frac{\lambda_i}{2}\sin\lambda_i$ (black dashed line), and (c) $2\frac{\sin\lambda_i}{\lambda_i}+\frac{\lambda_i^2}{\mathcal{K}}-1$ (black solid line) for $\mathcal{K}=(19.74; 78.96; 177.65)$.

time evolution of the average sheet displacement $\bar{\ell}$, i.e., the spring displacement, and the forcing f_i, i.e., the right hand side of Eq. (24). In the frame (a), corresponding to the stable configuration for $\mathcal{K}=18$, it can be observed that, after the initial transient, $\bar{\ell}$ and f_i are almost in phase opposition, because the spring-mass motion is forced at a frequency (about equal to 6.19) greater than its natural frequency ($\lambda_N\approx 4.12$). This is a general behavior found for all the stable values of $\mathcal{K}$. Furthermore, the oscillation period $\mathcal{T}$ of f_i is exactly twice the oscillation period τ of the system's energy, as can be observed by comparing the inset of frame (a) and Figure 4(a). The asymptotical stabilization of the system can be explained, from a dynamical point of view, by considering the effect of a continuously reducing forcing acting on a damped system. On the contrary, frames (b) and (c) correspond to unstable configurations. As will be clarified by the subsequent stability analysis, unstable configurations offer different scenarios in which, as $\mathcal{K}$ increases, the driving term f_i can result in phase, phase quadrature, and phase opposition with respect to the spring displacement $\bar{\ell}$. This is clearly confirmed in simulations of Figure 8 showing, in frame (b), the phase quadrature between $\bar{\ell}$ and f_i corresponding to the resonance condition for $\mathcal{K}=58.87$ and, in frame (c), the circumstance that $\bar{\ell}$ and its forcing term are almost in phase, with the frequency of f_i being lower than the natural one ($\lambda_N\approx 9.95$). Of course, also in unstable configurations, the system's energy oscillates with a period exactly matching the semi-period of the self-induced forcing, as can be observed for the resonance case depicted in Figures 5(a) and 8(b).

VI. SPECTRAL STABILITY ANALYSIS

A comprehensive methodology to analyze the problem governed by Eq. (20) consists of formulating a boundary value eigenvalues problem. The standard approach to obtain global solutions consists of separating the variables and assuming the following form of the disturbance: $\ell(x,t)=\hat{\ell}(x)\cdot e^{\lambda t}$. This leads to the eigenvalue problem

$$\lambda^2\hat{\ell}+(2\lambda U+F_r)\,D\hat{\ell}+U^2D^2\hat{\ell}=-\frac{\mathcal{K}}{H}\hat{\bar{\ell}} \tag{31}$$

with D denoting spatial derivative along x direction, $\hat{\ell}$ the eigenfunction, and λ the complex eigenvalue.

A. Analytical approach in no-gravity case

In the special case of no-gravity, $Fr=0$, it is straightforward to obtain the characteristic eigenvalue equation in closed form. By integrating the above equation over the whole length of the nappe

and by employing the relevant boundary conditions, $\hat{\ell}_0 = D\hat{\ell}_0 = 0$, one obtains that the average sheet deflection is a linear combination of $\hat{\ell}_1$ and $D\hat{\ell}_1$

$$\hat{\bar{\ell}} = -\frac{2\lambda\hat{\ell}(1) + D\hat{\ell}(1)}{\lambda^2 + \mathcal{K}} \tag{32}$$

and hence,

$$D^2\hat{\ell} + 2\lambda D\hat{\ell} + \lambda^2\hat{\ell} = \frac{2\lambda\hat{\ell}(1) + D\hat{\ell}(1)}{1 + \frac{\lambda^2}{\mathcal{K}}}.$$

Integrating the above equation produces

$$\hat{\ell} = \frac{\mathcal{K}\hat{\bar{\ell}}}{\lambda^2}\left[(1 + \lambda x)\, e^{-\lambda x} - 1\right]$$

and, as a consequence of Eq. (13),

$$\hat{v} = \frac{\mathcal{K}\hat{\bar{\ell}}}{\lambda}\left[(1 + \lambda x)\, e^{-\lambda x} - 1\right] - \mathcal{K}\hat{\bar{\ell}} x e^{-\lambda x}$$

from which, by taking into account Eq. (32), eigenvalues λ can be obtained as complex solutions of the characteristic eigenvalue equation

$$\frac{\mathcal{K}}{\mathcal{K} + \lambda^2}\left[\left(\frac{2}{\lambda} + 1\right)e^{-\lambda} - \frac{2}{\lambda}\right] + 1 = 0 \tag{33}$$

which, in agreement with a previous statement, does not admit a solution for $\mathcal{K} = 0$.

Apart from the trivial solution $\lambda = 0$, which is not an eigenvalue, Eq. (33) does not admit any real solution for $\mathcal{K} > 0$, in agreement with the physical considerations requiring that the disturbance has always an oscillating nature due to the driving mechanism of the air chamber. Conversely, complex solutions of Eq. (33) lie, in the complex plane, along a single branch since the 2nd order partial differential equation (20) admits just a single characteristic along which disturbances propagate, namely, $\frac{dx}{dt} = U$.

A straightforward manipulation of Eq. (33), consisting in separating its real and imaginary parts, yields the critical value $\mathcal{K}_{cr}$ of the air cushion stiffness corresponding to the transition from stable to unstable configurations. Frequencies of the marginally stable disturbances ($\lambda_r = 0$) can be graphically obtained by searching for the contact points among the functions arising from the complex manipulation of Eq. (33)

$$\begin{cases} \cos\lambda_i = 1 - \dfrac{\lambda_i}{2}\sin\lambda_i, \\ \cos\lambda_i = 2\dfrac{\sin\lambda_i}{\lambda_i} + \dfrac{\lambda_i^2}{\mathcal{K}} - 1. \end{cases} \tag{34}$$

Solutions depend on the value of the $\mathcal{K}$ parameter, however, the first contact point (corresponding to $\mathcal{K} = 19.74$) represents a triple point since there is a change in the stability for the solutions of the model equation (see Fig. 9). Note that the frequency of the first couple of marginally stable modes corresponds to a period matching the required crossing time t_{cross} so that the disturbances can be expelled into the sheet basin, in agreement with the ansatz of Sec. III.

B. Numerical approach

In the general case, eigenvalue problem (31) can be conveniently reformulated starting from Eqs. (13) and (14) and enforcing the global temporal modes position, so as to recast the governing equations into the following compact matrical form:

$$\lambda\begin{pmatrix} \hat{\ell} \\ \hat{v} \end{pmatrix} = \mathcal{A}\begin{pmatrix} \hat{\ell} \\ \hat{v} \end{pmatrix}, \tag{35}$$

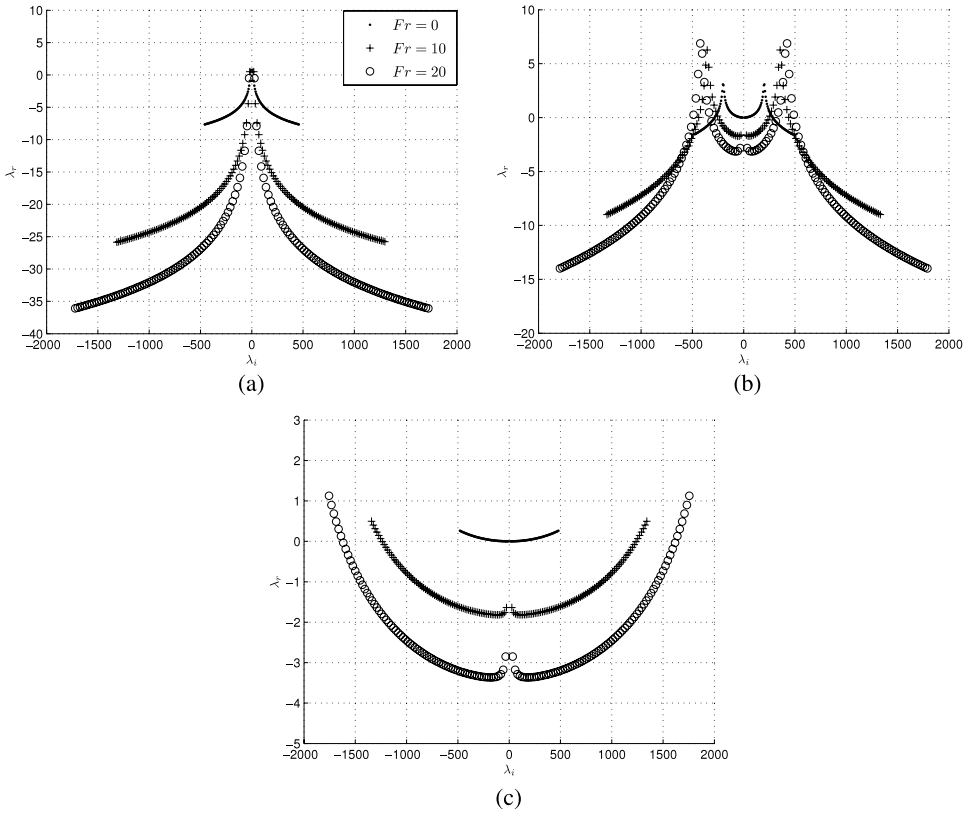

FIG. 10. Spectra obtained by varying gravity effects [Fr = 0 (·), Fr = 10 (+), and Fr = 20 (o)] for (a) $\mathcal{K} = 100$, (b) $\mathcal{K} = 4 \times 10^4$, and (c) $\mathcal{K} = 10^6$.

where the spatial operator is

$$\mathcal{A} \equiv \begin{pmatrix} -U \cdot \mathcal{D} & -\mathcal{I} \\ -\dfrac{\mathcal{K}}{H} \displaystyle\int_0^1 dx & -U \cdot \mathcal{D} \end{pmatrix}$$

with $\mathcal{I}$ denoting the identity operator.

For values of $Fr \neq 0$ (and $\mathcal{K} > 0$), eigenvalues and eigenfunctions are numerically computed by means of a Chebyshev collocation method, with both differential and integral terms being spectrally accurate. Figure 10 depicts the spectra obtained for various Froude numbers, evaluated for three typical values of stiffness of the air chamber inducing different shapes of distribution of the eigenvalues in the complex plane. The spectra are generally constituted of two symmetric branches with respect to the imaginary axis, each made of infinitely many eigenvalues, whose spreading rate is continuously varying with the gravity effect. The shape of the branches depends on the value assumed by the parameter $\mathcal{K}$ and results to be of three different possible configurations over the entire semi-infinite interval of positive $\mathcal{K}$ values. The major characteristic of the spectra, whatever the equivalent stiffness $\mathcal{K}$, is that each branch exhibits eigenvalues almost equally spaced in imaginary parts. Thus, two characteristic frequencies can be recognized, one related to the constant spacing of imaginary parts $\Delta\lambda_i$ and the other one to the imaginary part of the leading (i.e., most unstable) modes pair. The latter corresponds to the frequency at which damped spring-mass system (24) oscillates driven by the self-induced forcing f_i, whilst the former is related to the crossing time

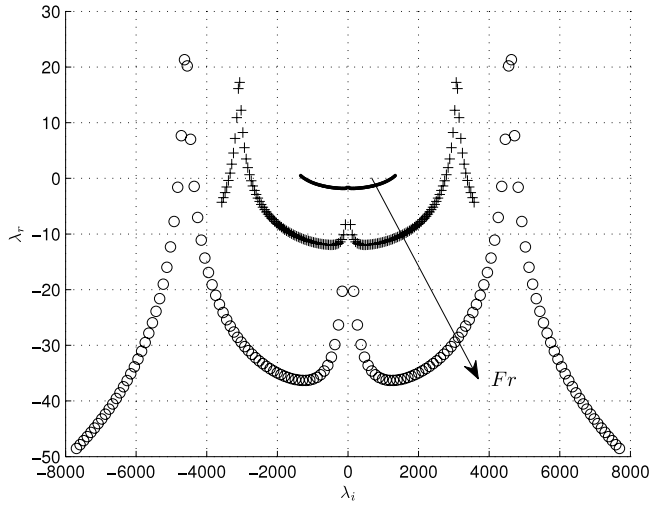

FIG. 11. Spectra obtained by varying gravity effects [Fr = 10 (·), Fr = 100 (+), and Fr = 500 (o)] for $\mathcal{K} = 10^6$.

$$t_{\text{cross}} = \int_0^1 \frac{dx}{\sqrt{1 + 2Fr\, x}} \tag{36}$$

so that, by varying the Froude number, it always results in $\Delta\lambda_{\text{i}} \approx \frac{2\pi}{t_{\text{cross}}}$.

The different configurations assumed by the spectrum as $\mathcal{K}$ is varied are strictly linked to the frequency assumed by the leading mode pair which, in turn, is correlated to the oscillation frequency of spring-mass oscillator (24). For stiffness values of the enclosure air small enough (e.g., see frame (a) of Figure 10), the leading mode pair is also the lowest frequency eigenvalues pair of the spectrum; as $\mathcal{K}$ increases, the frequency of fluid oscillator (24) increases accordingly and the leading modes shift outwards to higher frequencies, giving rise to a cascade of "inner" eigenvalue pairs having lower frequency in the neighborhood of the imaginary axis, as displayed in the typical configuration of frame (b); finally, for even higher $\mathcal{K}$ values, the oscillation frequency of the spring-mass system can result greater than the numerically computable highest frequency of the spectrum, leading to the shape depicted in frame (c).

As expected, gravity certainly plays a role in determining the shape of the spectrum for a given stiffness $\mathcal{K}$. This is clearly showed in Figure 11 in which, for the same air chamber stiffness value as Figure 10(c), the spectra computed for three different Froude numbers are reported. The initial parabola shaped spectrum represented also in Figure 10(c) changes as Fr increases and becomes analogous in shape to those of Figure 10(b), so that a typical configuration can be similarly obtained by properly choosing the couple of parameters Fr and $\mathcal{K}$. The reason for this characteristic behavior lies in the mutual role played by gravity and stiffness in influencing the oscillation frequency of the right hand side of Eq. (24). As the Froude number increases, the crossing time t_{cross} reduces correspondingly; the spacing $\Delta\lambda_{\text{i}}$ among the eigenvalues increases so that the oscillation period $\mathcal{T}$ of the spring-mass system results rapidly higher than the maximum period included into the spectrum computed at the lowest Froude number. As a consequence, the corresponding frequency, initially higher than that of most unstable modes at $Fr = 10$, appears into the "spreading" part of the spectra evaluated at higher Froude numbers, and moves inward as Fr goes up.

The overall stabilizing role played by gravity is clearly confirmed in each frame of Figure 10 and Figure 11. As the Froude number increases, the entire spectrum spreads in the complex plane moving the bulk of its eigenvalues towards even more stable regions. We stress once again that this is a consequence of the reduction of the crossing time acting as a stabilizing effect competing against the forcing mechanism due to the air chamber, according to the ansatz of Sec. III.

Figure 12 shows a map of the modal stability/instability regions associated with the leading mode complex pair of the spectrum, obtained for a selected range of $\mathcal{K}$ values and by varying the

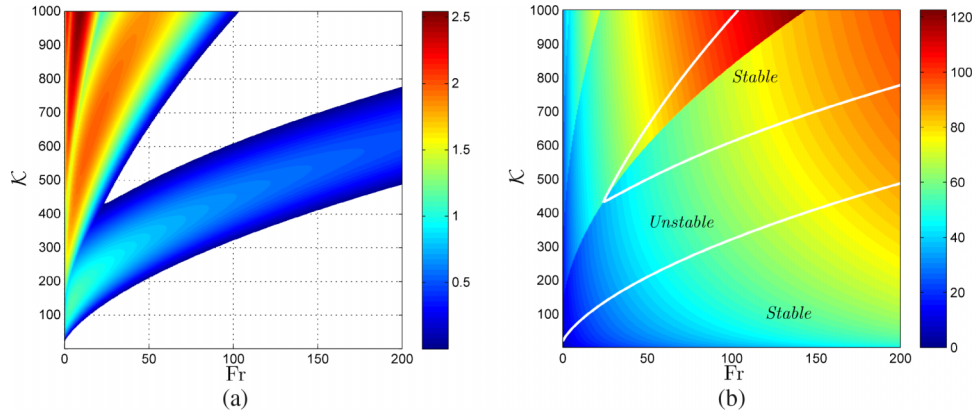

FIG. 12. Color maps of modal global behavior for a selected range of Froude number and $\mathcal{K}$ values. (a) is growth rate and (b) is frequency. White regions in frame (a) correspond to stable configurations.

Froude number from no-gravity case to sufficiently high gravity effects. Growth rates of disturbances are depicted in frame (a), where the color regions represent iso-level positive growth-rates (with stable configurations spotted by blank regions), while in frame (b), the corresponding frequencies of the fluid oscillator (24) are reported (the white lines represent the marginal modal curves).

The stabilizing effect induced by gravity on the asymptotic behavior of the system, driven by the leading mode, is clearly illustrated in Figure 12. The stability region in frame (a), already existing in the no-gravity case for values of $\mathcal{K} < 19.74$ (e.g., see Figure 9), broadens as described by the marginal stability curve roughly following the trend given by $\mathcal{K} = 26\sqrt{Fr} + 0.6Fr$. However, note that for higher $\mathcal{K}$ values, a further stable region occurs, which assumes a wedge-shaped conformation at its lower side and exhibits for higher Fr values the same trend as the marginal curve underlying. This typical behavior reproduces cyclically as $\mathcal{K}$ grows within the range of $(\mathcal{K}, Fr)$ values inspected (not shown herein). Thus, the map of growth-rate presents a periodic series of wedge-shaped stability regions as $\mathcal{K}$ increases, whose edges continuously shift towards higher Froude numbers. Figure 12(b) shows that in general, the oscillation frequency of the leading mode increases with increasing Froude numbers. Moreover, a discontinuous trend with $\mathcal{K}$ is observed at any fixed Fr due to the jump of the leading mode pair of the spectrum, giving rise to the characteristic onion structure depicted in Figure 12(b).

Such a typical modal behavior with $\mathcal{K}$ and Fr can be better appreciated by looking at Figures 13 and 14, showing parametric curves obtained by sectioning the maps of Figure 12 at fixed Fr and $\mathcal{K}$, respectively. Frames (a) and (b) of Figure 13 exhibit growth rate and frequency

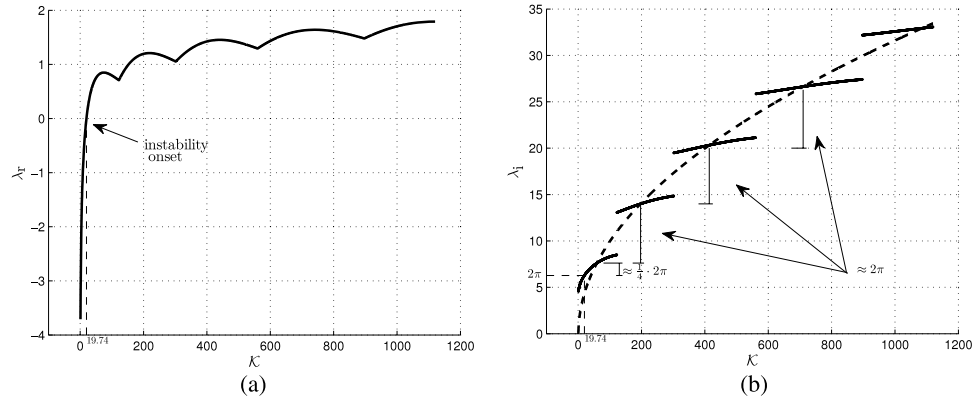

FIG. 13. Parametric trend with $\mathcal{K}$ of (a) growth-rate and (b) frequency of the leading mode pair, evaluated at $Fr = 0$. Dashed line in frame (b) represents the natural frequency variation of lumped system (24).

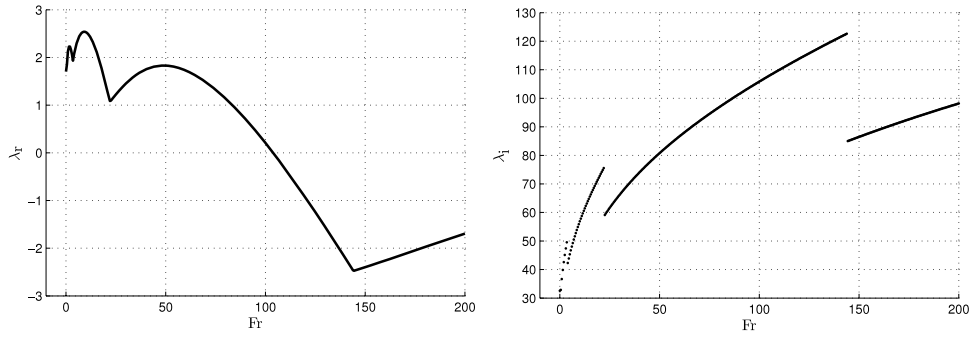

FIG. 14. Parametric trend with Fr of (a) growth rate and (b) frequency of the leading mode pair, evaluated at $\mathcal{K} = 1000$.

evolutions with $\mathcal{K}$ when gravity is neglected. Note, in particular, that the frequency plot (b) is piecewise discontinuous due to the presence of additional leading modes in the spectrum at discrete values of $\mathcal{K}$. The dashed line also present in plot (b) refers to the natural frequency variation of lumped system (24). The thin dashed segment in plot (a) marks the marginal value $\mathcal{K} = 19.74$ of null growth rate, to which the frequency of $\lambda_i = 6.28$ corresponds. In other terms, in the absence of gravity, the frequency of the marginal mode is related to the falling time, thus confirming the ansatz of Sec. III. Note also that this is not a resonance frequency, whose values are given by the intersections of the dashed line with the piecewise discontinuous line of Fig. 13(b). As can be seen inspecting the plot (b), the first value of the resonance frequency is found to be 7.61, with $7.61/6.28 = 1.21$, thus uncovering the *one-plus-one-quarter* criterion of the edge tones problem to a good accuracy. Furthermore, all other higher values are evenly spaced by 6.28. This very interesting result uncovers the theoretical considerations of Schwartz[1] and the experimental findings of Sato *et al.*,[7] which in turn resemble a major characteristic of the edge tone phenomenon.[12] In fact, the possible resonance frequencies are given by the relationship $2\pi(n + \frac{1}{4})$, where n is an integer. At the same time, Figure 14 reports the growth-rate (frame (a)) and frequency (frame (b)) trends obtained by varying the Froude number for the highest $\mathcal{K}$ value depicted in Figure 12. The unusual parabolic trend of Fig. 13(a), assumed by the growth-rate of each leading mode pair before being overwhelmed by the adjoining eigenvalue, is basically confirmed in the presence of gravity together with the stretching of the range of a single leading mode as Froude number goes up. Conversely, although gravity enhances the growth-rate of the unstable modes, it plays a stabilizing role because it moves the marginal $\mathcal{K}$ values upwards. Furthermore, the frequency curves of Figure 14(b), as Fr grows, move along segments having different slopes associated with each leading mode and the corresponding jumps in frequency follow a spreading trend consistent with the frequency associated to the crossing time, $\Delta\lambda_i$, whose negative amplitude is a result of the parametric behavior shown in Figure 11.

It should be pointed out that the perfect agreement found at $Fr = 0$ between the frequency of the marginally stable leading mode pair and the one linked to the spacing $\Delta\lambda_i$ is slightly lost in the presence of gravity, with an increasing discrepancy as the gravitational influence becomes more relevant. This can be observed in Figure 15 showing the analytical trend with the Froude number of t_{cross} together with the numerically computed period $\mathcal{T}$ of the spring-mass oscillator, associated with the leading mode. In the presence of a spatially developing base flow, the neutral stability criterion is fulfilled for oscillation periods $\mathcal{T}$ smaller than the corresponding crossing time t_{cross}.

VII. NON-MODAL ANALYSIS

In Sec. V, we reported that the direct numerical simulations, referring to an initial Gaussian-like pulse of the perturbed centerline deflection ℓ show that, in the presence of gravity, the total and kinetic energies exhibit transient amplifications even in situations when the flow system is asymptotically stable. Here, we aim to prove that such a circumstance is a robust feature of the

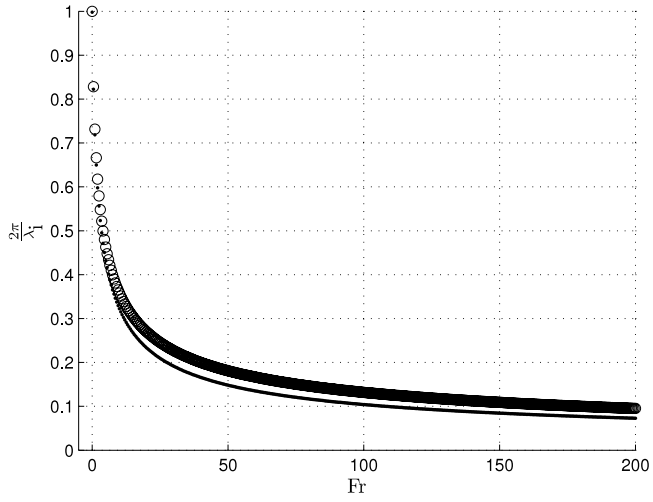

FIG. 15. Deviation with Froude number of the oscillation period $\mathcal{T}$ of the spring-mass system corresponding to the critical transition configurations (·) from the analytical predictions (o) of Eq. (36).

governing operator of model equation (20) linked to its non-normal character. In fact, we will show that transient amplifications of the disturbance energy can occur also in the absence of gravity. This is not in contrast to the previous findings of the numerical simulations, and it can be explained by considering that the standard procedure to evaluate the short-time trend of energy is based on searching the optimal disturbances, namely, the disturbances producing at each time-point the maximum amplification. In order to do this, we refer to a standard mathematical framework of the analysis of non-normal operators.[17–20]

The starting point is the reformulation of the initial-boundary value problem of Eqs. (13) and (14) in the Hilbert subspace S^N whose basis is constituted of the first N eigenfunctions satisfying the prescribed boundary and initial conditions.[19] If the temporal evolution problem is restated in the compact form

$$\frac{\partial \tilde{\mathbf{q}}}{\partial t} = \mathcal{A}\tilde{\mathbf{q}},$$

where the vector $\tilde{\mathbf{q}}(x,t)$ contains the disturbance flow variables $(\tilde{\ell},\tilde{v})$, expanded in the basis defined above, then, the temporal evolution process results governed accordingly by the system

$$\frac{d\mathbf{a}}{dt} = \sigma\mathbf{a}$$

with σ diagonal matrix of the first N eigenvalues and $\mathbf{a}$ vector of the expansion coefficients of the solution in the eigenfunctions basis.

In order to evaluate the norm of the disturbance energy, the inner product involving the energies defined by Eqs. (26) and (28) is adopted

$$E(t) = \|\tilde{\mathbf{q}}\|_E^2 = \frac{1}{2}\int_0^1 H\,(\tilde{v}\cdot\tilde{v}^*)\,dx + \frac{1}{2}\mathcal{K}\bar{\bar{\ell}}\cdot\bar{\bar{\ell}}^*, \tag{37}$$

where $*$ denotes the complex conjugate and the first and second terms on the right hand side refer, respectively, to the kinetic and elastic energy contributions. Following,[18] the scalar products are expressed in terms of the expansion coefficients by means of the use of the Hermitian matrix $\mathbf{M}$ of the inner products $M_{ij} = (\tilde{q}_i, \tilde{q}_j)$ between the eigenfunctions and the associated norm in S^N results

$$\|\tilde{\mathbf{q}}\|_E = \|\mathbf{F}\mathbf{a}\|_2$$

with $\mathbf{F}$ given by the $\mathbf{M} = \mathbf{F}^*\mathbf{F}$ decomposition.

If the operator $\mathcal{A}$ is normal then, $\mathbf{M}$ is the identity matrix, the eigenfunctions basis of $\mathcal{A}$ being orthogonal. On the contrary, if the operator $\mathcal{A}$ is non-normal, the diagonalization of the operator is

not unitary and the spectral analysis alone is not able to accurately describe the temporal evolution of the system, which has to be carried out by taking into account the transient behavior as well in a full initial value analysis.

To ascertain the non-normal character of the governing operator $\mathcal{A}$, an analysis of its pseudospectra and numerical range was performed. It is worth remembering that ϵ-pseudospectra of $\mathcal{A}$, for each $\epsilon > 0$, spot in the complex plane the isolevel curves of the resolvent norm $\|\mathcal{A} - z\mathcal{I}\|^{-1} = \epsilon^{-1}$, with $z \in \mathbb{C}$, and for non-normal operators, the value of such a norm can be significantly greater than $1/\text{dist}(z, \sigma(\mathcal{A}))$ corresponding to its value for normal operators. The numerical range is generally considered a useful tool to inspect the short-time growth in the energy norm of $\mathcal{A}$ according to the Hille-Yosida theorem, relating the initial energy rate of change to its maximum real coordinate, namely, the numerical abscissa. In effect, for a non-normal operator, the numerical abscissa lies in the positive real Gauss half-plane.[20]

The effect of the energy exchanges between fluid and air enclosure (e.g., refer to Eq. (29)) can be collected, regardless of the initial condition, into a single function, generally referred to as growth function

$$G(t) = \sup_{\tilde{\mathbf{q}}(x,0)\neq 0} \frac{\|\tilde{\mathbf{q}}(x,\, t)\|_E^2}{\|\tilde{\mathbf{q}}(x,\, 0)\|_E^2} = \|e^{\mathcal{A}t}\|_E^2. \tag{38}$$

The growth function $G(t)$ represents, for each time t, the highest energy amplification of a perturbation optimized over all possible initial conditions $\tilde{\mathbf{q}}(x,0)$ and it is hence the envelope of the energy evolution of all initial conditions with unit norm. The initial condition that attains the maximum gain in energy is commonly referred to as *optimal perturbation*. Here, the transient growth function $G(t)$ is computed via the eigenmode expansion method in which the spectral discretization, also employed for the computation of eigenvalues, is used. The energy norm is evaluated by means of a standard 2-norm, while the corresponding optimal perturbation is calculated via a Singular Value Decomposition (SVD) procedure of the transformed matrix exponential of gain function (38).

The non-normal character of the present governing operator can be recognized by observing the ϵ-pseudospectrum lines corresponding to selected values of $\mathcal{K}$ and Fr parameters, shown in Figure 16. A parametric trend in the Froude number is reported in frames (a)–(c), whilst a corresponding trend in the $\mathcal{K}$ parameter is provided in frames (d)–(f). ϵ-pseudospectra in frames (a)–(c) clearly show that an increase in the Froude number induces a strong non-normality whose strength extends basically on the left of the spectrum. The influence of the Fr number on the non-normality intensity is confirmed by the numerical range whose boundary lies even more deeply in the right complex half-plane as Fr goes up. A similar qualitative behavior can be observed in the frames (d)–(f) where the ϵ-pseudospectra show a less marked departure of the operator from the normality as the stiffness parameter $\mathcal{K}$ is increased. Although the heart of non-normality remains to the left of the spectrum, it extends more significantly on the right. The boundaries of the numerical range confirm that the level of non-normality increases with increasing $\mathcal{K}$.

Typical short-time trends of the growth function G as functions of $\mathcal{K}$ and Fr are depicted in Figure 17; with the aim of better showing these trends, in this framework, we refer to all stable configurations. Each frame of the figure reports the time scale t^* conveniently scaled with respect to the crossing time t_{cross}, in such a way that the range $0 < t^* < 2$ represents, for all the cases, the time needed by disturbances to cross twice the entire length of the sheet. In apparent contradiction with the trends previously obtained in terms of ϵ-pseudospectra and numerical range, the frame (a) shows that $G(t^*)$ peak decreases with increasing Fr. However, by looking at the inset of Figure 17(a), in which the growth functions at very short times are greatly zoomed, it is clear that the Hille-Yosida theorem is confirmed. Then, the result that $G(t^*)$ peak decreases with increasing Fr is due to the circumstance that the disturbances are expelled from the sheet outlet even more rapidly as Fr increases; the production term due to gravity, at the right hand side of Eq. (29), is overwhelmed by the negative convective total energy exchange at the outlet.

The effect of non-modal amplification of the disturbance energy can be examined also by inspecting the growth function over large times, as reported in Figure 18. The asymptotically unstable case depicted in Figure 18(a) shows that transient amplifications can generally occur also in the absence of gravity, but this is not in contrast with the findings of Figures 4(a) and 5(a) because these

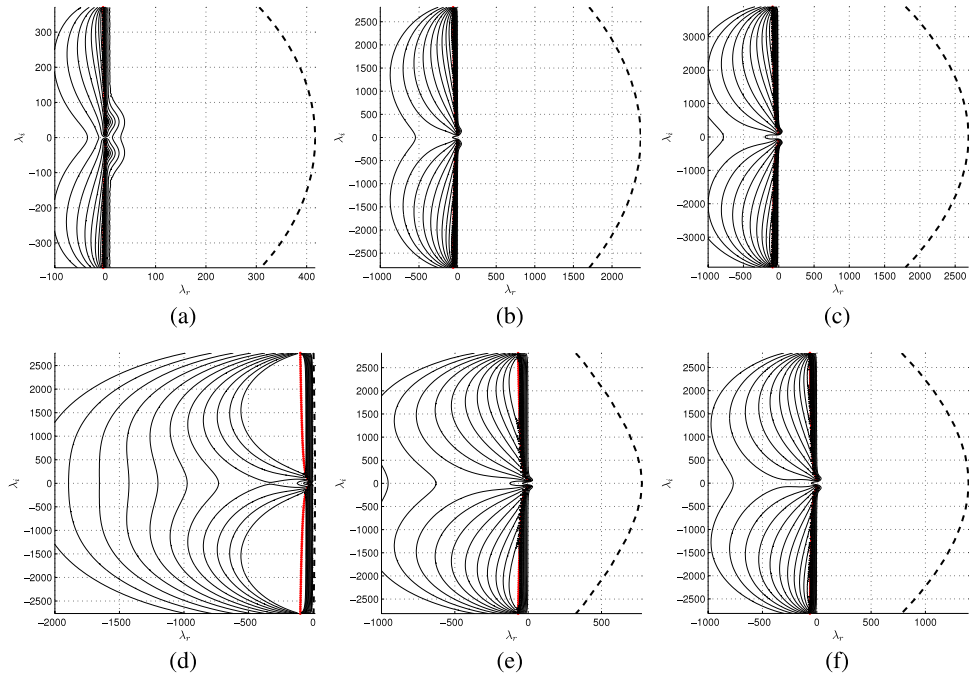

FIG. 16. Iso-contour lines of ϵ-Pseudospectrum (–) and numerical range (- -) for selected spectra (red dots) of the linearized operator $\mathcal{A}$ for various $\mathcal{K}$ at fixed $Fr = 100$ and various Fr at fixed $\mathcal{K} = 2000$. From outside to inside, the curves correspond to $\epsilon = [10, 10^{0.8}, 10^{0.6}, 10^{0.4}, 10^{0.2}, 1, 10^{-0.2}, 10^{-0.4}, 10^{-0.6}, 10^{-0.8}, 10^{-1}]$. (a) $\mathcal{K} = 2000$ and $Fr = 0$, (b) $\mathcal{K} = 2000$ and $Fr = 100$, (c) $\mathcal{K} = 2000$ and $Fr = 200$, (d) $\mathcal{K} = 10$ and $Fr = 100$, (e) $\mathcal{K} = 500$ and $Fr = 100$, and (f) $\mathcal{K} = 1000$ and $Fr = 100$.

latter refer to a specific initial condition, namely, Gaussian-like centerline perturbation and null lateral velocity, whilst the present results correspond to maximum (i.e., optimized over all the initial conditions) gain (38). A further look at Figure 18(a) allows us to appreciate the simultaneous presence of high-frequency oscillations due to the spring-mass interaction (namely, due to single-mode dynamics), as well as low-frequency oscillations related to the crossing time (namely, due to multimodal dynamics). At long times, the leading mode pair becomes dominant and the energy optimal amplification oscillates at high frequency only, around an average value growing exponentially with

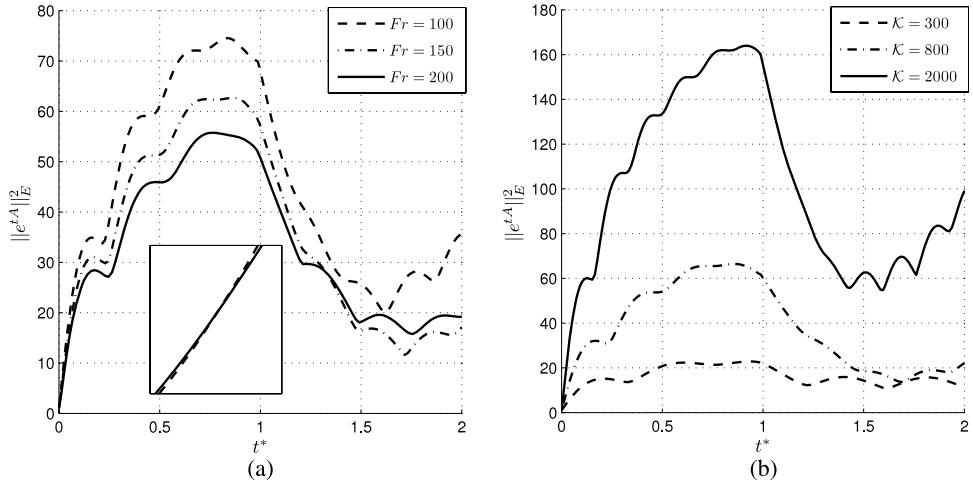

FIG. 17. Short-time transient growth energy trends for selected values of parameters Fr and $\mathcal{K}$. (a) $\mathcal{K} = 900$ and (b) $Fr = 100$.

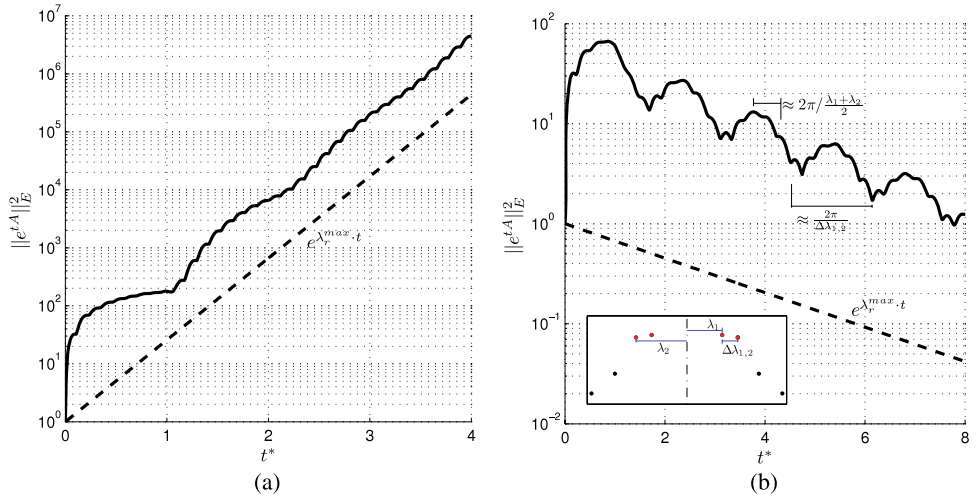

FIG. 18. Large time evolution of growth function G: *(a)* unstable case; *(b)* stable case. (a) $\mathcal{K} = 700$ and $Fr = 0$ and (b) $k = 800$ and $Fr = 100$.

growth rate equal to the real part of the leading eigenvalue. Figure 18(b) features the same basic behavior for a stable case. However, here, the interaction between single-mode and multimodal dynamics is more complex altering at short times the oscillations of both high- and low-frequency; as shown in the picture, the former are initially related to the averaged frequency of the first two eigenmodes having an almost coincident imaginary part, the latter can establish clearly only after about 5-6 crossing times. The interested reader can delve into the complex synchronization of single-mode and multimodal dynamics by referring to the paper of Coppola and de Luca.[21]

It seems interesting to show the comparison of typical spatial shapes of single most unstable eigenmodes with spatial shapes of optimal perturbations, in terms of both centerline nappe displacement and lateral velocity. Note that for the considered cases of Figures 19 and 20, the behavior

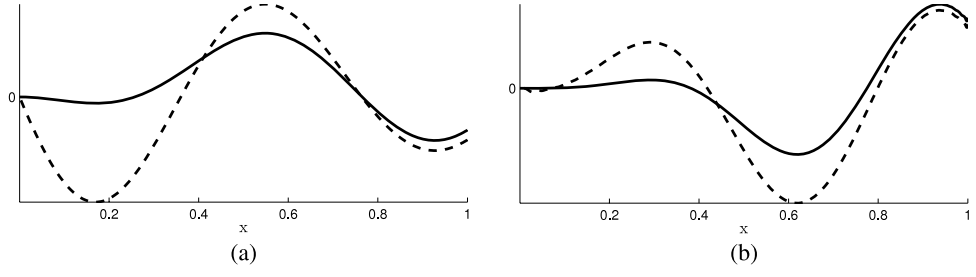

FIG. 19. Leading eigenmode (spring-mass eigenfunction) (a) and optimal perturbation (b) of ℓ (continuous line) and v (dashed line) perturbations, for $\mathcal{K} = 100$ and $Fr = 0$. Case referring to the spectrum displayed in Figure 10(a)(·).

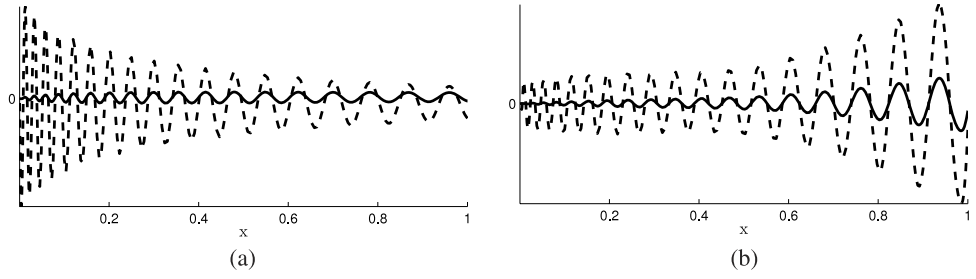

FIG. 20. Leading (spring-mass) eigenmode (a) and optimal perturbation (b) of ℓ (continuous line) and v (dashed line) perturbations, for $\mathcal{K} = 4 \cdot 10^4$ and $Fr = 20$. Case referring to the spectrum displayed in Figure 10(b)(o).

of the most unstable eigenmodes of ℓ and v exhibits the same spatial oscillation frequency as the corresponding optimal perturbation shapes, both in the presence and in the absence of gravity. Optimal perturbations are computed at a time corresponding roughly to a few t_{cross}, i.e., when the exponential asymptotic regime is attained.

VIII. CONCLUSIONS

The dynamic behavior of nappe oscillation has been revisited with reference to a physical model in which a thin liquid sheet interacts with a one-sided closed air chamber. The mutual influence of the air within the enclosure with the compliant nappe interface can produce self-induced forcing whose features have been widely investigated.

The analysis has been carried out by developing a simplified (inviscid, without surface tension effects) one-dimensional physical model that arises, in the context of a linearized formulation of free-interface convection dominated systems, by assuming a coordinate-type expansion for the flow variables.

The present contribution represents a step ahead in the knowledge of the phenomenon in two ways: first, it analyzes more in detail the spectrum of the frequencies of the system, and indicates that the oscillations of low frequency are related to the quasi-constant spacing of the imaginary parts of the eigenvalues (already known); it also identifies clearly that the high frequency oscillations have to be related to a global spring-mass oscillator model whose mass is that of the liquid sheet and the equivalent stiffness $\mathcal{K}$ of the spring is that of the air inside the enclosure, which experiences compression/expansion thermodynamic transformations. Second, an analogy is provided between the nappe oscillation problem and the edge tone problem, i.e., the acoustic tones produced when a jet of air strikes a wedge shaped edge.

The investigation has been carried out by means of both a modal (i.e., time asymptotic) and a non-modal (i.e., short-time transient) linear approaches, which are corroborated by direct numerical simulations of the governing equation. With the aim of yielding various physical insights, the analysis has been carried out from both a dynamics and energy perspective.

A major result is the determination of the instability onset based on the ansatz, fully confirmed by the numerical analysis, that the system is stable if the crossing time of a perturbation over the whole length of the domain is shorter than the period of the spring-mass oscillator. In the opposite situation, the self-forcing establishes itself, leading to instability. It should be stressed that this ansatz includes the gravity effects, in the sense that in the presence of gravity, a shorter crossing time is expected, and, accordingly, a higher $\mathcal{K}$ threshold of instability. Since the oscillator works in the driven regime, the oscillation period does not correspond to the natural frequency of oscillation and, in general, it cannot be determined in analytical closed form.

Moreover, in analogy with the acoustic phenomenon of edge tones, it is found that resonance occurs at frequencies *one integer-plus-one-fourth* times the instability onset frequency, where the basic frequency to be multiplied by $n + \frac{1}{4}$ is just the one related to the spacing among the imaginary parts of the eigenvalues. Complete maps of asymptotic growth rate and frequency in the parameters space $Fr,\mathcal{K}$ have been computed, showing in detail the characteristic multimodal nature of the nappe flow. Of course, the oscillation frequency observed in real life configurations depends on a selection mechanism, not considered here because beyond the scope of the paper.

[1] H. I. Schwartz, "Nappe oscillation," J. Hydraul. Div. **90**(6), 129–143 (1964).
[2] E. Naudascher and D. Rockwell, *Flow-Induced Vibrations: An Engineering Guide* (Dover, 1994).
[3] S. P. Lin, Z. W. Lian, and B. J. Creighton, "Absolute and convective instability of a liquid sheet," J. Fluid Mech. **220**, 673–689 (1990).
[4] L. de Luca and M. Costa, "Instability of a spatially developing liquid sheet," J. Fluid Mech. **331**, 127–144 (1997).
[5] L. de Luca, "Experimental investigation of the global instability of plane sheet flows," J. Fluid Mech. **399**, 355–376 (1999).
[6] N. S. Barlow, B. T. Helenbrook, and S. P. Lin, "Transience to instability in a liquid sheet," J. Fluid Mech. **666**, 358–390 (2011).
[7] Y. Sato, S. Miura, T. Nagamine, S. Morii, and S. Ohkubo, "Behavior of a falling water sheet," J. Environ. Eng. **2**, 394–406 (2007).
[8] H. Mori, T. Nagamine, R. Ito, and Y. Sato, "Mechanism of self-excited vibration of a falling water sheet," Trans. Jpn. Soc. Mech. Eng., Part C **78**(792), 2720–2732 (2012).

[9] N. Le Grand-Piteira, P. Brunet, L. Lebon, and L. Limat, "Propagating waves pattern in a falling liquid curtain," Phys. Rev. E **74**, 026305 (2006).
[10] P. J. Schmid and D. S. Henningson, "On the stability of a falling liquid curtain," J. Fluid Mech. **463**, 163–171 (2002).
[11] S. J. Weinstein, A. Clarke, A. G. Moon, and E. A. Simister, "Time-dependent equations governing the shape of a two-dimensional liquid curtain, part 1: Theory," Phys. Fluids **9**, 3625–3636 (1997).
[12] N. Curle, "The mechanics of edge-tones," Proc. R. Soc. London, Ser. A **216**(1126), 412–424 (1953).
[13] C. Mehring and W. A. Sirignano, "Nonlinear capillary wave distortion and disintegration of thin planar liquid sheets," J. Fluid Mech. **388**(69), 69–113 (1999).
[14] G. Coppola, F. De Rosa, and L. de Luca, "Surface tension effects on the motion of a free-falling liquid sheet," Phys. Fluids **25**(6), 062103 (2013).
[15] B. Crookston and B. Tullis, "Hydraulic design and analysis of labyrinth weirs. ii: Nappe aeration, instability, and vibration," J. Irrig. Drain. Div., Am. Soc. Civ. Eng. **139**(5), 371–377 (2013).
[16] M. Girfoglio, F. De Rosa, G. Coppola, and L. de Luca, "Global eigenmodes of free-interface vertical liquid sheet flows," WIT Trans. Eng. Sci. **79**, 285–295 (2013).
[17] S. C. Reddy, P. J. Schmid, and D. S. Henningson, "Pseudospectra of the Orr-Sommerfeld operator," SIAM J. Appl. Math. **53**(1), 15–47 (1993).
[18] S. C. Reddy and D. S. Henningson, "Energy growth in viscous channel flows," J. Fluid Mech. **252**, 209–238 (1993).
[19] P. J. Schmid and D. S. Henningson, "Optimal energy density growth in hagenpoiseuille flow," J. Fluid Mech. **277**, 197–225 (1994).
[20] L. N. Trefethen, "Pseudospectra of linear operators," SIAM Rev. **39**(3), 383–406 (1997).
[21] G. Coppola and L. de Luca, "On transient growth oscillations in linear models," Phys. Fluids **18**(7), 078104 (2006).

Global eigenmodes of free-interface vertical liquid sheet flows

M. Girfoglio, F. De Rosa, G. Coppola & L. de Luca
Dipartimento di Ingegneria Industriale, sez. Aerospaziale, Università di Napoli Federico II, Italy

Abstract

The global dynamics of unsteady free-interface vertical liquid sheet flows is studied, where the dynamics is termed global because it refers to the whole fluid system. The formal development of a proper mathematical model is presented initially, which accounts for pressure disturbances produced by the compliant interface in an air enclosure adjacent to the sheet. The linear spectral analysis (here restricted to sinuous disturbances only) shows that the surface tension is globally stabilizing, the spectrum exhibiting two typical branches related to the two characteristics curves of the governing equations. This basic finding is confirmed by means of both computations of the optimal amplifications (i.e. the greatest amplifications over all initial perturbations) of the relevant system energy and direct numerical simulations of the spatio-temporal evolution of an initial disturbance having the form of an interface Gaussian perturbation.

1 Introduction

Vertical liquid sheets are often used in industrial processes, classical examples being coating technology and paper making. In most of these applications the control of the global characteristics of the sheet is of great importance for the final quality of the product. The ability in suppressing undesired oscillations or nonuniformity in the steady configuration of the sheet, for example, usually reflects in a good quality of the fluid layer deposited under a moving substrate.

The modeling of the falling liquid sheet and of its interactions with the external ambient gas has been considered in various circumstances in the past, mainly within the context of linear stability analysis (cf. for example [1–4]). In these previous contributions the analysis of the system behaviour is usually conducted

WIT Transactions on Engineering Sciences, Vol 79,
www.witpress.com, ISSN 1743-3533 (on-line)
doi:10.2495/MPF130241

locally, while few studies have been developed for the global characteristics of the curtain when it strongly interacts with the external ambient gas [5, 6]. In this paper, a simple model for the deflection of the liquid sheet is initially derived under the assumptions of thin thickness and small initial perturbations. This model is then closed with the specification of the pressure field outside the sheet, which represents here the reaction of an air enclosure located on one side of the sheet. The equations are then studied theoretically, by employing both modal and non modal analysis, and numerically by a direct numerical simulation of the unsteady (linear) equations governing the evolution of disturbances.

2 The model

2.1 Governing equations

In order to derive a mathematical model for the unsteady evolution of a free-falling liquid curtain, we will refer to the sketch depicted in Fig. 1. Although in principle various types of interactions with the external gaseous ambient can be considered, hereafter the pressure disturbances produced by the curtain compliant interface within a two-dimensional air enclosure delimited by the curtain itself, rigid walls and a lower basin, will be analyzed. Viscous and splashing effects are neglected. The governing equations are the standard two-dimensional inviscid Euler equations in which gravity is retained. Kinematic and dynamic boundary conditions at the liquid-air interfaces are:

$$v^{\pm} = \frac{\partial y^{\pm}}{\partial t} + u^{\pm}\frac{\partial y^{\pm}}{\partial x} \tag{1}$$

$$p^{\pm} = p_a^{\pm} \mp \sigma \frac{\partial^2 y^{\pm}}{\partial x^2}\left[1 + \left(\frac{\partial y^{\pm}}{\partial x}\right)^2\right]^{-3/2} \tag{2}$$

where σ is the surface tension coefficient, $y^-(x,t)$ and $y^+(x,t)$ are the equations of the left and right boundaries of the sheet, respectively, $p_a^-(x,t)$ and $p_a^+(x,t)$ are the local values of the external (gas) pressure and the general definition $\varphi^{\pm}(x,t) = \varphi(x, y^{\pm}, t)$ has been employed, φ being one of the variables u, v and p (where u and v are the streamwise and lateral velocity components, respectively, and p is pressure).

Let us define the quantities $\widetilde{y}$ and $\overline{y}$ as the thickness and the location of sheet centerline:

$$\widetilde{y}(x,t) = y^+(x,t) - y^-(x,t) \tag{3}$$

$$\overline{y}(x,t) = \frac{y^+(x,t) + y^-(x,t)}{2}. \tag{4}$$

Following Mehring and Sirignano [7], a perturbative approach (in which the thickness of the sheet $\widetilde{y}$ is considered as the small parameter) is adopted, i.e. each

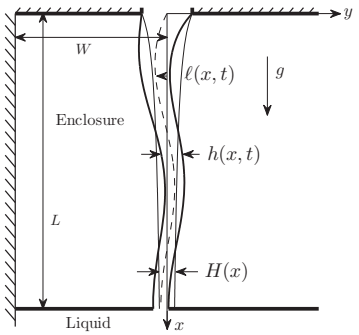

Figure 1: Geometrical configuration under consideration.

dependent variable φ is expressed as a power series in terms of $(y - \overline{y})$:

$$\varphi = \varphi_0(x,t) + \varphi_1(x,t)\,[y - \overline{y}] + \varphi_2(x,t)\,[y - \overline{y}]^2 \ldots$$

Such power series expansions are valid for $y \in (y^-, y^+)$ and hence the inequality $|y - \overline{y}(x,t)| \leq \widetilde{y}/2$ holds. By adapting the procedure employed in [7], the following set of equations for the lowest order terms in the expansion is derived:

$$\frac{\partial \widetilde{y}}{\partial t} + \frac{\partial (u_0 \widetilde{y})}{\partial x} = 0 \tag{5}$$

$$\frac{\partial \overline{y}}{\partial t} + u_0 \frac{\partial \overline{y}}{\partial x} = v_0 \tag{6}$$

$$\begin{aligned} \frac{\partial u_0}{\partial t} + u_0 \frac{\partial u_0}{\partial x} = {} & \boxed{g - \frac{1}{\rho_l}\left[\frac{\partial \overline{p}_{a0}}{\partial x} - \frac{\overline{p}_{a0}}{\widetilde{y}}\frac{\partial \overline{y}}{\partial x}\right]} \\ & + \frac{\sigma}{2\rho_l}\frac{\partial}{\partial x}\left[\left(\frac{f_+ + f_-}{2}\right)\frac{\partial^2 \widetilde{y}}{\partial x^2}\right] + \cdots + \frac{\sigma}{2\rho_l}\frac{\partial}{\partial x}\left[(f_+ - f_-)\,\frac{\partial^2 \overline{y}}{\partial x^2}\right] \\ & - \frac{\sigma}{\rho_l \widetilde{y}}\frac{\partial \overline{y}}{\partial x}\left[(f_+ + f_-)\,\frac{\partial^2 \overline{y}}{\partial x^2} + \frac{(f_+ - f_-)}{2}\frac{\partial^2 \widetilde{y}}{\partial x^2}\right] \end{aligned} \tag{7}$$

$$\frac{\partial v_0}{\partial t} + u_0 \frac{\partial v_0}{\partial x} = \boxed{-\frac{1}{\rho_l \widetilde{y}}\widetilde{p}_{a0}} + \frac{\sigma}{\rho_l \widetilde{y}}\left[(f_+ + f_-)\,\frac{\partial^2 \overline{y}}{\partial x^2} + \frac{(f_+ - f_-)}{2}\frac{\partial^2 \widetilde{y}}{\partial x^2}\right] \tag{8}$$

where

$$f_\pm = \left[1 + \left(\frac{\partial \overline{y}}{\partial x}\right)^2 \pm \frac{\partial \overline{y}}{\partial x}\frac{\partial \widetilde{y}}{\partial x} + \frac{1}{4}\left(\frac{\partial \widetilde{y}}{\partial x}\right)^2\right]^{-3/2} \tag{9}$$

and ρ_l is the liquid density. As usual the following positions are made:

$$\widetilde{p}_{a0} = p^+_{a0} - p^-_{a0}, \quad \overline{p}_{a0} = \frac{p^+_{a0} + p^-_{a0}}{2} \tag{10}$$

in which $p^{\pm}_{a0}$ are the first order approximation of a power-series expansion in the variable $(y - \overline{y})$ of the (still undefined) ambient gas pressures $p^{\pm}_a$. The boxed terms appearing in equations (7) and (8) are due to the developing nature of the flow under consideration (due to gravity) and were not considered in the original treatment of Mehring and Sirignano [7].

2.2 Base flow and linearized perturbation equations

The generic flow variable φ will be hereafter decomposed as the sum of a stationary (base) contribution and the perturbation:

$$\varphi_0(x,t) = \Phi(x) + \varphi(x,t). \tag{11}$$

Symmetry considerations give the following form for the base flow variables, denoted by capital symbols [8]:

$$U = U(x), \quad H = H(x), \tag{12}$$

$$V = 0, \quad \overline{Y} = 0, \quad \widetilde{P}_{a0} = 0, \quad \partial \overline{P}_{a0}/\partial x = 0 \tag{13}$$

$$\widetilde{F} = 0, \quad \overline{F} = F = \left[1 + \frac{1}{4}\left(\frac{\partial H}{\partial x}\right)^2\right]^{-3/2}. \tag{14}$$

By substituting these position in the nonlinear governing system (5–8) one obtains the following equations for the base flow variables:

$$UH = U_{\text{in}} H_{\text{in}} = \text{const.} \tag{15}$$

$$U\frac{\partial U}{\partial x} = g + \frac{\sigma}{2\rho_l}\frac{\partial}{\partial x}\left\{F\frac{\partial^2 H}{\partial x^2}\right\} \tag{16}$$

where U_{in} and H_{in} are, respectively, the average streamwise velocity and the sheet thickness at the inlet. These equations have been already derived in the context of steady flows and have been extensively studied in [8].

The linearized equations for the perturbation quantities u, v, ℓ and h (l referring to the centerline location of the sheet and h to its thickness) are:

$$\frac{\partial h}{\partial t} + \frac{\partial}{\partial x}(Uh + uH) = 0 \tag{17}$$

$$\frac{\partial \ell}{\partial t} + U\frac{\partial \ell}{\partial x} = v \tag{18}$$

$$\frac{\partial u}{\partial t} + \frac{\partial (Uu)}{\partial x} = -\frac{1}{\rho_l}\frac{\partial \overline{p}}{\partial x} + \frac{\sigma}{2\rho_l}\frac{\partial^2}{\partial x^2}\left(F\frac{\partial h}{\partial x}\right) \tag{19}$$

$$\frac{\partial v}{\partial t} + U\frac{\partial v}{\partial x} = -\frac{\widetilde{p}}{\rho_l H} + \frac{2\sigma}{\rho_l H}\frac{\partial}{\partial x}\left(F\frac{\partial \ell}{\partial x}\right) \tag{20}$$

Note that the set of equations (17–20) shows two separated systems for the variables h, u (equations (17) and (19)) and v, ℓ (equations (18) and (20)). These two systems will result decoupled if one can show that the values of $\widetilde{p}$ and $\overline{p}$ (relative to the ambient gas pressure perturbation) depend respectively on v, ℓ and on u, h. By following a standard terminology we will employ the term *varicose* with reference to disturbances involving variations in the thickness h and in the streamwise velocity u, and the term *sinuous* with reference to disturbances involving variations in the centerline position of the sheet ℓ and in the transverse velocity v.

2.3 Ambient gas pressure model

As depicted in Fig. 1, the present model of the external pressure field subjected to perturbation refers to the air enclosure located on one side of the curtain. This type of perturbation, which is induced by a compliant displacement of the sheet interface, was already analyzed by Schmid and Henningson [5], but they did not include surface tension effects. Assuming isentropic transformation of the air within the enclosure and behaviour of perfect gas, yields:

$$\widetilde{p} = -\frac{\gamma P_{a0}}{LW - \int_0^L \frac{H}{2}\, dx} \int_0^L \ell \, dx \tag{21}$$

$$\overline{p} = \frac{\gamma P_{a0}}{LW - \int_0^L \frac{H}{2}\, dx} \int_0^L \frac{h}{2} \, dx \tag{22}$$

where γ is the heat specific ratio, L the curtain length and W the transverse dimension of the air enclosure. For *varicose* disturbances, as shown by equations (19) and (22) the contribution related to the pressure term is null because $\overline{p}$ does not depend on x.

2.4 Non-dimensional equations and slender-sheet approximation

The equation of motion (15-16) and (17–20) can be conveniently re-written in non-dimensional form by employing the reference quantities:

$$L_r = U_{\text{in}}^2/g, \quad \ell_r = H_{\text{in}}, \quad u_r = U_{\text{in}}, \tag{23}$$

$$t_r = L_r/U_{\text{in}} = U_{\text{in}}/g, \tag{24}$$

$$v_r = \ell_r/t_r = \varepsilon U_{\text{in}}, \quad p_r = \rho_l g H_{\text{in}} = \varepsilon \rho_l U_{\text{in}}^2 \tag{25}$$

where $\varepsilon = H_{\text{in}}/L_r = H_{\text{in}} g/U_{\text{in}}^2$ is the *slenderness* parameter (reciprocal of Froude number). The equations (18) and (20) for sinuous disturbances, for example, reduce to:

$$\frac{\partial \ell^*}{\partial t^*} + U^* \frac{\partial \ell^*}{\partial x^*} = v^* \tag{26}$$

$$\frac{\partial v^*}{\partial t^*} + U^* \frac{\partial v^*}{\partial x^*} = \frac{1}{\mathrm{We}\, H^*} \frac{\partial}{\partial x^*} \left(F^* \frac{\partial \ell^*}{\partial x^*} \right) - \frac{\gamma}{H^*} \frac{P^*_{a0}}{L^* W^* - \varepsilon \int_0^{L^*} \frac{H^*}{2}\, dx^*} \int_0^{L^*} \ell^*\, dx^* \quad (27)$$

where $\mathrm{We} = \rho_l U_{\mathrm{in}}^2 H_{\mathrm{in}}/2\sigma$ is the Weber number, and F^* is:

$$F^* = \left[1 + \frac{1}{4} \varepsilon^2 \left(\frac{\partial H^*}{\partial x^*} \right)^2 \right]^{-3/2}, \quad (28)$$

stars denoting nondimensional quantities. By adopting a power series expansion in the small parameter ε^2, for the base flow variables, and an expansion in ε for the perturbation quantities,

$$U^* = U_0^* + \varepsilon^2 U_1^* + \varepsilon^4 U_2^* + \ldots \quad v^* = v_0^* + \varepsilon v_1^* + \varepsilon^2 v_2^* + \ldots$$
$$H^* = H_0^* + \varepsilon^2 H_1^* + \varepsilon^4 H_2^* + \ldots \quad \ell^* = \ell_0^* + \varepsilon \ell_1^* + \varepsilon^2 \ell_2^* + \ldots$$

the lowest order approximation for the base flow gives the non-dimensional version of the classic free-fall Torricelli's solution

$$U_0^* = \sqrt{1 + 2x^*}, \qquad H_0^* = \frac{1}{\sqrt{1 + 2x^*}}. \quad (29)$$

The sinuous perturbation equations, at zeroth order, are:

$$\frac{\partial \ell_0^*}{\partial t^*} + U_0^* \frac{\partial \ell_0^*}{\partial x^*} = v_0^* \quad (30)$$

$$\frac{\partial v_0^*}{\partial t^*} + U_0^* \frac{\partial v_0^*}{\partial x^*} = \frac{1}{\mathrm{We} H_0^*} \frac{\partial^2 \ell_0^*}{\partial x^{*2}} - \frac{k}{H_0^*} \int_0^{L^*} \ell_0^*\, dx^* \quad (31)$$

where $k = \gamma P_0^*/L^* W^*$.

3 Analysis of sinuous disturbances

In the present paper we will restrict our study to sinuous disturbances only, that will be analyzed both by determining their global eigenfunctions and by carrying out direct numerical simulations of the governing equations.

3.1 Linear global eigenfunctions

Global temporal modes are introduced by the following positions: $\ell_0^*(x^*, t^*) = L_0^*(x^*) e^{i\omega t^*}$ and $v_0^*(x^*, t^*) = V_0^*(x^*) e^{i\omega t^*}$. By substituting them in the governing

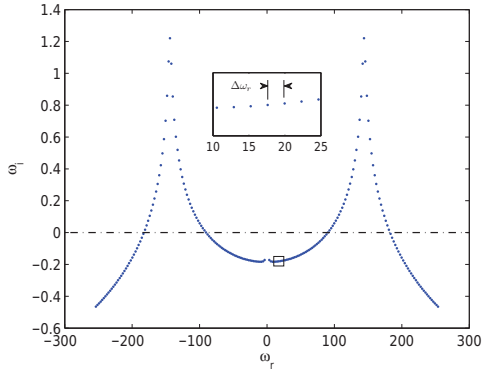

Figure 2: Spectrum for We $= \infty$ and $L^* = 6.25$.

equations (30)-(31) we obtain

$$\begin{bmatrix} I & -U_0^* D \\ -U_0^* D & \dfrac{1}{\mathrm{We} H_0^*} D^2 - \dfrac{k}{H_0^*} \int_0^{L^*} dx^* \end{bmatrix} \begin{pmatrix} L_0^* \\ V_0^* \end{pmatrix} = \mathrm{i}\omega \begin{pmatrix} L_0^* \\ V_0^* \end{pmatrix} \tag{32}$$

where D, D^2 and I are first derivative, second derivative and identity operators, respectively. The boundary conditions are $L_0^*(0) = V_0^*(0) = 0$. A Chebychev spectral collocation method has been used in order to solve the eigenvalues problem.

As usual in this kind of problems, once defined the meaningful energy of the system, it is convenient to find the optimal amplification of the energy, i.e. the greatest amplifications for all the possible initial conditions (the so-called growth function $G(t)$ [9]). For sinuous disturbances, the energy is defined as:

$$E(t) = \int_0^{L^*} H_0^* v_0^{*2}\, dx^* + \frac{1}{\mathrm{We}} \int_0^{L^*} \left(\frac{\partial \ell_0^*}{\partial x^*} \right)^2 dx^* \tag{33}$$

that takes into account both kinetic and surface tension contributions.

Two typical spectra obtained in the cases of absence of surface tension, We $= \infty$, and We $= 2$, both for $L^* = 6.25$, are depicted in Figs. 2 and 3, respectively.

Note that the former case corresponds to the situation analyzed previously by Schmid and Henningson [5]. In the presence of surface tension the spectrum preserves the symmetry properties, but the unstable modes of high frequency ω_r disappear, due to the stabilizing effects of the surface tension. Moreover, the presence of two distinct symmetrical branches is also evident, which is justified on the grounds of the hyperbolic character of the governing equations system. Neglecting the external pressure contribution, this last can be recast in a single

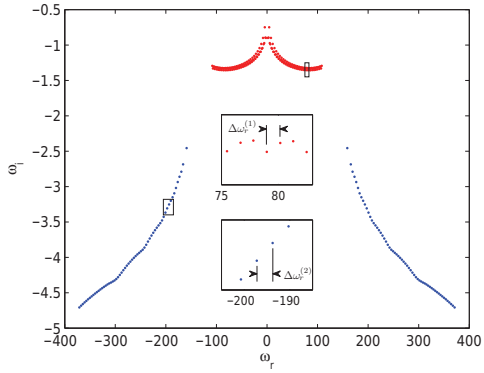

Figure 3: Spectrum for We $= 2$ and $L^* = 6.25$; the red branch refers to the slower characteristic, the blue branch to the faster one.

equation in terms of ℓ_0^*

$$U_0^* \left(U_0^* - \frac{1}{\mathrm{We}} \right) \frac{\partial^2 \ell_0^*}{\partial {x^*}^2} + 2U_0^* \frac{\partial^2 \ell_0^*}{\partial x^* \partial t^*} + \frac{\partial^2 \ell_0^*}{\partial {t^*}^2} + \frac{\partial \ell_0^*}{\partial x^*} = 0 \tag{34}$$

Equation (34) is a 2^{nd} order hyperbolic partial differential equation having two real and distinct characteristics given by (as an useful reference, see also [4]):

$$\frac{dx^*}{dt^*} = U_0^* \pm \sqrt{\frac{1}{\mathrm{We} U_0^*}} \tag{35}$$

Therefore, the two branches of the spectrum correspond to the two characteristics along which disturbances propagate; in order to support further this observation, the *fall times* (i.e. the times needed in order the sheet perturbation crosses the entire domain) related to the two characteristics,

$$T_{\mathrm{fall}}^{(1,2)} = \int_0^{L^*} \frac{dx^*}{U_0^* \pm \sqrt{\frac{1}{\mathrm{We} U_0^*}}} \tag{36}$$

have been evaluated ($T_{\mathrm{fall}}^{(1)} = 1.80$, $T_{\mathrm{fall}}^{(2)} = 5.38$) and related to the almost constant spacing between two subsequent eigenvalues belonging to the same branch measured along the ω_r axis ($\Delta\omega_r^{(1)}$ and $\Delta\omega_r^{(2)}$). It is found that this spacing agrees closely to free-fall frequency $f_{\mathrm{fall}}^{(1,2)} = 2\pi / T_{\mathrm{fall}}^{(1,2)}$. This behaviour was expected, because of some general results on the relation between the global spectrum morphology and oscillations timescales in linear evolutionary models [10]

Fig. 4(a) and (b) show that optimal global amplifications of energy calculated by considering separately eigenfunctions related to two branches of the spectrum exhibit an energy transient growth characterized by time-periodic oscillations with

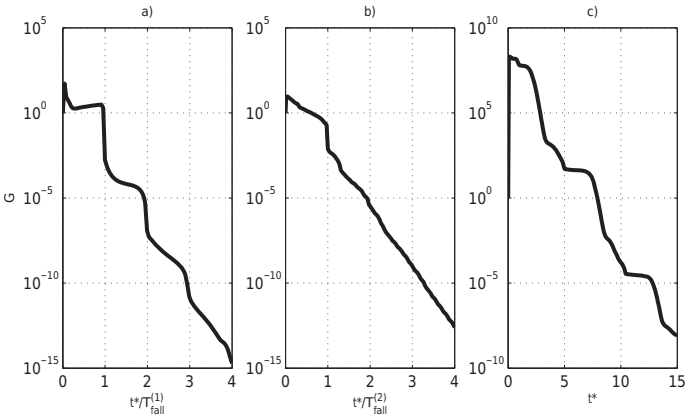

Figure 4: Optimal energy amplifications for We $= 2$ and $L^* = 6.25$; a) spectrum red branch only; b) spectrum blue branch only; c) overall.

very low peak values. The total gain curve is plotted in Fig. 4(c) where one can observe a very strong transient amplification because of coupling effects between the two branches of eigenvalues.

3.2 Direct numerical simulation

In order to validate in another way the results shown in the previous section, direct numerical simulations of the system (30-31), in the absence of the pressure term, have been carried out by using a 4^{th} order finite difference scheme for the discretization of spatial differential operators. For the temporal integration a semi-implicit *theta-method* scheme has been employed. The spatio-temporal evolution of the initial disturbance constituted by a Gaussian peak for ℓ_0^*, located near the origin, is reported in Fig. 5. Note that the initial packet splits while travelling down the sheet according to the different speeds of the two characteristics along with disturbances propagate.

4 Conclusions

The unsteady global dynamics behavior of a free-interface vertical liquid sheet flow has been studied, where such a behavior has been defined global because it refers to the entire fluid system as a whole. The first part of the paper dealt with the formal development of a proper mathematical model, which accounts of a particular kind of disturbances in the external gaseous ambient, constituted by an enclosure limited by solid walls, a bottom liquid basin and one of the two sheet interfaces.

A major finding is that the fluid system is stabilized by the surface tension. Moreover, since the unsteady dynamics can be described by means of a typical

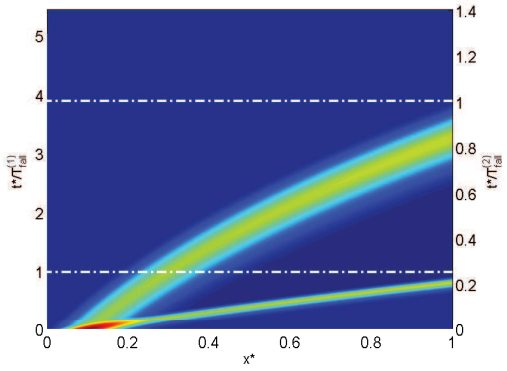

Figure 5: Spatio-temporal evolution of the initial disturbance for We $= 2$ and $L^* = 1$.

2^{nd} order partial differential equation of hyperbolic type, showing two distinct characteristic curves, the eigenvalues spectrum is typically characterized by two branches, each of them corresponding to disturbances eigenfunctions propagating along the two characteristic curves.

Another very interesting result is that both spectrum branches highlight a practically constant spacing among the values of their real parts, such a spacing being intimately connected to the *fall times* of the sheet perturbations over the height of the gas ambient enclosure. This result, which is typical of other convection-dominated dynamics systems, is confirmed under other two viewpoints.

A first comparison basis was offered by direct numerical simulations of the governing equations, that showed, among other features, how the initial disturbance imposed to the flow field under the form an interface Gaussian perturbation, evolved in the spatio-temporal framework by splitting itself into two wave-packets travelling at the expected speeds. In addition, a parallel investigation has been carried out in order to compute time trends of optimal amplifications of the significant system energy (accounting of both kinetic and surface tension contributions), where the term optimal refer to the greatest energy amplification over all initial perturbations. Both comparisons showed results in very close agreement with the spectral analysis performed in the initial part of the paper.

References

[1] S.P. Lin, Z.W. Creighton and B.J. Creighton, "Absolute and convective instability of a liquid sheet," J. Fluid Mech. **220**, 673 (1990).

[2] L. de Luca and M. Costa, "Instability of a spatially developing liquid sheet," J. Fluid Mech. **331**, 127 (1997).

[3] L. de Luca, "Experimental investigation of the global instability of plane sheet flows," J. Fluid Mech. **399**, 355 (1999).
[4] S. J. Weinstein, A. Clarke, A. G. Moon and E. A. Simister, "Time-dependent equations governing the shape of a two-dimensional liquid curtain, Part 1: Theory," Phys. Fluids. **9**, 3625 (1997).
[5] P. J. Schmid and D. S. Henningson, "On the stability of a falling liquid curtain," J. Fluid Mech. **463**, 163 (2002).
[6] H. Mori, T. Nagamine, R. Ito, Y. Sato, "Mechanism of self-excited vibration of a falling water sheet," Nihon Kikai Gakkai Ronbunshu, C Hen/Transactions of the Japan Society of Mechanical Engineers, Part C 78 (792) , pp. 2720–2732 (2012).
[7] C. Mehring and W. A. Sirignano, "Nonlinear capillary wave distortion and disintegration of thin planar liquid sheets," J. Fluid Mech. **388**, 69 (1999).
[8] G. Coppola, F. De Rosa and L. de Luca, "Surface tension effects on the motion of a free-falling liquid sheet," *in press* Phys. Fluids (2013).
[9] P. J. Schmid & D. S. Henningson, "Stability and Transition in Shear Flows," Springer (2001).
[10] G. Coppola and L. de Luca, "On transient growth oscillations in linear models," Phys. Fluids **18**, 078104 (2006).

Italian Association of Aeronautics and Astronautics
XXII Conference
Napoli, 9-12 September 2013

GLOBAL DYNAMICS OF GRAVITATIONAL LIQUID SHEET FLOWS

F. De Rosa[1*], M. Girfoglio[1], G. Coppola[1] and L. de Luca[1]

[1] Università di Napoli Federico II, Department of Industrial Engineering – Aerospace sect., P.le Tecchio 80, 80125 – Naples - Italy

*fortunato.derosa@unina.it

ABSTRACT

Unsteady free-interface vertical liquid sheet flows are studied from the global viewpoint, where the dynamics is termed global because it refers to the whole fluid system. The development of a proper mathematical model is presented initially, which accounts of pressure disturbances produced by the compliant interface in an air enclosure adjacent to the sheet. Our study has been restricted to the sinuous (unsymmetric) solution of the linearized set of equations. It is found that, in absence of surface tension, the optimal disturbance energy exhibits a transient growth characterized by high frequency and low frequency time-periodic oscillations; physical considerations are developed in order to estimate the relevant periods. In presence of surface tension, the low frequency oscillations disappear and the optimal disturbance energy goes quickly to zero, after exhibiting an initial reduced peak. In order to give insight on the physical relevance of such behaviours, an equation of energy budget is also derived which is used to estimate the contribution of the various physical effects evaluated via direct numerical simulation of the linearized model.

Keywords: liquid sheet flow, non modal amplification, energy budget

1 INTRODUCTION

In various industrial applications the control of the global characteristics of liquid sheet flows is of great importance for the final quality of the product. Vertical liquid sheets are often used in technological processes, classical examples being coating technology and papermaking. The ability in suppressing undesired ocillations or nonuniformity in the steady configuration of the sheet, for example, usually reflects in a good quality of the fluid layer deposited under a moving substrate.

The modeling of the falling liquid sheet and of its interactions with the external ambient gas has been considered in various papers in the past, mainly within the context of linear stability analysis (cfr. for example [1], [2], [3], [4]). In these previous contributions the analysis of the system behaviour is usually conducted locally, while few studies have been developed for the global characteristics of the curtain when it strongly interacts with the external ambient gas ([5], [6]). In this paper, a simple model for the deflection of the liquid sheet is initially derived under the assumptions of thin thickness and small initial perturbations. This model is then closed with the specification of the pressure field outside the sheet, which represents here the reaction of an air enclosure located on one side of the sheet. The equations are then studied numerically by a direct numerical simulation of the unsteady (linear) equations governing the evolution of disturbances.

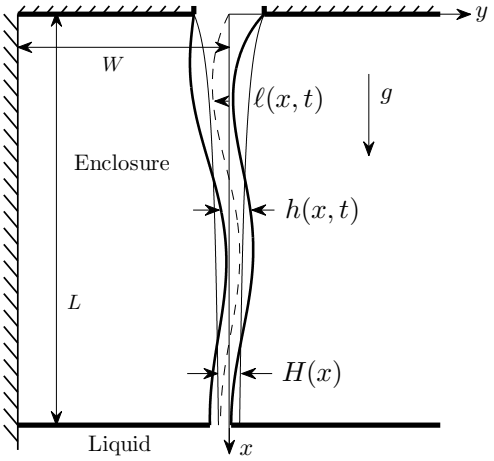

Figure 1: Geometrical configuration under consideration

2 THE MODEL

2.1 The governing equations

In order to derive a mathematical model for the unsteady evolution of a free-falling liquid curtain, we will refer to the sketch depicted in Figure 1. Although in principle various types of interactions with the external gaseous ambient can be considered, hereafter the pressure disturbances produced by the curtain compliant interface within a two-dimensional air enclosure delimited by the curtain itself, rigid walls and a lower basin, will be analyzed. Viscous and splashing effects are neglected. The governing equations are the standard two-dimensional inviscid Euler equations in which gravity is retained. Kinematic and dynamic boundary conditions at the liquid-air interfaces are:

$$v^{\pm} = \frac{\partial y^{\pm}}{\partial t} + u^{\pm}\frac{\partial y^{\pm}}{\partial x} \tag{1}$$

$$p^{\pm} = p_a^{\pm} \mp \sigma \frac{\partial^2 y^{\pm}}{\partial x^2}\left[1+\left(\frac{\partial y^{\pm}}{\partial x}\right)^2\right]^{-3/2} \tag{2}$$

where σ is the surface tension coefficient, $y^-(x,t)$ and $y^+(x,t)$ are the locations of the left and right boundaries of the sheet, respectively, $p_a^-(x,t)$ and $p_a^+(x,t)$ are the local values of the external (gas) pressure and the general definition $\varphi^{\pm}(x,t) = \varphi(x,y^{\pm},t)$ has been employed, φ being one of the variables u, v and p (where u and v are the streamwise and lateral velocity components, respectively, and p is pressure).
Let us define the quantities $\widetilde{y}$ and $\overline{y}$ as the thickness and the location of sheet centerline:

$$\widetilde{y}(x,t) = y^+(x,t) - y^-(x,t) \tag{3}$$

$$\overline{y}(x,t) = \frac{y^+(x,t)+y^-(x,t)}{2}. \tag{4}$$

Following Mehering and Sirignano [7], a perturbative approach (in which the thickness of the sheet $\widetilde{y}$ is considered as the small parameter) is adopted, i.e. each dependent variable φ is expressed as a power series in terms of $(y-\overline{y})$:

$$\varphi = \varphi_0(x,t) + \varphi_1(x,t)\,[y-\overline{y}] + \varphi_2(x,t)\,[y-\overline{y}]^2 \ldots$$

Such power series expansions are valid for $y \in (y^-, y^+)$ and hence the inequality $|y - \overline{y}(x,t)| \leq \widetilde{y}/2$ holds.
By adapting the procedure employed in [7], the following set of equations for the lowest order terms in the expansion is derived:

$$\frac{\partial \widetilde{y}}{\partial t} + \frac{\partial (u_0 \widetilde{y})}{\partial x} = 0 \tag{5}$$

$$\frac{\partial \overline{y}}{\partial t} + u_0 \frac{\partial \overline{y}}{\partial x} = v_0 \tag{6}$$

$$\frac{\partial u_0}{\partial t} + u_0 \frac{\partial u_0}{\partial x} = \boxed{g - \frac{1}{\rho_l}\left[\frac{\partial \overline{p}_{a0}}{\partial x} - \frac{\overline{p}_{a0}}{\widetilde{y}}\frac{\partial \overline{y}}{\partial x}\right]} + \frac{\sigma}{2\rho_l}\frac{\partial}{\partial x}\left[\left(\frac{f_+ + f_-}{2}\right)\frac{\partial^2 \widetilde{y}}{\partial x^2}\right] + \ldots$$
$$\ldots + \frac{\sigma}{2\rho_l}\frac{\partial}{\partial x}\left[(f_+ - f_-)\frac{\partial^2 \overline{y}}{\partial x^2}\right] - \frac{\sigma}{\rho_l \widetilde{y}}\frac{\partial \overline{y}}{\partial x}\left[(f_+ + f_-)\frac{\partial^2 \overline{y}}{\partial x^2} + \frac{(f_+ - f_-)}{2}\frac{\partial^2 \widetilde{y}}{\partial x^2}\right] \tag{7}$$

$$\frac{\partial v_0}{\partial t} + u_0 \frac{\partial v_0}{\partial x} = \boxed{-\frac{1}{\rho_l \widetilde{y}}\widetilde{p}_{a0}} + \frac{\sigma}{\rho_l \widetilde{y}}\left[(f_+ + f_-)\frac{\partial^2 \overline{y}}{\partial x^2} + \frac{(f_+ - f_-)}{2}\frac{\partial^2 \widetilde{y}}{\partial x^2}\right] \tag{8}$$

where

$$f_\pm = \left[1 + \left(\frac{\partial \overline{y}}{\partial x}\right)^2 \pm \frac{\partial \overline{y}}{\partial x}\frac{\partial \widetilde{y}}{\partial x} + \frac{1}{4}\left(\frac{\partial \widetilde{y}}{\partial x}\right)^2\right]^{-3/2} \tag{9}$$

and ρ_l is the liquid density. As usual the following positions are made:

$$\widetilde{p}_{a0} = p^+_{a0} - p^-_{a0}, \quad \overline{p}_{a0} = \frac{p^+_{a0} + p^-_{a0}}{2} \tag{10}$$

in which $p^\pm_{a0}$ are the first order approximation of a power-series expansion in the variable $(y - \overline{y})$ of the (still undefined) ambient gas pressures $p^\pm_a$. The boxed terms appearing in equations (7) and (8) are due to the developing nature of the flow under consideration (due to gravity and external pressure) and were not considered in the original treatment of Mehring and Sirignano [7].

2.2 Base flow and linearized perturbation equations

The generic flow variable φ will be hereafter decomposed as the sum of a stationary (base) contribution and the perturbation:

$$\varphi_0(x,t) = \Phi(x) + \varphi(x,t). \tag{11}$$

Symmetry considerations give the following form for the base flow variables, denoted by capital symbols [8]:

$$U = U(x), \quad H = H(x), \tag{12}$$

$$V = 0, \quad \overline{Y} = 0, \quad \widetilde{P}_{a0} = 0, \quad \partial \overline{P}_{a0}/\partial x = 0 \tag{13}$$

$$\widetilde{F} = 0, \quad \overline{F} = F = \left[1 + \frac{1}{4}\left(\frac{\partial H}{\partial x}\right)^2\right]^{-3/2}. \tag{14}$$

By substituting these position in the nonlinear governing system (5–8) one obtains the following equations for the base flow variables:

$$UH = U_{\text{in}} H_{\text{in}} = \text{const.} \tag{15}$$

$$U\frac{\partial U}{\partial x} = g + \frac{\sigma}{2\rho_l}\frac{\partial}{\partial x}\left\{F\frac{\partial^2 H}{\partial x^2}\right\} \tag{16}$$

where U_{in} and H_{in} are, respectively, the average streamwise velocity and the sheet thickness at the inlet. These equations have been already derived in the context of steady flows and have been extensively studied in [8].
The linearized equations for the perturbation quantities u, v, ℓ and h (l referring to the centerline location of the sheet and h to its thickness) are:

$$\frac{\partial h}{\partial t} + \frac{\partial}{\partial x}(Uh + uH) = 0 \tag{17}$$

$$\frac{\partial \ell}{\partial t} + U\frac{\partial \ell}{\partial x} = v \tag{18}$$

$$\frac{\partial u}{\partial t} + \frac{\partial (Uu)}{\partial x} = -\frac{1}{\rho_l}\frac{\partial \overline{p}}{\partial x} + \frac{\sigma}{2\rho_l}\frac{\partial^2}{\partial x^2}\left(F\frac{\partial h}{\partial x}\right) \tag{19}$$

$$\frac{\partial v}{\partial t} + U\frac{\partial v}{\partial x} = -\frac{\widetilde{p}}{\rho_l H} + \frac{2\sigma}{\rho_l H}\frac{\partial}{\partial x}\left(F\frac{\partial \ell}{\partial x}\right) \tag{20}$$

Note that the set of equations (17–20) shows two separated systems for the variables h, u (equations (17) and (19)) and v, ℓ (equations (18) and (20)). These two systems will result decoupled if one can show that the values of $\widetilde{p}$ and $\overline{p}$ (relative to the ambient gas pressure perturbation) depend respectively on v, ℓ and on u, h. By following a standard terminology we will employ the term *varicose* with reference to disturbances involving variations in the thickness h and in the streamwise velocity u, and the term *sinuous* with reference to disturbances involving variations in the centerline position of the sheet ℓ and in the transverse velocity v.

2.3 Ambient gas pressure model

As depicted in Fig.1, the model of the fluctuating external pressure field, with which the sheet interacts, refers to the air enclosure located on one side of the curtain. This type of perturbation, which is induced by a compliant displacement of the sheet interface, was already analyzed by Schmid and Henningson [5], but they did not include surface tension effects.
By assuming both a perfect gas model and an isentropic transformation for the state of the air within the enclosure, yields:

$$\widetilde{p} = -\frac{\gamma P_{a0}}{LW - \int_0^L \frac{H}{2}\,dx}\int_0^L \ell\,dx \tag{21}$$

$$\overline{p} = \frac{\gamma P_{a0}}{LW - \int_0^L \frac{H}{2}\,dx}\int_0^L \frac{h}{2}\,dx \tag{22}$$

where γ is the heat specific ratio, L the curtain length and W the transverse dimension of the air enclosure. For *varicose* disturbances, as shown by equations (19) and (22) the contribution related to the pressure term is null because $\overline{p}$ does not depend on x.

2.4 Non-dimensional equations and slender-sheet approximation

The equation of motion (15-16) and (17–20) can be conveniently re-written in non-dimensional form by employing the reference quantities:

$$L_r = U_{\text{in}}^2/g, \quad \ell_r = H_{\text{in}}, \quad u_r = U_{\text{in}}, \tag{23}$$

$$t_r = L_r/U_{\text{in}} = U_{\text{in}}/g, \tag{24}$$

$$v_r = \ell_r/t_r = \varepsilon U_{\text{in}}, \quad p_r = \rho_l g H_{\text{in}} = \varepsilon \rho_l U_{\text{in}}^2 \tag{25}$$

where $\varepsilon = H_{\text{in}}/L_r = H_{\text{in}}g/U_{\text{in}}^2$ is the *slenderness* parameter (reciprocal of Froude number).

The equations (18) and (20) for sinuous disturbances, for example, reduce to:

$$\frac{\partial \ell^*}{\partial t^*} + U^* \frac{\partial \ell^*}{\partial x^*} = v^* \tag{26}$$

$$\frac{\partial v^*}{\partial t^*} + U^* \frac{\partial v^*}{\partial x^*} = \frac{1}{\mathrm{We} H^*} \frac{\partial}{\partial x^*} \left(F^* \frac{\partial \ell^*}{\partial x^*} \right) - \frac{\gamma}{H^*} \frac{P^*_{a0}}{L^* W^* - \varepsilon \int_0^{L^*} \frac{H^*}{2} dx^*} \int_0^{L^*} \ell^* \, dx^* \tag{27}$$

where $\mathrm{We} = \rho_l U_{\mathrm{in}}^2 H_{\mathrm{in}} / 2\sigma$ is the Weber number, and F^* is:

$$F^* = \left[1 + \frac{1}{4} \varepsilon^2 \left(\frac{\partial H^*}{\partial x^*} \right)^2 \right]^{-3/2}, \tag{28}$$

stars denoting nondimensional quantities.
By adopting a power series expansion in the small parameter ε^2, for the base flow variables, and an expansion in ε for the perturbation quantities,

$$U^* = U_0^* + \varepsilon^2 U_1^* + \varepsilon^4 U_2^* + \ldots \quad v^* = v_0^* + \varepsilon v_1^* + \varepsilon^2 v_2^* + \ldots$$
$$H^* = H_0^* + \varepsilon^2 H_1^* + \varepsilon^4 H_2^* + \ldots \quad \ell^* = \ell_0^* + \varepsilon \ell_1^* + \varepsilon^2 \ell_2^* + \ldots$$

the lowest order approximation for the base flow gives the non-dimensional version of the classic free-fall Torricelli's solution

$$U_0^* = \sqrt{1 + 2x^*}, \qquad H_0^* = \frac{1}{\sqrt{1 + 2x^*}}. \tag{29}$$

The sinuous perturbation equations, at zeroth order, are:

$$\frac{\partial \ell_0^*}{\partial t^*} + U_0^* \frac{\partial \ell_0^*}{\partial x^*} = v_0^* \tag{30}$$

$$\frac{\partial v_0^*}{\partial t^*} + U_0^* \frac{\partial v_0^*}{\partial x^*} = \frac{1}{\mathrm{We} H_0^*} \frac{\partial^2 \ell_0^*}{\partial x^{*2}} - \frac{k}{H_0^*} \int_0^{L^*} \ell_0^* \, dx^* \tag{31}$$

where $k = \gamma P_0^* / L^* W^*$.

2.5 Derivation of the energy budget equation for sinuous disturbances

By multiplying the equation (31) by v_0^*, integrating over the sheet volume and applying the integration by parts, one obtains:

$$\frac{dE}{dt^*} = \underbrace{-v_0^{*2}\Big|_0^{L^*}}_{dE_1} \underbrace{-\frac{1}{\mathrm{We}} U_0^* \left(\frac{\partial \ell_0^*}{\partial x^*} \right)^2 \Bigg|_0^{L^*}}_{dE_2} \underbrace{+\frac{2}{\mathrm{We}} \frac{\partial \ell_0^*}{\partial x^*} v_0^* \Bigg|_0^{L^*}}_{dE_3}$$
$$\underbrace{-\frac{1}{\mathrm{We}} \int_0^{L^*} \frac{\partial U_0^*}{\partial x^*} \left(\frac{\partial \ell_0^*}{\partial x^*} \right)^2}_{dE_4} \underbrace{-2k \int_0^{L^*} v_0^* \left(\int_0^{L^*} \ell_0^* dx^* \right) dx^*}_{dE_5}, \tag{32}$$

where E is the flow system energy defined as:

$$E = \int_0^{L^*} H_0^* v_0^{*2} \, dx^* + \frac{1}{\mathrm{We}} \int_0^{L^*} \left(\frac{\partial \ell_0^*}{\partial x^*} \right)^2 dx^* \tag{33}$$

that takes into account both kinetic and surface tension contributions, and that formally is made dimensionless by means of the reference energy $\frac{1}{2} \rho_l \ell_r L_r v_r^2$.
The various contributions to the rate of change of energy in (32) have the following physical meaning:

i. dE_1 is the inlet-outlet convective exchange of kinetic energy

ii. dE_2 is the inlet-outlet convective exchange of surface tension energy

iii. dE_3 is a term derived from the integration by parts of the work done by the surface tension

iv. dE_4 is an energy production term due to the interaction of the disturbances field with the strain of the base flow (due to gravity)

v. dE_5 is the pressure work per unit time exchanged during the isentropic compression/expansion of the air enclosure

It should be noted that, while the dE_5 term can represent a rate of energy ceased to or extracted from the system during the compression or expansion of the air enclosure, respectively, the production term dE_4 is always negative, denoting a continuous energy transfer from the perturbation toward the base field.

3 ANALYSIS OF SINUOUS DISTURBANCES

In the present paper we will restrict our study to sinuous disturbances only, that will be analyzed by carrying out direct numerical simulations of the governing equations (30)-(31) and by analyzing the time behaviour of the terms of the energy budget equation (32).
By introducing the following positions, $\xi = \dfrac{\partial \ell_0^*}{\partial t^*}$ and $\eta = \dfrac{\partial \ell_0^*}{\partial x^*}$, it is possible to reformulate the system (30-31) in a more convenient way:

$$\begin{bmatrix} M & U_0^* \\ O & M \end{bmatrix} \begin{pmatrix} \xi \\ \eta \end{pmatrix} = \begin{bmatrix} -U_0^* D & -I + U_0^* \left(U_0^* - \dfrac{1}{\mathrm{We}} \right) D - k U_0^* \int_0^{L^*} D^{-1}\, dx^* \\ D & O \end{bmatrix} \begin{pmatrix} \xi \\ \eta \end{pmatrix} \quad (34)$$

where I, O, M and D are the identity, null, temporal derivative and spatial derivative operators, respectively. The boundary conditions assumed here are $\xi(0) = \eta(0) = 0$. The second raw of the system (34) represents the explicit enforcement of the Schwartz equality $\dfrac{\partial^2 \ell_0^*}{\partial t^* \partial x^*} = \dfrac{\partial^2 \ell_0^*}{\partial x^* \partial t^*}$ [9].
A Chebychev spectral collocation method has been used for the discretization of the spatial differential operators. For the temporal integration a semi-implicit ϑ-method scheme has been employed. The initial disturbance is constituted by the optimal global disturbance, i.e. the disturbance that maximizes the amplifications of the system energy for all the possible initial conditions, the so-called growth function $G(t)$. This last has been computed by following the methodologies described in [10].
The comparison between the temporal evolution of the energy optimal amplification and the temporal rate of change of the energy computed via direct numerical simulation is depicted in Figures 2 and 3 for the cases of absence of surface tension, $\mathrm{We} = \infty$, and $\mathrm{We} = 2$, respectively, and $L^* = 5$. The parameter k defined after equation (31) is kept equal to 576 in all the computations.
The case $\mathrm{We} = \infty$ is characterized by low frequency oscillations of optimal energy amplification (pulses of energy reproducing at regular time periods) and high frequency oscillations within each pulse. It is also evident that the pulse peaks exhibit a decreasing time behaviour due to the fact that only eigenfunctions associated to stable modes have been taken into account. In other terms, from this aspect, the flow system appears to be asymptotically stable, although the whole spectrum contains an unstable branch. The low frequency oscillations are produced by a continuous forcing (self-induced by the global dynamics) that triggers a new pulse on the left

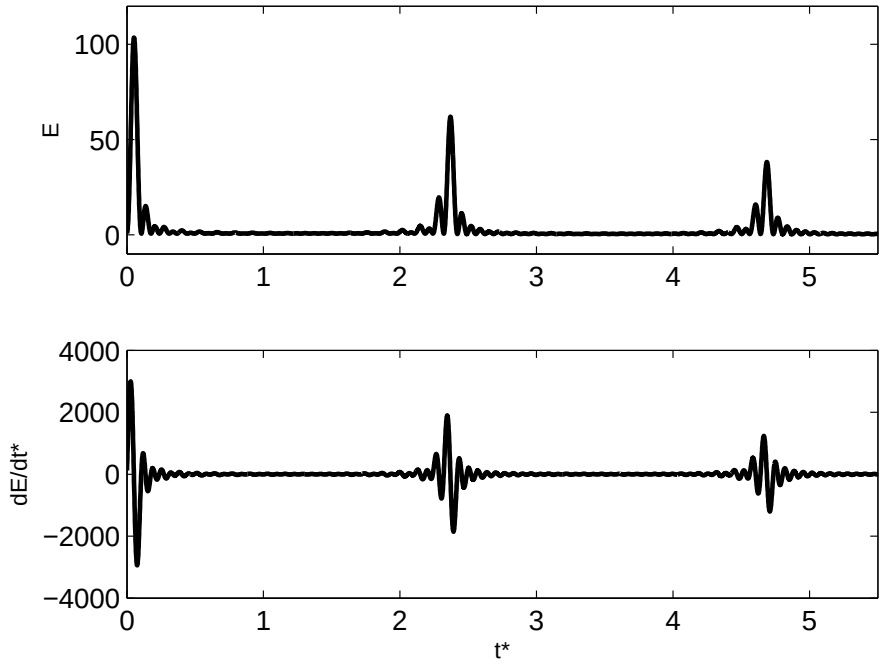

Figure 2: Optimal energy amplification E and direct numerical simulation of dE/dt^* for We $= \infty$ and $L^* = 5$

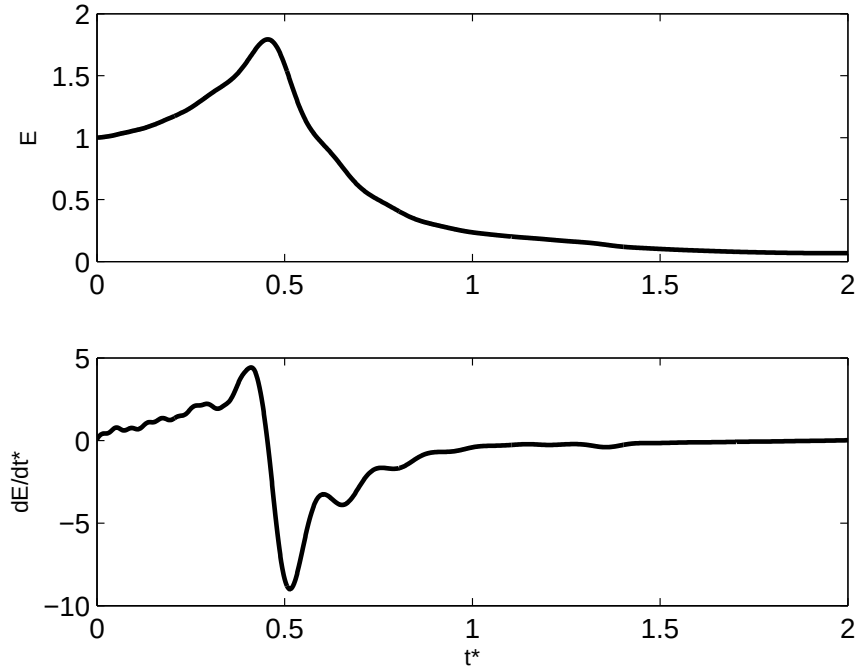

Figure 3: Optimal energy amplification E and direct numerical simulation of dE/dt^* for We $= 2$ and $L^* = 5$

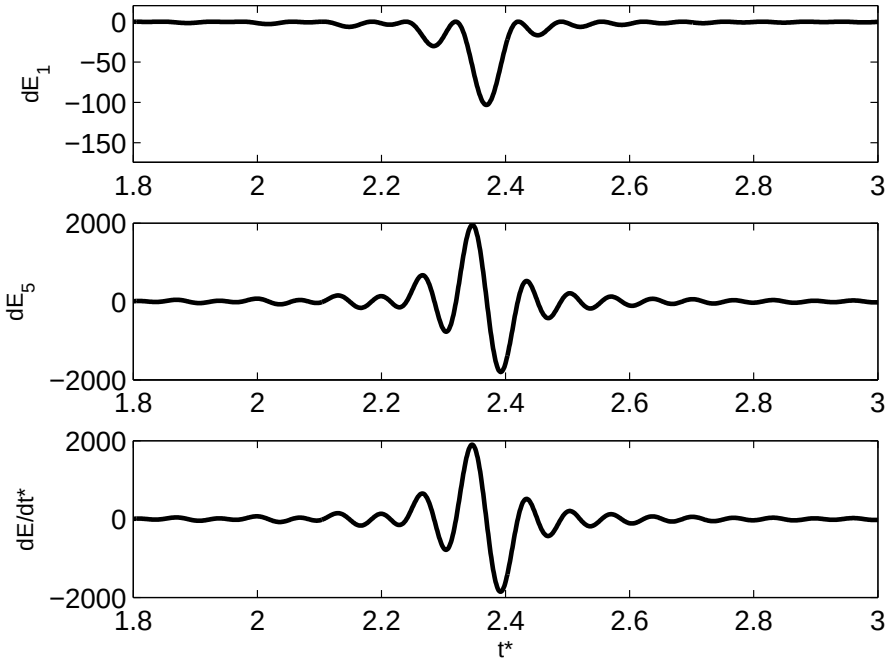

Figure 4: Energy budget terms and dE/dt^* for We $= \infty$ and $L^* = 5$

boundary when the previous pulse is being expelled from the right one. The period of such a behaviour is strictly related to the fall time of the sheet ([11], [12]). The high frequency oscillations, on the contrary, are due to the interaction of the compressed/expanded air cushion with the compliant sheet interface, acting like a mass (the liquid sheet) - spring (the air enclosure) system.

When the surface tension is present (We $= 2$ in Figure 3) the entire spectrum is stable and one pulse of energy amplification is only present, which decays asymptotically in time. This occurrence may be explained by considering that the asymptotic stable nature of the system prevents the triggering of a subsequent pulse when the first one is expelled.

Figures 4 reports, for We $= \infty$, a detailed view of the time variation of the second pulse of $\dfrac{dE}{dt^*}$ showed in the previous Figure 2, together with the corresponding trends of dE_1 and dE_5 (the other terms being of course null in this case). It is clearly evident that the energy amplification is essentially caused by the work done per unit time by the enclosure pressure, dE_5. In correspondence of the expulsion of the pulse the outlet convective exchange of kinetic energy yields a negative contribution (the analogous inlet contribution vanishes because of the imposed boundary condition).

The period of the high frequency oscillations of $\dfrac{dE}{dt^*}$ (namely of the pressure work) can be estimated by considering that the flow system can be globally modeled as a lumped one-degree of freedom spring-mass system, where the equivalent elastic constant of the spring (the air cushion) is

$$k_{eq} = \frac{\gamma P^*_{a0} L^*}{W^*} \tag{35}$$

whilst the equivalent mass (of the liquid) is given by

$$m_{eq} = \int_0^{L^*} H^*_0 \, dx^* \tag{36}$$

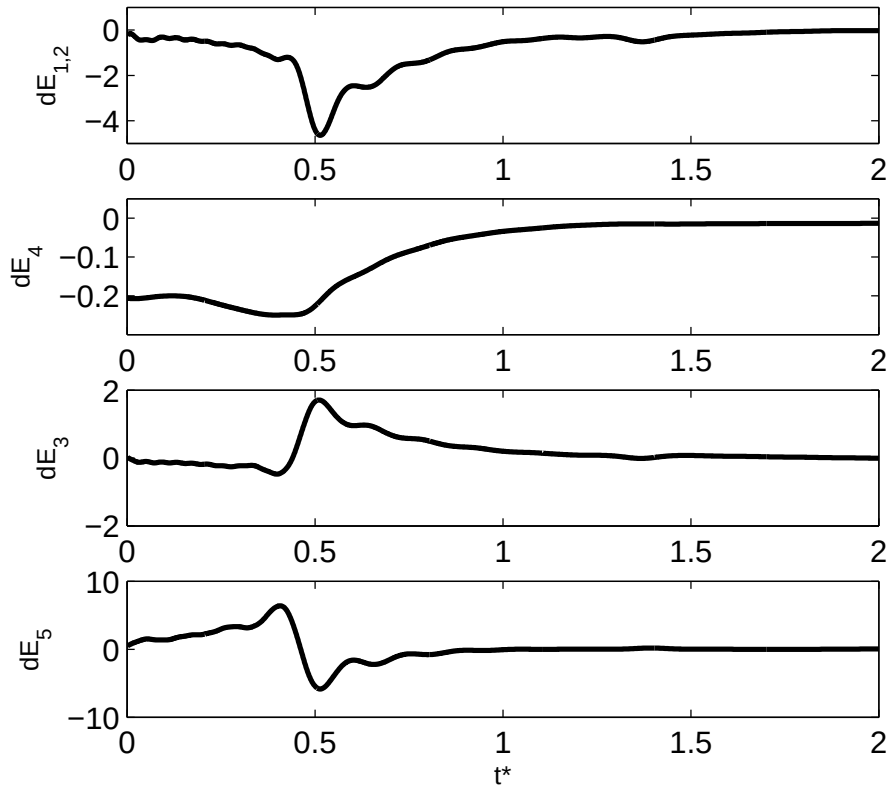

Figure 5: Energy budget terms for We $= 2$ and $L^* = 5$

The oscillation period can be evaluated accordingly as

$$T_p = 2\pi\sqrt{\frac{m_{eq}}{k_{eq}}} = 0.08 \tag{37}$$

which is in strict agreement with the numerical computations of Figure 4.
In Figure 5, the relevant energy budget terms are depicted, for We $= 2$; the outlet convective exchanges of kinetic and surface tension energies have been conveniently substituted by their sum $dE_{1,2}$ which, as for We $= \infty$, exhibits a negative peak when the disturbance comes out from the domain; dE_5 exhibits only an oscillation cycle because of stabilizing effects caused by the surface tension; dE_4 acts as an energy destruction term that is transferred from the disturbance to the base flow.
In order to further appreciate the role played by the various terms of the energy balance, some specific simulations have been carried out for We $= 2$ in the absence of external pressure, where the initial shape of the perturbed interface is a gaussian pulse located at the inlet boundary.
Figure 6 shows the time evolution of system energy as well as its rate of change, while Figure 7 depicts the various contributions to the budget. It should be considered that in the presence of the surface tension the initial packet splits while travelling down the sheet according to the different speeds of the two characteristic curves along with disturbances propagate [12]. The played rule by the term dE_4 is crucial in this case; it causes the initial decay rate showed by the energy trend of Figure 6. All the other terms evaluated at the exit boundary exhibit two peaks when each of two packets is expelled; this behaviour can be explained by interpreting the time variations of such terms as lagrangian variations of the slope of the gaussian shape of the pulse evaluated by an observer located at the exit boundary, while the pulse is travelling outwards.

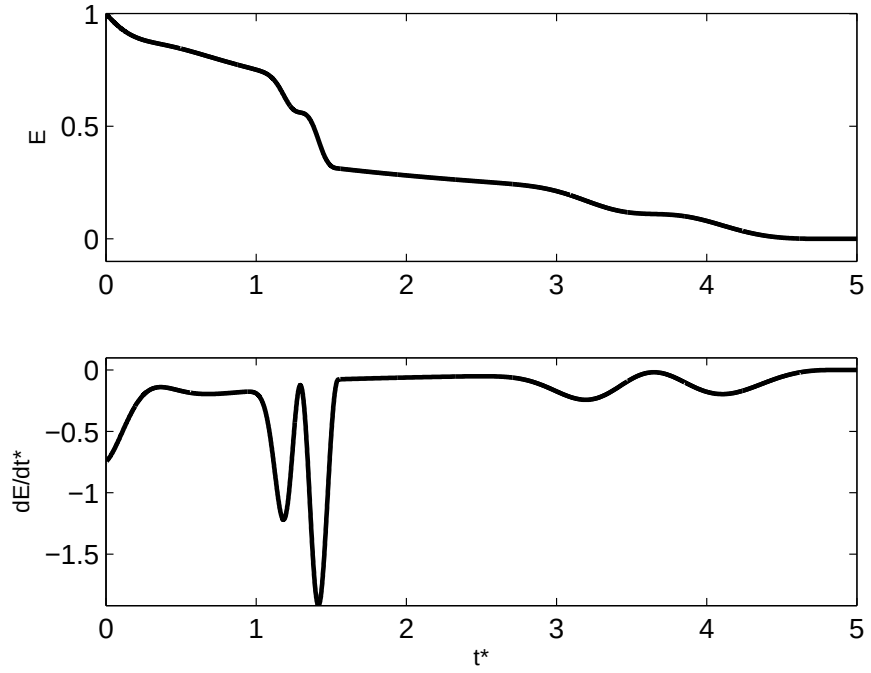

Figure 6: Gaussian disturbance energy and its derivative for We $= 2$ and $L^* = 5$

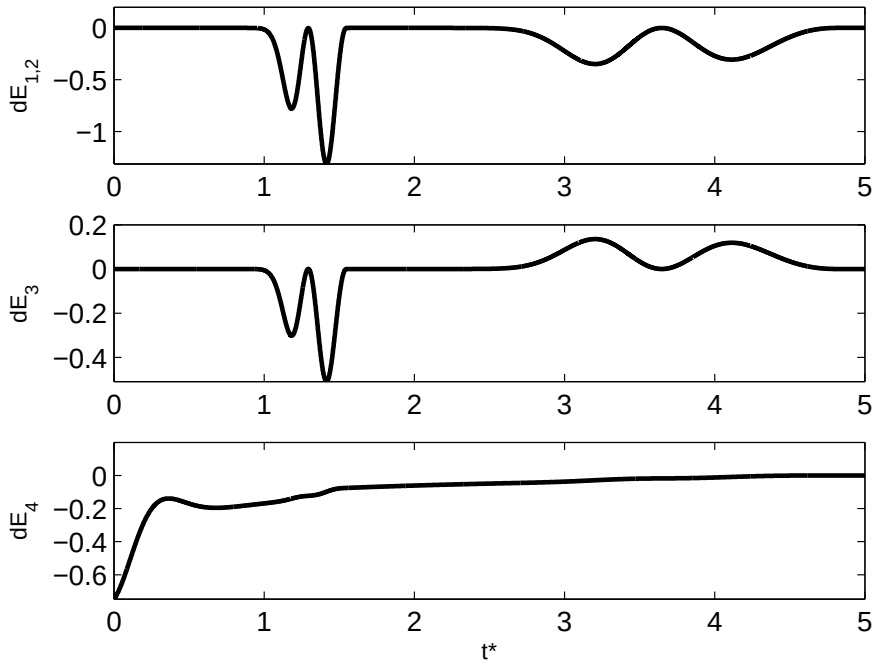

Figure 7: Gaussian disturbance energy budget terms for We $= 2$ and $L^* = 5$

4 CONCLUDING REMARKS

The unsteady global dynamics behavior of a free-interface vertical liquid sheet flow has been studied, where such a behavior has been defined global because it refers to the entire fluid system as a whole. The first part of the paper dealt with the formal development of a proper mathematical model, which accounts of a particular kind of disturbances in the external gaseous ambient, constituted by an enclosure limited by solid walls, a bottom liquid basin and one of the two sheet interfaces.
When the surface tension is absent ($We = \infty$) the time trend of the flow system energy exhibits low frequency and high frequency oscillations. The first ones are due to the continuous triggering of a new disturbance pulse at the inlet boundary, while the latter ones are related to the interaction of the air enclosure with the liquid sheet, acting as a spring-mass lumped system.
The surface tension (case of $We = 2$) shows a stabilizing effect that is responsible of the presence of only one energy peak of the energy amplification.

ACKNOWLEDGEMENTS

This work has been developed within the F.A.R.O. project, funded by Compagnia di S. Paolo and Polo delle Scienze e delle Tecnologie of Università degli Studi di Napoli Federico II.

REFERENCES

[1] S.P. Lin, Z.W. Creighton and B.J. Creighton, "Absolute and convective instability of a liquid sheet," J. Fluid Mech. **220**, 673 (1990).

[2] L. de Luca and M. Costa, "Instability of a spiatially developing liquid sheet," J. Fluid Mech. **331**, 127 (1997).

[3] L. de Luca, "Experimental investigation of the global instability of plane sheet flows," J. Fluid Mech. **399**, 355 (1999).

[4] S. J. Weinstein, A. Clarke, A. G. Moon and E. A. Simister, "Time-dependent equations governing the shape of a two-dimensional liquid curtain, Part 1: Theory," Phys. Fluids. **9**, 3625 (1997).

[5] P. J. Schmid and D. S. Henningson, "On the stability of a falling liquid curtain," J. Fluid Mech. **463**, 163 (2002).

[6] Y. Sato, S. Miura, T. Nagamine, S. Morii and S. Ohkubo, "Behavior of a falling water sheet," J. of Environment and Engineering. **2**, 394 (2007).

[7] C. Mehring and W. A. Sirignano, "Nonlinear capillary wave distortion and disintegration of thin planar liquid sheets," J. Fluid Mech. **388**, 69 (1999).

[8] G. Coppola, F. De Rosa and L. de Luca, "Surface tension effects on the motion of a free-falling liquid sheet," Phys. Fluids. **25** (6), 062103 (2013); doi: 10.1063/1.4810751

[9] Z. Jackiewicz, R.A. Renaut, "A note on stability of pseudospectral methods for wave propagation," Journal of Computational and Applied Mathematics **143**, 143 (2002).

[10] P. J. Schmid & D. S. Henningson, "Stability and Transition in Shear Flows," Springer (2001).

[11] G. Coppola and L. de Luca, "On transient growth oscillations in linear models," Phys. Fluids **18** (7), 078104 (2006).

[12] M. Girfoglio, F. De Rosa, G. Coppola and L. de Luca, "Global eigenmodes of free-interface vertical liquid sheet flows," WIT Transactions on Engineering Sciences. **79**, 285, ISSN: 1743-3533 (2013).